


Assessing Agulhas leakage



Erik van Sebille

Assessing Agulhas leakage

Het schatten van het Agulhas lekverlies

(met een samenvatting in het Nederlands)

Proefschrift

ter verkrijging van de graad van doctor aan de Universiteit Utrecht op
gezag van de rector magnificus, prof. dr. J. C. Stoof, ingevolge het
besluit van het college voor promoties in het openbaar te verdedigen
op 26 oktober 2009, des middags te 4.15 uur

door

Erik van Sebille

geboren op 20 augustus 1981, te Rotterdam

Promotoren: Prof. dr. W. P. M. de Ruijter
Prof. dr. P. J. van Leeuwen

This research was sponsored by the SRON User Support Programme under Grant EO-079, with financial support from the Netherlands Organization for Scientific Research, NWO.

Assessing Agulhas leakage

Erik van Sebille

ISBN: 978-90-393-5131-4

Printed in August 2009 by Ipskamp drukkers in Enschede, the Netherlands.

This work is licensed under the Creative Commons Attribution 3.0 License. To view a copy of this license, visit <http://creativecommons.org/licenses/by/3.0/>

Cover: Coastline of Africa in the Agulhas region.

"How inappropriate to call this planet Earth when it is quite clearly Ocean."

Arthur C. Clarke (1917 – 2008)

Contents

1	Introduction	1
1.1	The Agulhas system in the global overturning circulation	1
1.2	Interocean exchange versus Agulhas leakage: The return flow problem	4
1.3	Adjacent gyres: The Agulhas stagnation point	5
1.4	Bathymetry of the Agulhas region	6
1.5	Dynamical features in the Agulhas system	8
1.6	Variability in the Agulhas system	16
1.7	Estimating the magnitude of Agulhas leakage	17
1.8	Numerical Lagrangian floats as water samplers	19
1.9	Central question in this dissertation	20
2	Lagrangian trajectory model validation	25
2.1	Introduction	26
2.2	The two-sample Kolmogorov–Smirnov test	28
2.3	The Agulhas region data	31
2.4	Qualitative skill assessment	34
2.5	Model validation along one-dimensional sections	36
2.6	Two-dimensional model validation	40
2.7	Conclusions and discussion	41
3	Fast decay of Agulhas rings	45
3.1	Introduction	46
3.2	The model	48
3.3	Upstream control of float fate	52
3.4	The decay of relative vorticity	55
3.5	Change in feature size	59
3.6	Comparison with the decay of two-dimensional turbulence	64
3.7	Conclusions and discussion	65
4	Agulhas ring energy in the Atlantic Ocean	69
4.1	Introduction	70
4.2	The model	72
4.3	Flat bottom energy transfer time scales	76
4.4	Meridional ridge energy transfer time scales	78

4.5	Implementing a meridional overturning circulation	82
4.6	Response of the meridional overturning circulation	85
4.7	Conclusions and discussion	87
5	Relating Agulhas leakage to the retroflexion location	91
5.1	Introduction	92
5.2	Tracking the Agulhas Current	93
5.3	Relating the retroflexion front retreat to ring size	95
5.4	Measuring the Lagrangian Agulhas leakage transport	98
5.5	Relating Agulhas leakage to sea surface height	101
5.6	Application to altimetry data	103
5.7	Conclusions and discussion	106
6	Relating Agulhas leakage to the Agulhas Current strength	109
6.1	Introduction	110
6.2	The model	111
6.3	Relating Agulhas system inflow and outflow	111
6.4	Inertial outcropping	112
6.5	Application in a monitoring program	114
6.6	Conclusions and discussion	117
7	Relating Agulhas leakage to fluxes at the GoodHope line	119
7.1	Introduction	120
7.2	The model	122
7.3	Qualitatively comparing the flux profiles	123
7.4	An optimum thermohaline threshold method	125
7.5	An optimum Euclidean integration method	131
7.6	Conclusions and discussion	135
8	Conclusions: Assessing Agulhas leakage in the real ocean	137
8.1	Comprehending Agulhas leakage	137
8.2	Estimating the magnitude of Agulhas leakage	139
8.3	Outlook	142
	Bibliography	145
	Summary	155
	Samenvatting (in Dutch)	159
	Epilogue	163
	Curriculum vitae	165

Chapter 1

Introduction

1.1 The Agulhas system in the global overturning circulation

Due to its large thermal inertia, the world ocean plays an important role in climate variability on the decadal to millennial time scales [Broecker, 1997]. While the shorter of these time scales (less than approximately 50 years) are associated mainly with variability in the horizontal wind-driven circulation, the longer of these time scales are related to variability in the global overturning circulation [Schmitz Jr, 1995; Van Aken, 2007].

The global (meridional) overturning circulation is related to variations in density within the ocean. To first order the ocean is stably stratified with denser water at larger depths. The energy in the ocean supplied by the wind and tides is partly used to mix dense water from the deep ocean upwards into the thermocline [Munk and Wunsch, 1998]. In order to close the mass balance, the water which is brought upwards in this way eventually has to return to the deep ocean by sinking. While the upwelling occurs in many regions of the world ocean, the sinking occurs at only a few specific locations: in the northern Atlantic Ocean and adjoining regional seas and around the edges of Antarctica.

When the water gains buoyancy (either through cooling by the atmosphere and brine rejection around the edges of Antarctica or through cooling by the atmosphere and evaporation in the northern Atlantic Ocean) it is able to sink and form Deep Water. Since the regions of upward diffusion are far away from the regions of sinking, there is a lateral mass flux associated with this vertical mass exchange [e.g. Ganachaud and Wunsch, 2000]. In the thermocline the water flows from the Indian and Pacific Oceans to the northern Atlantic Ocean and the edges of Antarctica, while the flow in the deep ocean is the other way around (Fig. 1.1).

It is thought that the global overturning circulation can play an important role in rapid climate change [Clark et al., 2002; Bryden et al., 2005b] since it

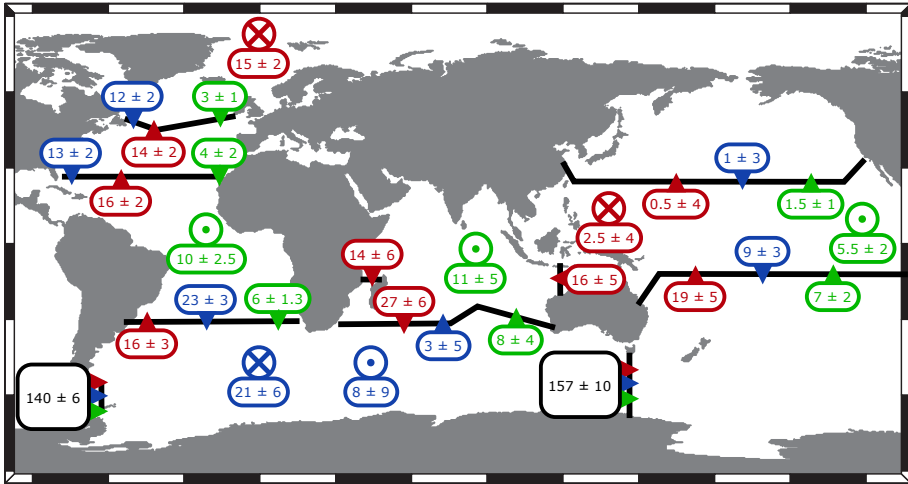


Figure 1.1: A three-layer schematic of the global meridional overturning circulation, with deep water in green labels, intermediate water in blue labels, and thermocline water in red labels. The Southern Ocean estimates (black labels) are for the total water column. Estimates of the transport across horizontal sections are given together with the cross-isopycnal fluxes (\otimes downward and \odot upward, totals for the entire basins) in sverdrup ($1 \text{ sverdrup} \equiv 10^6 \text{ m}^3 \text{ s}^{-1}$). The uncertainties in these fluxes are also given. This figure is adapted from Fig. 2 of *Ganachaud and Wunsch* [2000], who used hydrographic sections from the WOCE program in an inverse modeling study. Note especially the order of magnitude difference in fluxes between the two Southern Ocean sections and all other sections.

controls a large portion of the global poleward heat transport, especially in the northern Atlantic Ocean. Simple analytical models and numerical model simulations suggest [*Stommel, 1961; Rahmstorf et al., 2005*] that the Atlantic meridional overturning circulation has multiple equilibria, with an ‘on’ state (when there is formation of North Atlantic Deep Water) and an ‘off’ state (when there is no such formation). The system might be able to switch between these two stable regimes by salt anomalies or perturbations of the fresh water budget in the regions of Deep Water formation.

Such salt anomalies could either be created locally (by for instance large-scale melting events and consequent pulses of fresh water), or be imported from other parts of the world ocean. There are three major pathways of the thermocline return branch of the Atlantic meridional overturning circulation into the Atlantic Ocean [e.g. *Donners and Drijfhout, 2004*]: (1) from the Pacific Ocean to the Atlantic Ocean through Drake Passage, (2) from the Pacific Ocean to the Atlantic Ocean through Bering Strait and the Arctic Ocean, and (3) from the Indian Ocean to the Atlantic Ocean through the Agulhas region.

In contrast to the first two pathways, which are (sub)polar, the route through the Agulhas region is subtropical. The consequence of this is that the water returning into the Atlantic Ocean via the Agulhas region is warmer

and more saline than the water flowing via the other two routes. *Weijer et al.* [1999, 2002] showed in a numerical ocean model, later confirmed by *Marsh et al.* [2007], that a salt anomaly in the South Atlantic Ocean is advected northward on time scales of decades. Once the anomaly arrives in the regions of North Atlantic Deep Water formation it can affect the buoyancy of the water, change the formation rate of Deep Water, and thereby alter the strength of the Atlantic meridional overturning circulation. Thus the Agulhas region seems to have a large influence on the formation rate of Deep Water in the northern Atlantic Ocean [*Gordon*, 1986] and hence European climate [*Vellinga and Wood*, 2002].

The possibly large impact on North Atlantic Deep Water formation of the interocean exchange around Africa, the so-called warm water route of the global overturning circulation, is not only acknowledged in numerical ocean modeling studies. There is evidence from paleoceanographic studies that Northern Hemisphere climate variability and (the termination of) glacial cycles are closely linked to the magnitude of the flux of thermocline water from the Indian Ocean to the Atlantic Ocean. Based on planktic foraminiferal proxies in sediment cores, where different species indicate the presence of different water masses, *Peeters et al.* [2004] show that during Northern Hemisphere glacial periods the flux of thermocline water from the Indian Ocean to the Atlantic Ocean was strongly reduced. The role of the Indian–Atlantic interocean exchange seems to be particularly large in the resumption of the North Atlantic Deep Water production. Both *Knorr and Lohmann* [2003] and *Peeters et al.* [2004] find that the termination of glacial periods is led by an increased flux of warm Indian Ocean water into the Atlantic Ocean.

It is not completely apparent how exactly North Atlantic Deep Water formation and interocean exchange are related. The temporal resolution in the paleoceanographic proxies is generally too low to determine the relative timing of quickly (centennial time scale) succeeding events. A decrease in North Atlantic Deep Water formation could be caused by a decrease in the Indian–Atlantic interocean exchange, or vice versa. However, there are arguments for the first causal sequence, where the northern Atlantic Ocean trails the Agulhas region. As shall be discussed later in this introductory chapter, the circulation in the Agulhas system is predominantly wind-driven.

Changes in the magnitude of Indian–Atlantic interocean exchange are thus primarily related to changes in the Indian Ocean wind field [*De Ruijter*, 1982]. *Howard and Prell* [1992] have shown that the wind-driven gyres and their associated fronts in the Indian Ocean migrate with the glacial cycles and *Zharkov and Nof* [2008a,b] show that the interocean exchange can be seized when the latitude where the magnitude of the wind stress curl is zero in the Indian Ocean moves northward. Therefore, a northward move of the wind pattern might cause the Indian Ocean circulation to be disconnected from the Atlantic Ocean circulation, effectively choking the Indian–Atlantic interocean exchange. Note that such studies, however, do not truly solve the cause and effect problem, as they pose new questions on the relation between Indian Ocean wind patterns and North Atlantic Deep Water formation. Since the components of the global

climate are so intertwined, searching for a clear causal sequence might be very difficult.

On interannual and decadal time scales, however, high-resolution model studies suggest that changes in the Agulhas system circulation are able to perturb the formation rate of North Atlantic Deep Water [Bjastoch *et al.*, 2008b,c]. The interocean fluxes south of Africa, especially the flux of thermocline water from the Indian Ocean to the Atlantic Ocean, might be a precursor of Atlantic meridional overturning circulation variability. That is why the goal of this dissertation, an assessment of the Indian–Atlantic interocean exchange, is needed: Both for an increase in the comprehension of the system’s sensitivity and variability and to propose a possible design of a monitoring system. Ultimately, such a monitoring system might be employed to predict changes in the Atlantic meridional overturning circulation on interannual to decadal time scales.

1.2 Interocean exchange versus Agulhas leakage: The return flow problem

In the previous section, the fluxes in the Agulhas region have been discussed in terms of the Indian–Atlantic interocean exchange. The topic of this dissertation, however, is Agulhas leakage. In the nomenclature used here, these two terms stand for different concepts. Interocean exchange is the two-way vertically integrated flux between the Indian Ocean and the Atlantic Ocean. Agulhas leakage, on the other hand, is here defined as only that part of the interocean exchange flowing from the Indian Ocean to the Atlantic Ocean. More specifically, Agulhas leakage is the water that flows through the Agulhas Current and gets into the South Atlantic Ocean.

The Indian–Atlantic interocean exchange is, as already discussed, closely related to the Atlantic meridional overturning circulation, which is in turn closely related to heat and salt fluxes in the Atlantic Ocean. To understand the influence of the Indian–Atlantic interocean exchange on North Atlantic Deep Water formation, however, it does not suffice to know what the thermohaline (temperature and salinity) properties of the water imported into the Atlantic Ocean are. The North Atlantic Deep Water formation rate also depends on the thermohaline properties of the water exported from the Atlantic Ocean [e.g. Rahmstorf, 1996; Weijer *et al.*, 1999; Huisman *et al.*, 2009]. This problem was already identified by Gordon [1985], who stated that uncertainties in the estimate of heat fluxes into the Atlantic Ocean can to a large extent be attributed to the problem of determining the heat transport of the deep flow from the Indian Ocean to the Atlantic Ocean.

The thermohaline properties of Atlantic–Indian transport are even less known than the properties of the Indian–Atlantic transport (the Agulhas leakage). Beal and Bryden [1997] have observed a northward flowing undercurrent near the continental slope at 32°S in the Indian Ocean. The undercurrent is 6 Sv in strength ($1 \text{ Sv} = 10^6 \text{ m}^3 \text{ s}^{-1}$) and consists of North Atlantic Deep

Water and Antarctic Intermediate Water. *Arhan et al.* [2003] estimated from hydrographic sections that 11 Sv of North Atlantic Deep Water is exported from the Atlantic Ocean into the Indian Ocean, with only 3 Sv in a northward flowing undercurrent and the rest flowing eastward. This 3 Sv magnitude of the undercurrent was confirmed by *Casal et al.* [2009] using in situ current profiles.

There have been attempts to quantify the interocean exchange of heat and salt [e.g. *Treguier et al.*, 2003; *Reason et al.*, 2003], but these are often confined to fluxes within the thermocline (upper ocean) in a regional model. One of the most extensive of these studies is by *You et al.* [2003], who investigated the circulation of intermediate water masses in the Agulhas region using floating instruments and hydrographic stations. However, also this study did not consider the depth-integrated fluxes and the authors could therefore not give an estimate of the net volumetric fluxes in the Agulhas region.

The interocean exchange south of Africa can only be studied in a global context and on interdecadal time scales. The methods employed in this dissertation are not suited for studying interocean exchange in such a way. The focus is therefore shifted to Agulhas leakage, as that is easier to quantify but may still elucidate on the dynamics of the Agulhas system.

1.3 Adjacent gyres: The Agulhas stagnation point

The Agulhas leakage was treated in section 1.1 in the perspective of the global overturning circulation. However, the circulation in the Agulhas region is predominantly horizontal and controlled by the wind stress. Both the Indian Ocean and South Atlantic Ocean have a subtropical gyre system (Fig. 1.2). The western boundary current of the Indian Ocean subtropical gyre is the Agulhas Current, the Brazil Current plays the same role in the South Atlantic Ocean subtropical gyre. South of these two gyres, in the Southern Ocean, lies the Subtropical Front. This front is the most northern of a series of fronts in the Antarctic Circumpolar Current.

In contrast to what is depicted in the cartoon of Fig. 1.2, these three circulation systems are not disconnected. Due to eddy mixing, there is exchange of water between the southern branches of the subtropical gyres and the Antarctic Circumpolar Current [e.g. *De Szoeké and Bennett*, 1983]. Since the Indian Ocean and South Atlantic Ocean subtropical gyres are also connected (through the Agulhas leakage), the entire system can be regarded as one large gyre encompassing two oceans. This supergyre [*Speich et al.*, 2002] might even be considered to also include the subtropical gyre of the southern Pacific Ocean through Tasman leakage.

The Agulhas region is the locus of these three circulation systems. The point where the three gyres meet can be regarded as a stagnation point [*De Ruijter*, 1982]. The location of this stagnation point controls the fate of water as it flows into the Agulhas region. In this concept, water that flows from the

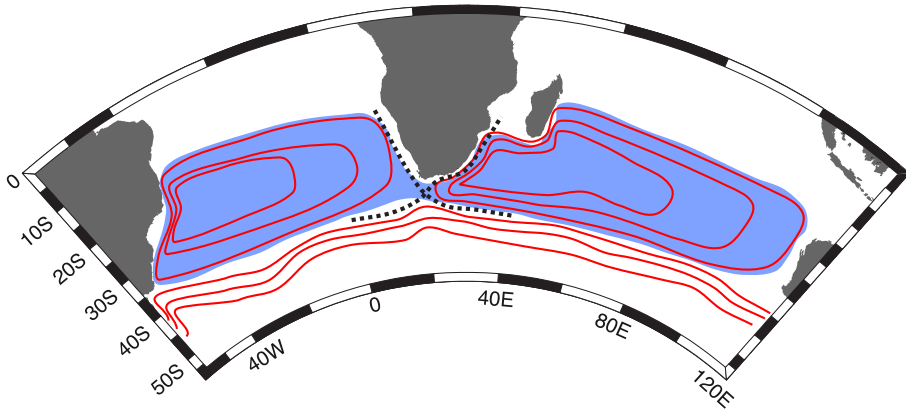


Figure 1.2: A schematic (red lines) of the three circulation systems adjacent to the Agulhas region: the South Atlantic Ocean subtropical gyre, the Indian Ocean subtropical gyre, and the Subtropical Front of the Antarctic Circumpolar Current in the Southern Ocean. The circulation in the two gyres is counterclockwise, the flow along the front is eastward. This leads to a stagnation point in the circulation south of Africa, denoted by the intersection of the two thick dashed lines. These two dashed lines separate the system in four circulation patterns. On the southwest/northeast line the flow is towards the stagnation point, while it is away from the stagnation point on the northwest/southeast line. The blue area denotes the supergyre, the gyre encompassing the Indian and Atlantic Oceans [Speich *et al.*, 2002].

Indian Ocean towards the stagnation point from north of the dividing line (the southwest/northeast dashed line in Fig. 1.2) ends in the Atlantic Ocean as Agulhas leakage, whereas water south of this line ends in the Indian Ocean. The location of the stagnation point and dividing lines is not constant in time. This concept is not entirely correct, as shall be shown in this dissertation (chapter 3), but it illustrates the subtle interaction between the three oceans in the Agulhas region. The concept of a stagnation point also highlights the sensitivity of the magnitude of Agulhas leakage to changes in not only the Indian Ocean circulation but also the other two oceans. Furthermore, it shows that quantifying the magnitude of Agulhas leakage, a small flux in the vicinity of three much larger circulation systems, may prove very difficult.

1.4 Bathymetry of the Agulhas region

Despite its important role in the global ocean circulation, the Agulhas system is to a large extent controlled by the details of the bathymetry in the Agulhas region [e.g. Lutjeharms and Van Ballegooyen, 1984; Lutjeharms and Webb, 1995]. The Agulhas region extends eastward and westward of the southernmost point of Africa (Cape Agulhas at 20°E) for some 2500 km (Fig 1.3). The continental shelf around Cape Agulhas is broad, forming the shallow Agulhas

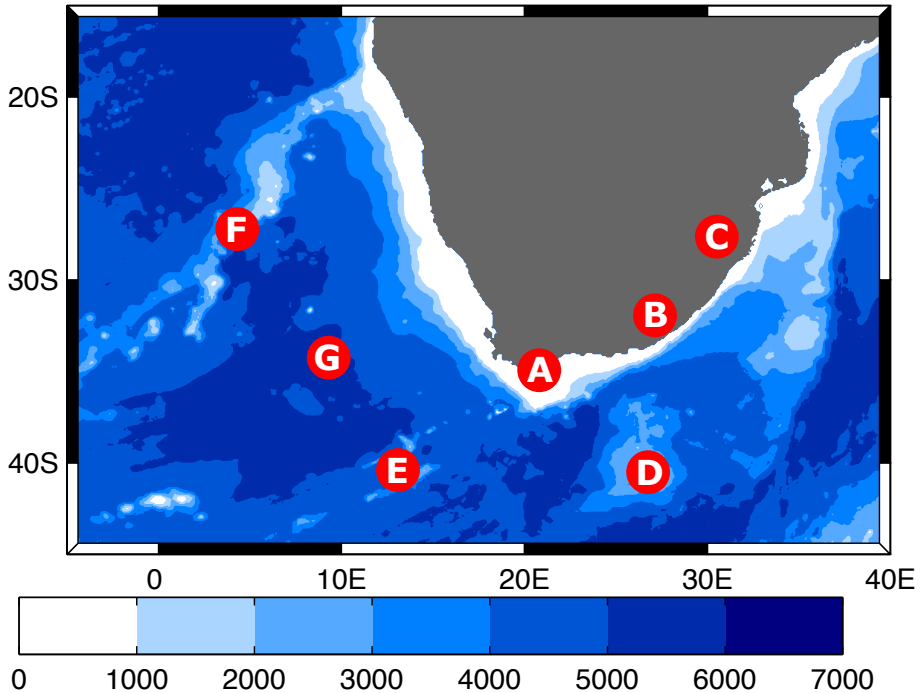


Figure 1.3: The bathymetry of the greater Agulhas region, in meter. The letters denote the key bathymetric features in the region as described in the text: (A) the Agulhas Bank, (B) the steep continental slope, (C) the Natal Bight, (D) the Agulhas Plateau, (E) the Agulhas Ridge, (F) the Walvis Ridge, and (G) the Cape Basin.

Bank (feature A in Fig. 1.3) which is no more than 150 m deep. Moving northeastward into the Indian Ocean, the width of the continental shelf quickly decreases. Along the southeastern African coast the continental slope is narrow and steep (feature B in Fig. 1.3), until the slope widens again at the Natal Bight (feature C in Fig. 1.3). The Agulhas Plateau (feature D in Fig. 1.3) is a 3000 m high rise southeast of the Agulhas Bank, a few hundred kilometers offshore in the Indian Ocean, which has a profound influence on the Agulhas system (see also section 1.5.3).

In the Atlantic Ocean, the most prominent bathymetric features are the two southwestward oriented ridges. The Agulhas ridge (feature E in Fig. 1.3) starts at Cape Agulhas and has some high peaks that seem to influence the path of Agulhas rings [Matano, 1996]. The second ridge is the Walvis Ridge (feature F in Fig. 1.3), 1500 km north of Cape Agulhas, which is a 3000 m high narrow and steep ridge. The area between the two Atlantic Ocean ridges is the Cape Basin (feature G in Fig. 1.3). Boebel *et al.* [2003a] introduced the term ‘Cape Cauldron’ for this region, as the coherent mesoscale structures (eddies) passing through the basin vigorously mix the different water masses in this region.

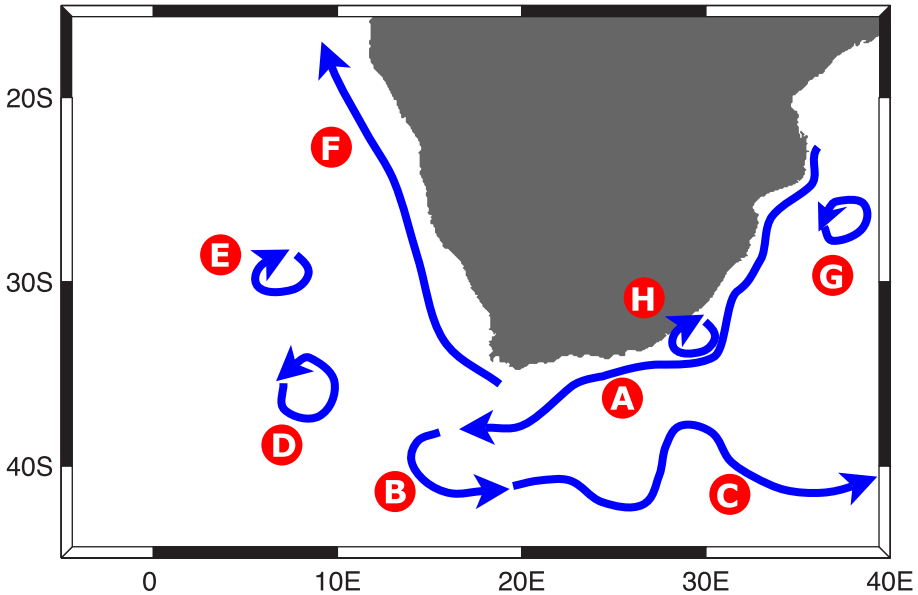


Figure 1.4: Schematic depicting the major features in the Agulhas system, as discussed in the text: (A) the Agulhas Current, (B) the Agulhas Current retroflexion, (C) the Agulhas Return Current, (D) an Agulhas ring, (E) other types of leakage, (F) the Benguela Current, (G) an eddy from the East Madagascar Current, and (H) a Natal pulse.

1.5 Dynamical features in the Agulhas system

The important role played by the Agulhas system in the global ocean circulation and climate might in part explain the growing interest in this region from the global physical oceanography community. In the last decade three important manuscripts on the Agulhas region have been published, to which this dissertation in general and this introductory chapter in particular are much indebted. First published of these was the review article on the Agulhas system by *De Ruijter et al.* [1999], synthesizing many of the observational results and placing these in a theoretical framework. A few years later came the special issue of *Deep-Sea Research II*, introduced by *Richardson et al.* [2003], publishing the results of the KAPEX and MARE field experiments augmented with some state-of-the-art numerical ocean model studies. The most recent was the book on the Agulhas system by *Lutjeharms* [2006], culminating much oceanographic knowledge on the region in an extensive overview with references to more than 800 scientific articles.

Focusing on the dynamics of the Agulhas system, there are a number of features that play a crucial role in the magnitude and sensitivity of Agulhas leakage (Fig. 1.4). Many of these features have been recognized for centuries already [*Lutjeharms et al.*, 1992], but their dynamics is still not completely understood. The Agulhas system has some features which are not found anywhere

else. Study of the system might therefore contribute greatly to the advancement of certain topics in dynamical oceanography. This will be illustrated by the discussion below of eight prominent and relevant features in the Agulhas system.

1.5.1 The Agulhas Current

The Agulhas Current (feature A in Fig. 1.4) is the western boundary current of the Indian Ocean subtropical gyre and is among the strongest western boundary currents in the world. It transports the Indian Ocean water into the Agulhas region. *Bryden et al.* [2005a] have measured the properties of the Agulhas Current at 32°S and they report a mean poleward transport of 70 Sv. The variability in transport, however, is large and the instantaneous transport ranges from 9 Sv to 121 Sv (although the lower of these transport values might also be related to offshore meanderings of the Agulhas Current so that it is outside the mooring array, see also section 1.5.7). At 32°S, where the continental slope is steep and narrow (Fig. 1.3), the Agulhas Current is only 200 km wide and 2200 m deep.

Feron et al. [1992] have reconstructed a tight recirculation of the Agulhas Current, of the order of tens of sverdrups, from satellite altimetry data. This tight recirculation is also present in the mean dynamic topography of *Rio and Hernandez* [2004] and in numerical ocean models [e.g. *Boudra and De Ruijter*, 1986]. It is caused by a rectification process of the circulation, a net time mean volume transport due to eddies [*Cessi et al.*, 1987], which can only be seen in time averaged sea surface height fields and not in snapshots [*Casal et al.*, 2009].

East of the Agulhas Bank, where the continental slope gets less steep, the Agulhas Current detaches from the continent. This detachment from the continental slope occurs by outcropping (see also section 6.4). In the explanation of *Ou and De Ruijter* [1986], a free streamline is created when there is an outcropping of the pycnocline. The magnitude of the terms in the vorticity balance are changed as the coastal current becomes a free jet. *Boudra and Chassignet* [1988] have investigated this change in a numerical study on the potential vorticity balance of the Agulhas Current (Fig. 1.5). When the current is attached to the continent, advection of relative vorticity balances the viscosity term at the parameter settings of their model. As a free jet, on the other hand, the advection of relative vorticity is balanced by stretching and planetary vorticity advection.

1.5.2 The Agulhas Current retroflection

After the Agulhas Current detaches from the continental slope and becomes a free jet, it retroflects [*Gordon*, 2003]. This retroflection is a tight loop of the current (feature B in Fig. 1.4) and has qualitatively been described by for instance *Lutjeharms and Van Ballegooyen* [1988]. The Agulhas Current retroflection connects the westward flowing Agulhas Current with the eastward

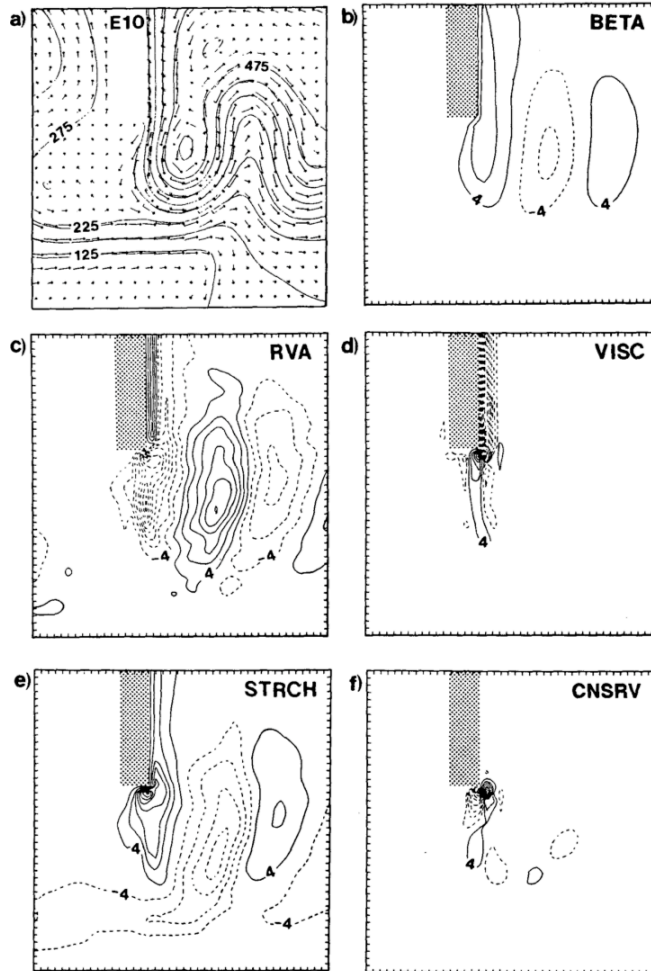


Figure 1.5: Results from the idealized three-layer numerical study by *Boudra and Chassignet* [1988, their Fig. 9] mimicking the Agulhas system. The shaded area is a Southern Hemisphere continent with no-slip boundary conditions. All panels show the five year mean in the upper layer of the model. Panel (a) shows the flow pattern, where the intense western boundary current retroflects as it detaches from the continent. The other five panels show the magnitude of the different terms of the potential vorticity balance: (b) the planetary vorticity advection, (c) the relative vorticity advection, (d) the eddy viscosity term, (e) the stretching term, and (f) the conservation of potential vorticity and enstrophy. The last term is a numerical artifact which results from the discretization of the vorticity balance and has no analogue in the differential vorticity equation. The contour interval for these potential vorticity terms is $8 \cdot 10^{-12} \text{ s}^{-1}$. Near the coast, the balance is between relative vorticity advection and viscosity. In the retroflexion area and the return current, the balance is between relative vorticity advection, stretching, and planetary vorticity advection.

flowing Agulhas Return Current. The retroflection is related to the supergyre (see section 1.3), as the Indian Ocean and South Atlantic Ocean subtropical gyres are only separated when the retroflection is complete and all transport in the Agulhas Current flows directly into the southern branch of the Indian Ocean subtropical gyre.

The Agulhas Current is not the only western boundary current that retroflects (the Brazil, the North Brazil, and the East Australia Currents do the same), but it is the only one that does so in the open ocean. *De Ruijter* [1982] was the first to analytically investigate under what conditions a free jet might retroflect.

According to the review by *De Ruijter et al.* [1999] there are five mechanisms which control the Agulhas Current retroflection: the amount of inertia in the Agulhas Current (which is related to the advection of relative and planetary vorticity), the slope of the background stratification (which works on the stretching term in the potential vorticity balance because isopycnals may get squeezed from the Indian to the Atlantic Oceans), the curvature of the coastline (which can initiate outcropping of the current), the bathymetry (which can steer the free jet), and the curl of the wind field (which determines the shape of the Indian Ocean subtropical gyre to which the retroflected current connects).

In a modeling study focused on the role of inertia, *Dijkstra and De Ruijter* [2001b] added a sixth control parameter to the list: eddy viscosity. According to the steady state modeling study, the Agulhas Current retroflection can be in two regimes in a numerical ocean model. In the inertial regime a strong Agulhas Current leads to an early detachment from the coast. Due to the curvature of the African continent such an upstream detachment leads to a more eastward retroflection, which in turn results in a low Agulhas leakage transport (see also chapter 6). In the viscous regime the Agulhas leakage transport is also low as the Agulhas Current is viscously choked. In between these two regimes, the Agulhas leakage transport is much higher. For some values of eddy viscosity the retroflection might even seize, creating a supergyre where all Agulhas Current water flows into the Atlantic Ocean. The latter states can be found only in models, particularly in low-resolution ones, when the eddy viscosity is too high. The high eddy viscosity leads to a thick (> 100 km) frictional boundary layer and the Agulhas Current will have less inertia per unit transport than in the inertial regime.

1.5.3 The Agulhas Return Current and early retroflections

After retroflecting, the current flows eastward as the Agulhas Return Current (feature C in Fig. 1.4). This current may be regarded as the southern branch of the Indian Ocean subtropical gyre. As shown by *Boebel et al.* [2003b], the initial path of the Agulhas Return Current seems to be controlled to a large extent by the Agulhas Plateau. After flowing past the Agulhas Plateau the current continues meandering. These downstream meanders are quasi-steady in time and have a wavelength of 500 – 700 km, which seems to result from

the balance between planetary vorticity advection and advection of ‘curvature vorticity’ [Ochoa and Niiler, 2007].

Sometimes the Agulhas Current retroflects east of the Agulhas Plateau. Such events are called early retroflections as the retroflexion is shifted anomalously far upstream in these events. There is not much known about early retroflections as only two have been observed in the real ocean: in 1986 [Shannon *et al.*, 1990] and at the end of 2000 [De Ruijter *et al.*, 2004]. This second documented early retroflexion lasted for more than half a year and in that time no Agulhas rings were formed. Due to the limited length of the satellite altimetry data set (less than 20 years), the frequency of early retroflections is difficult to determine. In many models, however, early retroflections seem to be too common. Biastoch *et al.* [2008c], for instance, report early retroflections at frequencies of once per two years, although this apparent discrepancy with the altimetry data might also be due to a shorter time span in which the Agulhas Current retroflexion has to be anomalously east before it constitutes an early retroflexion.

The location of the Agulhas Current retroflexion seems to be bimodally distributed, which the existence of prolonged early retroflections suggests. The retroflexion is then either west of the Agulhas Plateau in which case the magnitude of Agulhas leakage is normal, or east of the Plateau and in the latter case the flux of water into the Atlantic Ocean is negligible [Matano, 1996; Speich *et al.*, 2006]. The system might be able to switch between these two states when the forcing is changed. This view of the Agulhas leakage as being ‘on’ or ‘off’ depending on the position of the Agulhas Current retroflexion relative to the Agulhas Plateau may help in providing an explanation of how the magnitude of Agulhas leakage might have varied in a paleoceanographic context (section 1.1). Such a hypothesis, that because of different wind patterns during glacial periods the Agulhas leakage was ‘off’, is put forward by Peeters *et al.* [2004], confirmed in paleoceanographic data by Bard and Rickaby [2009], and verified by Zharkov and Nof [2008a] in a simple model.

1.5.4 Agulhas rings

The Agulhas Current retroflexion is not a steady loop. Its position varies in time and in that process Agulhas rings are shed from the westernmost extremity of the Agulhas Current. Agulhas rings (feature D in Fig. 1.4) are anticyclonic eddies which, after detachment from the Agulhas system, can move into the Atlantic Ocean.

Agulhas rings are large-scale features which can easily be detected in satellite data, both of sea surface temperature and sea surface height. This is one of the reasons why there have been many studies on the translation and geometry of these rings [Byrne *et al.*, 1995; Beismann *et al.*, 1999; Schouten *et al.*, 2000; Doglioli *et al.*, 2007]. An in situ investigation of the vertical structure of an Agulhas ring was performed by Van Aken *et al.* [2003] during the MARE experiment. From the aggregation of these studies it appears that Agulhas rings

have a radius of 150 – 200 km and that surface velocities can exceed 1 m s^{-1} . A ring is shed from the Agulhas Current retroflection every 2 – 3 months but that there may also be sustained periods (more than six months) without any ring being shed.

Agulhas rings are considered to be the most important transport agents of Indian Ocean water into the Atlantic Ocean. The decay of these anticyclones has therefore been studied extensively, both in models [*Kamenkovitch et al.*, 1996; *Drijfhout et al.*, 2003; *Donners et al.*, 2004; *De Steur et al.*, 2004; *Doglioli et al.*, 2007; *De Steur and Van Leeuwen*, 2009] and using observations [*Olson and Evans*, 1986; *Byrne et al.*, 1995; *Goni et al.*, 1997; *Schouten et al.*, 2000; *Schmid et al.*, 2003; *Richardson and Garzoli*, 2003]. From these studies, it appears that Agulhas rings go through considerable transformation in the Cape Basin. This affects the size, number, and thermohaline properties of the rings as well as the amount of water advected within the rings.

Several descriptions of the ring shedding mechanism have been presented. In the description by *Ou and De Ruijter* [1986] and further discussed by *Lutjeharms and Van Ballegooyen* [1988] and *Feron et al.* [1992], the essential component is that the western front of the Agulhas Current slowly moves westward most of the time. At some moment, the loop formed by the Agulhas Current and Agulhas Return Current occludes, an Agulhas ring pinches off, and the western front experiences an instantaneous eastward retreat. This loop occlusion cycle then starts over again with a slow westward movement of the front.

A different mechanism of the dynamics of the Agulhas Current retroflection and its associated ring shedding has been proposed by *Nof and Pichevin* [1996] and *Pichevin et al.* [1999]. In their ‘retroflection paradox’, based on a reduced gravity model of a retroflecting current, Agulhas rings are not formed due to instabilities in the retroflection loop, but are a necessity to be able to close the nonlinear momentum balance within the Agulhas region. Integrating over the entire region, the westward ageostrophic momentum imported by the Agulhas Current can not be balanced by the eastward ageostrophic momentum exported by the Agulhas Return Current. In the solution to the retroflection paradox, the additional westward export of ageostrophic momentum required to close the balance occurs through Agulhas rings.

This mechanism has further been discussed by *Van Leeuwen and De Ruijter* [2009], who prove that the momentum balance is unlikely to be closed when the system is assumed to be steady state, even in a multilayer description of the system. For a balance closure there has to be temporal variability in the Agulhas Current retroflection. This temporal variability can either be the shedding of Agulhas rings or variability in the position of the Agulhas Current retroflection. This latter possibility was overlooked by *Nof and Pichevin* [1996] in their discussion of the retroflection paradox.

A third mechanism explaining the shedding of Agulhas rings is put forward by *Dijkstra and De Ruijter* [2001a]. In contrast to the other two mechanisms, which focus on the local dynamics of ring formation, this mechanism deals with

a basin-wide incitement of ring shedding. The authors show in an (equivalent) barotropic shallow water model that Rossby basin modes can trigger variability near the retroflection. The anomalies which result from the variability can have a frequency and spatial pattern very similar to those of Agulhas rings. In their explanation, therefore, ring shedding is dominated by the basin modes and the large-scale circulation of the Indian Ocean.

1.5.5 Other types of leakage

The water which constitutes Agulhas leakage separates from the Agulhas Current mainly in the form of Agulhas rings. However, Agulhas cyclones (feature E in Fig. 1.4) are also occasionally spawned, mostly from the inshore side of the Agulhas Current as it detaches from the continental slope [Penven *et al.*, 2001]. These cyclones, smaller in size than anticyclonic Agulhas rings, can also advect the water in their core through the Cape Basin [Lutjeharms *et al.*, 2003], although it is not completely clear yet what the origin of the water inside these cyclones is. It might be water from the Agulhas Current, in which case it is Agulhas leakage, but it could also be water drawn locally from the Agulhas Bank.

Once they are spawned, these Agulhas cyclones and rings quickly decay [Byrne *et al.*, 1995; Schouten *et al.*, 2000]. Away from the Agulhas Current retroflection, therefore, a significant amount of Agulhas leakage is not trapped within eddies anymore. Instead, the water may be in small filaments [De Steur *et al.*, 2004]. Lutjeharms and Cooper [1996] observed that these filaments might also be peeled directly from the Agulhas Current.

Nevertheless, the Agulhas leakage is mixed with other water masses in the Cape Basin [Boebel *et al.*, 2003a]. Water initially in Agulhas rings may quickly be expelled from these rings to form small filaments. This implies that when Agulhas leakage is grouped into fractions by cyclones, by rings, and by filaments (as done by Doglioli *et al.* [2006]), the results depend on how far from the Agulhas Current retroflection the grouping is performed.

The relevance of such a categorization in types of leakage lies in the fate of the Agulhas leakage: Once Agulhas rings cross the Walvis Ridge their decay rate decreases and the water within the rings can be advected in the subtropical gyre of the South Atlantic Ocean. Water not within Agulhas rings, on the other hand, might have a completely different fate. In fact, the latter category might have a larger impact on the Atlantic meridional overturning circulation because part of the water not within Agulhas rings can escape the subtropical gyre and be advected directly to the northern Atlantic Ocean via the North Brazil Current.

1.5.6 The Benguela Current

The water which is advected by features spawned from the Agulhas Current retroflection is not the only northward flux in the southeastern Atlantic Ocean.

As was already explained in the discussion of the Agulhas stagnation point in section 1.3, the South Atlantic Ocean subtropical gyre has northward flow on its eastern side. This branch of the subtropical gyre is generally referred to as the Benguela Current [*Fennel, 1999*] (feature F in Fig. 1.4). On the inshore side of the current, the wind-driven Ekman transport divergence causes significant upwelling. This vertical circulation has been observed to advect tropical water southward [*Gordon et al., 1995*].

The Benguela Current is tightly linked to the Agulhas system. There is interaction between the features spawning from the Agulhas Current retroflection and the Benguela Current [*Richardson and Garzoli, 2003*]. During a 1992 – 1993 measurement campaign at 30°S in the Benguela Current in combination with an inverse modeling study, *Garzoli and Gordon [1996]* found that the northward transport consists for 25% of Indian Ocean water, 50% of Atlantic Ocean water, and 25% of water mixed from these sources.

1.5.7 Upstream connections

There is evidence that the timing of loop occlusions and variability in Agulhas ring shedding events are influenced upstream in the Agulhas Current by barotropic instabilities. The steep continental slope suppresses the development of these barotropic instabilities in most of the Agulhas Current, according to the study by *De Ruijter et al. [1999]*. At the Natal Bight, however, the slope angle decreases somewhat and barotropic instabilities can form if the Agulhas Current is perturbed. Such perturbations can come from eddies that are spawned at the southern tip of Madagascar [*Schouten et al., 2002*] (feature G in Fig. 1.4) or that move through the Mozambique Channel [*Biastoch and Krauss, 1999*].

The barotropic instabilities of the Agulhas Current at the Natal Bight express themselves as small cold-core cyclones, often referred to as Natal pulses [*Lutjeharms and Roberts, 1988*], which grow on the inshore side of the Agulhas Current (feature H in Fig. 1.4). The barotropic instability forms a wave-like perturbation on the Agulhas Current, which can grow up to 170 km. This offshore migration of the Agulhas Current leads to the generation of a small cyclone on the inshore side which, due to upwelling, has a cold core.

Natal pulses have an important impact on the timing of Agulhas ring shedding event. *Van Leeuwen et al. [2000]* correlated meander generation at the Natal Bight with Agulhas ring shedding and found a 165 day lag between the two. An explanation for this correlation may be that the arrival of a Natal pulse in the Agulhas Current retroflection can trigger a loop occlusion by short-circuiting the Agulhas Current and Agulhas Return Current.

Indeed, *Penven et al. [2006]* and *Biastoch et al. [2008c]* used numerical ocean models to show that Natal pulses control the timing of Agulhas ring shedding events and the variability in Agulhas ring paths. The magnitude of Agulhas leakage, however, was not affected by artificially suppressing the generation of Natal pulses.

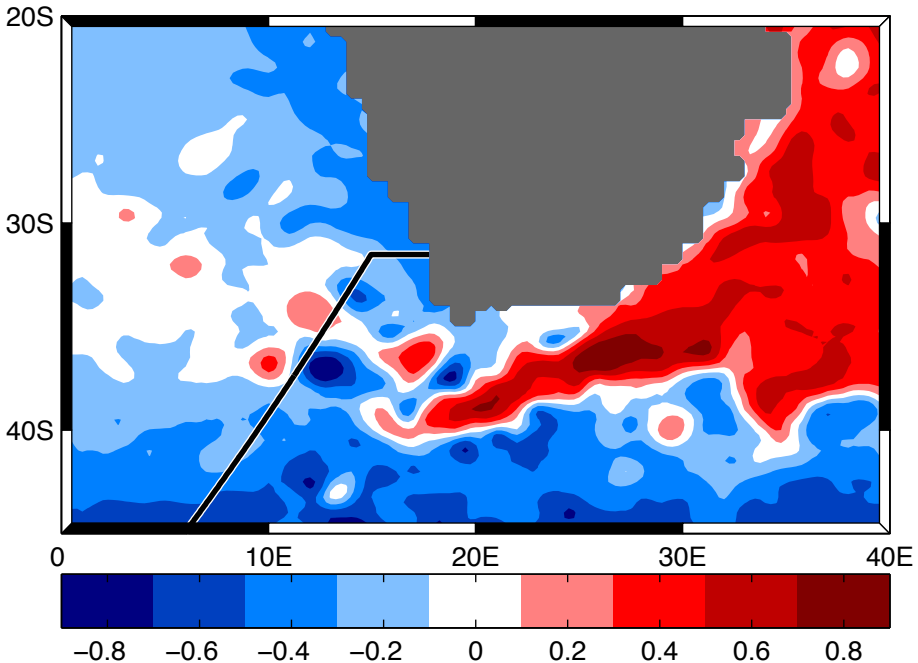


Figure 1.6: A weekly composite of altimetry data, in meter, in the Agulhas region in the week of 18 July 2007. The sea level anomaly from the AVISO data center is combined with the *Rio and Hernandez* [2004] geoid to yield an absolute dynamic topography. Most of the features depicted in the schematic of Fig. 1.4 can be identified, albeit somewhat masked by the noisy the sea surface height field. The black line marks the location of the GoodHope line (see section 1.7).

1.6 Variability in the Agulhas system

The identification of the individual features that have been discussed in the previous section can sometimes be difficult. This is illustrated in snapshots of the Agulhas region (such as from satellite altimetry data, Fig. 1.6), where the individual features are somewhat obfuscated by the high levels of mesoscale noise. This noise is an expression of the mesoscale variability in the region, which is induced mainly by eddies.

Another type of variability comes through large-scale variations in the remote forcing. The Indian Ocean, source region of the Agulhas Current, has a strong seasonal cycle related to the monsoon system [*Schott and McCreary Jr.*, 2001] and an interannual mode of variability related to the Indian Ocean Dipole [e.g. *Palastanga et al.*, 2006, 2007; *Behera et al.*, 2008]. Although one would expect that these modes of variability have an impact on the Agulhas system, that point is not settled yet. Studying the intra- to interannual variability is difficult, as even state-of-the-art models have problems in accurately reproducing the levels of variability in the Indian Ocean. This was for instance shown

by *Van der Werf et al.* [2009] in a study on variability in the Mozambique Channel.

The wind-driven seasonal variability in the southern Indian Ocean is radiated westward by barotropic Rossby waves. However, this variability is somewhat damped due to topographic blocking as it crosses the Madagascar Ridge south of Madagascar, according to numerical ocean model studies by *Matano et al.* [1999] and *Matano et al.* [2002]. *Fetter et al.* [2007], on the other hand, have used a medium-resolution numerical model to show that interannual variability in the Agulhas region is due to the wind fields over the southern Indian Ocean. Comparing realistically forced model runs to climatologically forced model runs, the authors find no damping influence of the Agulhas region bathymetry. This might be related to the baroclinic response of the ocean on these time scales.

Within the Agulhas region itself, numerical ocean models produce some variability in the Agulhas region on seasonal time scales. *Hermes et al.* [2007] have shown that in their numerical ocean model the Agulhas Current strength varies on an intra-annual basis, with most transport in austral spring. *Matano et al.* [1998] have used altimetry data to study the seasonal variation in Agulhas Current retroflexion location, and found that there is a difference between summer and winter. *Ffield et al.* [1997] used hydrographic information from the WOCE cruises to estimate the seasonal variability in the southern Indian Ocean. Although they find a clear seasonal cycle, the effect of this variability on the Agulhas Current strength is limited. There has not yet been a study on the impact of seasonal variability in the Agulhas Current on the magnitude of Agulhas leakage.

1.7 Estimating the magnitude of Agulhas leakage

Although it is easier than determining the vertically integrated net Indian–Atlantic interocean exchange (section 1.2), measuring the magnitude of Agulhas leakage is extremely complex. There is no consensus in the literature on the mean amount of the Agulhas leakage, let alone its variability. The range in historical estimates is large (Tab. 1.1), from less than 5 Sv to more than 40 Sv (although the larger of these are from modeling studies). Most studies, however, report Agulhas leakage magnitudes somewhere between 10 and 20 Sv. The estimates depend not only on the model and method used, but also on the location where the magnitude of Agulhas leakage is assessed.

In this dissertation, the magnitude of Agulhas leakage is generally determined over the GoodHope line (*Anson et al.* [2005], see Fig. 1.6), as it is outside but still close to the Agulhas Current retroflexion (see also section 3.2). Halfway between the Agulhas and Walvis ridges, the GoodHope line is centrally located within the Cape Basin. After a short 250 km zonal excursion, the section follows a southwestward oriented TOPEX/POSEIDON-JASON1 ground track. Among others, the GoodHope line serves as an Expendable

Authors	Study type	Location	Leakage
Based on observations			
<i>Gordon</i> [1986]	NADW formation	Global	14
<i>Gordon et al.</i> [1987]	Hydrography	Cape Basin	10
<i>Gordon et al.</i> [1992]	Hydrography	Cape Basin	9
<i>Schmitz Jr</i> [1995]	Synth. of observations	Global	4
<i>Ganachaud and Wunsch</i> [2000]	Inverse modeling	30°S	17
<i>Garzoli and Goni</i> [2000]	Altimetry	Cape Basin	17
<i>Boebel et al.</i> [2003a]	Float trajectories	Cape Basin	10
<i>Richardson</i> [2007]	Float trajectories	Cape Basin	15
Based on models only			
<i>Döös</i> [1995]	Numerical floats	Global	21
<i>Matano and Beier</i> [2003]	Eulerian model fluxes	Cape Basin	20
<i>Treguier et al.</i> [2003]	Eulerian model fluxes	30°S	11
<i>Donners and Drijfhout</i> [2004]	Numerical floats	20°E	22
<i>Donners and Drijfhout</i> [2004]	Numerical floats	Equator	10
<i>Speich et al.</i> [2006]	Numerical floats	Cape Basin	41
<i>Doglioli et al.</i> [2006]	Numerical floats	Cape Basin	14
<i>Hermes et al.</i> [2007]	Retroreflection index	Currents	40%

Table 1.1: Some of the historical estimates of the magnitude of Agulhas leakage, in sverdrup, from the literature. The estimates are grouped by those based on observations (often in combination with a simple model) and those based on numerical ocean model studies. The estimate by *Ganachaud and Wunsch* [2000] also includes diapycnal mixing of water in the Southern Ocean and Drake Passage leakage. The estimate from *Hermes et al.* [2007] is based on a retroreflection index, the transport of the Agulhas Return Current scaled by the transport in the Agulhas Current. This ratio is 0.60 in the model and assuming an Agulhas Current strength of 75 Sv, this leads to a leakage of 30 Sv.

Bathythermograph XBT section between Africa and Antarctica [*Swart et al.*, 2008]. Twelve Pressure Inverted Echo Sounders (PIES) have been deployed on the GoodHope line in the period 2003 – 2005 in the ASTTEX program [*Byrne and McClean*, 2008]. In her dissertation, *Baker-Yeboah* [2008] utilizes the PIES sensors to study Agulhas ring propagation over the GoodHope line.

There are at least four methods which can be utilized to estimate the magnitude of Agulhas leakage. Some of the methods are well suited for use in the real ocean, while others are more appropriate in a modeling context. Each of these methods has its strengths and weaknesses, as shall be discussed below.

The first method which can be used to estimate the magnitude of Agulhas leakage is based on satellite altimetry, either to count rings [e.g. *De Ruijter et al.*, 1999] or to use as input for a simple geostrophic model [e.g. *Garzoli and Goni*, 2000]. Using altimetry yields only rough estimates, as it is assumed that the signature of each Agulhas ring is similar, transporting a comparable amount of water in the case of ring counting or having the same baroclinic structure in

the case of geostrophic models. Furthermore, leakage by small-scale filaments is often not taken into account.

A second method utilizes a combination of inverse modeling and hydrographic estimates [e.g. *Gordon et al.*, 1987, 1992; *Schmitz Jr.*, 1995]. The advantage of this method is that Agulhas leakage is directly placed within a global circulation [*Ganachaud and Wunsch*, 2000]. However, the method relies on scarce observations and generally can not give any estimate on the variability of Agulhas leakage.

A third method with which the magnitude of Agulhas leakage can be estimated is based on Eulerian fluxes from a model [e.g. *Matano and Beier*, 2003; *Treguier et al.*, 2003; *Hermes et al.*, 2007]. In principle, an Eulerian Agulhas leakage flux can be calculated by integrating two-dimensional (model) velocities perpendicular to a predefined area. The difficulty lies in posing the correct boundaries for this integration area so that only fluxes which can be attributed to Agulhas leakage are integrated. Because of the vicinity of the South Atlantic Ocean subtropical gyre and the Southern Ocean Subtropical Front (see section 1.3), choosing the correct boundaries is not trivial (see also chapter 7).

A fourth method applicable for estimating the magnitude of Agulhas leakage is based on an analysis of Lagrangian float trajectories [e.g. *Döös*, 1995; *Boebel et al.*, 2003a; *Donners and Drijfhout*, 2004; *Speich et al.*, 2006; *Doglioli et al.*, 2006; *Richardson*, 2007]. By releasing floats in the Agulhas Current and then determining how many of them end up in the Atlantic Ocean, the magnitude of Agulhas leakage can be estimated. The problem is that large amounts of floats have to be released to reduce the uncertainty level, which is expensive (either computationally in the case of models, or financially in the case of the real ocean). However, because the setup of the method comes so close to the definition of Agulhas leakage used here, this method appears to be most apt for assessing the magnitude of Agulhas leakage (section 1.2).

1.8 Numerical Lagrangian floats as water samplers

Since the interocean trajectories of floats launched in the Agulhas Current are so closely related to the definition of Agulhas leakage, its magnitude can best be assessed using such floats. Floats can be deployed in the real ocean, which has been done in the KAPEX program [*Richardson et al.*, 2003; *Boebel and Barron*, 2003], in the Argo program (<http://www.argo.ucsd.edu>), or in the drifting buoy program from the Global Drifting Buoy Data Assembly Center at the NOAA Atlantic Oceanographic and Meteorological Laboratory (see *Richardson* [2007] for an application in the Agulhas region). However, the number of trajectories in these observational data sets is never more than a few hundred. This limits the ability to do statistics on the trajectories.

In a model, however, the number of floats deployed can be much higher, in the order of millions. Such numerical Lagrangian floats are advected with the modeled flow [e.g. *Döös*, 1995; *De Vries and Döös*, 2001; *Lacorata et al.*,

2001]. One of the algorithms to compute the trajectories of these floats, also employed in this dissertation, is by *Blanke and Raynaud* [1997]. Within a grid cell, each of the three velocity components is assumed to vary linearly between the two opposing faces of that cell. For each float, the entry and exit times and locations for a grid cell are then calculated by advecting the float with the linearly changing velocity profile.

A disadvantage of advecting Lagrangian floats within an Eulerian framework is that the floats themselves can not carry any properties. There is no intrinsic temperature, salinity, or relative vorticity that is attached to a particular float and which can change over time. Instead, these properties can only be computed by interpolating the appropriate Eulerian fields onto the position of the Lagrangian float, a procedure which is prone to errors for the nonlinear momentum equations. The only exception to this lack of properties is the volume transport. Each float represents a certain volume, which is determined when the float is released. This volume can be used to determine fluxes as floats cross a particular plane.

Ideally, computation of the trajectories is done in parallel with the time integration of the model governing equations. The temporal resolution of the model velocity fields is then highest, which limits the errors in path integration. However, this is often (also here) unfeasible due to computational limitations. In that case, the offline archives of model velocity are used to advect the particles. The advantage of offline schemes is that they are computationally cheap and efficient to parallelize, at the cost of a reduced accuracy as model output is only available on a low temporal resolution.

1.9 Central question in this dissertation

The goal of this introductory chapter was to convey that the Agulhas system is both relevant in climate studies as well as interesting from a physical and dynamical oceanographic perspective, but that the mechanisms governing the system (in essence the dynamics of the potential vorticity balance and the retroreflection of a free jet) are not completely understood. The system is the locus of three major wind-driven circulation systems and is critical in setting the thermohaline properties of the Atlantic Ocean. The result is that the horizontal and vertical ocean circulations are highly intertwined in the Agulhas region.

One of the most important quantities in the Agulhas system is the magnitude of Agulhas leakage, which is here defined as the amount of water within the Agulhas Current that ends up in the Atlantic Ocean (see also section 1.2). This magnitude of Agulhas leakage might be regarded as a measure for the strength of the coupling between the Indian Ocean and the Atlantic Ocean. A better comprehension of processes affecting Agulhas leakage may yield enhanced understanding of the Agulhas system's role in global climate. Monitoring the magnitude of Agulhas leakage might therefore be a smart objective in global climate change research.

Monitoring the magnitude of Agulhas leakage is not easy, as also indicated by the large range in historical estimates (Tab. 1.1). The magnitude of Agulhas leakage is an order of magnitude smaller than the transports by two of the three circulation systems in the vicinity: the Antarctic Circumpolar Current and the Indian Ocean subtropical gyre. Moreover, the intermittent and mesoscale nature of Agulhas leakage complicates its assessment. Combined with the multitude of definitions for Agulhas leakage and the difficulties even state-of-the-art models have in accurately simulating the Agulhas region circulation, there appears to be a necessity for more comprehension of the physical mechanisms controlling Agulhas leakage before designing a monitoring program.

On the other hand, there appears to be an urgent need for an index of Agulhas leakage. In situ observations of the magnitude of Agulhas leakage are expensive and difficult, but the region is too important to neglect. For monitoring purposes, therefore, an Agulhas leakage index would be convenient. Many key oceanic processes are captured within an index to facilitate the monitoring of their state (i.e. the NINO3/4 and AMO indices). To date, there is no index of Agulhas leakage. Although the subtleties of the regional circulation do not easily lend themselves to be lumped into one bulk number, it might be worthwhile to try to develop a first-order estimate of the magnitude of Agulhas leakage which is easy to measure.

In view of the considerations stated above on the difficulty of determining and monitoring the magnitude of Agulhas leakage, the central question that is treated in this dissertation is

Central Question:

Can the magnitude of Agulhas leakage and the processes which control it be assessed?

Because observations of Agulhas leakage are so scarce, we will employ numerical ocean models to answer the central question. The advantage of using such models is twofold. First of all, long time series can be computed at relatively low cost, which enhances the strength of statistical analysis. Furthermore, the amount of information on the three-dimensional structure of the ocean is much higher in a model than when observations are used. At each model grid cell and at high resolution, all velocity and thermohaline properties are available. This facilitates more thorough analysis of the data.

The advantages of using a numerical ocean model come at a cost. The model is never a perfect representation of reality, neither at individual snapshots nor in a statistical sense. Before employing the model, therefore, its skill has to be assessed. This is done in chapter 2, where a novel method is described to determine the skill of numerical Lagrangian float trajectories using the paths of drifting buoys in the real ocean. Employing this method in the Agulhas region leads to one model (the AG01 model of *Biastoch et al.* [2008b,c]) that seems to possess sufficient skill and can be used for further analysis of the Agulhas

leakage.

The structure of Agulhas leakage is investigated in chapter 3. Before the magnitude of Agulhas leakage can be related to other monitorable quantities (so that a proxy or index for Agulhas leakage might be established), it is important to determine in what form Agulhas leakage gets into the Atlantic Ocean: either as Agulhas rings, Agulhas cyclones, filaments, or other coherent structures (see also section 1.5.5). An analysis of relative vorticity of the water along the float trajectories seems to suggest that the bulk of Agulhas leakage spawns from the Agulhas Current in large rings, but these quickly decay. Once at the GoodHope line, on the other hand, most of the leakage is in large low relative vorticity patches.

The time series of Agulhas leakage transport can be related to other quantities in the model. The goal is then to isolate a quantity (or set of quantities) which may be related to the Agulhas leakage transport, so that monitoring of that quantity yields an estimate of the magnitude of Agulhas leakage. It appears that the applicability of the relations between the monitorable quantities and Agulhas leakage depends on the time scale of interest, as the relations are significant on either interannual, seasonal, or monthly smoothing times. These smoothing times can be justified as long as they are shorter than the time scales on which Agulhas leakage affects the strength of the Atlantic meridional overturning circulation. This latter time scale is investigated in chapter 4, where a simple adiabatic two-layer model is employed to study the Agulhas ring baroclinic energy radiation time scales to the regions of North Atlantic Deep Water formation.

The first monitorable quantity is introduced in chapter 5. This monitoring strategy is based on the location of the Agulhas Current retroflexion, which can be obtained from satellite altimetry. Besides the low costs, using altimetry data also has the advantage that almost twenty years of data are already available. It appears that when the Agulhas Current retroflexion is farther westward the magnitude of Agulhas leakage is generally higher. This relation between the location of the Agulhas Current retroflexion and the magnitude of Agulhas leakage on seasonal time scales is the basis for the monitoring strategy.

The second monitorable quantity tested is based on the strength of the Agulhas Current and is discussed in chapter 6. On interannual time scales, the study shows that the Agulhas Current strength is correlated to the magnitude of Agulhas leakage. A weaker Agulhas Current leads to more Agulhas leakage. As the Agulhas Current is more confined in its location than the locations where Agulhas leakage crosses the GoodHope line, it is easier to measure.

The last monitorable quantity is introduced in chapter 7, where it is shown that it might be feasible to measure the magnitude of Agulhas leakage at the GoodHope line itself. A monitoring array might be constructed with which Eulerian fluxes can adequately be determined on monthly time scales. The relation between the observations from the array and Agulhas leakage is based on measuring the flux of only the warm and saline water over the GoodHope line. However, this monitoring strategy requires a large mooring array and will

thus be very expensive.

Coming back to the main research question, there appear to be at least three methods to estimate the magnitude of Agulhas leakage in the real ocean: either by determining the location of the Agulhas Current retroflexion in satellite altimetry, by monitoring the Agulhas Current strength, or by measuring the Eulerian flux across the GoodHope line. Probably, however, the ultimate monitoring approach is a combination of these. This is further discussed in the conclusions to this dissertation, chapter 8.

Chapter 2

Lagrangian trajectory model validation

This chapter is based on the work published as:

Van Sebille, E., P. J. van Leeuwen, A. Biastoch, C. N. Barron, and W. P. M. de Ruijter (2009), Lagrangian validation of numerical drifter trajectories using drifting buoys: Application to the Agulhas system, *Ocean Model.*, 29, 269–276.

Abstract

The skill of numerical Lagrangian drifter trajectories in three numerical models is assessed by comparing these numerically obtained paths to the trajectories of drifting buoys in the real ocean. The skill assessment is performed using the two-sample Kolmogorov–Smirnov statistical test, a test well suited for skill testing when the size of the data sets is orders of magnitude apart. To demonstrate the assessment procedure, it is applied to three different models of the Agulhas region. The test can either be performed using crossing positions of one-dimensional sections in order to test model performance in specific locations, or using the total two-dimensional data set of trajectories. The test yields four quantities: (1) a binary decision of model skill, (2) a confidence level which can be used as a measure of goodness-of-fit of the model, (3) a test statistic which can be used to determine the sensitivity of the confidence level, and (4) cumulative distribution functions that aid in the qualitative analysis. The ordering of models by their confidence levels is the same as the ordering based on the qualitative analysis, which suggests that the method is suited for model validation. Only one of the three models, a $1/10^\circ$ two-way nested regional numerical ocean model, might have skill in the Agulhas region. The other two models, a $1/2^\circ$ global model and a $1/8^\circ$ assimilative model, might have skill only on some sections in the region.

2.1 Introduction

Assessing the skill of numerical ocean models is an important step before the data produced by such a model can be analyzed and interpreted. Special projects have been set up to facilitate the comparison of different numerical ocean models within a fixed framework (e.g. the Coordinated Ocean-ice Reference Experiments (CORE), *Griffies et al. [2009]*). One of the problems of such skill assessment is that the observations to which the model should be verified are scarce in space and time. The skill assessment is therefore often limited to a subset of the full three-dimensional velocity and thermohaline fields.

Historically, verification is predominantly qualitative, where one or more specific model variables are compared to observations of these variables. The advantage of this qualitative method is that it introduces the expertise of the modeler in selecting fields and regions that are more important than others. However, the qualitative method also introduces subjectiveness into the skill assessment procedure.

There are objective methods to assess the model skill. *Hetland [2006]* introduced a way to calculate the improvement of a model with respect to some climatology. Using statistics on the complete model domain, however, has the disadvantage that dynamically relevant regions (such as the western boundary currents) are treated similar to dynamically less important regions. This is a relevant problem especially when the subsequent data analysis is done using numerical Lagrangian floats, tracers that are advected with the flow. These floats often cluster in some regions of the model domain and only the model skill in these regions is relevant for the aptitude of the float data. Ideally, these regions should therefore have more weight in the skill assessment. A way to accomplish this focus on dynamically relevant regions is to base the skill assessment on the float trajectories themselves.

The assumption behind trajectory verification is that only skillful models produce trajectories with similar properties as drifting buoys. Thus, a high skill in float trajectories implies that the underlying model is highly skilled. Here, we present a quantitative method to assess the skill of a set of numerical drifters. Using drifting buoy trajectories from the real ocean, the probability can be calculated that the drifting buoys and the numerical drifters are drawn from the same distribution.

For assimilative models, where it is the objective for the model to represent the ocean state as accurately as possible, *Barron et al. [2007]* have developed a technique to compare drifting buoy trajectories with the trajectories of numerical drifters. The authors seed numerical drifters at the locations where drifting buoys are observed and then calculate the deviation of model and in situ paths as a function of time. However, many models are non-assimilative and for these models one-to-one comparison of buoys and numerical drifters is futile as the forcing is different between the model and drifting buoy trajectories. And even if the forcing is similar, nonlinearity leads to de-coupling (or rather de-timing) between the circulation and the forcing, and thereby an

increased error between observed and modeled trajectories. Verification of such non-assimilative float trajectories should be done in a statistical sense, where the distribution functions of the two kinds of drifters are compared rigorously.

Lagrangian data is often used in examinations of relative and absolute dispersion. Such estimates of dispersion would be useful in quantifying important aspects of Agulhas circulation. For example, *Drijfhout et al.* [2003] identify dispersion through Rossby wave radiation as a key factor in the decay of Agulhas rings. *Lacorata et al.* [2001] used Lyapunov exponents to characterize the drifter paths and assess the dispersion of drifting buoys. *Manning and Churchill* [2006] track the spread within drifter clusters in an alternate approach to estimating dispersion.

Drifter observations used within the present Agulhas study, however, are not well distributed for these type of methods, which analyze group characteristics of among multiple pairs or clusters of simultaneously trajectories with initially small separation. Numerical simulations of drifter trajectories can be designed to support dispersion studies, but the validity of such studies requires that the simulated trajectories are representative of the true local circulation. The focus of the present study is to present a technique to assess whether the advection patterns in the model drifters agree with patterns in the real ocean. Model results that are shown to be sufficiently representative of observed characteristics could then be more credible in subsequent studies focused on dispersion characteristics.

Although drifting buoys have been deployed for over a decade now, and large numbers of buoys have been released, the total number of drifting buoys in a mesoscale region such as the Agulhas region is relatively small. The number of numerical floats seeded within a typical model is $10^5 - 10^7$ whereas the number of drifting buoys is in the order of $10 - 10^2$, many orders of magnitude smaller. This small number of drifting buoy trajectories limits the ability to use standard statistical tools. A common χ^2 -test, for example, requires histograms with at least five members in each bin. This confines the number of bins and consequently reduces the accuracy and strength of the method. A statistical test which is better suited for this problem is the two-sample Kolmogorov–Smirnov test, which does not require binning the data.

In this chapter, the Kolmogorov–Smirnov test is applied to a set of experiments in the Agulhas system [*De Ruijter et al.*, 1999; *Lutjeharms*, 2006], where numerical floats are continuously seeded in the upstream Agulhas Current and then tracked as they move through the Agulhas region. The highly nonlinear behavior of the flow in this region, with its Agulhas Current retroreflection and mesoscale eddies (see also section 1.5), serves as an ideal test case to investigate the strengths and weaknesses of the assessment method presented here.

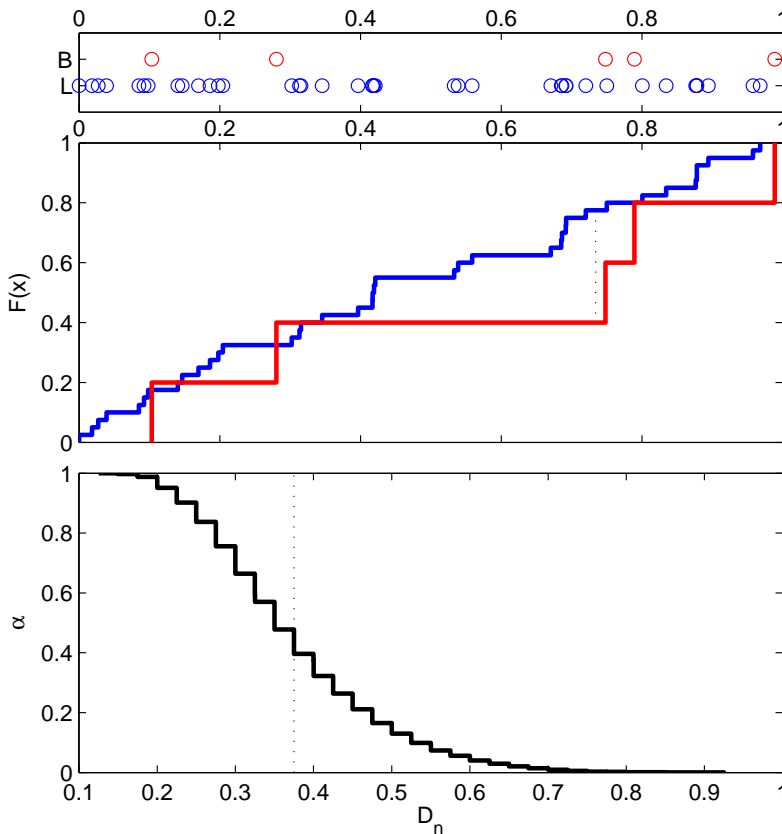


Figure 2.1: An illustration of the two-sample Kolmogorov–Smirnov test. The test is performed using two random one-dimensional data sets B (red circles) and L (blue circles), with $N_B = 5$ and $N_L = 40$ (upper panel), both drawn from a uniform distribution. Cumulative distribution functions, the fraction of data points below some value x , have been computed from these two data sets (middle panel; red line for data set B and blue line for data set L). The test statistic D_n of Eq. (2.1) is denoted by the dotted line (with a value of 0.38). This test statistic is related to a confidence level α by a Monte Carlo process where D_n is calculated for 10^5 uniformly distributed data sets of similar N_B and N_L (lower panel). In this particular case the confidence level is 0.47, the value for α on the ordinate where the $D_n = 0.38$ line and the cumulative density function of all D_n s intersect. Since $\alpha > 0.05$, this leads to the (correct) conclusion that B and L are drawn from the same distribution.

2.2 The two-sample Kolmogorov–Smirnov test

To measure the agreement between the distribution functions of the numerical drifter data set and the drifting buoy data set, the two-sample Kolmogorov–

Smirnov test (2KS-test) is used [Massey Jr., 1951]. The 2KS-test is designed to test the hypothesis that two data sets B (in this case drifting buoys) and L (in this case numerical Lagrangian drifters) are taken from the same underlying distribution. This underlying distribution does not need to be known. The two data sets need to be (one-dimensional) vectors of independent and identically distributed real numbers and they may have different lengths N_B and N_L , since the 2KS-test is also powerful when $N_B \ll N_L$. The 2KS-test starts out with formulating the null hypothesis (which will be rejected or not) that the data sets B and L share an underlying distribution. After that, there are four steps (Fig. 2.1).

First, cumulative distribution functions $F_B(x)$ and $F_L(x)$ are constructed from the data sets B and L . These functions give the fraction of data below x , which is in this application the location along a horizontal section. They are zero below the minimum value in the data set and one above the maximum value. At each member of the (sorted) data set they increase with $1/N$. By construction, $F(x) = 0.5$ denotes the median of the data set.

Secondly, a test statistic is calculated. For the 2KS-test, this test statistic is the largest distance between $F_B(x)$ and $F_L(x)$:

$$D_n = \sup_x \left| F_B(x) - F_L(x) \right| \quad (2.1)$$

Other tests use different test statistics, such as the Cramér-Von-Mises test where the test statistic is the area between $F_B(x)$ and $F_L(x)$. However, these tests are not necessarily more powerful [Conover, 1980].

As a third step, a confidence level α is assigned to the test statistic D_n , given the data set lengths N_B and N_L . These two data set lengths are converted to one pseudo-length:

$$N = \frac{N_B N_L}{N_B + N_L} \quad (2.2)$$

after which the two-sample Kolmogorov–Smirnov test is similar to the ordinary Kolmogorov–Smirnov test. Note that for $N_B \ll N_L$, the length of the numerical drifter data set is unimportant as $N \approx N_B$.

The theory behind the 2KS-test states that, although the distributions of B and L may be unknown, D_n follows the Kolmogorov distribution and thus each combination of D_n and N corresponds to exactly one α . The transformation from D_n to α can be done using a lookup table [Sveshnikov, 1968; Conover, 1980], but here it is computed using a Monte Carlo simulation. In such a Monte Carlo simulation, a cumulative distribution function $F_{D_n}(\alpha)$ is acquired by repeatedly taking random samples of lengths N and calculating the test statistic. The advantage of using a Monte Carlo simulation over a lookup table is that it is much more accurate, at the cost of increased computing time.

Finally, the null hypothesis is rejected when α is below some value. In this

chapter, we use the 95% confidence interval. This leads to the decision rule:

$$\text{The model: } \begin{cases} \text{has no skill} & \text{if } \alpha \leq 0.05; \\ \text{might have skill} & \text{if } \alpha > 0.05. \end{cases} \quad (2.3)$$

which means that when $\alpha \leq 0.05$ it is more than 95% certain that the drifting buoy trajectories and numerical drifter trajectories do not share an underlying distribution and hence the model is not good. If, on the other hand, $\alpha > 0.05$ it means that it is not certain whether the distributions of B and L are different. Although this technically only means that we can not say that the model is faulty, it will be used here as evidence that the model might have skill.

Note that in this formulation the 2KS-test only returns ‘has no skill’ or ‘might have skill’. However, there is also information in the test statistic D_n and the confidence level α . They can be used for intermodel comparison. In addition, the cumulative distribution functions $F_B(x)$ and $F_L(x)$ can aid in subjective analysis of the model skill as they reveal where model and reality diverge most.

The one-dimensional two-sample Kolmogorov–Smirnov test has been extended to two-dimensional data sets by *Peacock* [1983]. The procedure is very similar in two dimensions, except for the conversion from B and L to $F_B(x, y)$ and $F_L(x, y)$. In two dimensions, there are four ways to define a cumulative distribution function, depending on where $F(x, y)$ is defined to be zero (Fig. 2.2). This is related to the possible orderings in x and y . As suggested by *Peacock* [1983], preliminary D_n s are computed for each of these four orderings, and the largest of these is selected as the representative D_n for the set, since that gives the smallest value for α ,

$$D_n = \max \left(\sup_{x,y} \left| F_B(x, y) - F_L(x, y) \right| \right) \quad (2.4)$$

For a given N and D_n , the confidence level α is higher in the two-dimensional than in the one-dimensional 2KS-test (Fig. 2.3). This is probably because the average distance between N points in two dimensions is larger than in one dimension.

For sufficiently large data sets ($N > 10$), the 2KS-test is much more sensitive to changes in D_n than to changes in N (Fig. 2.3). If it is assumed that the data set is an unbiased subsample of the underlying distribution, so that D_n does not change when one data set member is added, the sensitivity of α is dominated by the change in N . For $N > 10$, the maximum sensitivity $|d\alpha/dN| = 0.05$. Furthermore, the sensitivity around the critical $\alpha = 0.05$ value, which is the basis for the decision rule, Eq. (2.3), is always less than 0.01. That means that a decision will not have to be changed when $0.05 < \alpha < 0.06$ if one data point is added, under the assumption that D_n is constant. But even if the data set is extremely biased, the addition of one extra member to data set B can never change D_n by more than $1/N_B$, the height of each step in $F_B(x)$.

The advantage of the 2KS-test is that it is independent of a norm to compute the distance between the two data sets. Such a norm is required in the minimum

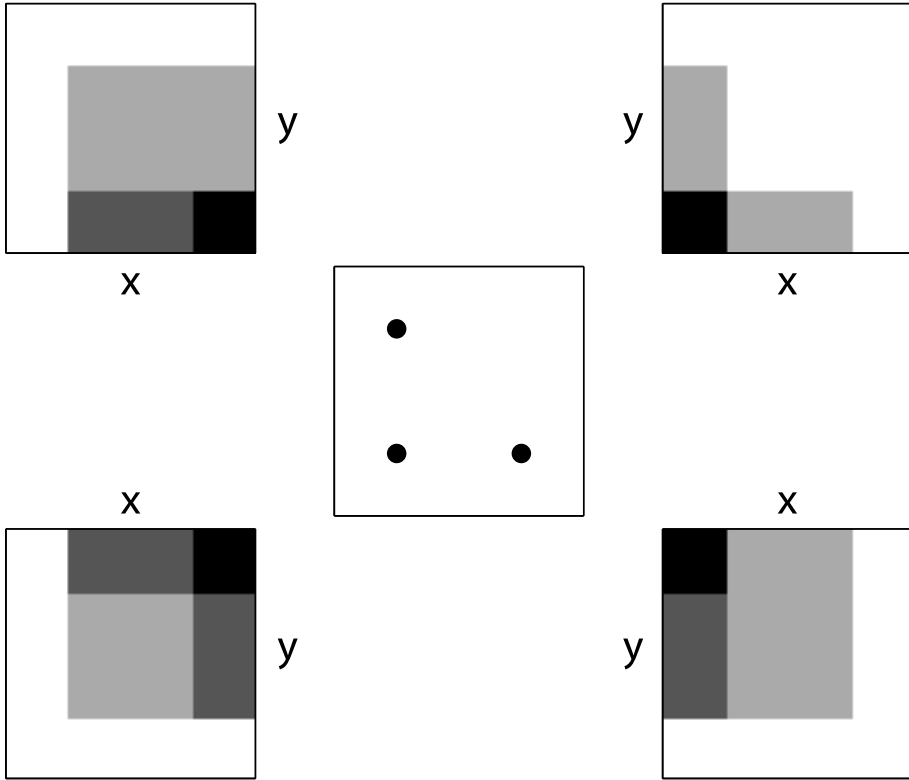


Figure 2.2: The cumulative distribution functions (CDFs) that can be defined from a two-dimensional data set. Due to the orderings that can be made in the x and y dimensions, there are at least four different CDFs in two dimensions, where there is only one in one dimension. The middle panel shows an example data set where $N = 3$. The four corner panels show the four very different CDFs that result when the ordering is started in the respective corner of the (x, y) -domain. The color scale is such that white is zero and blue is one. In the case of the two-dimensional 2KS-test, the ordering is chosen which results in the largest value of D_n .

spanning tree rank histogram method [Gombos *et al.*, 2007], and this choice introduces subjectiveness into the method. The 2KS-test is, apart from a critical confidence level where the hypothesis is rejected, completely choice-free and thereby objective. Together with the ability of the 2KS-test to work for a large range of data set lengths, this makes the 2KS-test very appropriate for this oceanographic application.

2.3 The Agulhas region data

The 2KS-test is applied in the Agulhas region using drifting buoy trajectories as data set B and numerical drifter trajectories as data set L . The numerical

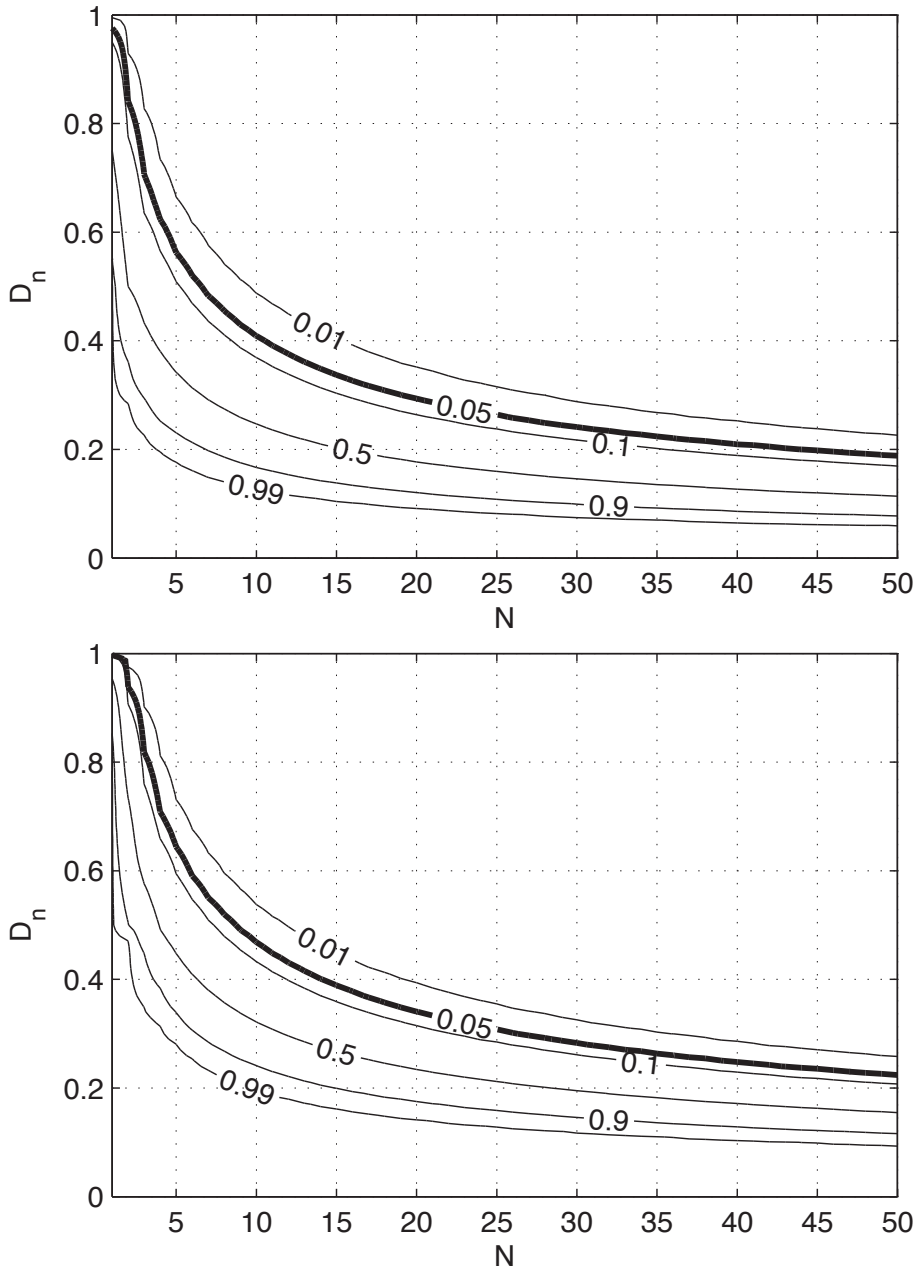


Figure 2.3: The confidence level α as a function of N and D_n for the one-dimensional (upper panel) and two-dimensional (lower panel) two-sample Kolmogorov–Smirnov test. For a given N and D_n , the latter gives a higher confidence level.

drifter trajectories are obtained by seeding drifters in three different models, which means that there are actually three different data sets L . Having three different model data sets aids in assessing the strengths and weaknesses of the 2KS-test.

The complexity and nonlinearity of the Agulhas system, where the Indian Ocean and Atlantic Ocean meet, makes it an ideal test case for the 2KS-test. The region is fed by three distinct sources: the Agulhas Current in the north-east, the South Atlantic Ocean subtropical gyre in the west, and the Antarctic Circumpolar Current in the southwest (see section 1.3). The system is populated with mesoscale cyclones and anticyclones, which vigorously mix the water from these three source regions in the Cape Basin [Boebel *et al.*, 2003a]. The float experiments are designed to determine the magnitude of Agulhas leakage, which is the water flowing from the Indian to the Atlantic Ocean in the warm upper-branch return flow of the meridional overturning circulation [Gordon, 1985].

The three numerical data sets are from Lagrangian float experiments inside three different models: NCOM, ORCA, and AG01. The models vary in their ability to simulate the complicated Agulhas system dynamics, and this provides an opportunity to gauge the strength of the 2KS-test in this oceanographic context.

The $1/8^\circ$ Global NCOM is an assimilative model in which satellite observations of sea surface height and temperature are used to derive synthetic profiles of temperature and salinity [Barron *et al.*, 2006, version 2.5]. Using seven years of model data (1998 – 2004), Lagrangian floats have been seeded daily at 30°S at 14 different depth levels in the upper 1000 m. For each 0.1 Sv flowing southward through a grid cell, one float is seeded [cf. Donners *et al.*, 2004]. Floats are only seeded in the southward flowing core of the Agulhas Current. After the floats have been seeded, their paths are integrated for two years using the 4th-order Runge-Kutta approach [Barron *et al.*, 2007]. Daily offline velocity fields are interpolated to the depth levels of the float integration, using a time step of one hour. If the floats hit bathymetry or the domain borders, integration is stopped. Being isobaric, the drifters remain on their initial depth levels. The total number of floats that is released is $1.5 \cdot 10^6$.

The $1/2^\circ$ global ocean–sea-ice ORCA model [Biastoch *et al.*, 2008a] is based on NEMO [Madec, 2006, version 2.3]. It is forced with the *Large and Yeager* [2004] 6-hourly data set for wind and thermohaline forcing, over the period 1958 – 2004. The numerical floats are released at 32°S , employing the ARIANE package [Blanke and Raynaud, 1997]. In contrast to the integration scheme used in NCOM, the floats are isopycnal. In the period 1992 – 2004, using the five day resolution model output, the floats are tracked for five years. In total, $1.3 \cdot 10^6$ floats are released.

The $1/10^\circ$ AG01 model [Biastoch *et al.*, 2008b,c] is a two-way nested grid inside the ORCA model, that spans the greater Agulhas region ($20^\circ\text{W} - 70^\circ\text{E}$; $47^\circ\text{S} - 7^\circ\text{S}$). The two-way nesting procedure allows the AG01 model to both receive its boundary conditions from the base model and to update the base

model [Debreu *et al.*, 2008]. The numerical float trajectories are computed in a similar way as in ORCA. In 37 years, $5.5 \cdot 10^6$ floats are released at 32°S .

The ‘true’ trajectories, data set B , are taken from a subset of the drifting buoy data set from the Global Drifting Buoy Data Assembly Center at the NOAA Atlantic Oceanographic and Meteorological Laboratory. The surface buoys have a drogue at 15 m depth. Richardson [2007] has used similar drifters to estimate the magnitude of Agulhas leakage and was able to identify some new features in the Agulhas region using all drifter trajectories in the domain. Here, the drifter data set has been limited to drifting buoys that flow downstream within the Agulhas Current. Since the numerical drifter release location is different between the models, two drifting buoy trajectory data sets are used. The trajectories start when the drifting buoys cross 30°S (NCOM) or 32°S (ORCA and AG01). Only that part of the trajectories is taken into account that is within the Agulhas region. These drifter trajectory boundaries are at 32°S and 40°E in the Indian Ocean, at 47°S in the Southern Ocean, and at 20°S and 20°W in the Atlantic Ocean. In total, the trajectories of 51 (NCOM) and 47 (ORCA and AG01) drifting buoys are used, in the period between 1995 and 2008.

In all three numerical models, floats are released throughout a large part of the water column. The drifting buoys, however, have a drogue at 15 m depth. Therefore, only the numerical floats in the upper 15 m of the models are used, and the models are only tested on their skill in the upper ocean (see also the discussion, section 2.7). Technically, the numerical drifters released in AG01 and ORCA are not even drifters, as they are isopycnal and allowed to change their depth. If a float is within the upper 15 meter, it is added to the drifter data set, irrespective of its depth history. This means that when floats resurface they suddenly reappear in the data set. However, we expect that the number and effect of resurfacing floats is minor.

2.4 Qualitative skill assessment

Although the goal in this chapter is to introduce a quantitative method for assessing the skill of a numerical ocean model, we will start with qualitatively verifying the model results. This aids the interpretation of the results obtained in the next section when the 2KS-test is applied.

The three models show very diverse behavior in the Agulhas region (Fig. 2.4). Of the drifting buoys in the real ocean approximately 25% end up in the Atlantic Ocean, and this is in agreement with recent estimates of the magnitude of Agulhas leakage [Doglioli *et al.*, 2006; Richardson, 2007]. In NCOM this fraction is much lower and this shows in the model trajectory density, which is very low in the Atlantic Ocean. However, the location and direction of the path taken by the Agulhas rings seems adequate. The Agulhas Return Current, at 37.5°E is better sampled.

The drifter density in ORCA reveals that the path of the Agulhas leakage is directed too zonally, with the majority of the numerical drifters flowing

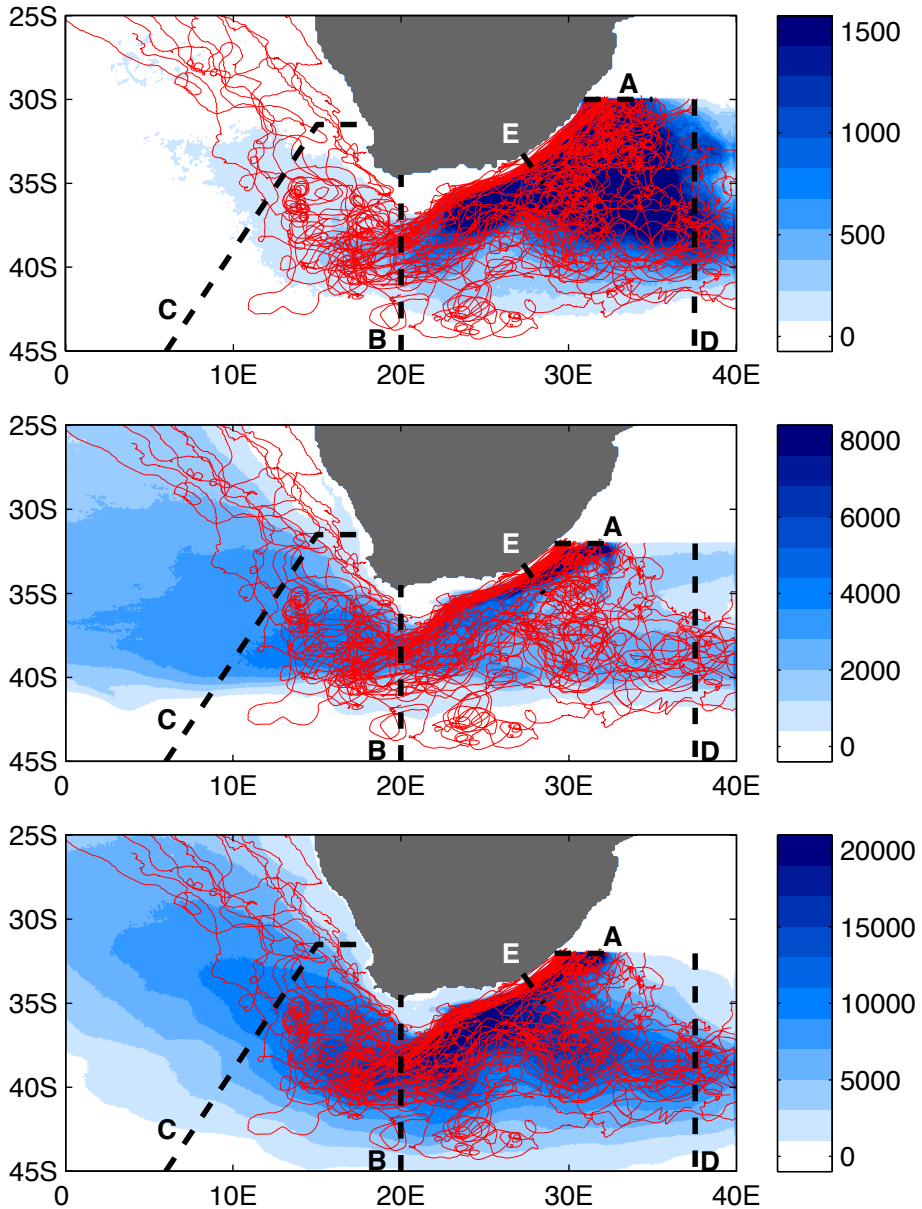


Figure 2.4: The paths of the drifting buoys (red lines) after they have crossed the release latitude in the Agulhas Current and the density of numerical drifter trajectories (blue patches) for numerical drifters in the upper 15 m in NCOM (upper panel), the ORCA model (middle panel), and the AG01 model (lower panel). Because the number of numerical drifters released in each model is different, the color scales are also different. The dashed lines denote the locations where the crossing positions of numerical drifters and drifting buoys are compared, the letters are for reference with Fig. 2.5 and Tab. 2.1.

westward after they round the Cape of Good Hope. This is an expression of the so-called Indian–Atlantic supergyre [*De Ruijter*, 1982, see also section 1.3]. In the Agulhas Return Current, at 37.5°E , a curious bipartitioning can be seen. All drifting buoys flow eastward between 35°S and 42°S , but in the model there is an extra core around 33°S . A third discrepancy between the drifting buoys and the numerical drifters in ORCA is in the southward extent of the trajectories, which is to some degree also observed in NCOM. The numerical drifters do not reach latitudes more southward than 41°S .

In AG01 the drifting buoy and numerical drifter distributions are much more in agreement, although the numerical drifters seem to enter the Atlantic Ocean on a too western course. No drifting buoys reach 0°E more southward than 25°S , but a vast amount of the numerical drifters from AG01 cross that longitude south of 30°S . Another discrepancy is in the return flow, where the distribution of numerical drifters is wider in latitude than that of the drifting buoys.

In summary, AG01 is qualitatively the best model. Although it has some deficiencies (too southward Agulhas leakage, too wide return flow), the area of maximum densities of the drifting buoys and numerical drifters coincide. The skill of NCOM is less, most notably in the fraction of drifters that get into the Atlantic Ocean (see also the discussion, section 2.7). ORCA, at $1/2^{\circ}$ resolution, seems to be the least skillful model with a preference for zonal flow.

2.5 Model validation along one-dimensional sections

The qualitative judgment of the skills of the three different models from the previous section can be quantified using the 2KS-test. For this, one-dimensional sections are taken at key locations in the Agulhas region. They are (A) the longitude of release at 30°S (NCOM) or 32°S (ORCA and AG01), (B) the highly variable retroreflection at 20°E , (C) the crossing of the Agulhas leakage through the GoodHope line [*Swart et al.*, 2008, see also section 1.7], (D) the Agulhas Return Current location at 37.5°E , and (E) the Agulhas Current core attached to the continental slope as it passes Port Elizabeth and turns westward.

For each of the sections and all drifters, the position where the drifter crosses that section is added to the data set. Both the numerical and real ocean drifters may cross a section multiple times. If that is the case, the individual members of the data set are not independent anymore and the 2KS-test is formally not valid. To assure independence, each drifter can therefore be in the data set only once. A way to resolve this is by adding the position of only the last crossing of each drifter to the data set. Using the first crossing instead of the last appears not to change the conclusions on model skill drawn below.

The data sets yield cumulative distribution functions similar to the one from Fig. 2.1. The qualitative skill assessment of section 2.4 can be quantified using these cumulative distribution functions (Fig. 2.5), and the resulting confidence level α can be used to decide on the skill of the model over each of these five

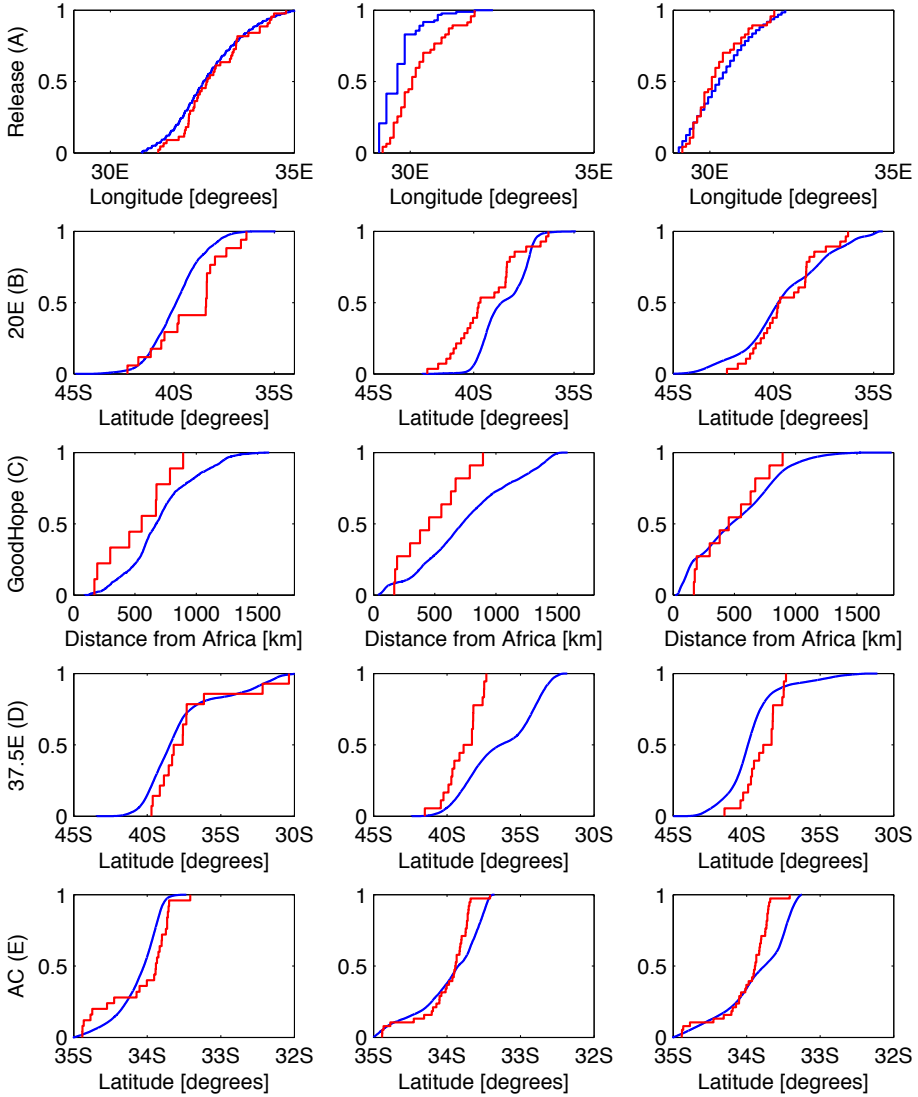


Figure 2.5: The cumulative density functions $F(x)$ for drifting buoys B (red) and numerical drifters L (blue) for the five different sections depicted in Fig. 2.4 on each row. Results are shown from NCOM (left column), the ORCA model (middle column), and the AG01 model (right column). Since the numerical drifters in AG01 and ORCA are released at a different latitude than in NCOM, the drifting buoy data sets are also somewhat different. As the length of L is in the order of 10^5 , the blue lines appear smooth except at the release latitude. The confidence levels associated with these cumulative distributions functions are tabulated in Tab. 2.1.

	Section	NCOM	ORCA	AG01
A	Release latitude	0.26	$2.0 \cdot 10^{-8}$	0.21
B	20°E	$1.7 \cdot 10^{-3}$	$5.5 \cdot 10^{-4}$	0.79
C	GoodHope line	0.44	$7.2 \cdot 10^{-2}$	0.47
D	37.5°E	0.49	$6.2 \cdot 10^{-6}$	$1.4 \cdot 10^{-2}$
E	Current core	$6.4 \cdot 10^{-3}$	$2.4 \cdot 10^{-4}$	$7.4 \cdot 10^{-7}$

Table 2.1: Confidence levels α for the two-sample Kolmogorov–Smirnov test applied to the five different sections shown in Fig. 2.4 and Fig. 2.5 for the three different models. According to the decision rule, Eq. (2.3), sections where $\alpha < 0.05$ (the gray cells in the table) are sections where the model does not have skill.

sections (Tab. 2.1).

At the latitude of release, both NCOM and AG01 perform well. In ORCA, on the other hand, the numerical drifter release locations are too far west, which implies that the modeled Agulhas Current is too confined to the African coast. This coastal confinement might be related to the absence of inshore cyclones that push the Agulhas Current offshore. These cyclones, called Natal pulses [Lutjeharms and Roberts, 1988, see also section 1.5.7], are not resolved on a $1/2^\circ$ grid such as that in ORCA.

Note that the drifter release locations in the ARIANE package, which is used in ORCA and AG01, are not continuous. Instead, drifters are only released in the center of the grid cells. Because the resulting distribution function is discrete, the transformation from test statistic D_n to confidence level α has to be performed using the finite sums method described by Conover [1980]. This method yields confidence levels smaller than those for continuous distribution functions.

At 20°E, the section that cuts through the Agulhas Current retroflection, only AG01 might have skill. As also observed in the qualitative skill assessment, drifter trajectories do not get southward enough in ORCA. In NCOM, on the other hand, some numerical drifters are located too far southward.

At the GoodHope line, both NCOM and AG01 might have skill, even though both models have drifter crossings too far offshore. But because there are only 11 drifting buoy crossings at this section, D_n is allowed to be larger before the decision has to be taken that the model has no skill (Fig. 2.3). Even ORCA might have skill, with a confidence level slightly higher than 0.05. One of the deficiencies of the one-dimensional 2KS-test is demonstrated here. NCOM severely underestimates the magnitude of Agulhas leakage, but because the crossing positions of the drifters that do make it to the Atlantic Ocean are good, the model is designated skillful at the GoodHope line.

At 37.5°E, only NCOM might have skill. In ORCA the drifters cross too far northward, which is the expression of the bipartition also observed in Fig. 2.4. The qualitative annotation on AG01 at 37.5°E, that the spread of drifters is too wide compared to the drifting buoys, is confirmed in Fig. 2.5. Moreover, the

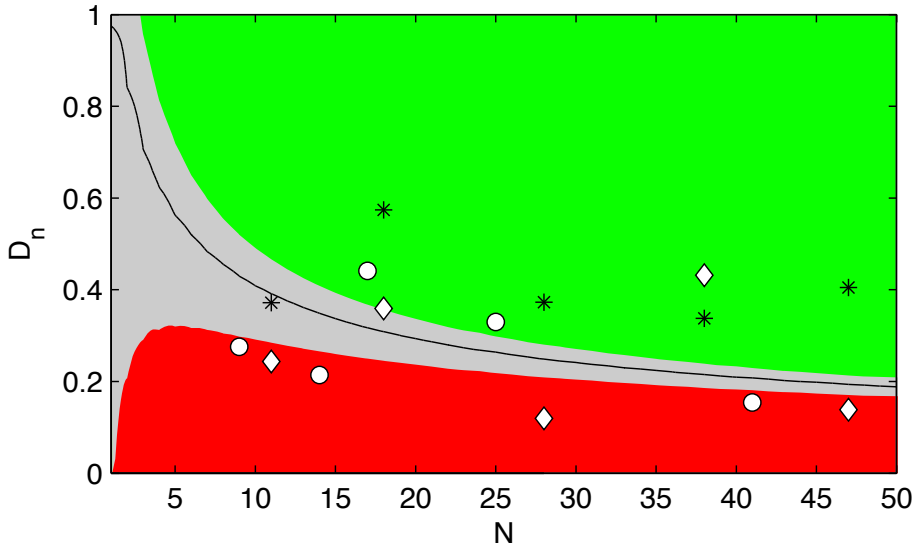


Figure 2.6: Combinations of drifting buoy data set length N and test statistic D_n for the five sections of Fig. 2.4 and Tab. 2.1 for NCOM (circles), the ORCA model (asterisks) and the AG01 model (diamonds). The black line is the line where $\alpha = 0.05$, the divider between a model that lacks skill and a model that might have skill according to the decision rule, Eq. (2.3). The gray area denotes the region where in the worst-case scenario one extra drifting buoy could make α cross the 0.05 line. Only decisions inside this area are subject to change when an extra drifter is introduced, while in the red (no skill) and green (might have skill) areas this decision will not be changed on the introduction of an extra buoy.

median of the drifter crossings is more southward in AG01 than in the drifting buoy data.

According to the results tabulated in Tab. 2.1, none of the models have skill in the Agulhas Current as the numerical drifters are more coast-bound than the drifting buoys (Fig. 2.5). However, the difference is in the order of tens of kilometers and is mainly due to the details in the bathymetry. All models use a land-mask which ends slightly too far northward and does not fully resolve the inner-shelf bathymetry. This causes a slight bias between the Agulhas Current core as sampled by the drifting buoys and in the models. This cross section shows that one should be careful when applying the 2KS-test, especially if sections are very short.

Based on these five sections, it can be concluded that AG01 and NCOM are the best models, with possible skill at three sections. ORCA might have skill only at the GoodHope line. The highest confidence level α is found at 20°E in AG01, with only a 20% probability that the numerical drifters and the drifting buoys are from a different distribution. This is above the critical confidence level of $\alpha = 0.05$ from the decision rule, Eq. (2.3).

The sensitivity of these results can be estimated by determining how the decisions would change if an extra drifting buoy crossing was added to the data sets of each section (Fig. 2.6). This figure denotes for each of the models and sections in Fig. 2.5 what the values for N and D_n are. Moreover, it shows the robustness of the skill decision since it divides the $N - D_n$ space in three regions depending on what can happen to the model skill decision if one new drifting buoy crossing is added to data set B . These are: a region where a model will never have skill when B is extended by one buoy; a region where a model might always have skill when B is extended by one buoy; and a region where the decision might have to be changed by the extension of B . As discussed in section 2.2, adding one extra member to data set B can alter $F_B(x)$ by only $1/N_B$, and consequently the change in D_n is also at most $1/N_B$.

Only the decision at the GoodHope line in ORCA could change in this worst-case scenario; all other decisions are immune to one extra drifting buoy crossing. Note that the dashed lines in Fig. 2.6 denote the maximum influence region. In reality, an extra buoy crossing would probably fall within the already found distribution and the change in D_n would likely be much smaller than $1/N_B$.

2.6 Two-dimensional model validation

In the previous section, it has been concluded that both NCOM and AG01 might have skill at three of the five sections. However, from Fig. 2.4, it is clear that the numerical drifter trajectories in AG01 are in better agreement with the drifting buoy trajectories than they are in NCOM. This qualitative statement can be quantified using the two-dimensional 2KS-test, which yields a domain-wide measure of near-surface model skill.

One can not simply use the 2KS-test as described in section 2.2, since the individual points that make up a trajectory are certainly not independent. This is because the location of a drifter at a certain moment is to a large extent determined by its former location. However, independence is required for the 2KS-test to be valid. To circumvent this problem of high interdependence of the data set, two ways are presented to adjust the two-dimensional 2KS-test.

2.6.1 Time-dependent confidence levels

The trajectory data sets are not independent because they contain information on the location of a drifter over a course of time. But this interdependence can be removed by taking only one position per drifter into account. To do this, the release of each drifter is synchronized to $t = 0$. Then, if the drifter positions are available at resolution Δt , the two-dimensional 2KS-test can be performed at every moment $t = n\Delta t$. This results in time series of the test statistics $D_n(t)$ and confidence levels $\alpha(t)$.

As time increases, the number of drifters in the model domain decreases because the drifters exit as they cross the domain boundaries. The two-

dimensional 2KS-test is only valid for $N \gtrsim 10$ [Peacock, 1983]. Therefore, the time series for α is trimmed to the moment that the number of drifting buoys in the model domain reaches ten. This occurs after six months in NCOM and after five months in ORCA and AG01. Using only the $\alpha(t)$ for the time that $N > 10$ yields mean confidence levels of $5.3 \cdot 10^{-3}$ (NCOM), $1.9 \cdot 10^{-2}$ (ORCA), and 0.11 (AG01). Using a five months window for NCOM instead of a six month window increases the mean confidence level to $4.2 \cdot 10^{-3}$. The conclusion must therefore be that, using this method and the decision rule, Eq. (2.3), only AG01 might possess skill when all drifter trajectories are taken into account.

2.6.2 Estimating the degrees of freedom

A second way to estimate the confidence level for the interdependent complete trajectories is by just ignoring the interdependence. Using the complete data sets, cumulative distribution functions can be calculated. From these cumulative distribution functions, a test statistic can be calculated just as in Eq. (2.4). Although formally the interdependence of the points in the data set prevents the 2KS-test from being valid, the test statistic D_n does possess information.

This procedure yields values for the test statistic D_n of 0.25 for NCOM, 0.31 for ORCA, and 0.18 for AG01. If one assumes complete dependence of all data points on one trajectory, the number of degrees of freedom is just the number of drifting buoy trajectories, 51 for NCOM, and 47 for ORCA and AG01. Taking this amount of drifting buoys for N in the conversion from D_n to α leads to confidence levels of $8.0 \cdot 10^{-3}$ (NCOM), $4.3 \cdot 10^{-4}$ (ORCA), and 0.24 (AG01). This is an upper limit for the confidence level, as the relation between N and α is inverse so that more degrees of freedom lead to lower values of α (Fig. 2.3). From this upper limit, it must be concluded that ORCA and NCOM possess no skill in accordance with the decision rule, Eq. (2.3). The AG01 model might possess skill for $N = 47$, but the confidence level drops below 0.05 when $N = 82$.

2.7 Conclusions and discussion

We have applied the two-sample Kolmogorov–Smirnov test (2KS-test) to data sets of drifting buoys and numerical Lagrangian drifter trajectories. This test yields two numbers, the test statistic D_n and the confidence level α , which can be used to determine the skill of the model trajectories when the drifting buoy trajectories are taken as the truth. Moreover, the 2KS-test delivers a binary decision on the skill of the model. Depending on the value of α , the model either might have skill (when $\alpha > 0.05$) or has no skill (when $\alpha \leq 0.05$). These numbers come from the 95% confidence interval with which the hypothesis that numerical drifters and drifting buoys are drawn from the same distribution can be rejected.

The 2KS-test has been applied to three different models. The numerical drifter trajectories in the $1/2^\circ$ ORCA model are so different from the drift-

ing buoy trajectories that the model has skill in neither four out of five one-dimensional sections, nor in a two-dimensional sense. Only at the GoodHope line might the model have some skill, all be it not very robust. The $1/10^\circ$ AG01 model might have skill in three out of five sections, and in the two-dimensional sense. The assimilative $1/8^\circ$ NCOM has no skill in the two-dimensional sense, but it might possess skill in three out of five sections. This illustrates that, while a model may lack skill overall in a domain, it may have skill in certain locations. It also shows that the eleven buoy crossings through the GoodHope line might be too little for the 2KS-test to be useful, as this is the only section where the objective (based on the test) and subjective (based on eyeball verification) skill decisions differ.

Not only has AG01 the highest confidence levels in the Agulhas region, with a mean Agulhas leakage magnitude of 16.7 Sv it is also closest to estimates from many other studies [e.g. *Doglioli et al.*, 2006; *Richardson*, 2007]. NCOM, on the other hand, has a mean Agulhas leakage of only 1.5 Sv in addition to its lower confidence levels. This underestimation of the magnitude of Agulhas leakage is probably related to the mean location of the Agulhas Current retroflexion, which is too far eastward in NCOM. However, it is unclear why a high-resolution assimilative model is so underachieving in the Agulhas region. The low confidence levels of ORCA can probably be attributed to consequences of its low resolution. Due to the poor representation of the oceanic mesoscale in combination with the high explicit and numerical eddy viscosity the model shows a rather linear behavior. This results in an overestimation of the magnitude of Agulhas leakage of 32 Sv in ORCA [*Biastoch et al.*, 2008c] and a relatively prominent supergyre [*Biastoch et al.*, 2008b]. But, as is also the case with these three models, diagnosing why a model lacks or might possess skill is much more difficult than assessing its skill.

In the implementation of the 2KS-test described here, model skill is a binary quantity: it is either 1 or 0. However, for model comparison the confidence level is probably a much better quantity. Using the magnitude of α also gets rid of the only choice which has to be made when applying the 2KS-test: the choice for a critical confidence level. The presence of only one tuning parameter is one of the strengths of the 2KS-test. We have chosen the 95% confidence interval for the critical value of α . Note that a larger confidence interval leads to a lower critical confidence level α . The confidence level is defined in this way so that ‘better’ models have higher confidence levels, which is more intuitive than the other way around. Using the $\alpha = 0.05$ critical confidence level differentiates between a subjectively good model (AG01) and two subjectively bad models (NCOM and ORCA). But for confidence intervals between 90% and 98%, none of the decisions made have to be changed. This is the case neither in the one-dimensional sections nor the two-dimensional basin-wide assessment, except for the problematic decision on ORCA model skill at the GoodHope line.

The 2KS-test is here applied using drifting buoy trajectories as data set *B*. The disadvantage is that this confines the assessment to the skill of the upper 15 m. This is not a limitation of the method, but of the data set. In principle,

other Lagrangian data sets (e.g. Argo floats or acoustically tracked subsurface floats such as in RAFOS experiments) can also be used. There are two requirements for float data sets to be useful. Their temporal resolution should be high (a problem with Argo floats, which surface typically once a month), and the number of trajectories should be sufficient (which is often a problem with RAFOS experiments).

The 2KS-test might even be applied to data sets beyond those of Lagrangian drifters or floats. In an Eulerian framework, the distribution of for instance model temperature at some grid cell could be compared to the distribution of temperature as obtained by a mooring. If one is interested in model – mooring validation of the complete distribution of some field, the 2KS-test can give a quick and objective measure of skill. However, an analysis of spectrum would be more suitable if one is interested in assessing the variability. That is because all temporal information is disregarded in the construction of the cumulative distribution function $F(x)$.

Chapter 3

Fast decay of Agulhas rings

This chapter is based on the work:

Van Sebille, E., P. J. van Leeuwen, A. Biastoch, and W. P. M. de Ruijter (2009), On the fast decay of Agulhas rings, *submitted*.

Abstract

The Indian Ocean water that ends up in the Atlantic Ocean detaches from the Agulhas Current retroflection predominantly in the form of Agulhas rings and cyclones. Using numerical Lagrangian float trajectories in a high-resolution numerical ocean model, the fate of coherent structures near the Agulhas Current retroflection is investigated. It is shown that within the Agulhas Current, upstream of the retroflection, the spatial distributions of floats ending in the Atlantic Ocean is to a large extent similar to the spatial distribution of floats ending in the Indian Ocean. This indicates that the probability of floats to contribute to Agulhas leakage is uniform over the Agulhas Current, and that Agulhas leakage occurs mostly through the detachment of Agulhas rings.

After the floats detach from the Agulhas Current, the ambient water quickly loses its relative vorticity. Within 10 months, 90% of the floats are within water with almost no net relative vorticity. The Agulhas rings thus seem to decay and lose much of their water in the Cape Basin. A cluster analysis reveals that most water in the Agulhas Current is within clusters of 180 km in diameter. Halfway the Cape Basin there is an increase in the number of smaller clusters, probably related to filaments. However, there is also an increase in the number of larger clusters with low relative vorticity, which carry the bulk of the Agulhas leakage transport through the Cape Basin. This upward cascade with respect to the length scales of the leakage, in combination with a power-law decay of the magnitude of relative vorticity, might be an indication that the decay of Agulhas rings is somewhat comparable to the decay of two-dimensional turbulence.

3.1 Introduction

The entrainment of Indian Ocean water into the Atlantic Ocean is called Agulhas leakage and its source is the Agulhas Current, the western boundary current of the Indian Ocean subtropical gyre [Gordon, 1985; Lutjeharms, 2006, see also section 1.5]. Of the volume flux carried by the Agulhas Current, however, only approximately 25% takes part in this interocean exchange. Once the Agulhas Current has detached from the continental slope, potential vorticity conservation causes the westward flowing current to retroflect. The bulk of the water in the Agulhas Current is then advected back into the Indian Ocean [De Ruijter *et al.*, 1999].

One of the reasons why Agulhas leakage is relevant is because of its role of transporting heat and salt from the Indian Ocean to the Atlantic Ocean. Once advected northward in the Atlantic Ocean, this heat and salt can influence the Atlantic meridional overturning circulation [Weijer *et al.*, 2002; Biastoch *et al.*, 2008c, see also section 1.1], although not all Agulhas leakage crosses the equator [Donners and Drijfhout, 2004]. A large portion recirculates in the South Atlantic Ocean subtropical gyre [De Ruijter and Boudra, 1985]. This latter route is closely connected to the subtropical supergyre [Speich *et al.*, 2002], a gyre encompassing both the Indian Ocean and the Atlantic Ocean (and possibly the Pacific Ocean too). Nevertheless, the magnitude of interocean exchange south of Africa is considered to be closely linked to the northern Atlantic Ocean [Knorr and Lohmann, 2003; Peeters *et al.*, 2004]. This considered, Agulhas leakage is here defined as the flux of water carried by the Agulhas Current at 32°S that does not retroflect back into the Indian Ocean but ends up in the Atlantic Ocean (see also section 1.2).

The water which constitutes Agulhas leakage was suggested to be mainly trapped inside large anticyclones called Agulhas rings [Gordon, 1986]. These rings can be tracked in altimetry data to move into the Atlantic Ocean, while decaying and releasing their heat and salt content [Byrne *et al.*, 1995; Beismann *et al.*, 1999; Schouten *et al.*, 2000; Van Aken *et al.*, 2003; De Steur *et al.*, 2004; Doglioli *et al.*, 2007]. From the aggregation of these studies it appears that a typical Agulhas ring has a radius of 150 – 200 km and that the surface velocities can exceed 1 m s⁻¹. A ring is shed from the Agulhas Current retroflection every 2 – 3 months.

Recently, however, it has been suggested that advection of water by large-scale Agulhas rings is only one of the mechanisms in which water can get from the Indian Ocean to the Atlantic Ocean. Boebel *et al.* [2003a] and Matano and Beier [2003] have shown that cyclones, although they are generally smaller than the anticyclonic Agulhas rings, also play an important role in the interocean exchange. Furthermore, Treguier *et al.* [2003] found in a model study that more than half of the heat and salt transported by Agulhas leakage at 30°S is not carried by eddies, but advected in smaller filaments. The important role played by filaments was also suggested by Lutjeharms and Cooper [1996].

This grouping in three categories (anticyclones, cyclones, and non-rotating

filaments or patches) may hold implications for the fate of temperature and salt anomalies as they enter the Atlantic Ocean. Agulhas rings have a longer life span than filaments, and can therefore advect their thermohaline properties farther into the Atlantic Ocean. As shown by *Weijer et al.* [2002], the response of the Atlantic meridional overturning circulation strength to Agulhas leakage sources is sensitive to the path of these thermohaline anomalies. Water that is advected within the Benguela Current rather than in Agulhas rings may end up farther north, where the probabilities of crossing the equator are higher [*Donners and Drijfhout*, 2004].

Apart from the Agulhas leakage due to coherent features which have detached from the Agulhas Current, there might also be an interocean flux related to a continuous current. *Gordon et al.* [1995] have shown the existence of a Good Hope Jet on the continental slope in the Cape Basin. This Good Hope Jet is an intense frontal jet forced by the wind-induced upwelling at the western African coast. It is unknown what the volume transport of the jet is and what the sources of that transport are. Part of the jet will originate from the South Atlantic Ocean subtropical gyre, but there might also be a direct connection from the Indian Ocean. The inshore portion of the Agulhas Current might round the Cape of Good Hope, feeding directly into the Good Hope Jet.

Doglioli et al. [2006] have grouped Agulhas leakage into a part advected by cyclones, a part advected by anticyclones, and a part advected by the background flow. The authors have used a high-resolution model to determine the net rotation of numerical Lagrangian floats as they are advected through the Cape Basin (see section 1.4 for its location). This was done by computing the spin parameter of each trajectory, a parameter that is related to the net rotation of a trajectory throughout the entire Cape Basin. The result from this study was that 13% of the Agulhas leakage transport was due to Lagrangian floats with anticyclonic rotation, 17% of the Agulhas leakage transport was due to Lagrangian floats with cyclonic rotation, and 70% of the Agulhas leakage transport was in Lagrangian floats that had a negligible net rotation.

Although the study of *Doglioli et al.* [2006] is very thorough, there are some caveats to using trajectories across the entire Cape Basin. The eddies in the Cape Basin can experience multiple splitting and merging events [*Schouten et al.*, 2000; *Boebel et al.*, 2003a] and floats might enter and exit cyclones and anticyclones multiple times in their journey through the basin. This effect might be obfuscated when net rotation along an extended section of the float's path is computed because a float which is in an anticyclone for half of its journey before being trapped in a cyclone may have a very small net curl. In combination with the relatively low number of floats used, this makes the results of *Doglioli et al.* [2006] uncertain.

The apparent discrepancy between studies reporting that Agulhas rings are the dominant agent of leakage and studies finding that Agulhas leakage is mainly in non-rotating filaments may be due to the location where the Agulhas leakage transport is measured. Both *Byrne et al.* [1995] and *Schouten et al.* [2000] have shown that Agulhas rings experience decay after they have spawned

from the Agulhas Current retroflection. *Byrne et al.* [1995] report a 1700 km e -folding distance when rings were tracked in space and *Schouten et al.* [2000] observe a fast decay in the first 10 months when rings were tracked in time. It might therefore be that the results of grouping Agulhas leakage in anticyclones, cyclones, and non-rotating filaments depend on how far away from the Agulhas Current retroflection the grouping is performed.

Although the studies of *Byrne et al.* [1995] and *Schouten et al.* [2000] have provided a lot of insight on the temporal and spatial scales of Agulhas ring decay, there are several questions that these studies have not been able to answer. First of all, it is unclear what happens with the debris of Agulhas rings, the water which was initially trapped in the rings. *De Steur et al.* [2004] suggested that this debris forms initially in filaments, but did not elude on their fate. Furthermore, the dynamical behavior soon after a ring has been shed is still unknown, as the tracking technique in satellite data used by *Byrne et al.* [1995] and *Schouten et al.* [2000] does not work when the Agulhas rings are still close to the Agulhas Current retroflection.

In this chapter we will use a time series of numerical Lagrangian float trajectory data to address the fate of the water which forms Agulhas leakage. After introducing the model setup (section 3.2), we will investigate how and where the bifurcation of Agulhas leakage and Agulhas Return Current water is controlled, by grouping the floats by the ocean in which they end up (section 3.3). Then, the decay of rotating features will be examined by analyzing the relative vorticity of the water as the floats detach from the Agulhas Current (section 3.4). Finally, we will investigate what the decrease in relative vorticity does to the size of the coherent features (section 3.5).

3.2 The model

The magnitude of Agulhas leakage is in this study estimated from the transport as sampled by numerical Lagrangian floats which are seeded in the Agulhas Current. The Lagrangian floats are advected (see section 1.8) using three-dimensional five day averaged velocity fields from the AG01 model [*Biastoch et al.*, 2008b,c]. This is a $1/10^\circ$ numerical ocean model of the Agulhas region ($20^\circ\text{W} - 70^\circ\text{E}$; $47^\circ\text{S} - 7^\circ\text{S}$) based on the NEMO code [*Madec*, 2006, version 2.3]. The model has 46 vertical layers, with layer thicknesses ranging from 6 m at the surface to 250 m at depth. The model employs partial cells at the ocean floor for a better representation of bathymetry.

The regional AG01 model is nested within a global model, ORCA, a $1/2^\circ$ global ocean–sea-ice model which is also based on NEMO. The two-way nesting allows for information exchange between the two models [*Debreu et al.*, 2008]. Not only are the boundary conditions of the high-resolution AG01 model taken from the low-resolution ORCA model, but the low-resolution ORCA model also gets updated by the high-resolution AG01 model at shared grid points. The Agulhas region dynamics is therefore affected by the global circulation, and

vice versa. In this approach, the two models have to be run simultaneously. The two models are forced with the CORE data set of daily wind and surface forcing fields [*Large and Yeager, 2004*] for the period 1958 – 2004. The model is spun up for ten years, which leaves a 37 year time series at five day resolution (1968 – 2004) for Eulerian analysis.

The AG01 model is the model that comes best out of the three-model quantitative skill assessment of chapter 2, so it is most apt for assessing the circulation of the Cape Basin. Furthermore, a comparison of the modeled sea surface height variability to the root mean square variability from satellite altimetry (Fig. 3.1) shows that the model performs reasonably in the Cape Basin, the area where the Agulhas rings experience most decay. The altimetry data used is from the AVISO project: More than 15 years of weekly merged sea level anomalies in the Agulhas region on a $1/4^\circ$ resolution, combined with the *Rio and Hernandez [2004]* mean dynamic topography.

The trajectories of the numerical Lagrangian floats are integrated using the ARIANE package [*Blanke and Raynaud, 1997*]. Floats are released every five days in a 300 km zonal section of the Agulhas Current core at 32°S . The number of floats which are released at a particular moment is based on the transport per grid cell. Each float represents a certain transport, with a maximum of 0.1 Sv. Using the five day mean velocity fields, the floats are advected for a maximum of five years. When a float hits one of the trajectory boundaries, the integration of that float is stopped. These trajectory boundaries are at 32°S and 40°E in the Indian Ocean, at 47°S in the Southern Ocean, and at 5°S and 20°W in the Atlantic Ocean. The floats are isopycnal, which means that they are not bound to a particular model layer. *Biastoch et al. [2008b,c]* have used the same model and Lagrangian techniques to simulate Agulhas Current transport and Agulhas leakage.

In the 37 year period, $5.6 \cdot 10^6$ floats are released, which constitutes a mean Agulhas Current transport at 32°S of 64 Sv. On the five day resolution, however, the Agulhas Current strength ranges from 30 Sv to 128 Sv. As shown by *Biastoch et al. [2009]*, the strength of the Agulhas Current in the model is in agreement with over a year of in situ measurements by *Bryden et al. [2005a]*, who report an Agulhas Current range from 9 Sv to 121 Sv, with a mean of 70 Sv. After the five year integration period, only 3% of the numerical floats have not exited the domain. The mean magnitude of Agulhas leakage in the model is 16.7 Sv (see also section 5.4). This is higher than the mean magnitude of Agulhas leakage in the study of *Biastoch et al. [2008c]*, which was based on the same model but used only the first four years of the float data set.

A float contributes to the Agulhas leakage transport F_{AL} when it ends in the Atlantic Ocean. The transport which the float represents is added to the time series of Agulhas leakage when the float crosses the GoodHope line for the last time. The GoodHope line is a virtual section between South Africa and Antarctica in the Atlantic Ocean (Fig. 3.2). The line currently serves as an XBT-section [*Swart et al., 2008*] and between 2003 and 2005 twelve Pressure Inverted Echo Sounders (PIES) have been deployed on the line in the ASTTEX

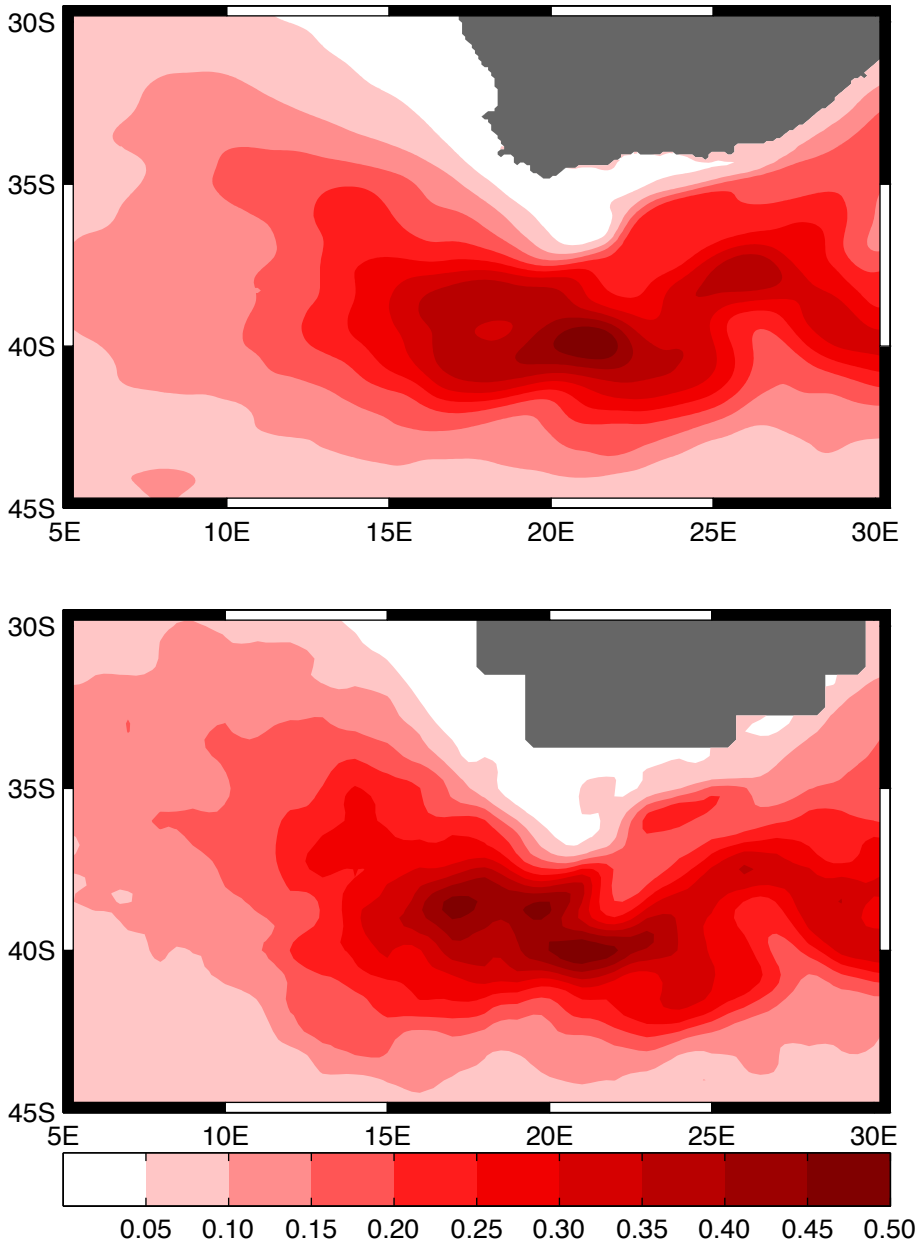


Figure 3.1: The root mean square variability in sea surface height in the Cape Basin in the AG01 model (upper panel) and in the AVISO altimetry data (lower panel), in meter on the same scale. The modeled variability in the Cape Basin is generally of the right magnitude in the model, although the small-scale variability is somewhat underestimated in the model.

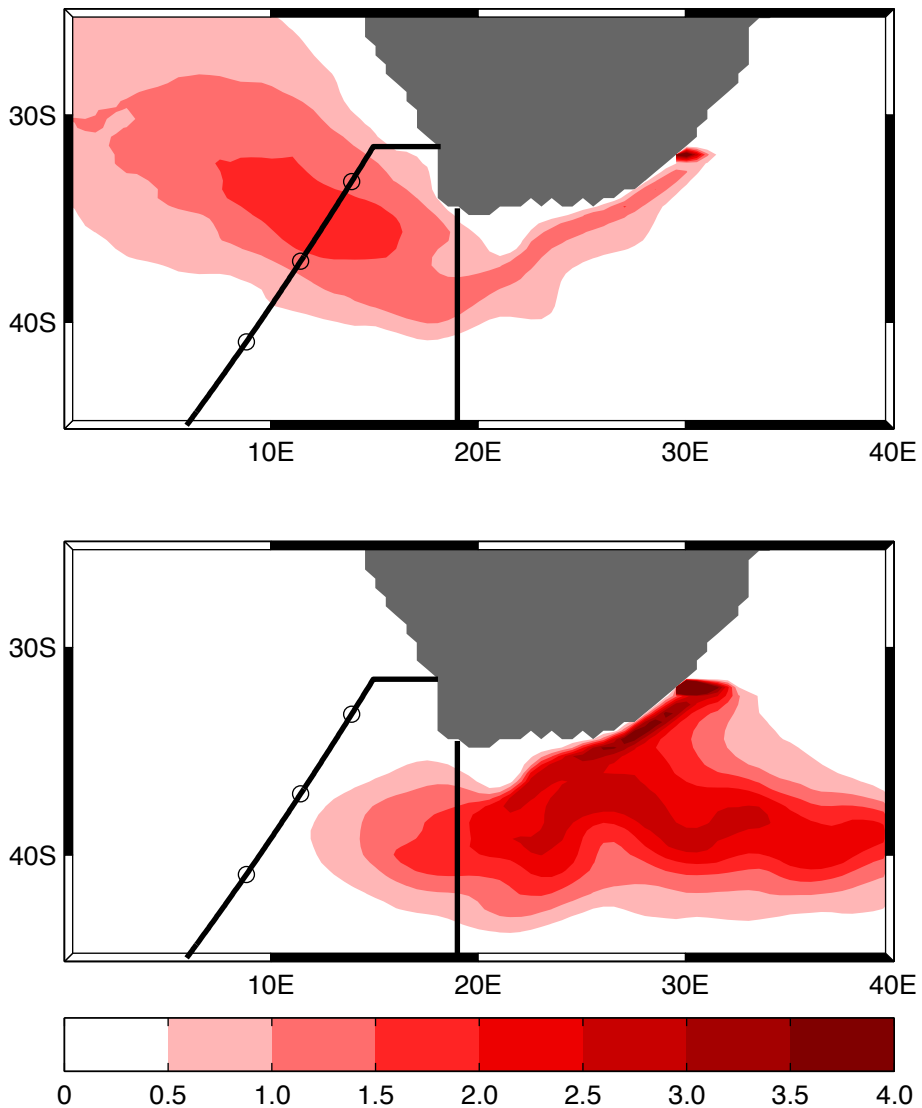


Figure 3.2: The density of the numerical float trajectories for floats that end up in the Atlantic Ocean (upper panel) and floats that end of in the Indian Ocean (lower panel), in sverdrup on the same scale. The density is calculated on a $0.5^\circ \times 0.5^\circ$ grid. The thick black lines in the Atlantic Ocean denote the location of the GoodHope line, with the circles the positions of the 500 km, 1000 km, and 1500 km offshore points. The lines at 19°E are an indication of the mean Agulhas Current retroflection position. The vast majority of floats that cross the GoodHope line end up in the Atlantic Ocean, making it a suitable section for measuring the magnitude of Agulhas leakage.

program [Byrne and McClean, 2008]. The line runs right through the Cape Basin, which is known for its vigorous mixing and mesoscale eddies [Boebel *et al.*, 2003a]. After a short 250 km zonal excursion, the section follows a southwestward oriented TOPEX/POSEIDON-JASON1 ground track.

By categorizing the floats on the basis of the ocean in which they end, the aptness of the GoodHope line for measuring the magnitude of Agulhas leakage can be demonstrated (Fig. 3.2). On the one hand, the flux through the GoodHope line by numerical floats that end in the Indian Ocean is negligible. Spurious fluxes from water that retroreflects back into the Indian Ocean are therefore small. On the other hand, the GoodHope line is still close to the Agulhas Current retroflection, so that the time lag between a float separating from the Agulhas Current and crossing the line is not too large. Note that this does not mean that the fluxes over the GoodHope line are exclusively Agulhas leakage as there are also fluxes of water crossing the line which originate from the South Atlantic Ocean subtropical gyre and the Antarctic Circumpolar Current (see also section 1.3).

3.3 Upstream control of float fate

The ratio between floats ending up in the Atlantic Ocean and floats ending up in the Indian Ocean is roughly 1 : 3. That means that a float has an approximately 25% probability of ending in the Atlantic Ocean. The question is whether that probability is uniform over the entire Agulhas Current or whether there is a bias based on the path of the float within the current. This question is related to the problem of how floats are ‘leaked’ into the Atlantic Ocean. One may propound two mechanisms by which Agulhas leakage is separated from water that recirculates in the Indian Ocean.

In the first mechanism, the water is disentangled based on its offshore distance and thus the float fate also depends on the offshore distance. At the Agulhas Current retroflection, there could be a bifurcation of the flow with the inshore part of the current core flowing predominantly into the Atlantic Ocean and the offshore part retroreflecting into the Indian Ocean. The gain of shear-generated cyclonic relative vorticity on the inshore side of the current core could aid in steering the inshore part of the Agulhas Current into the Atlantic Ocean, while the retroflection of the offshore part could be aided by the excess anticyclonic vorticity. *Beal and Bryden* [1999] have shown from observations of the Agulhas Current core at 32°S that such a structure of the relative vorticity (cyclonic on the inshore side, anticyclonic on the offshore side) is indeed present in the Agulhas Current, as is expected in any western boundary current.

In the second mechanism, Agulhas leakage occurs mainly through mesoscale ring shedding events. This mechanism is essentially the loop occlusion mechanism, as proposed by *Ou and De Ruijter* [1986] and further discussed by *Lutjeharms and Van Ballegooyen* [1988] and *Feron et al.* [1992]. When the Agulhas Current connects to the Agulhas Return Current east of the retroflec-

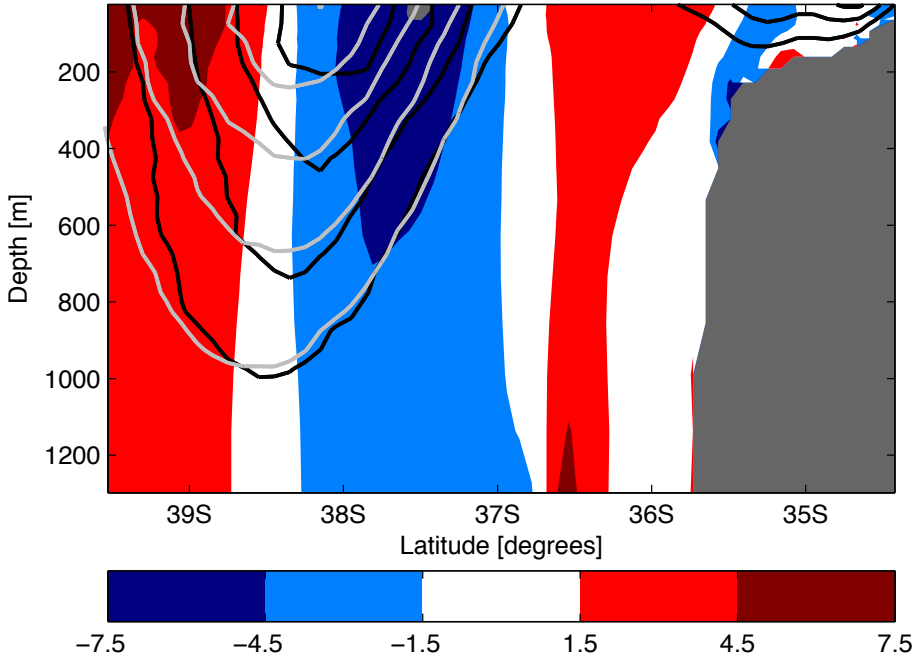


Figure 3.3: The location of float crossings at 19°E for floats that end up in the Atlantic Ocean (black contours) and floats that up end in the Indian Ocean (gray contours). The contour interval is 0.1% of the total transport per category. The colored patches show the time averaged relative vorticity at this longitude, in 10^{-6} s^{-1} . At 19°E , the current has detached from the continental slope (see also chapter 6). Except for the small core of water (2 Sv) containing only floats that end in the Atlantic Ocean over the Agulhas Bank, the distributions are to a large extent similar, especially on the inshore side of the Agulhas Current where the mean relative vorticity is cyclonic. This is an indication for the loop occlusion mechanism as the main mechanism controlling Agulhas leakage.

tion location, a shortcut is formed. The remains of the retroflection west of the shortcut detach from the Agulhas Current and can move into the Atlantic Ocean. Due to the reminiscent anticyclonic rotation, these remains form an Agulhas ring.

The similar distributions for the two float categories within the Agulhas Current core at 19°E (Fig. 3.3) are evidence for the ring shedding event mechanism and not so much for the current bifurcation mechanism since the distributions would then be more disjunct. Nevertheless, the inshore side of the Agulhas Current does possess cyclonic relative vorticity (Fig. 3.3) but this cyclonic vorticity is apparently not sufficient to have a large influence on the Agulhas Current retroflection. This is not very remarkable, as the Agulhas system is controlled by planetary vorticity and stretching rather than relative vorticity [Boudra and Chassignet, 1988].

These similar distributions of retroflected and leaked floats are interesting

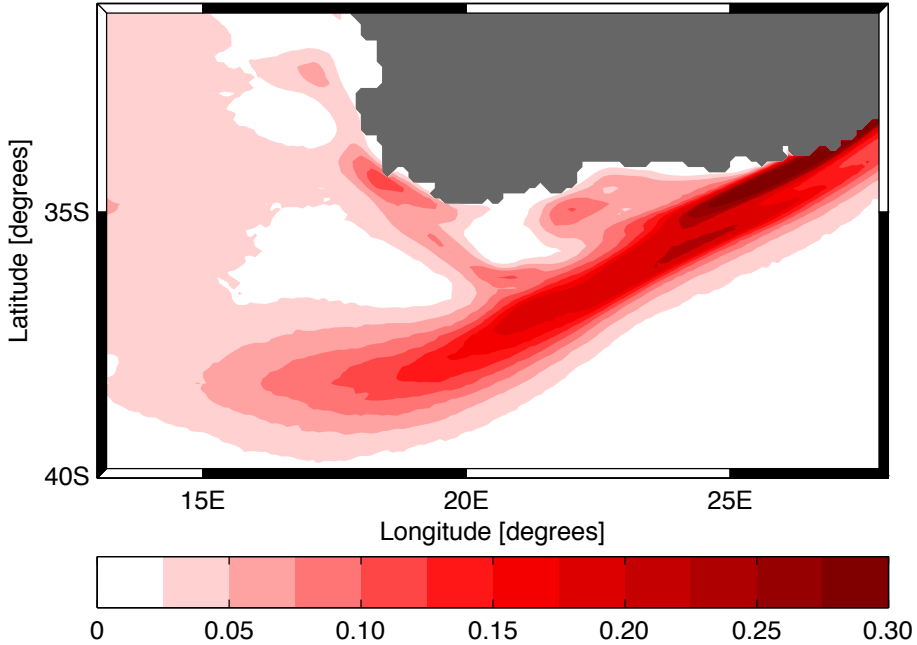


Figure 3.4: The latitude of float crossing in the uppermost model layer as a function of longitude for floats that end in the Atlantic Ocean, in $10^{-6} \text{ Sv m}^{-2}$. Most floats are advected within the Agulhas Current core until 19°E , but there is also a direct connection into the Atlantic Ocean over the Agulhas Bank that bifurcates from the Agulhas Current east of 20°E .

in view of the results by *Beal et al.* [2006]. These authors showed, based on hydrographic sections, that the Agulhas Current is not well mixed with respect to its source waters. There are basically two pathways into the Agulhas Current: through the Mozambique Channel and south of Madagascar. *Beal et al.* [2006] found that the waters which flow through the Mozambique Channel are located predominantly on the inshore side of the Agulhas Current, while the water masses from south of Madagascar stay predominantly on the offshore side. This implies that in the Atlantic Ocean there would be a bias towards Mozambique Channel water when the probability for a float to end up in the Atlantic Ocean is higher on the inshore side of the current. But since that probability to end up in the Atlantic Ocean seems to be more or less uniform across the Agulhas Current, the bias in different source water masses in Agulhas leakage is probably small.

However, there might be a minor role played by the current bifurcation mechanism. Close to the coast, on the Agulhas Bank, there is a secondary core of Agulhas leakage water (Fig. 3.3). This core consists of floats within water of cyclonic relative vorticity that have detached from the Agulhas Current more upstream (Fig. 3.4). The mean transport sampled by floats that

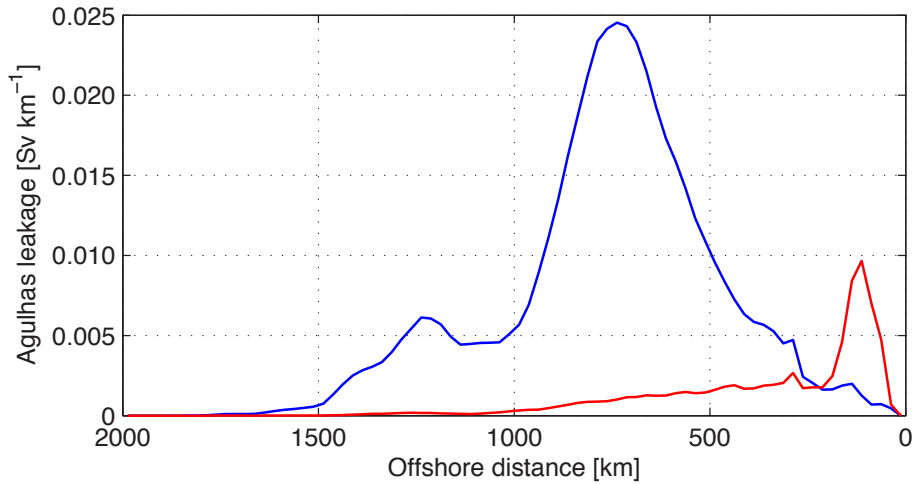


Figure 3.5: The distribution of Agulhas leakage as a function of offshore distance at the GoodHope line for floats that cross 19°E north of 36°S (red line) and floats that cross it south of 36°S (blue line). The latitude of 36°S separates floats in the Agulhas Current core from floats in the shallow continental shelf core (see Fig. 3.3). Almost half of the floats in the continental shelf core stay within 200 km of the coast, which is the location of the Good Hope Jet [Bang and Andrews, 1974]. Of the floats in the Agulhas Current core, on the other hand, only a minor fraction crosses the GoodHope line near the coast.

cross 19°E north of 36°S (the latitude that divides the two cores in Fig. 3.3) is only 2 Sv, in contrast to the more than 14 Sv transported south of that latitude. Nevertheless, the coastal core is a persistent and continuous feature (not shown).

The coastal core might be related to the Good Hope Jet, a frontal boundary current feeding into the Benguela Current [Bang and Andrews, 1974; Gordon *et al.*, 1995, see also section 1.5.6]. According to Fennel [1999], the current is formed by trapping of coastal Kelvin waves on the thermal front created by the Benguela upwelling. It appears that much of the water in the coastal shelf core at 19°E feeds directly into the Good Hope Jet (Fig. 3.5), as almost half of the floats within the shelf core at 19°E cross the GoodHope line at a maximum offshore distance of 200 km. In this numerical model, therefore, there is a small but significant amount of direct and continuous Agulhas leakage over the Agulhas Bank, feeding into the Good Hope Jet.

3.4 The decay of relative vorticity

In the previous section it has been shown that within the model it seems that leakage from the Agulhas Current occurs predominantly through the loop occlusion mechanism and Agulhas ring detachment. However, Doglioli *et al.* [2006] found that within the Cape Basin the transport by floats with anticyclonic

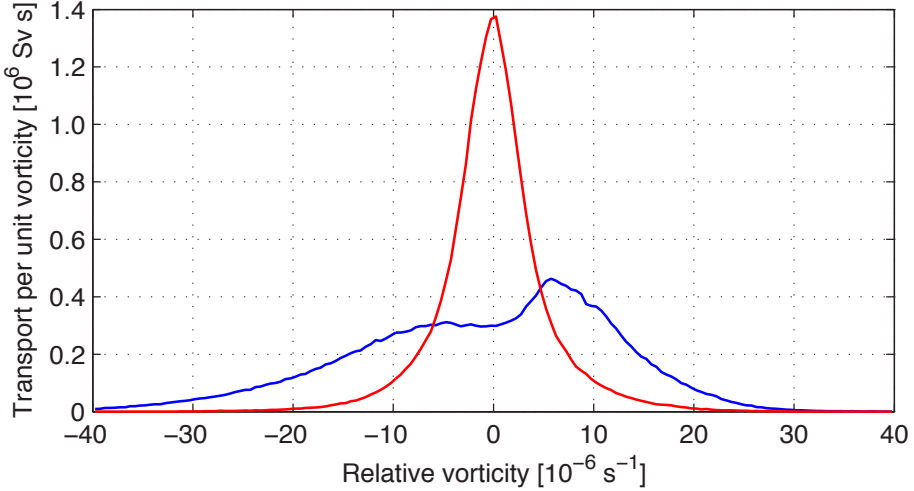


Figure 3.6: The distribution of Agulhas leakage as a function of relative vorticity for floats that cross 19°E south of 36°S , as they cross 19°E (blue line) and as they cross the GoodHope line (red line). The areas under the two distributions are equal, since only the floats that end in the Atlantic Ocean are used and each float that crosses 19°E also crosses the GoodHope line. At 19°E , the magnitude of relative vorticity is high and on their path towards the GoodHope line the floats lose that relative vorticity.

curl is only a small fraction of all Agulhas leakage. These two results could be connected if the Agulhas rings decay before they reach the Cape Basin. The water will then lose its relative vorticity and the floats will stop spinning. To test this hypothesis, the relative vorticity of the water at the locations where the floats cross 19°E is compared to the relative vorticity of the water at the locations where the floats cross the GoodHope line. Only floats that end in the Atlantic Ocean and cross 19°E south of 36°S are considered, as the floats north of 36°S seem to have a different leakage mechanism and are associated with the Good hope Jet instead of Agulhas rings.

Between 19°E and the GoodHope line the floats move into water with much smaller relative vorticity (Fig. 3.6). The tails of the relative vorticity distribution collapse on the journey through the Cape Basin. Within the Agulhas Current core at 19°E , the distribution of relative vorticity is skewed and peaks at $5 \cdot 10^{-6} \text{ s}^{-1}$. At the GoodHope line, however, the distribution of relative vorticity peaks at zero and is nearly symmetric around that peak.

In order to compare the distributions of this relative vorticity analysis with the results from *Doglioli et al.* [2006], the floats have to be categorized in cyclones, anticyclones, and calm water. We do this by choosing a critical vorticity $\zeta_{crit} = 5 \cdot 10^{-6} \text{ s}^{-1}$ that divides Agulhas leakage into cyclonic ($\zeta < -\zeta_{crit}$), non-rotating ($-\zeta_{crit} \leq \zeta \leq \zeta_{crit}$), and anticyclonic leakage ($\zeta > \zeta_{crit}$). The choice for $\zeta_{crit} = 5 \cdot 10^{-6} \text{ s}^{-1}$ comes from the study by *Van Aken et al.* [2003]. These authors measured the properties of Agulhas ring ‘Astrid’ and reported values

	At 19°E	At the GoodHope line	By <i>Doglioli et al.</i> [2006]
Cyclonic motion	4.4	1.5	2.5
Non-rotating water	3.2	9.1	10.1
Anticyclonic motion	4.5	1.5	1.9

Table 3.1: The float-determined Agulhas leakage transport, in sverdrup, for different categories of floats within the Agulhas Current core at 19°E, at the GoodHope line, and from the study by *Doglioli et al.* [2006] using the net spin of trajectories in the Cape Basin. Note that the total magnitude of Agulhas leakage in this study is lower than that in the study by *Doglioli et al.* [2006] because floats in the Good Hope Jet have been disregarded here. Although the way in which the transports are determined differ between this study and that of *Doglioli et al.* [2006], the results in the Cape Basin are comparable. Approximately 70% of the transport is in non-rotating, calm water. Within the Agulhas Current core, on the other hand, the transport is approximately equipartitioned between the three categories.

for relative vorticity in the upper 1000 m between $5 \cdot 10^{-6}$ and $20 \cdot 10^{-6} \text{ s}^{-1}$.

The categorization using $\zeta_{crit} = 5 \cdot 10^{-6} \text{ s}^{-1}$ leads to comparable results at the GoodHope line as the categorization procedure used by *Doglioli et al.* [2006] in the entire Cape Basin (Tab. 3.1, note that these numbers depend on the choice for ζ_{crit}). Away from the Agulhas Current retroflection, approximately 70% of Agulhas leakage is in water with negligible relative vorticity. Near the retroflection, on the other hand, leakage is much more equipartitioned between the three categories.

In order to investigate the transformation of high relative vorticity leakage to much lower relative vorticity leakage, the floats that cross 19°E south of 36°S are tracked until they reach the GoodHope line. In contrast to the relative vorticity analysis above, which was done by two-dimensional interpolation of relative vorticity on the location where floats crossed the GoodHope line or the 19°E section, the relative vorticity of the floats is now tracked in time. Every five days during their migration towards the GoodHope line, the relative vorticity of the water at the location of the float is determined by a three-dimensional linear interpolation. Only the first ten years of the model output are used, which yields $3.2 \cdot 10^5$ trajectories with a mean length of 120 days.

The change in relative vorticity appears to be closely related to the decay of Agulhas rings after they are shed from the Agulhas Current retroflection (Fig. 3.7). The decay rate of the magnitude of relative vorticity over all floats in the Agulhas Current core at 19°E that end up in the Atlantic Ocean is comparable to the mean decay rate found by *Schouten et al.* [2000]. These authors tracked 21 Agulhas rings in satellite altimetry and recorded their maximum height anomaly. In both studies the decay of Agulhas rings stops after approximately ten months. Even though the two curves in Fig. 3.7 are obtained by a very different method for estimating ring decay, the decay rates are very similar.

The fraction of floats within cyclonically rotating water appears to reduce

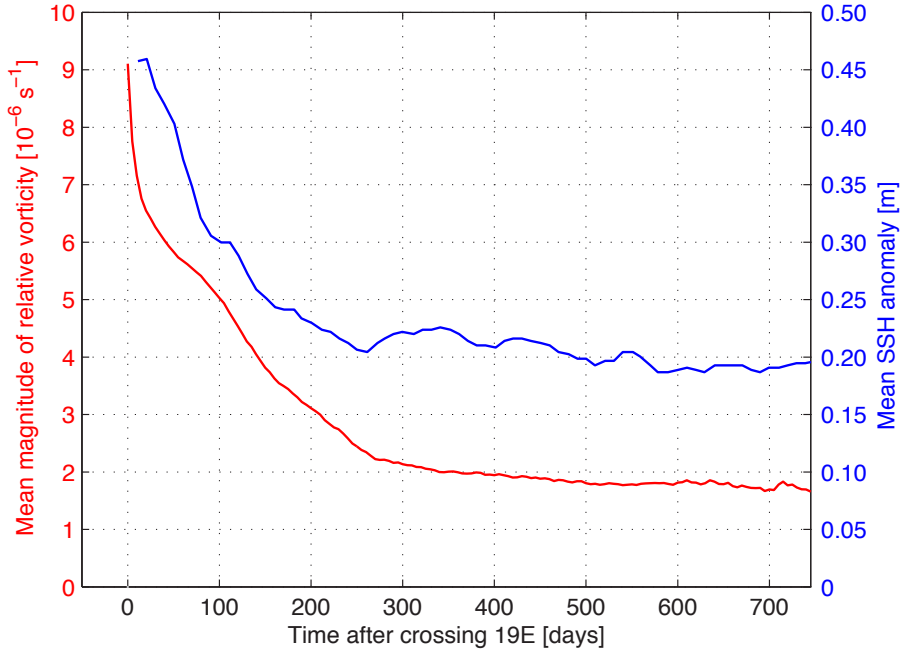


Figure 3.7: The mean magnitude of relative vorticity as a function of time as the floats move from 19°E to the GoodHope line (red line, left axis). The blue line (right axis) shows the decay rate of Agulhas rings, as found by *Schouten et al.* [2000] from satellite altimetry. Note that the relative timing of the two lines is not exact, as the tracking of Agulhas rings generally started westward of 19°E . Nevertheless, the decay rates are to a large extent comparable which is somewhat remarkable given that the two are very different measures of ring decay.

much faster than the fraction of floats within anticyclonically rotating water (Fig. 3.8). Within 300 days, almost 95% of the floats are within calm water (using the $\zeta_{crit} = 5 \cdot 10^{-6} \text{ s}^{-1}$ categorization). But where the decrease of water with anticyclonic vorticity is almost linear over that period, the fraction of water with cyclonic vorticity approximately halves within the first month. A small fraction of this decrease of the number of floats within water with cyclonic vorticity might be the result of the divergence of the flow on the surface of the cyclones, expelling the floats away from the cyclones. However, the time scale is so short that the decay of Agulhas cyclones themselves must play an important role too. One explanation for the faster decay of water with cyclonic relative vorticity might be that some of this water is situated at the edges of Agulhas rings. Therefore, it might be peeled off first when the rings decay.

If it is assumed that the sum of planetary and relative vorticity is conserved (so neglecting stretching and dissipative processes in the potential vorticity balance), the northward migration of Agulhas rings and cyclones leads to an increase in planetary vorticity and consequently a decrease in relative vortic-

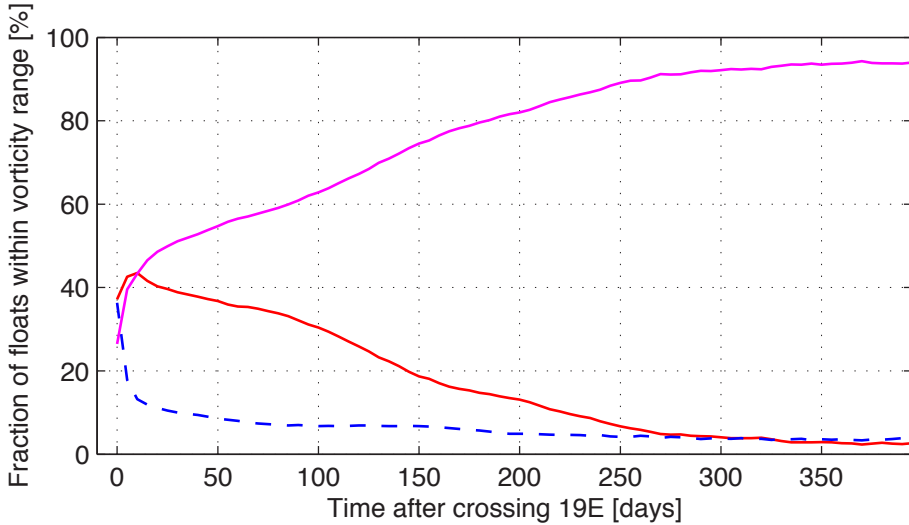


Figure 3.8: The fraction of floats within a certain vorticity category as a function of time as the floats move from 19°E to the GoodHope line. The floats are grouped in anticyclonically rotating water ($\zeta > \zeta_{crit}$, red line), cyclonically rotating water ($\zeta < -\zeta_{crit}$, blue line), and non-rotating water ($-\zeta_{crit} \leq \zeta \leq \zeta_{crit}$, magenta line), with $\zeta_{crit} = 5 \cdot 10^{-6} \text{ s}^{-1}$. At any moment, the sum of the three lines is 100%. At 19°E, the floats are approximately equally partitioned over the three classes (see Tab. 3.1) and as they move into the Cape Basin floats in anticyclonic water and cyclonic water move into calm water. Note that the fraction of floats in cyclonic water appears to decay much faster than the fraction of floats in anticyclonic water.

ity. This effect counteracts the decay of Agulhas cyclones, but may enhance the decay of Agulhas rings. The fast decay of Agulhas cyclones is even more remarkable in that respect.

One may argue that, since only floats between 19°E and the GoodHope line are used in the analysis of the decay rate of relative vorticity, the results are biased towards floats that stay close to the Agulhas Current retroflection for a long time. The floats that are quickly advected over the GoodHope line in Agulhas rings are only taken into account for a short time in the analysis and this may affect the temporal evolution of the partitioning. However, the distribution of relative vorticity as the floats cross the GoodHope line (Tab. 3.1 and Fig. 3.6) shows that the flux of relative vorticity over that line is much more towards calm water than at 19°E, and this Eulerian result does not suffer from biases due to dawdling floats.

3.5 Change in feature size

The analysis of the change in relative vorticity at float locations between 19°E and the GoodHope line revealed that Agulhas leakage detaches from the Agul-

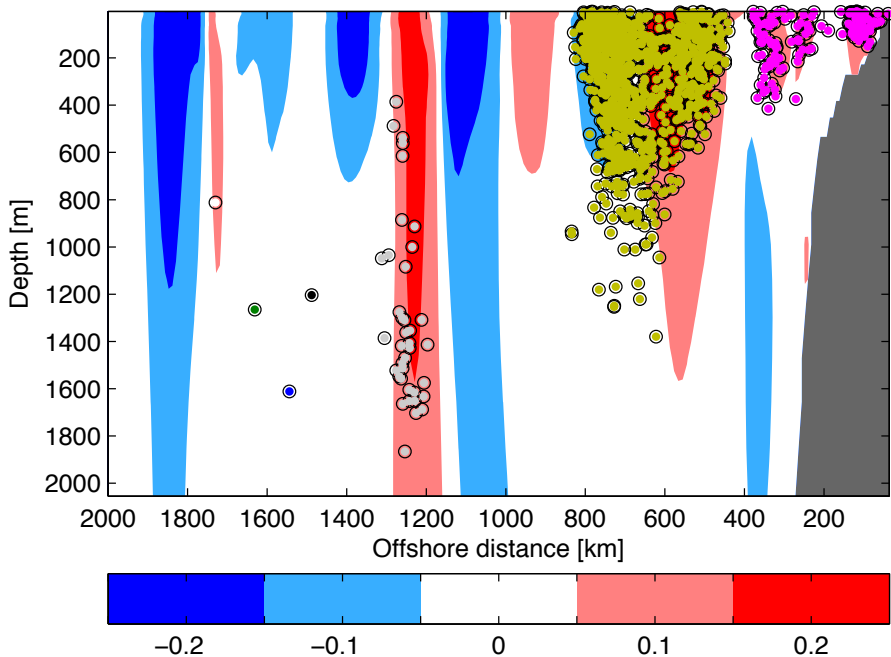


Figure 3.9: An example of the float clustering algorithm: The crossing locations of all 1121 floats that cross the GoodHope line for the last time on 28 November 1971 (colored dots). The colored patches denote the velocity perpendicular to the GoodHope line, in meter per second. The clustering produces seven clusters, each denoted by a different color. This is a typical clustering at the GoodHope line, with one or two very large clusters (diameters of larger than 300 km and large amounts of floats) and a number of much smaller clusters.

has Current retroflection within water with anticyclonic and cyclonic relative vorticity, but that this relative vorticity is quickly decayed. After ten months, values of relative vorticity are so low that the vast majority of floats can not be considered inside eddies anymore. This raises the question in what kind of structures these floats are trapped then.

There are at least three types of non-eddy structures with which floats can be advected into the Atlantic Ocean, and they can be distinguished by their size. First of all, floats can be trapped in coherent filaments: small (~ 50 km) structures that are the debris of Agulhas ring disintegration [Lutjeharms and Cooper, 1996; De Steur *et al.*, 2004]. Secondly, floats can be advected in bulk by patches, larger coherent structures of water without significant rotation. And finally, floats may break away from coherent structures and get advected individually within the northwestward flow set by the South Atlantic Ocean subtropical gyre.

To investigate how important each of these three non-eddy structures are,

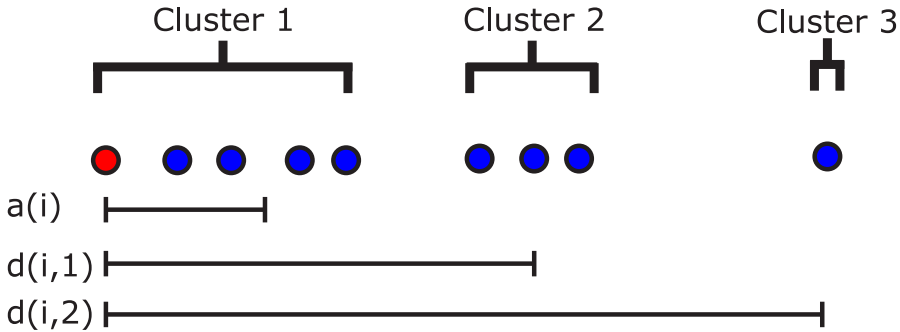


Figure 3.10: An example of the silhouette score algorithm, for nine floats within three clusters. For a certain float i (the red float in the figure), the mean distance to all other floats within its own cluster is computed as $a(i)$. The mean distance to all floats within each of the other clusters C is computed as $d(i, C)$. The silhouette score $s(i)$ of the float is then computed by Eq. (3.1) and Eq. (3.2). In this example, the silhouette score of float i is approximately 0.6. This procedure for calculating silhouette scores was proposed by *Rousseeuw* [1987].

the spatial scales associated with the leakage can be determined using a cluster analysis. At each model snapshot, the floats crossing both 19°E and the Good-Hope line are clustered according to their mutual distance (Fig. 3.9). This means that floats which are close together will be in the same cluster, while floats which are far apart will be in different clusters. The result is that each float is being assigned to a cluster, which may consist of a single float to several hundreds of floats. The set of these clusters is called a clustering.

The clustering analysis is performed using a minimum distance approach. At the start of the analysis, each cluster consists of exactly one float. Then, the two clusters that are closest together are merged. This merging is repeated until all floats are in one cluster. The merging steps can be visualized in a dendrogram, with the distance at which two clusters are merged on the ordinate. The clusters are then the connected branches of a horizontal cross section through the dendrogram at a particular height.

In advance, it is unknown how many clusters of floats there are in any snapshot. To determine the optimum number of clusters, clusterings with one to ten clusters are computed. A skill is associated with each of these ten tested clusterings, and the clustering with the highest skill is chosen.

The skill is defined as the mean of the silhouette scores of the clustering [*Rousseeuw*, 1987]. The silhouette score of a float represents that float's distance to floats within its cluster compared to the distance to floats in other clusters (Fig. 3.10). Two quantities are computed for each float i in a certain cluster A : $a(i)$ the average horizontal distance between float i and all other floats in its cluster A ; and for all other clusters $d(i, C)$ the average horizontal distance between float i and all floats in cluster C . The cluster closest to i is

selected and denoted by

$$b(i) = \min_{C \neq A} d(i, C) \quad (3.1)$$

and the silhouette score for float i is then defined as

$$s(i) = \frac{b(i) - a(i)}{\max \{a(i), b(i)\}} \quad (3.2)$$

A silhouette score of +1 means that the float is indisputably within the correct cluster and a silhouette score of -1 means that it has a better place in another cluster. This approach results in clusterings with typically four to five clusters and a mean silhouette score of 0.81.

Ideally, the clustering algorithm would be applied to the entire data set at once, rather than for each snapshot individually. However, this involves computation of the horizontal distances between all float crossing locations, resulting in a $1.9 \cdot 10^6 \times 1.9 \cdot 10^6$ matrix. This is computationally unfeasible, and therefore the clustering has been limited to model snapshots. At any snapshot there are in the order of 500 float crossings, which results in a much better manageable 500×500 distances matrix.

When only floats that cross 19°E south of 36°S are used, clusters that have components both north and south of 36°S are broken. This leads to erroneous clusterings. Therefore, all floats ending up in the Atlantic Ocean are considered in the clustering analysis. This is in contrast to the relative vorticity analysis of section 3.4, where only floats that cross 19°E south of 36°S are taken into account.

Near the Agulhas Current retroflexion, at 19°E , there are two peaks in the distribution of clusters based on their diameter (Fig. 3.11). Many clusters are smaller than 10 km. As these clusters represent a negligible amount of Agulhas leakage they are predominantly related to clusters containing only one float. The second peak lies around 180 km, and this peak is probably related to the Agulhas Current core, which typically has such a width. Most of the Agulhas leakage transport is within clusters of diameters 180 – 300 km.

At the GoodHope line, the number of very small clusters (< 10 km) has not changed much. The peak at 180 km, on the other hand, has been smeared out towards both smaller and larger clusters. Apparently, the vigorous mixing in the Cape Basin does not only cause clusters to break into smaller filaments, but also to merge into much larger clusters. The increase in the number of small clusters (< 150 km) at the GoodHope line has a very limited effect on the amount of Agulhas leakage in these clusters (lower panel of Fig. 3.11). The largest change between 19°E and the GoodHope line is that larger clusters (> 200 km) become more important.

An analysis of the mean relative vorticity in the clusters shows that the magnitude of relative vorticity has decreased from 19°E to the GoodHope line (Fig. 3.12). Near the Agulhas Current retroflexion, the mean relative vorticity

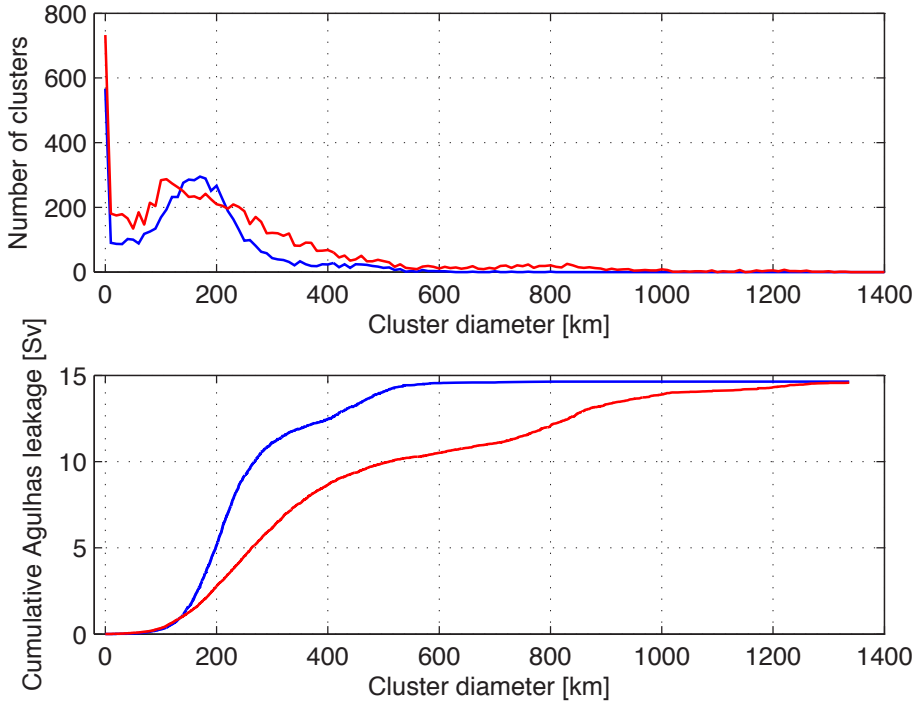


Figure 3.11: The distribution of cluster radius (upper panel), the largest horizontal distance between any two members in a cluster, for the clustering at 19°E (blue line) and at the GoodHope line (red line). The number of very small clusters (< 10 km) is comparable at both sections. At 19°E , there is a maximum around 180 km associated with the width of the Agulhas Current. At the GoodHope line, this peak has spread to both smaller clusters but also to much larger clusters. The cumulative magnitude of Agulhas leakage as a function of cluster radius (lower panel) reveals that most leakage at 19°E is within clusters around 200 km in diameter. At the GoodHope line, however, most transport is bipartitioned in clusters with diameters around 300 km and with diameters around 850 km. Apparently, some clusters break into smaller pieces, while other merge into much larger clusters.

of large clusters is not very different from that of small clusters. At the GoodHope line, on the other hand, the large clusters have almost no mean relative vorticity, and only smaller clusters have some rotation. This result confirms the considerations on relative vorticity decay from section 3.4.

The small clusters (< 150 km in diameter) may be related to Agulhas rings and cyclones. Many of them have significant relative vorticity (Fig. 3.12). A 100 – 150 km radius is also typical for an Agulhas ring in the real ocean [e.g. *Van Aken et al.*, 2003]. The larger clusters, however, are not simply large rings. They have almost no relative vorticity, and therefore probably no expression in the sea surface height. These large clusters might therefore be difficult to observe in the real ocean, despite that they carry most of the Agulhas leakage

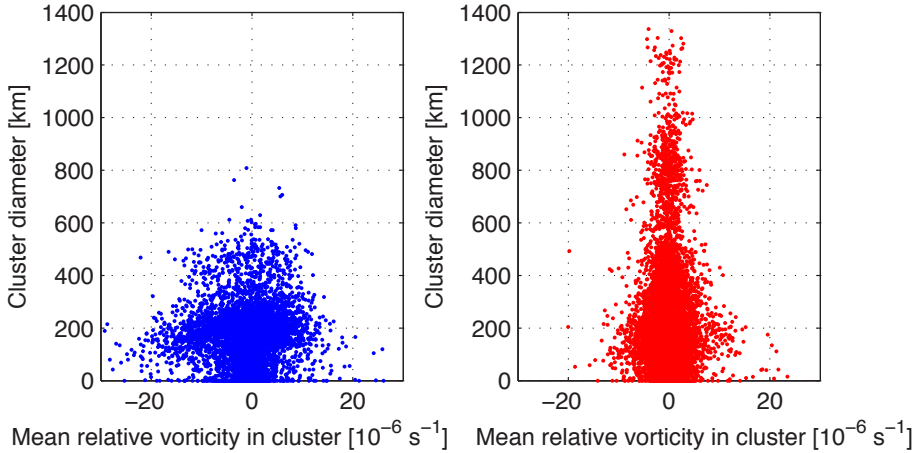


Figure 3.12: The diameter of the clusters as a function of the mean relative vorticity within these clusters at 19°E (left panel, blue dots) and at the GoodHope line (right panel, red dots). The magnitude of mean relative vorticity of the clusters is much larger at 19°E than at the GoodHope line. This result complements Fig. 3.6, which showed (on a per-float basis) the same collapse of relative vorticity.

transport over the GoodHope line.

3.6 Comparison with the decay of two-dimensional turbulence

The increase in the number of large clusters with low relative vorticity may be related to concepts from two-dimensional turbulence [e.g. *Tennekes, 1978; Carnevale et al., 1991*]. Unlike in three-dimensional turbulence, where vortices break into smaller vortices until they are dissipated by (molecular) viscosity, vortices in two-dimensional turbulence tend to merge into larger structures [*Clercx et al., 1999*]. These larger structures have a lower mean relative vorticity. This upward cascade in wavelengths might also be occurring in the Cape Basin, where the high relative vorticity eddies seem to merge into larger low relative vorticity patches.

It is hard to quantify this cascade from the clustering analysis, but it can be done using the decay of the magnitude of relative vorticity of the individual floats (the data in Fig. 3.7). When plotted on a log-log scale, the decay of the magnitude of relative vorticity in the first 100 days appears to behave as a power-law (Fig 3.13). Such a power-law is typically seen in turbulence decay [e.g. *McWilliams, 1989; Maassen et al., 1999*], where the relative vorticity as a function of time is of the form

$$\zeta(t) \sim t^\xi \tag{3.3}$$

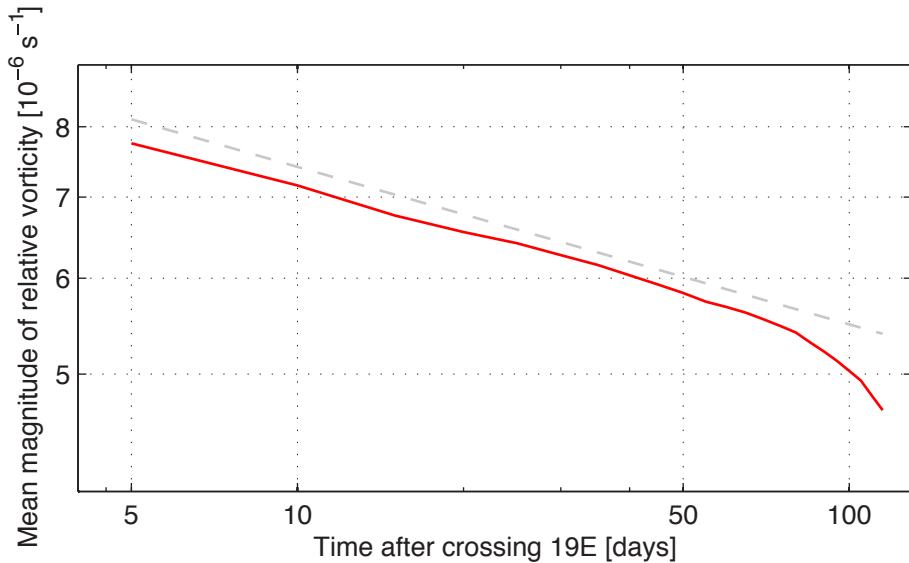


Figure 3.13: The decay of relative vorticity on a log-log scale, for the first 120 days after the floats have crossed 19°E . The red line is similar to the red line of Fig. 3.7, only on a different scale. This is done to highlight that in the early stages of decay the Agulhas leakage seems to behave like two-dimensional turbulence, where the decay of relative vorticity also obeys a power-law [Clercx *et al.*, 1999]. The gray dashed line is the $\xi = -0.13$ power-law scaling.

In this case, the fitting parameter of the power-law is $\xi = -0.13$. This is larger than the fitting parameter in freely decaying two-dimensional turbulence, where the value is typically -0.30 [e.g. Clercx *et al.*, 1999]. That might have to do with the large discrepancy between idealized turbulence studies and the representation of turbulence in this numerical ocean model. Most studies of two-dimensional turbulence are based on homogeneous (the properties of the turbulence being independent of location) and isotropic (the turbulence properties being equal in all directions) conditions for the flow. In the AG01 model, however, the flow is forced by wind patterns and steered by the bathymetry. The circulation in the model can therefore not be considered isotropic nor homogeneous. Furthermore, the spatial resolution and Reynolds parameter regime of even this state-of-the-art numerical ocean model is far from what is used in decaying turbulence studies. Nevertheless, it is interesting to see that the decay of relative vorticity in the model behaves like a power-law.

3.7 Conclusions and discussion

Using numerical float trajectories in a high-resolution two-way nested regional ocean model, we have investigated the decay of Agulhas rings and cyclones

close to the Agulhas Current retroflection. It appears that between the Agulhas Current retroflection and the GoodHope line in the Cape Basin, the floats that were initially in Agulhas rings and cyclones are quickly expelled into large patches with low relative vorticity. This fast decay of eddies near the Agulhas Current retroflection can explain the large discrepancy between studies trying to group Agulhas leakage in fractions by Agulhas rings, Agulhas cyclones, and other forms of leakage. It appears that the result of such grouping methods is sensitive to the location where the grouping is performed.

The decay of eddies was investigated using two different methods: by assessing the relative vorticity of the water around a float, and by employing a cluster analysis. The results of these methods are complementary. In both methods it appears that, when floats move through the Cape Basin from the Agulhas Current retroflection to the GoodHope line, they quickly lose their relative vorticity. When the floats cross the Cape Basin, the bulk of leakage is in large-scale patches (200 – 1000 km in diameter) with low relative vorticity. Similar behavior is seen in the decay of two-dimensional turbulence, where there is an energy cascade to the larger scales.

The comparable cross-current distributions of floats ending in the Atlantic Ocean and floats ending in the Indian Ocean suggests that float fate is predominantly determined by the moment when floats get through the retroflection area, and whether they are in a ring shedding event. Only floats on the Agulhas Bank have a much higher probability of ending in the Atlantic Ocean through the Good Hope Jet but they make up only 2 Sv of the Agulhas leakage transport.

There might seem to be a discrepancy in the use of Lagrangian floats in this study. On the one hand, the floats are treated as point particles which are passively advected within the model circulation. The floats are isopycnal, but can move into areas of different temperature and salinity. On the other hand the floats have a transport, approximately 0.1 Sv, which is used to assess the magnitude of Agulhas leakage. Finite-volume floats can only change their thermohaline properties if they are allowed to mix the water they carry with the ambient water. But if the transport by a float is mixed on its route to the Atlantic Ocean it will get diluted and its transport as it crosses the GoodHope line is not pure Agulhas Current water anymore, as is required by the definition of Agulhas leakage in section 1.2.

However, this is not a real contradiction. The point is that the floats do not *carry* a volumetric transport, but that they *represent* a transport. As such, they are point particles which have no volume and therefore also lack thermohaline properties. The Agulhas Current is sampled according to its transport when the floats are released. The float-determined Agulhas leakage transport is thus a statistical quantity rather than a deterministic quantity. The accuracy of the Agulhas leakage transport time series will increase when more floats are released so that each represents a smaller transport. As a typical float in this study represents only $2.2 \cdot 10^{-5}\%$ of the total volume transport by all floats, we can assume that the Agulhas leakage transport time series is reasonably

accurate. Thus, the apparent dichotomy is not real.

The quick loss of relative vorticity by Agulhas leakage is probably controlled by changes in the potential vorticity balance. Potential vorticity is conserved in the absence of dissipation, but relative vorticity can be converted to other terms in the balance, such as stretching. *Boudra and Chassignet* [1988] have extensively studied this, but in a simple model. Ideally, this conversion between the terms in the vorticity balance would be studied in a high-resolution model such as the one used here. Combining the balance terms with Lagrangian float trajectories could yield more insight on why the loss of relative vorticity is so fast in the Agulhas Current retroflection region.

Chapter 4

Agulhas ring energy in the Atlantic Ocean

This chapter is based on the work published as:

Van Sebille, E. and P. J. van Leeuwen (2007), Fast northward energy transfer in the Atlantic due to Agulhas rings, *J. Phys. Oceanogr.*, 37, 2305-2315.

Abstract

The transit time of wave energy radiated by an Agulhas ring released in the southern Atlantic Ocean to the northern Atlantic Ocean is investigated in an adiabatic two-layer numerical ocean model. Of particular interest is the arrival time of baroclinic energy in the northern part of the Atlantic Ocean, since this is related to variations in the meridional overturning circulation. The influence of the Mid-Atlantic Ridge is also studied, since this meridional ridge allows for conversion from barotropic to baroclinic wave energy and the generation of topographic waves.

Barotropic energy from the ring is present in the northern part of the model basin within 10 days. From that time on, the barotropic energy keeps rising to attain a maximum 500 days after initiation. This is independent of the presence or absence of a meridional ridge in the model basin. Without a ridge in the model, the travel time of the baroclinic signal is 1300 days. This is similar to the transit time of the ring from the eastern to the western coast of the model basin. In the presence of the ridge, the baroclinic signal arrives in the northern part of the model basin after approximately 10 days, which is the same time scale as that of the barotropic signal. Apparently, the ridge can facilitate the energy conversion from barotropic to baroclinic waves and the slow baroclinic adjustment can be bypassed.

The meridional overturning circulation, parameterized in two ways as either a purely barotropic or a purely baroclinic phenomenon, responds also after 1300 days. The ring temporarily increases the overturning strength. The presence of the meridional ridge does not alter the time scales.

4.1 Introduction

The spatial and temporal distribution of temperature and salt within the Atlantic Ocean is determined by many processes. In this chapter, the focus is on two of these. One is the North Atlantic Deep Water formation near Greenland [e.g. *Schmitz Jr*, 1995; *Ganachaud and Wunsch*, 2000, see also section 1.1] and the associated concept of the meridional overturning circulation. The other is the leakage of warm and saline Indian Ocean water into the Atlantic Ocean south of Africa in the form of Agulhas leakage [e.g. *Gordon*, 1986; *Lutjeharms*, 1996; *De Ruijter et al.*, 1999; *Boebel et al.*, 2003a; *De Ruijter et al.*, 2005, see also section 1.5].

The meridional overturning circulation is the global scale circulation with enhanced downwelling in the Labrador Sea and near Greenland, and upwelling in the Antarctic Circumpolar Current, the Indian Ocean and the Pacific Ocean. Although the exact mechanisms behind the meridional overturning circulation are still disputed [e.g. *Rahmstorf*, 1996], the forcing is thought to be the density fluxes at the ocean surface and the resulting meridional density difference in the Atlantic Ocean [e.g. *Weijer et al.*, 2002]. *Ganachaud and Wunsch* [2000] estimate the strength of the North Atlantic Deep Water formation as 15 ± 2 Sv and the northward heat flux that is associated with this circulation as about 1.3 PW. This warms Europe by approximately 10 K [*Rahmstorf and Ganopolsky*, 1999], making the climate in Europe sensitive to changes in the strength of the meridional overturning circulation [*Broecker*, 1997; *Clark et al.*, 2002; *Vellinga and Wood*, 2002].

In the surface return flow of the meridional overturning circulation, Agulhas rings are the link between the Indian Ocean and the Atlantic Ocean [*Gordon*, 1986]. The warm and saline western boundary Agulhas Current flows poleward to the Cape Agulhas, where it retroflects back into the Indian Ocean. In this retroflexion area, large Agulhas rings are being shed that move into the southern Atlantic Ocean. These eddies are thought to play a crucial role in the total meridional overturning circulation [e.g. *De Ruijter et al.*, 1999, and references therein]. In their variability, they form a key link in climate change processes such as (de)glaciations as the relatively high salinity of the Indian Ocean can precondition the Atlantic Ocean waters involved in the North Atlantic Deep Water formation [*Knorr and Lohmann*, 2003; *Peeters et al.*, 2004].

It has been attempted before to quantify the influence of Agulhas rings on the meridional overturning circulation strength. *Weijer et al.* [2002] used a low-resolution (3.5° in zonal and meridional direction) and highly diffusive global ocean circulation model to study the response of the overturning strength on a heat and salt anomaly located in the southern Atlantic Ocean. The legitimacy of using such a model can be disputed, as waves and currents are not well represented, thereby strongly underestimating the radiation of energy. This energy transfer through waves can, however, be an important factor in baroclinic processes such as the meridional overturning circulation [e.g. *Saenko et al.*, 2002].

The way in which perturbations can radiate energy through a basin was investigated by *Johnson and Marshall* [2002a,b]. In a high-resolution reduced gravity model the authors show that perturbations (modeled to represent sudden changes in the overturning) can, via a consecutive chain of Kelvin and Rossby waves, transport energy over an entire basin and even between hemispheres. *Primeau* [2002] and *Cessi and Otheguy* [2003] also discuss the way in which energy input by Southern Ocean winds is redistributed in a double hemisphere ocean basin.

The questions addressed in this chapter focus first of all on the time scale on which an Agulhas ring can adiabatically (i.e. only through its dynamical structure and not its stratification) influence the wave activity and kinetic energy in the northern Atlantic Ocean. Due to the baroclinic nature of the meridional overturning circulation, the time scale of main interest will be that of the baroclinic mode. We will therefore focus on the amount of baroclinic energy available in the northernmost part of the Atlantic Ocean.

Secondly, the influence of the Mid-Atlantic Ridge on this time scale will be discussed. The influence of such ridges on both barotropic and baroclinic waves has been discussed before [e.g. *Wang and Kobalinsky*, 1994; *Barnier*, 1988; *Tailleux and McWilliams*, 2000; *Tailleux*, 2004]. Moreover, many authors [*Kamenkovitch et al.*, 1996; *Beismann et al.*, 1999; *De Steur and Van Leeuwen*, 2009] have already shown that a ridge can significantly deform an Agulhas ring. When the ring is deformed, baroclinic energy is released from the ridge, thereby increasing the amount of available baroclinic energy. The ridge can also facilitate the conversion from barotropic to baroclinic wave energy. When this happens in the northern Atlantic Ocean, it can result in a significant decrease of the travel time since it bypasses the relatively slow baroclinic waves traveling through the southern Atlantic basin.

To this end, a two-layer primitive equations model was used. By releasing a ring in the southern part of the domain, the dynamical response of the system is modeled. The time it takes for this ring energy to arrive in the northernmost part of the model Atlantic basin is used as a proxy for the response time of the meridional overturning circulation.

The meridional overturning circulation can also be implemented in the model and in this way the direct effect of the rings on the overturning strength can be studied. It is difficult to parameterize a diabatic phenomenon such as the overturning circulation in an adiabatic two-layer model and therefore two different approaches have been taken. Although they both have their imperfections, the results are to some extent similar and reinforce each other.

In section 4.2, the two-layer model and the implementation of the Agulhas ring are discussed. The time scales of the responses in the northern Atlantic Ocean are presented in section 4.3 and the role of the Mid-Atlantic Ridge in this is discussed in section 4.4. The two different parameterizations for the meridional overturning circulation are introduced in section 4.5, and these are applied in section 4.6 when the impact of the ring on the meridional overturning circulation is discussed. The conclusions and discussion are given in section 4.7.

4.2 The model

In order to facilitate both a baroclinic and a barotropic mode of the circulation, a two-layer model has been implemented. The governing equations in this model are the primitive equations for a layer $i = \{1, 2\}$:

$$\begin{aligned} \frac{\partial u_i}{\partial t} - v_i(\zeta_i + f) + \frac{1}{2} \frac{\partial(u_i^2 + v_i^2)}{\partial x} &= -P(x) + D \left(\frac{\partial^2 u_i}{\partial x^2} + \frac{\partial^2 u_i}{\partial y^2} \right) \\ \frac{\partial v_i}{\partial t} + u_i(\zeta_i + f) + \frac{1}{2} \frac{\partial(u_i^2 + v_i^2)}{\partial y} &= -P(y) + D \left(\frac{\partial^2 v_i}{\partial x^2} + \frac{\partial^2 v_i}{\partial y^2} \right) \\ \frac{\partial h_i}{\partial t} &= \frac{\partial u_i h_i}{\partial x} + \frac{\partial v_i h_i}{\partial y} \end{aligned} \quad (4.1)$$

in which $f = \cos(\phi)$, $\zeta_i = \frac{\partial v_i}{\partial x} - \frac{\partial u_i}{\partial y}$ is the relative vorticity, and D is the viscosity coefficient. The pressure term $P(k)$ is formulated as

$$P(k) = \begin{cases} g \frac{\partial \eta_1}{\partial k} & \text{for } i = 1 \\ g \frac{\partial \eta_1}{\partial k} + \Delta \rho g \frac{\partial \eta_2}{\partial k} & \text{for } i = 2 \end{cases} \quad (4.2)$$

The interface elevation η_i is related to the layer thickness h_i through

$$h_i = \eta_i - \eta_{i+1} + H_i \quad (4.3)$$

with the condition that $\eta_3 = 0$. Furthermore, H_i is the undisturbed layer thickness, $H_1 = 500$ m and $H_2 = 4000$ m. The reduced density is $\Delta \rho = \frac{\rho_2 - \rho_1}{\rho_1} = 0.002$.

The equations are integrated on a domain of 60° in zonal and 120° in meridional direction, where the equator is centered halfway up the model basin (Fig. 4.1). Some experiments require the presence of a Mid-Atlantic Ridge. This ridge is implemented as a 1000 m high obstacle meridionally oriented halfway across the model basin. The ridge height falls linearly to zero over 500 km.

The governing equations are discretized on an Arakawa C-grid [Mesinger and Arakawa, 1976; Kowalik and Murty, 1993] with 25 km spacing in both the meridional and zonal directions. This resolution is still eddy permitting at 30° S where the Rossby radius of deformation is 40 km. The time step is 40 seconds. Curvature terms have been neglected. As pointed out by Cessi and Otheguy [2003], this is allowed as long as the frequency of the Rossby waves is low. In that case, the metric terms $f = \cos(\phi)$ in the phase speed and the term that relates distance to longitude cancel each other. The time it takes a signal to zonally cross the ocean basin is therefore equal in this model to that in a full spherical model.

At the eastern and western boundary a no-slip boundary condition is prescribed ($u = v = 0$). Changing the boundary condition to free-slip (where $\frac{\partial v}{\partial y} = u = 0$) does not change the main features of the circulation. The boundary conditions on the northern and southern boundary are free-slip. Note that

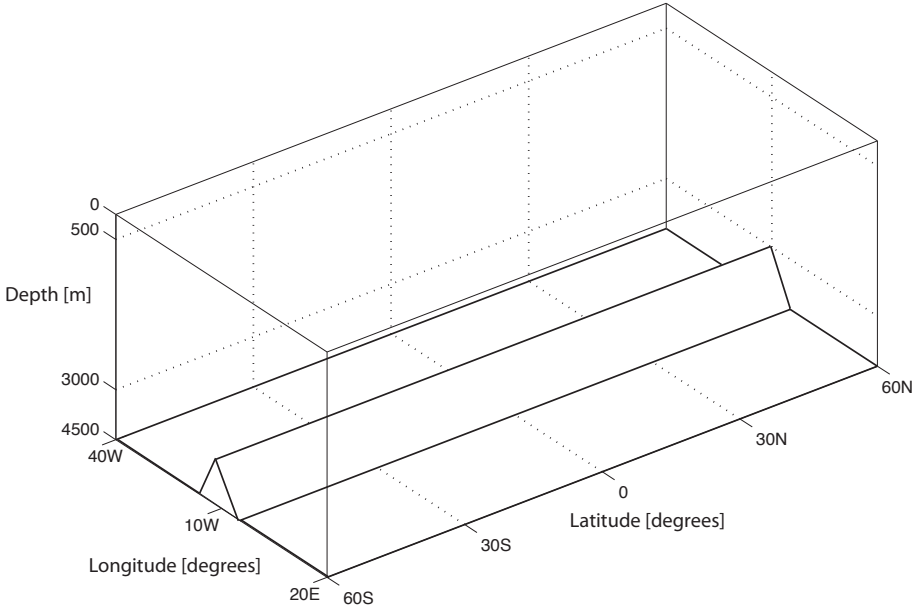


Figure 4.1: The geometry and bathymetry of the model. The northern and southern boundaries are at 60°N and 60°S and the eastern and western boundaries are at 40°W and 20°E . The meridional ridge is incorporated in only one of the two model configurations.

this implies that the southern boundary could act as a waveguide for Kelvin waves. This is unwanted, as the southern boundary represents the connection with the circumpolar Southern Ocean. Tests, however, have shown that the zonal flux of energy through the southern-most 100 km of the domain is only 3% of the total zonal flux.

The Agulhas ring is modeled as a Gaussian-shaped mass perturbation with an e -folding length scale of 112 km. The maximum sea surface height anomaly is $\eta_1^{\max} = 50$ cm and the corresponding depression of the interface between the two model layers is $\eta_2^{\max} = -200$ m. The ring has a swirl velocity (since $\eta_1^{\max} > -\Delta\rho \eta_2^{\max}$). All values are taken to represent a typical Agulhas ring [Van Aken *et al.*, 2003; Drijfhout *et al.*, 2003].

In order to minimize gravity wave noise upon initialization, the ring has a prescribed cyclogeostrophic velocity field. In such a velocity field, the Coriolis force is balanced by both the pressure gradient force and the centrifugal force [De Steur *et al.*, 2004]. At initiation, the ring is corotating with maximum velocities $V_1 = 0.6$ m s $^{-1}$ and $V_2 = 0.1$ m s $^{-1}$ in the upper and lower layer, respectively. The ring is released without any initial translational velocity at (30°S , 10°E). This is beyond the GoodHope line, so well after the ring has detached from the Agulhas Current retroflexion (see also chapter 3).

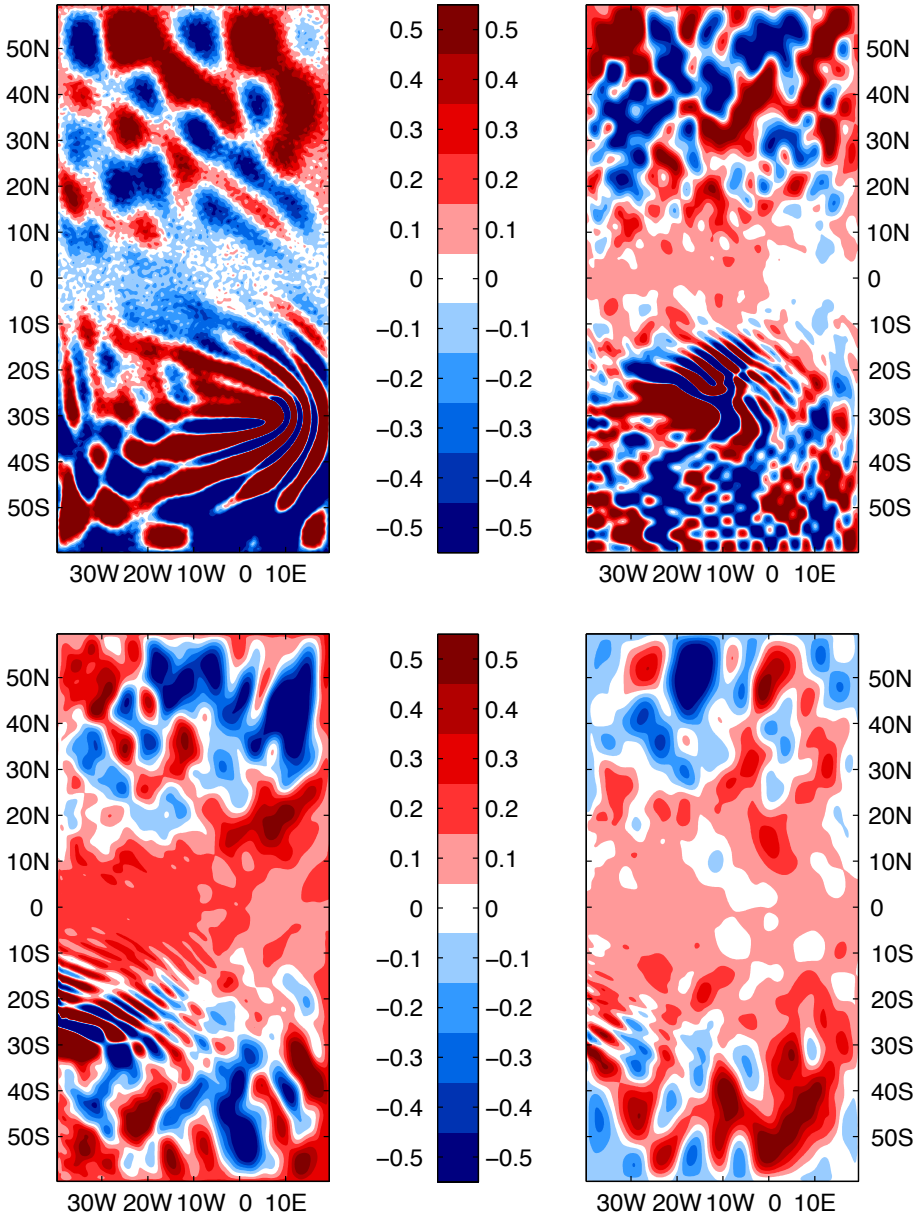


Figure 4.2: Four snapshots of the sea surface height in the model run with a flat bottom after 100 days (top left panel), 800 days (top right panel), 1500 days (bottom left panel), and 2200 days (bottom right panel). The scale runs from -0.5% to 0.5% of the initial maximum ring height (0.5 m). The ring slowly moves westward, radiating short ($\lambda \ll R_d$) Rossby waves in an envelope.

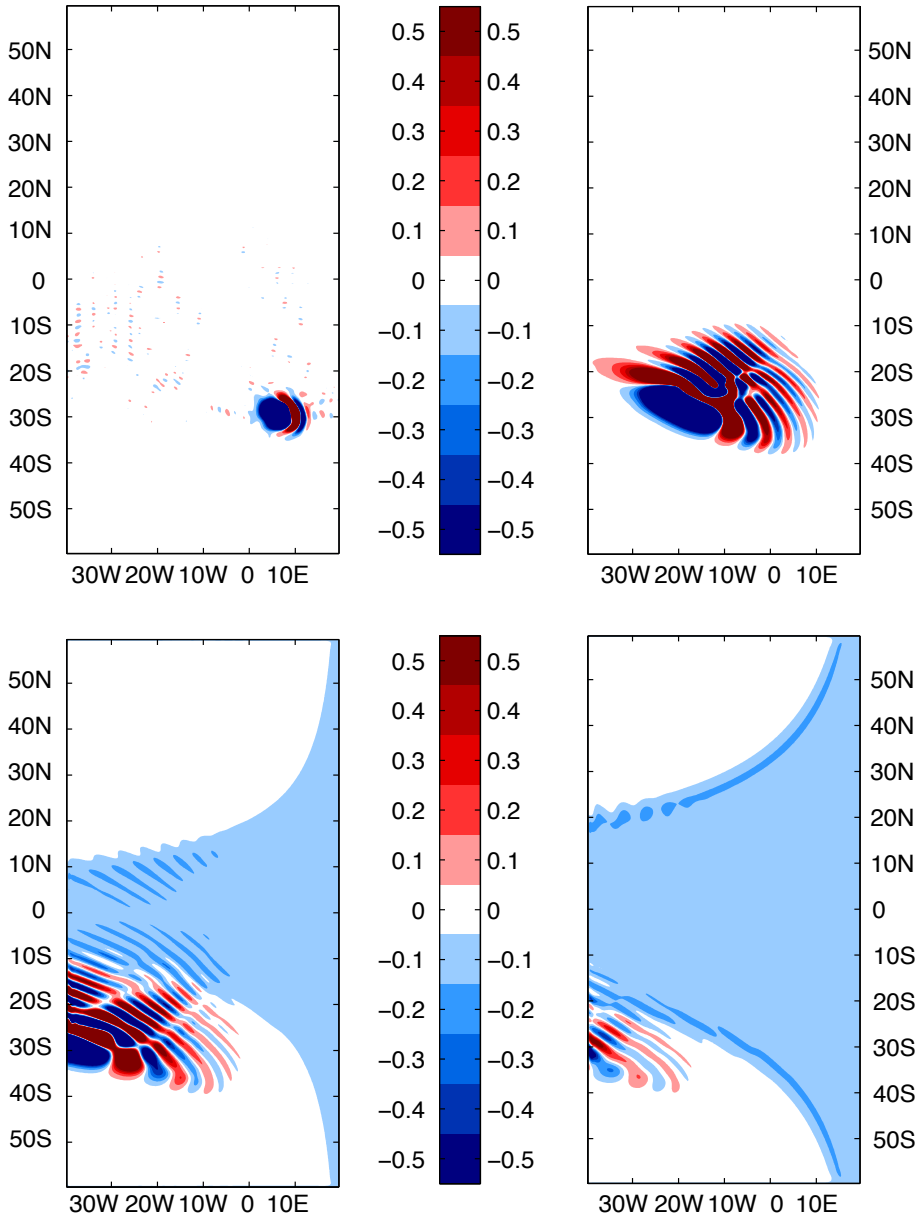


Figure 4.3: Four snapshots of the interface elevation in the model run with a flat bottom after 100 days (top left panel), 800 days (top right panel), 1500 days (bottom left panel), and 2200 days (bottom right panel). The scale runs from -0.5% to 0.5% of the initial maximum interface depression (200 m). The ring slowly moves westward and as it hits the western boundary, Kelvin waves transport mass along the equator to the eastern coast where a Rossby basin mode emerges.

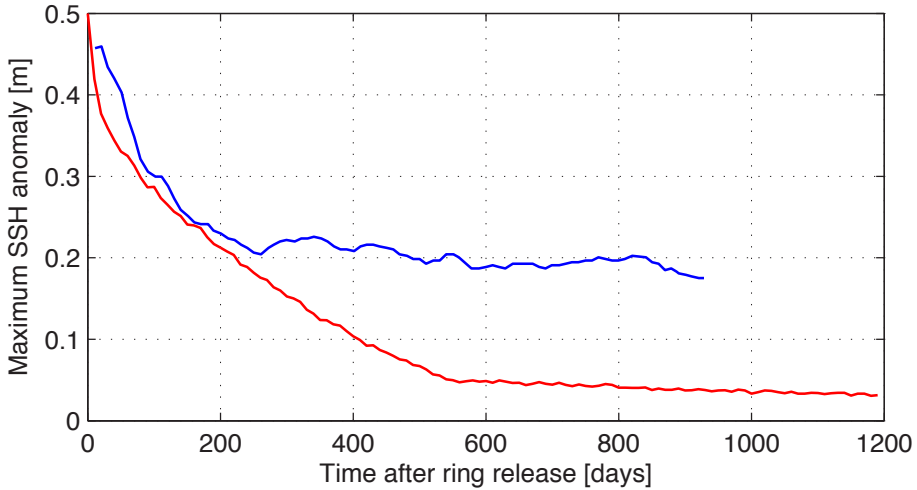


Figure 4.4: The decay of the maximum sea surface height of the ring as a function of time in this model (red line) and as found by *Schouten et al.* [2000] from satellite altimetry (blue line).

4.3 Flat bottom energy transfer time scales

The model described in the previous section has been integrated over 2500 days for the model configuration with a flat bottom, so without a meridional ridge (Fig. 4.2 and Fig. 4.3). In order to appreciate the fine structure of the deviations, the figures have been cut off to only 0.5% of the initial maximum sea surface height and interface depression (i.e. $2.5 \cdot 10^{-3}$ m and 1.0 m, respectively).

In the figures, the ring can clearly be seen moving westward, due to the β -effect [e.g. *Nof*, 1983; *Van Leeuwen*, 2007]. From consecutive snapshots, the phase velocity of the Agulhas ring can be estimated at 3.8 cm s^{-1} . This is in good agreement with the theoretical value for an anticyclone, a bit larger than the baroclinic Rossby wave speed of $c = \beta R_d^2 = 3.67 \text{ cm s}^{-1}$ at 30°S , with R_d the internal Rossby radius of deformation. The decay of the maximum sea surface height of the perturbation is shown in Fig. 4.4. In the first 300 days, the decay is similar to the decay of Agulhas rings as observed from satellite altimetry [*Schouten et al.*, 2000]. After this time, the ring in the model keeps disintegrating, to equilibrate at a lower height than the rings found by *Schouten et al.* [2000]. From these considerations, it can be concluded that the implementation and resulting behavior of the perturbation in this study is in sufficient resemblance with what is known about Agulhas ring dynamics from observations and theory.

When the ring reaches the western boundary of the model basin, the ring energy is transformed to a Kelvin adjustment wave. *Liu et al.* [1999] discuss the transformation from Rossby waves to Kelvin waves and show that the Kelvin

adjustment wave is capable of transporting mass northward to the equator. Such a redistribution of the negative mass anomaly of the Agulhas ring is also observed in this model, since the interface behind the Rossby basin mode wave is depressed (Fig. 4.3).

When the Kelvin wave on the western coast of the southern Atlantic Ocean reaches the equator, the coastal Kelvin adjustment wave will travel eastward as an equatorial Kelvin adjustment wave. After the mass anomaly has reached the eastern side of the domain, two Kelvin adjustment waves will deflect poleward. As they do this, the resulting eastern coastal Kelvin adjustment waves will radiate long Rossby waves into the basin. The sequence of an incoming equatorial Kelvin wave to poleward Kelvin waves and long westward Rossby waves has previously been described by *Anderson and Rowlands* [1976] and it has also been reported by *Johnson and Marshall* [2002b] and *Primeau* [2002] in their model studies.

The snapshots of the sea surface height (Fig. 4.2) reveal that the response time for the barotropic mode of the Agulhas ring is short, as kinetic energy (sea surface height variability) is already present in the northern Atlantic Ocean after 100 days. To better quantify the amount of energy present, a time series of the mean barotropic kinetic energy between 45°N and 55°N is computed (Fig. 4.5). Within 10 days, the amount of barotropic energy starts to rise sharply. The response of the ocean to a small perturbation ($\lambda \ll \bar{R}_d$, with \bar{R}_d the external Rossby radius of deformation) has previously been addressed by *Longuet-Higgins* [1965] and *Tang* [1979]. They showed that the energy will be radiated in an envelope to all directions with the maximal Rossby wave phase speed, $c = \beta \bar{R}_d^2$, which leads to a travel time from 30°S to 50°N of less than a day.

The amount of barotropic energy attains a maximum value after 500 days. To explain this time scale, two effects have to be taken into account. In the first 500 days, the ring height decreases drastically (Fig. 4.4). During this decay, energy is released into the basin, yielding an increase of the amount of barotropic energy away from the ring. After 500 days, the ring decay slows down, and only little extra energy is radiated. On the other hand, the continuous dissipation of energy decreases the total amount of energy in the basin. These two effects oppose each other and explain the peak in barotropic energy after 500 days.

From the snapshots of the interface elevation (Fig. 4.3) it appears that the mass anomaly associated initially with the Agulhas ring has reached the northernmost part of the model basin after 1500 days. This is confirmed in a time series of the baroclinic energy between 45°N and 55°N (Fig. 4.6). Note that the scales of Fig. 4.5 and Fig. 4.6 are a factor 10^3 different. This is due to the fact that the barotropic energy reaches the northernmost part of the basin much sooner than the baroclinic energy. When the baroclinic signal arrives, much of the energy has dissipated.

The high peak in northern baroclinic energy within the first 100 days is due to the fact that the ring is not in perfect equilibrium and radiates inertial

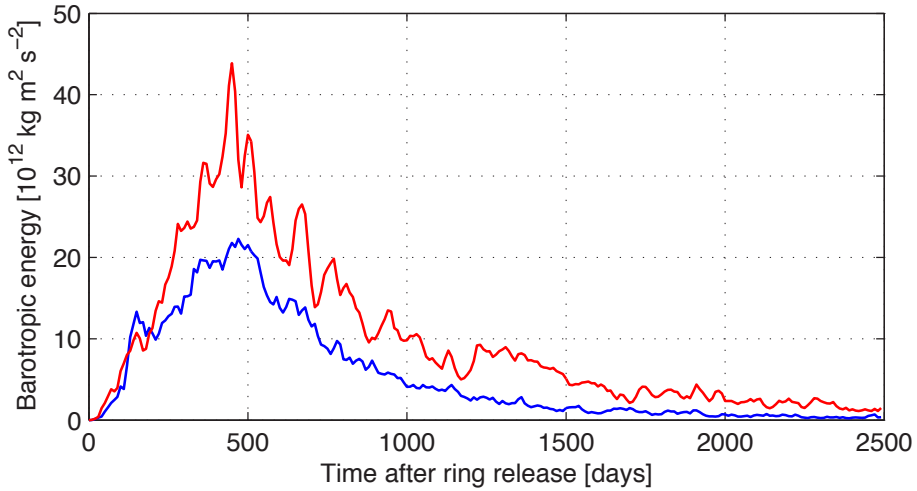


Figure 4.5: The domain averaged barotropic kinetic energy between 45°N and 55°N as a function of time for the model run with a flat bottom (red line) and with a meridional ridge (blue line).

gravity waves which quickly dissipate. These inertial gravity waves are also present in the barotropic energy, but do not stand out from the much larger energy level of the Rossby waves.

When the gravity wave noise has dissipated, the baroclinic energy level is negligible until day number 1300. From then on, the baroclinic energy rises as the eastern coastal Kelvin adjustment wave arrives at 45°N . The level of baroclinic energy remains significant until the end of the experiment. Ignoring the early-stage inertial gravity wave noise, the response time of the baroclinic mode can be estimated to 1300 days. Note that due to the high phase speed of the coastal Kelvin wave relative to that of the Rossby wave, the latter dominates this time scale. In other words, it is the time it takes the ring to zonally cross the model basin which largely determines the time scale.

4.4 Meridional ridge energy transfer time scales

The next question is how the travel times are altered by the meridional ridge. It is clearly visible that the barotropic energy is to some extent obstructed by the ridge (Fig. 4.7). After 100 days, there is a difference in sea surface height variance between the eastern and the western half of the model basin. As the ring itself crosses the ridge, after approximately 800 days, the energy can be released in the western half of the basin.

In the first snapshot of the interface elevation from the model run with a meridional ridge (Fig. 4.8), it can be seen that the ridge forces baroclinic topographic waves. There is significant energy on the ridge just west of the ring,

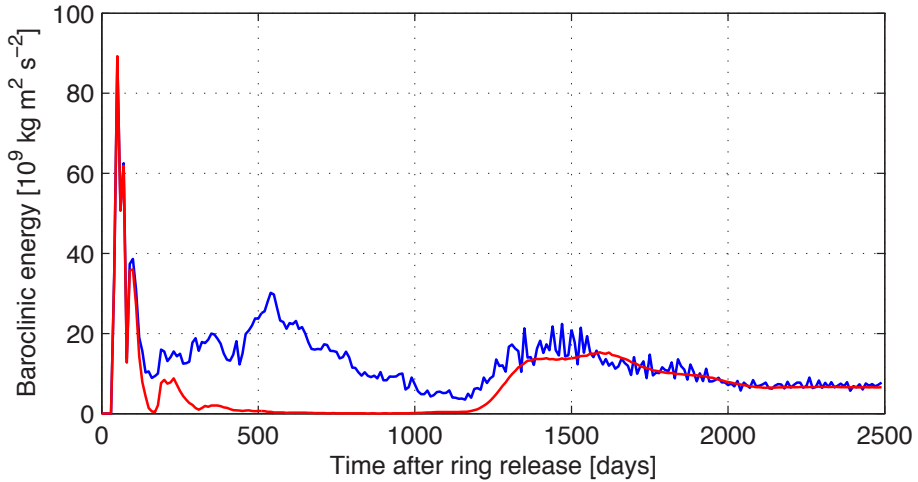


Figure 4.6: The domain averaged baroclinic kinetic energy between 45°N and 55°N as a function of time for the model run with a flat bottom (red line) and with a meridional ridge (blue line). After 1300 days, the baroclinic energy in the flat bottom case rises as the coastal Kelvin adjustment wave arrives in the northern part of the basin. The response time of the baroclinic mode in the flat bottom case is therefore 1300 days. If a ridge is included, the level of energy is high from initiation on and the response time is comparable to that of the barotropic energy. Note the difference in vertical scale with Fig. 4.5.

where the barotropic energy is also at its maximum (see Fig. 4.7). As the ring passes the ridge, it completely deforms. However, this has little consequences for the evolution of the interface basin mode Rossby wave as depicted in the last two snapshots. The snapshots are very similar to those of the flat bottom model run.

The level of barotropic energy in the northernmost part of the model basin is in the run with a ridge generally lower than in the run with a flat bottom (see Fig. 4.5). The baroclinic energy (see Fig. 4.6), on the other hand, is higher than in the flat bottom run. This supports the idea that the ridge can indeed facilitate the conversion from barotropic to baroclinic energy. After 1800 days, when the baroclinic Rossby basin mode is well established, this effect is suppressed and there is almost no difference between model runs with and without a ridge. The barotropic energy level remains lower than in the flat bottom run, indicating stronger dissipation on the ridge.

The amount of baroclinic energy does not drop to zero after the gravity wave noise has dissipated, after 400 days. Instead, it is at a level comparable to that of the response after 1300 days in the flat bottom run. One can therefore conclude that the time scale is drastically shortened by the meridional ridge. It is unfortunate that the initial noise obscures the situation for the first 100 days, but it is reasonable to estimate the response time of the baroclinic mode in this

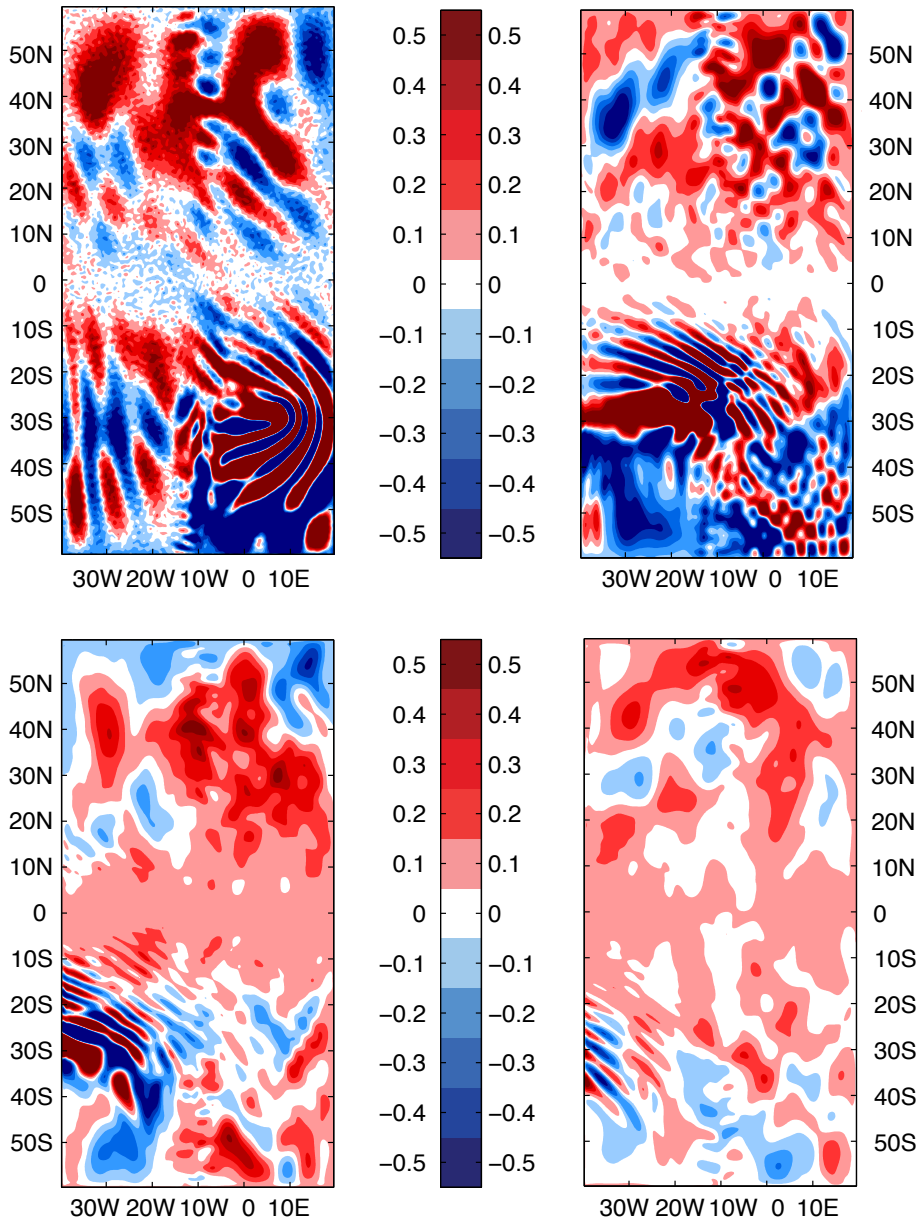


Figure 4.7: Four snapshots of the sea surface height in the model run with a meridional ridge after 100 days (top left panel), 800 days (top right panel), 1500 days (bottom left panel), and 2200 days (bottom right panel). The scale runs from -0.5% to 0.5% of the initial maximum ring height (0.5 m).

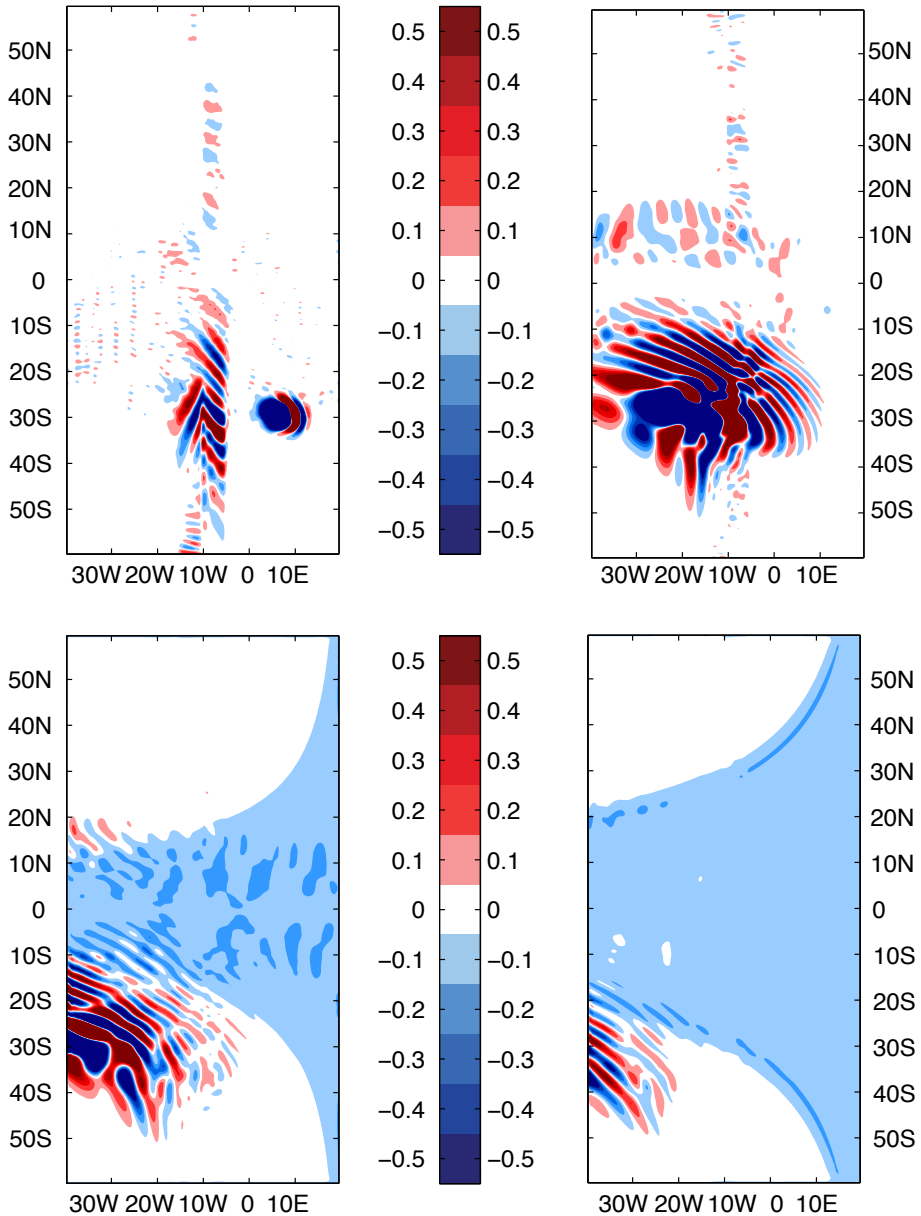


Figure 4.8: Four snapshots of the interface elevation in the model run with a meridional ridge after 100 days (top left panel), 800 days (top right panel), 1500 days (bottom left panel), and 2200 days (bottom right panel). The scale runs from -0.5% to 0.5% of the initial maximum interface depression (200 m).

case equal to that of the barotropic mode (i.e. in the order of 10 days).

Fig. 4.8 gives the impression that baroclinic topographic Rossby waves are responsible for the northward transport of baroclinic wave energy. However, the group velocity of these waves is much too small to support the fast response in the Northern Hemisphere. Instead, the baroclinic wave energy in the Northern Hemisphere is locally generated by energy conversion of barotropic to baroclinic waves at the ridge. This view is supported by the peak of the baroclinic energy around day 500 (compare Fig. 4.5 with Fig. 4.6).

4.5 Implementing a meridional overturning circulation

In the previous section the responsive time scale circulations of the transfer of energy from the southern to the northern Atlantic Ocean have been discussed. It is however still debatable whether the energy that is associated with the ring is sufficient to affect the strength of the meridional overturning circulation significantly.

In attempt to test the quantitative response of the meridional overturning circulation on an Agulhas ring, two different implementations of this circulation have been developed: a pressure-driven and a flux-driven parameterization. The first parameterization uses the zonally averaged barotropic pressure difference between the Southern and Northern Hemisphere and the second uses the baroclinic meridional mass flux at 40°N.

One of the few implementations of overturning circulations in a two-layer model in the literature is due to *Andersson and Veronis* [2004]. In their model, the mass flux is set to a prescribed value, and then used to exchange mass between layers with vertical velocity $w_0(x, y)$. With an appropriate choice of $w_0(x, y)$, this is an overturning in the sense that what is removed from the upper layer can be inserted in the lower layer in the downwelling region and vice versa in the upwelling region.

This description can not be used in our experiment because w_0 must be an observable instead of a parameter. What we need therefore is a relation between some observable in the model $f(h, u, v)$ and the overturning strength Ψ . In this case

$$f(h, u, v) \sim \Psi = \int w_0 dA \quad (4.4)$$

in which dA is the region where the overturning is applied.

The Ψ as calculated in Eq. (4.4) varies heavily on short time scales. Therefore, this relation is implemented using the average of Ψ over a 30 day period. In this way, noise due to short time scale feedback mechanisms is drastically reduced.

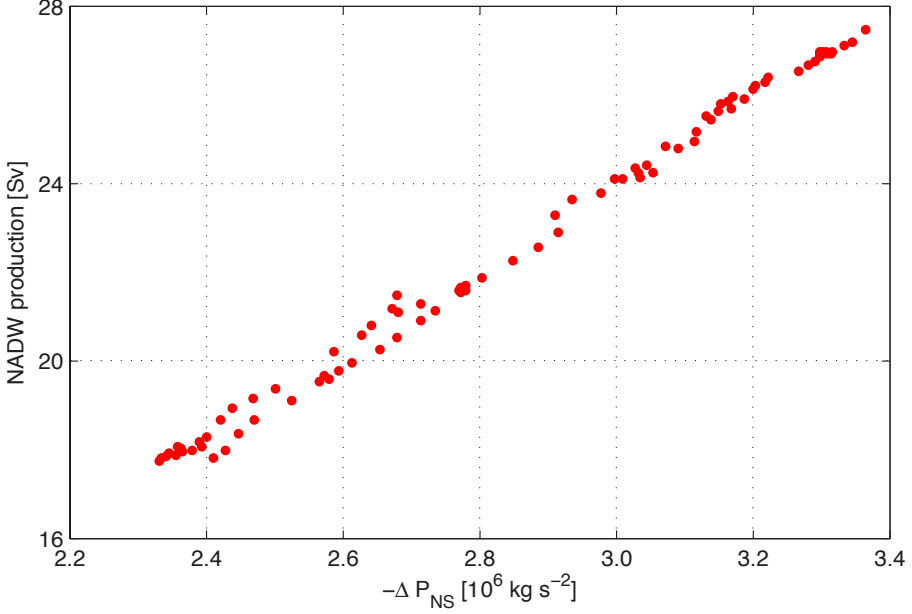


Figure 4.9: The production of North Atlantic Deep Water as a function of the total meridional pressure difference between 53°N and 30°S in the Hamburg LSG model run performed by *Weijer et al.* [2002, their Fig. 6].

4.5.1 A pressure-driven parameterization

To get an expression for Ψ in terms of h , u , and v , the linear relation found by *Weijer et al.* [2002] can be used (Fig. 4.9). It relates the zonally averaged meridional large-scale pressure gradient to the North Atlantic Deep Water formation rate. The relation can be implemented by computing the difference in zonally averaged pressure at the sea surface between two prescribed latitudes. Using hydrostatic equilibrium, this yields a relation which only involves the zonally averaged sea surface height $\tilde{\eta}$:

$$\begin{aligned} \Psi &= \Psi_0 + c \Delta P_{NS} = \Psi_0 + c \int_{-H_1}^0 \left[\int_{-H_0}^{\tilde{\eta}_N} \rho_1 g \, dz - \int_{-H_0}^{\tilde{\eta}_S} \rho_1 g \, dz \right] dz \\ &= \Psi_0 + c H_1 \rho_1 g [\tilde{\eta}(\theta_N) - \tilde{\eta}(\theta_S)] \end{aligned} \quad (4.5)$$

where $H_1 = 500$ m is the undisturbed upper layer depth and H_0 is the level of no motion. In *Weijer et al.* [1999], $H_0 = 1500$ m, but in our case it drops out and does not have to be specified. $\Psi_0 = 1.0$ Sv is a bias required to initiate the overturning circulation from an ocean at rest and $c = -7.5 \text{ m}^3 \text{ s kg}^{-1}$ is the slope which has been determined by *Weijer et al.* [1999].

The latitudes at which $\tilde{\eta}$ is calculated are still open. *Weijer et al.* [2002] used $\theta_N = 53^\circ\text{N}$ and $\theta_S = 30^\circ\text{S}$. We have used several values for latitudes θ_N

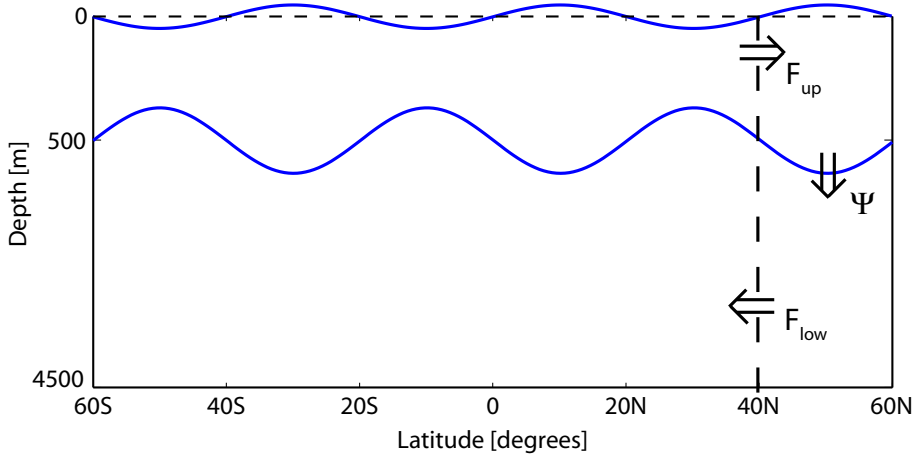


Figure 4.10: Schematic of the flux-driven parameterization for a meridional overturning in a two-layer model. The strength of the overturning circulation is the difference between the northward transport in the upper layer (F_{up}) and the southward transport in the lower layer (F_{low}), both calculated at 40°N .

and θ_S to test the sensitivity of the results. θ_N and θ_S were always on different hemispheres. The large-scale features of the responses are not very sensitive to the exact choice of latitudes.

Obviously, this implementation for the overturning strength is not optimal. First of all, there is no indication that the linear relation, which was deduced from a thermohaline multilevel model, can be used in this highly simplified adiabatic model. Secondly, the use of Eq. (4.5) effectively only takes the sea surface height into account. By doing this, the distinction between barotropic and baroclinic signals is neglected. This is an issue, as it was argued before that only the baroclinic signals can directly influence the meridional overturning circulation.

4.5.2 A flux-driven parameterization

A different approach to designing a parameterization is to return to the conceptual idea of the overturning circulation (Fig. 4.10). When the upper layer of the model represents the northward flowing limb of the circulation and the lower layer represents the return flow, mass conservation can be used to formulate the overturning circulation: At some latitude, half of the difference between the northward transport through the upper layer and the southward transport through the lower layer must be transported from the upper to the lower layer. This transport then is the North Atlantic Deep Water formation and its magnitude is Ψ .

The formulation of this flux-driven overturning circulation can be written

as

$$\Psi = \Psi_0 + \frac{1}{2} \left[\int_{\theta_N} v_1 h_1 dx - \int_{\theta_N} v_2 h_2 dx \right] \quad (4.6)$$

where $\theta_N = 40^\circ\text{N}$ is the latitude at which the fluxes are calculated. Note that Eq. (4.6) uses the volumetric fluxes, instead of the mass fluxes. Using the Boussinesq approximation, however, these are equal. Further note that only baroclinic signals have an effect on Ψ in this parameterization.

This implementation has its drawbacks too, just like the pressure-driven parameterization. In this formulation, it is assumed that all excess water north of a certain latitude will participate in the North Atlantic Deep Water formation. In the real ocean, however, water in the upper layer could be stored north of 40°N for some time to be released later as a southward flux. However, indirect support for this parameterization comes from sea-going studies, since this is the way in which the strength of the meridional overturning circulation is measured [e.g. Bryden *et al.*, 2005b].

4.6 Response of the meridional overturning circulation

In both parameterizations, the model is initiated without any Agulhas ring in order to facilitate the spin-up of the meridional overturning circulation. After 2500 and 4000 days in the flux-driven and pressure-driven implementation respectively, the overturning strength Ψ is in a statistical steady state.

When the runs with the two parameterizations have fully spun up, an Agulhas ring is released after which the overturning circulation responds (Fig. 4.11). In the figure, the response of the overturning on a ring has been compared to the response without a ring, yielding the quantity

$$\langle \Psi_{\text{diff}} \rangle = \langle \Psi_{\text{Ring}} \rangle - \langle \Psi_{\text{NoRing}} \rangle \quad (4.7)$$

where $\langle \dots \rangle$ is the 50 days moving average operator used in order to eliminate small-scale fluctuations. The magnitude of the response is different in the two parameterizations, where the flux-driven one yields ten times higher overturning strength fluctuations. This is partly due to the choice of tuning parameters, which gives the flux-driven parameterization a much higher sensitivity than the pressure-driven parameterization.

Both parameterizations agree that a ring enhances the overturning strength between 1300 and 1500 days after release. The first instance at which the overturning difference is significantly nonzero for an extended time is after 1300 days. Before this, essentially nothing happens to the overturning parameterizations. Beyond 1500 days, the flux-driven parameterization gets

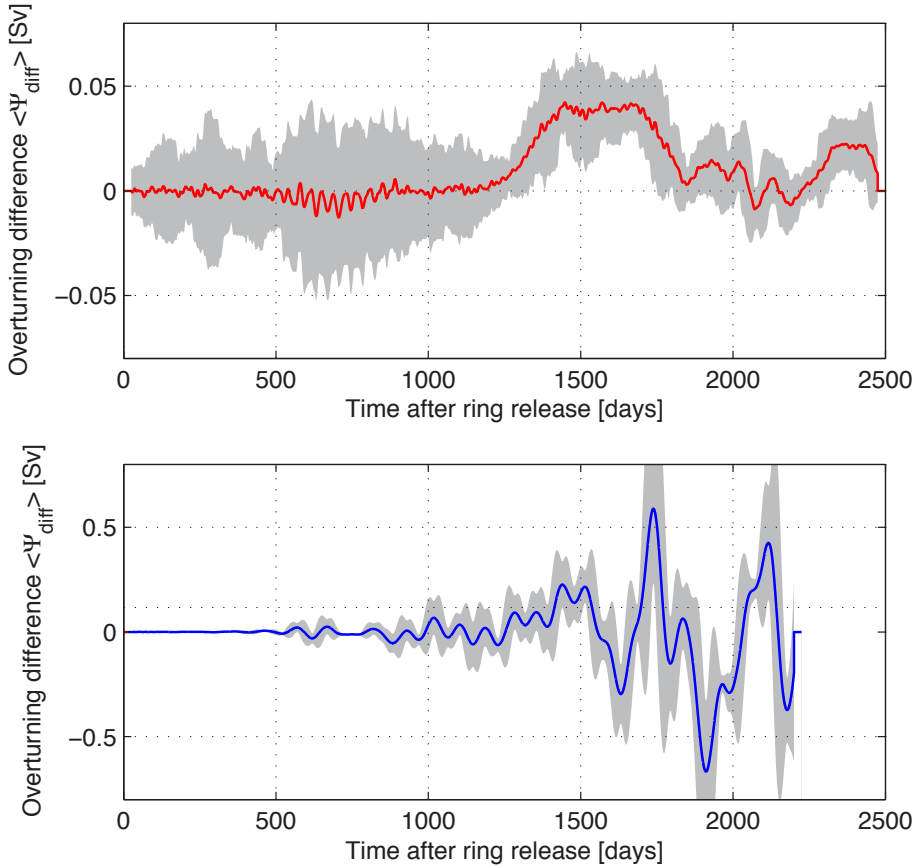


Figure 4.11: The overturning strength difference $\langle \Psi_{\text{diff}} \rangle$ for the pressure-driven parameterization (upper panel) and the flux-driven parameterization (lower panel), both in the model configuration with a flat bottom. The gray area denotes the 95% confidence band. Note the difference in vertical scales.

unstable which results in large fluctuations in overturning strength. Apparently, the feedbacks are much stronger than in the pressure-driven parameterization. In this last implementation, the overturning strength difference returns to zero after 1800 days.

The presence of a meridional ridge in the basin does not drastically change the overturning difference (Fig. 4.12). The first significant nonzero difference occurs after 1300 days in both parameterizations. After that, the overturning difference stays positive until day 2000 in the pressure-driven parameterization, somewhat longer than in the setup without a meridional ridge.

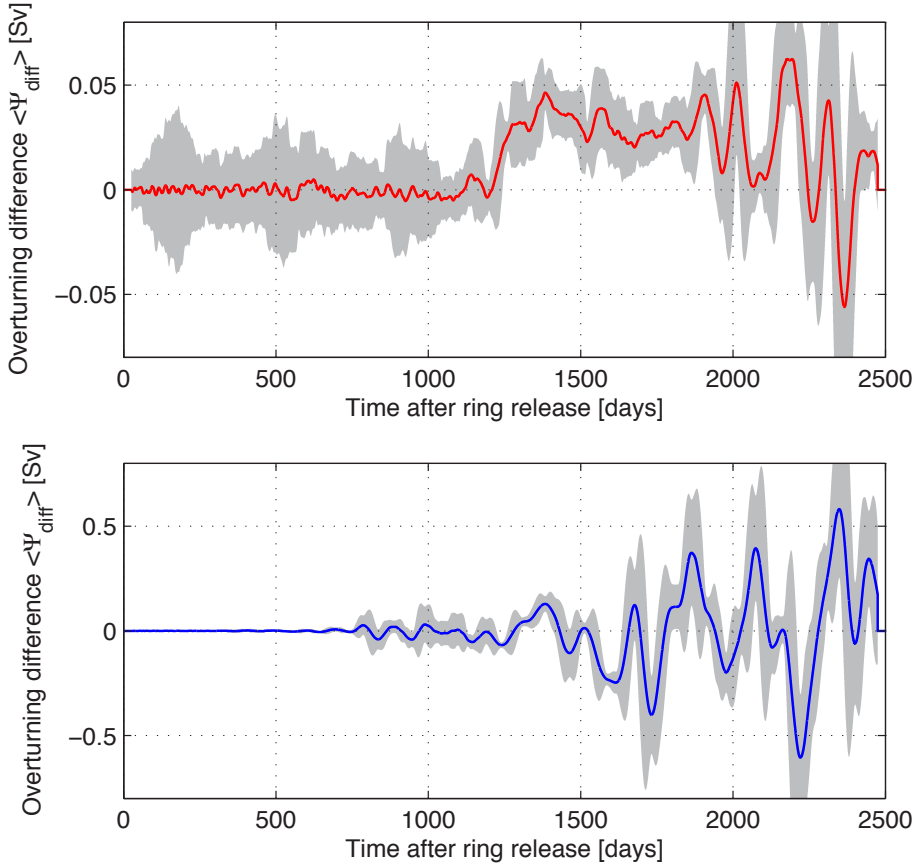


Figure 4.12: The overturning strength difference $\langle \Psi_{\text{diff}} \rangle$ for the pressure-driven parameterization (upper panel) and the flux-driven parameterization (lower panel), both in the model configuration with a meridional ridge. The gray area denotes the 95% confidence band. Note the difference in vertical scales.

4.7 Conclusions and discussion

A set of numerical experiments has been conducted to investigate the kinetic energy transit time and route of Agulhas ring-like perturbations traveling to the northern Atlantic Ocean. Particular attention has been given to the role of the Mid-Atlantic Ridge on the shortcutting of the route and time scale on which baroclinic energy is transported northward.

The model runs show that the time it takes for barotropic kinetic energy to be radiated to the northernmost part of the model basin is in the order of 10 days, although the bulk arrives after 500 days. In a basin with a flat bottom, the amount of baroclinic kinetic energy increases after 1300 days, yielding the baroclinic time scale. Due to the large difference in Kelvin and

Rossby wave phase speeds, this scale is largely determined by the transit time of the ring traveling from its initial position to the western boundary of the basin. It will therefore be sensitive to the latitude at which the ring travels (through the Rossby wave phase speed) and the zonal distance between the coasts.

When a 1000 m high meridional ridge is placed on the ocean floor, the level of baroclinic energy between 45°N and 55°N is high from initiation on. The ridge can facilitate the conversion of barotropic kinetic energy to baroclinic kinetic energy and this mechanism shortcuts the slow westward path of the ring.

One can debate this conclusion by remarking that the longitude at which the baroclinic energy enters the northernmost part of the model basin is different in the two model configurations. In the flat bottom run, the energy enters near the eastern coast. In the configuration with a meridional ridge, on the other hand, it is released on the ridge. The exact location of North Atlantic Deep Water formation seems to be more in the Nordic Seas and the Labrador Sea. The time it takes for the baroclinic energy to zonally cross half the basin at high latitudes is even larger than the 1300 days presented here. The conclusion that the ridge significantly reduces the response time scale is therefore still valid.

The meridional overturning circulation, implemented with two different parameterizations, responds with a significant increase in strength 1300 days after the ring has been released. In the flux-driven parameterization, the overturning gets unstable after that but in the pressure-driven parameterization the overturning returns to normal strength 1800 days after the ring has been released. This means that the overturning strength is affected for almost 1.5 years on this Agulhas ring. As rings shed every two to three months, one might expect (non-linear) interactions between multiple rings further enhancing the overturning response.

The presence of a meridional ridge does not reduce the time it takes for the overturning to respond. This is in contrast to the baroclinic energy level, which clearly shows a reduction in transfer time. Apparently, the amount of energy transferred to the northern part of the basin by the meridional ridge is insufficient to alter the overturning strength in this last parameterization. The typical time scale encountered in this study (in the order of three years) is similar to that found by *Johnson and Marshall* [2002b], but shorter than the time scales found by *Primeau* [2002] and *Cessi and Otheguy* [2003]. In both latter cases, however, this is due to the smaller zonal extent of the basin, and in *Primeau* [2002] the somewhat smaller baroclinic Rossby deformation radius also increases the zonal transit time. In all experiments, this zonal transit time sets the time scale and the physical mechanisms are therefore not different.

This study is idealized in many ways. For one, the wind-driven gyres have not been implemented. It is expected that this omission will have little effect on the transit time in the southern Atlantic Ocean, since the Agulhas rings soon enter the central latitude of the subtropical gyre and indeed take about three

years to cross the Atlantic basin in reality. Part of the ring water enters the Benguela Current, but the mean flow velocities of the current and its westward extension are similar to that of the ring velocity.

How significant is a $2.5 \cdot 10^{-3}$ m sea surface height anomaly? This is the scale that is used in Fig. 4.2 and Fig. 4.7. One can only say that the time scales presented in this chapter are significant in the sense that they emerge from both the energy level analysis and the overturning parameterization. A 0.05 Sv change in overturning strength per ring is not very large, but as said before some eight rings may shed in the 1.5 years that the overturning is affected. Given that the overturning is solely increased by a ring, multiple rings may reinforce each other to a more significant overturning enhancement.

In the turbulent real ocean, the ring signal will be diluted. In the northern Atlantic Ocean, part of the ring energy will end up in the Gulf Stream and carried farther northward. However, the advective time scales will be larger than the propagation speed of the adjustment Kelvin waves [e.g. *Weijer et al.*, 2002]. It is again the dilution of the signal that will reduce its significance. On the other hand, as shown by *Weijer et al.* [2002], the salt anomaly related to the Agulhas ring tends to strengthen on its northward journey due to excess evaporation. This increases the influence of the rings. Since our model is adiabatic these phenomena could not be studied and we concentrate on the baroclinic wave energy.

Chapter 5

Relating Agulhas leakage to the retroreflection location

This chapter is based on the work:

Van Sebille, E., C. N. Barron, A. Biastoch, F. C. Vossepoel, P. J. van Leeuwen, and W. P. M. de Ruijter (2009), Relating Agulhas leakage to the Agulhas Current retroreflection location, *submitted*.

Abstract

The relation between the Agulhas Current retroreflection location and the magnitude of Agulhas leakage, the transport of water from the Indian to the Atlantic Ocean, is investigated in a high-resolution numerical ocean model. First of all, it is found that sudden eastward retreats of the Agulhas Current retroreflection loop are linearly related to the shedding of Agulhas rings, where larger retreats generate larger rings. Furthermore, a method is developed to estimate the amount of leakage from sea surface height information. Using numerical Lagrangian floats, a linear relation is found between the magnitude of Agulhas leakage and the location of the Agulhas Current retroreflection three months earlier, both binned to three month averages. In the relation, a more westward location of the Agulhas Current retroreflection corresponds to an increased transport from the Indian Ocean to the Atlantic Ocean. Using a linear regression, the magnitude of Agulhas leakage can be estimated within a confidence band of 15 Sv when the westward extent of the Agulhas Current retroreflection is known.

5.1 Introduction

The Agulhas region, the region southeast and south of Africa where the Indian Ocean and Atlantic Ocean meet, plays a key role in the warm upper-branch return flow of the Atlantic meridional overturning circulation [Gordon, 1986; Weijer *et al.*, 1999; Peeters *et al.*, 2004; Biastoch *et al.*, 2008b, and chapter 4]. The southward flowing Agulhas Current is the western boundary current of the Indian Ocean subtropical gyre. After separating from the continental slope near the southern tip of Africa, it flows southwestward until approximately 19°E, at which point it turns back into the Indian Ocean as the Agulhas Return Current [Lutjeharms and Van Ballegooyen, 1988]. In this so-called retroflexion loop, 4 – 6 Agulhas rings are shed per year. These anticyclones have diameters up to 300 km and transport thermocline water from the Indian Ocean to the Atlantic Ocean [e.g. De Ruijter *et al.*, 1999; Lutjeharms, 2006].

The total volume flux of the Agulhas Current at 32°S is on the order of 70 Sv [Bryden *et al.*, 2005a]. The bulk of this flux is recirculated in the subtropical gyre of the Indian Ocean, and only an estimated 5 – 15 Sv gets into the Atlantic Ocean as Agulhas leakage [Gordon *et al.*, 1992; De Ruijter *et al.*, 1999; Reason *et al.*, 2003]. Agulhas leakage is defined here as the water that is transported in the Agulhas Current and flows from the Indian Ocean into the Atlantic Ocean.

Estimating the magnitude of Agulhas leakage has proven to be difficult both in models and reality. This is in part because of the vigorous mixing in the Cape Basin, the area southwest of the African continent. Because coherent structures entering this basin are often quickly destructed, Boebel *et al.* [2003a] dubbed the region the ‘Cape Cauldron’. One way to estimate the magnitude of Agulhas leakage is to integrate the velocity as a function of depth and distance from the African coast. The problem with this Eulerian method, however, is that the Cape Basin is not only drained from the Indian Ocean, but also from the Atlantic Ocean and the Southern Ocean. When estimating the magnitude of Agulhas leakage, these three sources of Cape Basin water have to be disentangled. Due to the turbulent nature of the flow in the Cape Basin and the resulting mixing, identifying separate water masses might be complicated, which is a main drawback of Eulerian velocity-based transport estimates.

An example of an Eulerian approach to estimating of the magnitude of Agulhas leakage is the Benguela Sources and Transports (BEST) experiment [e.g. Garzoli and Gordon, 1996], where Inverted Echo Sounder data is assimilated in a two-layer geostrophic model. The resulting transport time series has been combined with altimetry data by Goni *et al.* [1997] and Garzoli and Goni [2000] to yield a method to derive geostrophic baroclinic transports from altimetry data alone. The mean transport of 4 Sv obtained in this way is low compared to other estimates. Moreover, the authors admit that they have problems distinguishing Agulhas leakage from other sources of transport.

Dijkstra and De Ruijter [2001b] have proposed an Eulerian retroflexion index for the magnitude of Agulhas leakage, applied also by Hermes *et al.* [2007]. Their index is based on the ratio between Agulhas Current inflow and

Agulhas Return Current outflow as determined by volumetric fluxes of three-dimensional velocity fields from a numerical ocean model. Although powerful in models, this index can not be used in the real ocean where three-dimensional velocity field data sets are not available. Moreover, it is generally not easy to separate the Agulhas Return Current flow, which had its origin in the Agulhas Current, from other eastward flowing water masses such as the Antarctic Circumpolar Current. This makes the retroreflection index sensitive to latitudinal shifts in the Southern Ocean frontal system near the Agulhas Return Current.

Because of the problems of mixed water masses, the Lagrangian volume transport might be a more appropriate measure of the magnitude of Agulhas leakage in a numerical model. Employing the trajectories of Lagrangian floats is an unambiguous and exact way to assess how much of the interocean flux originated in the Indian Ocean [Speich *et al.*, 2006; Biastoch *et al.*, 2008c]. The drawback of using Lagrangian fluxes, however, is that these too are unavailable in the real ocean.

Currently, only altimeter products provide sustained observations of the ocean state in the Agulhas region. Sea surface height time series are available on high-resolution time scales and for almost 20 years. In this study, therefore, we relate the float-determined Agulhas leakage transport to information from modeled sea surface height, with the purpose to find the sea surface signature of Agulhas leakage. The location of the Agulhas Current western front is used as a proxy for ring shedding events and the amount of Agulhas leakage [Ou and De Ruijter, 1986; Lutjeharms and Van Ballegooyen, 1988; Feron *et al.*, 1992].

In this study, results from a $1/10^\circ$ numerical ocean model [Biastoch *et al.*, 2008b,c] are used to retrieve a linear relation between the magnitude of Agulhas leakage and the most western longitude of the Agulhas Current retroreflection loop. The method of finding the westward extent of the Agulhas Current retroreflection and the numerical ocean model are introduced in section 5.2. In section 5.3, we find (as a side-step) a relation between the speed of the eastward retreat in the Agulhas Current retroreflection and the surface area of shedded Agulhas rings. The procedure for determining the magnitude of Agulhas leakage, using numerical Lagrangian floats, is described in section 5.4. In section 5.5, the westward extent of the Agulhas Current retroreflection is related to the magnitude of float-determined Agulhas leakage to yield an estimate of leakage from sea surface height data only. In section 5.6, then, the linear estimate is applied to altimetry data. This yields a first order estimate of the magnitude of Agulhas leakage and can be used to quantify early retroreflections from altimetry. This chapter ends with conclusions and discussion in section 5.7.

5.2 Tracking the Agulhas Current

Isolines of (model) sea surface height have been used before to track the location of the Agulhas Current [e.g. Lutjeharms and Van Ballegooyen, 1988; Boebel *et al.*, 2003b]. In this study, the position of the Agulhas Current path is tracked

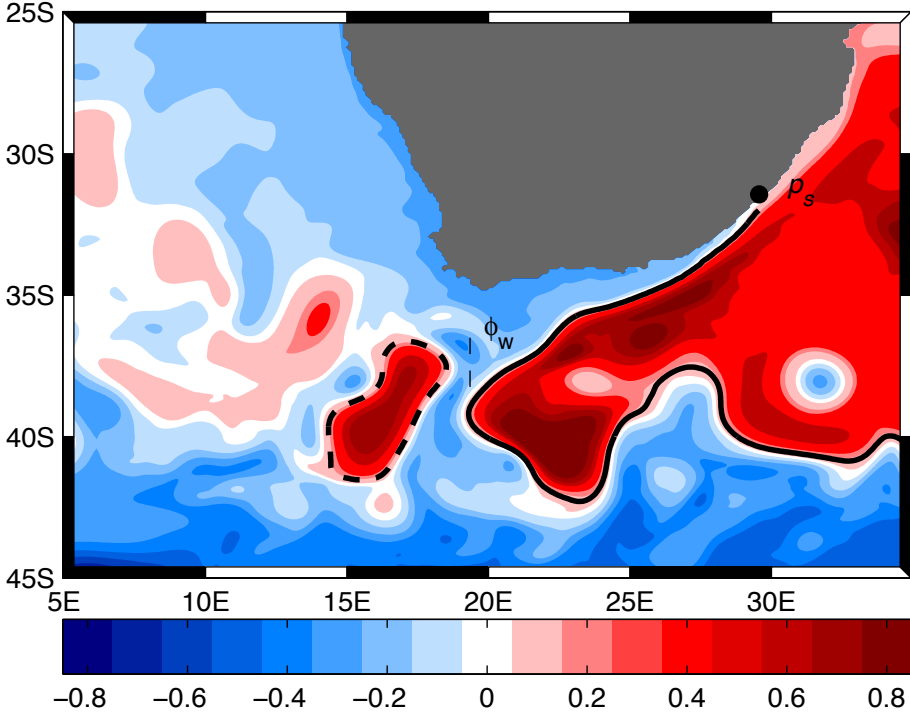


Figure 5.1: A snapshot of dynamic topography (in meter) on 20 November 2002 from the AG01 model. The thick black line is the Agulhas Current path C_A , starting at point p_s , as detected by the algorithm. The dashed closed contour is the associated ring found by the ring detection algorithm. The westward extent of the current is indicated by ϕ_w .

by the following algorithm. From the sea surface height $h(\phi, \theta)$, geostrophic velocities $v_g(\phi, \theta)$ are calculated. Using geostrophic velocity from sea surface height instead of model velocity fields has the advantage that the algorithm can also be applied to data sets where absolute velocity is unavailable, such as altimetry.

At 32°E , the grid cell p_s with highest southwestward geostrophic velocity is selected (Fig. 5.1). A counter-clockwise contour $C_A(\phi, \theta)$ is drawn along all grid cells with height equal to $h(p_s)$. C_A extends to p_e , the grid cell where the geostrophic velocity falls below a threshold value of $0.4|v_g(p_s)|$. This value is chosen so that p_e is typically located east of 50°E . C_A resembles a proper retroflection when three additional conditions are satisfied: p_e should be east of p_s , C_A should extend south of 37°S , and C_A should not close onto itself.

From the Agulhas Current contour $C_A(\phi, \theta)$ a proxy is formed. The variability of the Agulhas Current retroflection is best observed in its longitudinal location [Lutjeharms and Van Ballegooyen, 1988], so the westward extent of the Agulhas Current might serve as an appropriate proxy. In Fig. 5.1 this

longitude is denoted as ϕ_w , which is defined as

$$\phi_w = \min_{\phi} (C_A(\phi, \theta)) \quad (5.1)$$

The algorithm is applied to the $1/10^\circ$ AG01 model [Bjastoch *et al.*, 2008b,c], the same model as used in chapter 3. The model grid covers the greater Agulhas region ($20^\circ\text{W} - 70^\circ\text{E}$; $47^\circ\text{S} - 7^\circ\text{S}$), nested into the ORCA model. The latter is a global ocean–sea-ice model on $1/2^\circ$ grid. Both models are based on the NEMO code [Madec, 2006, version 2.3]. The nesting approach is two-way [Debreu *et al.*, 2008], allowing the high-resolution AG01 nest to receive its open boundary values from the ORCA base model and to update the base model with data from the nest, thereby embedding the Agulhas system into the large-scale circulation. Both models have 46 vertical layers, with layer thicknesses ranging from 6 m at the surface to 250 m at depth, and employ partial cells at the ocean floor for a better representation of bathymetry. The two models are forced with the CORE data set of daily wind and surface forcing fields [Large and Yeager, 2004] for the period 1958 – 2004. The model output is available as the average of five day intervals. It was demonstrated that the mesoscale dynamics reflected in the decadal variability of the Atlantic meridional overturning circulation [Bjastoch *et al.*, 2008b].

Bjastoch *et al.* [2008c] have demonstrated that the high-resolution nest captures the transport and currents of all components of the greater Agulhas system with substantial success, including perturbations in the Mozambique Channel and east of Madagascar. The data set comprises model output over the period 1968 – 2004 and the algorithm for tracking C_A succeeds in 99% of the snapshots.

The 1% of the snapshots where no proper contour can be detected seem to be related to events when extremely intense Natal pulses [Lutjeharms and Roberts, 1988] pass at 32°S . At some of these occasions the Agulhas Current temporarily meanders offshore so much that it can not be tracked anymore (although when a Natal pulse is present at 32°S the algorithm in most occasions does not fail in finding a proper contour). Note that this does not necessarily mean that there is a bias in the ϕ_w data set, as it takes the Natal pulses a few months to reach the Agulhas Current retroreflection and possibly affect the westward extent [Van Leeuwen *et al.*, 2000]. This lag will assure that the moment of Natal pulse crossing at 32°S is uncorrelated to ϕ_w .

5.3 Relating the retroreflection front retreat to ring size

In the sea surface height field, Agulhas rings are the most notable transport agent of Agulhas leakage. Although it is difficult to track the paths of these rings in noisy sea surface height data, ring shedding events themselves can more easily be detected. Several descriptions of the ring shedding mechanism

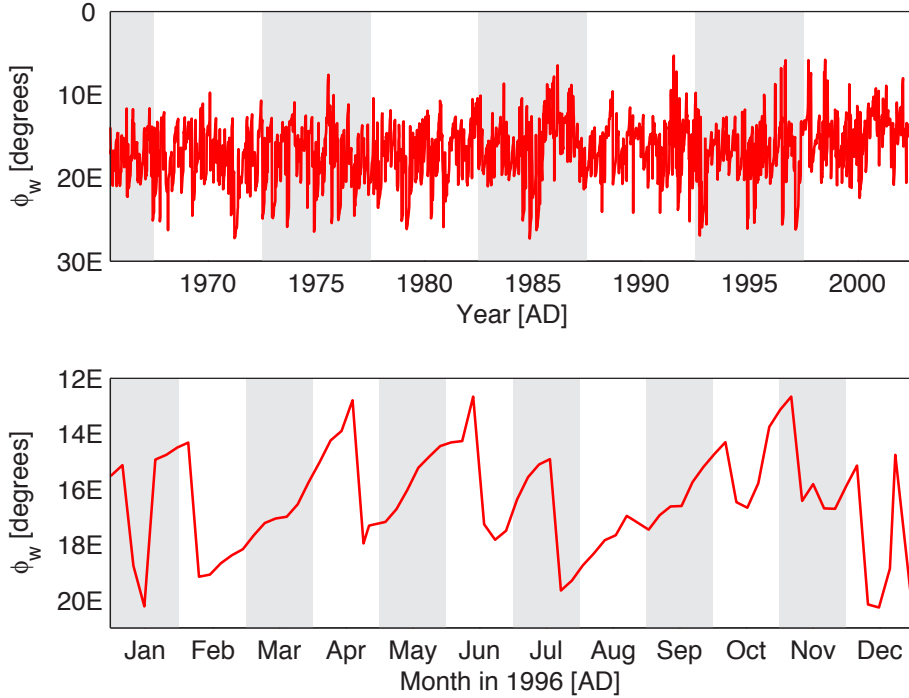


Figure 5.2: Time series of the westward extent ϕ_w of the Agulhas Current for the AG01 model (upper panel) and a zoom of the westward extent ϕ_w for the year 1996 only (lower panel). The sawtooth behavior in the lower panel is an indication for the loop occlusion mechanism described by *Lutjeharms and Van Ballegooyen* [1988] and *Feron et al.* [1992]. In this mechanism, a slow westward movement of the Agulhas Current front is followed by a fast eastward retreat as an Agulhas ring is pinched off.

have been proposed. In one of these [*Ou and De Ruijter*, 1986; *Lutjeharms and Van Ballegooyen*, 1988; *Feron et al.*, 1992], the essential component is that the western front of the Agulhas Current slowly moves westward most of the time. At some moment, the loop formed by the Agulhas Current and Return Current occludes, an Agulhas ring pinches off, and the western front experiences an instantaneous eastward retreat.

The model time series shows evidence for the retroflection loop occlusion (Fig. 5.2). The histogram of the change in westward extent, $\Delta\phi_w/\Delta t$ is skewed, with a large peak at slower westward speeds and a smaller peak at higher eastward speeds (not shown). This is an indication for saw-tooth behavior, where the current retreat is quick as a ring sheds off, and the current progradation is slow as the Agulhas Current retroflection moves west.

Using $\Delta\phi_w/\Delta t$, ring shedding events can be detected. Whenever the Agulhas Current experiences a large retreat on the five day interval ($\Delta\phi_w/\Delta t > 0.4$ degree day $^{-1}$) this is considered a loop occlusion event and an associated

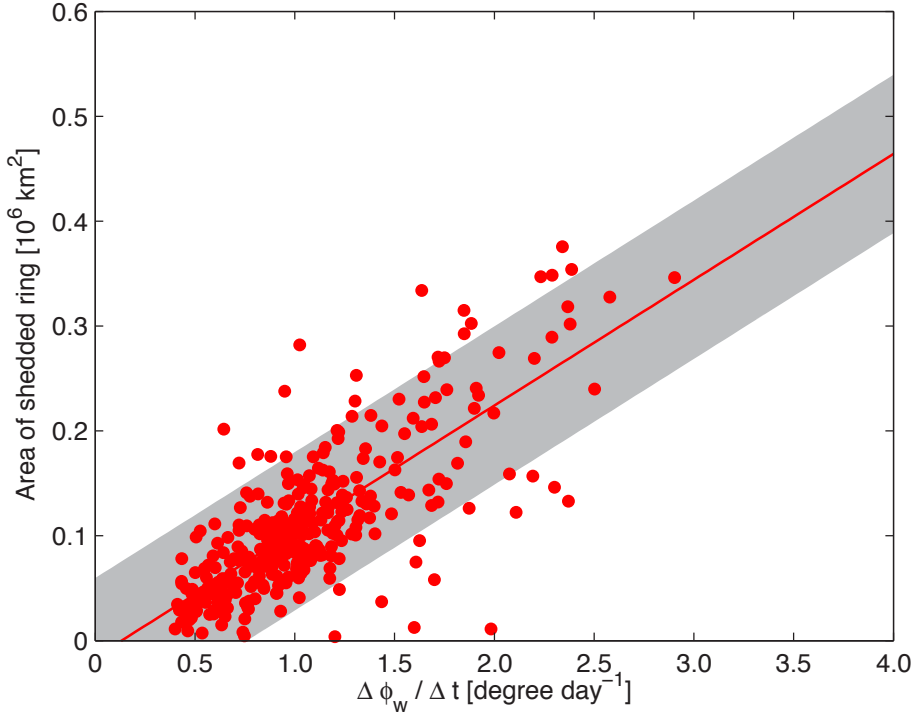


Figure 5.3: The change in front location for loop occlusion events for the AG01 model (when $\Delta \phi_w / \Delta t > 0.4$ degree day⁻¹) versus the area of the associated ring being shed. The red line is the best linear fit, with the gray area denoting the 90% confidence band. The correlation coefficient of the data set is 0.77.

ring is sought in the dynamic height $h(\phi, \theta)$. An associated ring is defined as a closed contour of height equal to that of $C_A(\phi, \theta)$, located in a $1^\circ \times 5^\circ$ area west of ϕ_w (Fig. 5.1). Since it is close to ϕ_w , which has just experienced a sudden retreat, and has the same height as $C_A(\phi, \theta)$, we assume that the ring has just shed from the Agulhas Current. If a ring is found, the area inside the contour is taken as a measure of the ring size. If multiple closed contours are found, the one closest to ϕ_w is taken to be the associated ring.

There appears to be a relation in the model data between the magnitude of front retreat and ring size (Fig. 5.3). A larger retreat of the Agulhas Current retroflexion results in a larger ring being shed. Note however, that this does not have to mean that the amount of Agulhas leakage is larger. Rings which have been shed are sometimes recaptured by the slowly westward protruding Agulhas Current. Therefore, the magnitude of Agulhas leakage can better be derived somewhat farther away from the retroflexion, in the Cape Basin.

5.4 Measuring the Lagrangian Agulhas leakage transport

To quantify the possible relation between ϕ_w and the magnitude of Agulhas leakage, an assessment of the Agulhas leakage transport is made by tracking numerical floats. This is the same data set as used in chapter 3. The float trajectories in the AG01 model are computed using the ARIANE package [Blanke and Raynaud, 1997], similar to the attempt by Biastoch *et al.* [2008c] to estimate the long-term statistics of the modeled interocean exchange. The isopycnal floats are released at 32°S. The initial transport per float is capped at 0.1 Sv, but a large portion of the floats represent a lower transport to allow for sampling in grid cells where transport is lower than 0.1 Sv. The floats are integrated for five years, so that most floats reach the domain boundaries. The total number of floats released in the model is $5.6 \cdot 10^6$, launched over a period of 37 years (1968 – 2004). After the five year integration period, only 3% of the numerical floats have not exited the domain. The mean model Agulhas Current transport at 32°S is 64 Sv.

Using the float data, a time series of the Agulhas leakage transport is constructed for the model. Only floats of which the final position is west of the GoodHope line (see Fig. 1.6 or Fig. 3.2) are taken into account. The GoodHope line [Swart *et al.*, 2008] is a combined XBT and PIES line currently used to estimate Eulerian fluxes. Choosing this line facilitates future comparison between the Lagrangian fluxes presented here and in situ Eulerian estimations.

The transport of each float crossing the GoodHope line is added to the Agulhas leakage flux $F_{AL}(t)$, where t is the last time the float crosses the line. In this way, floats that cross the line several times are only added to the Agulhas leakage flux time series once, at the moment of their last crossing if that is into the Atlantic Ocean. The flux from floats that cross the GoodHope line and end in the Indian Ocean is negligible (see also Fig. 3.2).

The estimates of the magnitude of Agulhas leakage in literature have a large range, from 4 Sv [Schmitz Jr, 1995; Garzoli and Gordon, 1996] to 22 Sv [Donners and Drijfhout, 2004]. However, most studies report an estimate of 11 – 17 Sv. These estimates are based on different methods, such as water mass analysis [Gordon *et al.*, 1992], altimetry [Garzoli and Goni, 2000], Eulerian model fluxes [Reason *et al.*, 2003], numerical Lagrangian floats [Doglioli *et al.*, 2006; Biastoch *et al.*, 2008c], or drifting buoy trajectories [Richardson, 2007]. However, none of these studies provide an estimate of the (interannual) variability of Agulhas leakage as the time series obtained in these measurement campaigns or model runs is generally too short to yield higher order statistics.

The 37 year long time series in the AG01 model allows for an estimation of the variability of the modeled Agulhas leakage transport. The average leakage in the model is 16.7 Sv, with a variability of 9.2 Sv (Fig. 5.4). When a one year moving average window is applied to smooth the Agulhas leakage transport time series, there is clear interannual variability, with Agulhas leakage trans-

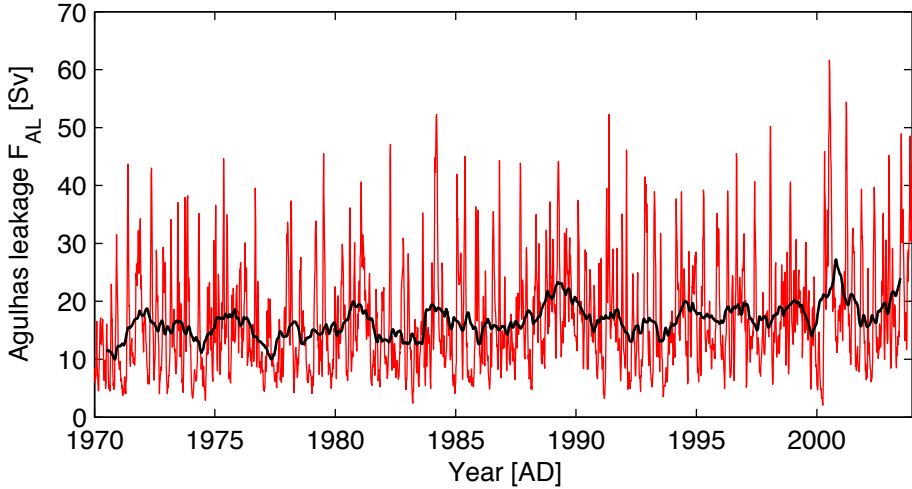


Figure 5.4: Time series of the Agulhas leakage transport F_{AL} , the flux of water sampled by the numerical floats over the GoodHope line in red, and the one year smoothed time series in black. The mean magnitude of Agulhas leakage is 16.7 Sv, with a standard deviation of 9.2 Sv. The Agulhas leakage transport never gets to zero on this five day resolution.

ports ranging between 10 and 25 Sv.

There is a 0.18 Sv/year linear trend in the time series. This is probably related to a 20% decrease in wind stress curl over the Indian Ocean in the period 1968 – 2002 in the *Large and Yeager* [2004] data set. This decrease in wind stress curl may cause a weaker Indian Ocean subtropical gyre, and hence a weaker Agulhas Current. As there is an anticorrelation between Agulhas Current strength and the magnitude of Agulhas leakage (see chapter 6), the reduced wind stress curl would imply an enhanced leakage.

The mean leakage over a five day period can peak at more than 50 Sv. This is the case when an Agulhas ring passes through the section, and a large bulk of Agulhas Current water is advected over the GoodHope line. The leakage never goes to zero, so there is always some small background leakage on the five day resolution used here.

Since the float positions are available on five day resolution only, the calculation of crossing positions at the GoodHope line introduces at least three kinds of errors. First of all, by using five day means, some of the small-scale features of the Agulhas leakage may be smeared out and not correctly sampled. A second error may be introduced since the trajectories are computed using velocity fields which are updated only every five days. During the time steps following the update the velocity fields do not change. Finally, an error may be introduced since the float intersections with the GoodHope line are calculated by a linear mapping onto the GoodHope line, but the float trajectories are certainly not straight between consecutive model snapshots.

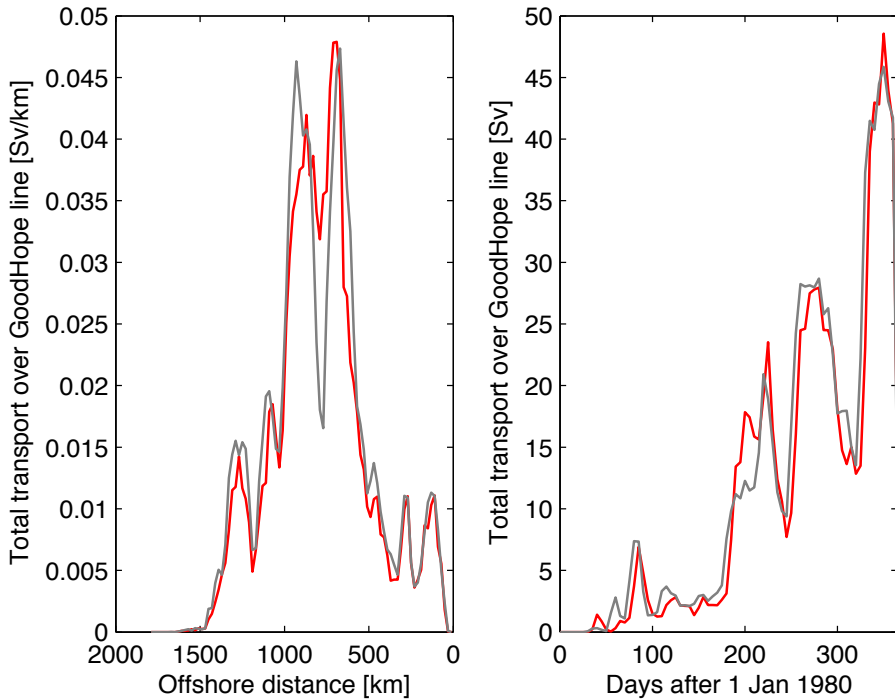


Figure 5.5: Float-determined transport over the GoodHope line for the default model run using five day averaged model fields (red lines), and a short run using one-day averaged model fields (gray lines). Only float trajectories starting in 1980 are used. The transport as a function of offshore distance (left panel) and the transport over the GoodHope line as a function of time (right panel) are shown. Apart from a decreased transport in the one-day averaged model fields at 750 km offshore, the transport variability is quite similar, both in space and time.

The error in GoodHope line crossing position can be investigated by testing the modeled Agulhas leakage transport dependency on the temporal resolution. For the year 1980, an experiment was done where numerical floats were advected using one day averaged model fields. The trajectories in this experiment are not more than one year long. The float crossings at the GoodHope line in this experiment can be compared to the float crossings in the experiment on five day resolution (Fig. 5.5). The agreement between the crossings is high, both in spacing ($R = 0.95$) and timing ($R = 0.97$).

The only major discrepancy between the two experiments is found in the crossing locations through the GoodHope line, where the relative void in float crossings at 750 km offshore is much deeper in the one day resolution experiment than it is in the five day resolution experiment. The bipartitioning seems to be related to the peak in transport over the GoodHope line around day 275, as it disappears when the float data set is reduced to only crossings in the first 200 days of 1980 (not shown). But apart from this feature, reducing the float

integration to five day resolution does not seem to affect the float crossings at the GoodHope line.

5.5 Relating Agulhas leakage to sea surface height

Both the modeled westward extent ϕ_w and the modeled Agulhas leakage transport F_{AL} are highly variable, which is due to the intermittent nature of the shedding of Agulhas rings (Fig. 5.2 and Fig. 5.4). The crosscorrelation between these two quantities is maximum at a lag of 105 days. Such a lag agrees roughly with the time it takes the Agulhas rings to drift from the location where they are shed to the GoodHope line, a distance of approximately 500 km (from 17.5°E to 12°E). *Byrne et al.* [1995] and *Schouten et al.* [2000] found an Agulhas ring translation speed in this region of 5 km day⁻¹, which leads to a comparable translation time (100 days).

Since the amount of noise in the area is high the time series are subsampled to three month bins. We choose a 95 day low-pass filter, as it yields the best signal-to-noise ratio: a high crosscorrelation level between T_{AL} and Φ_w on the one hand, and a low crosscorrelation significance level on the other. These considerations lead to the following definition of the westward extent and Agulhas leakage transport:

$$\Phi_w(t) = \langle \phi_w(t - \tau) \rangle \quad (5.2)$$

$$T_{AL}(t) = \langle F_{AL}(t) \rangle \quad (5.3)$$

where $\tau = 105$ days and $\langle \dots \rangle$ is the 95 day binning operator.

The correlation between the time series of Φ_w and T_{AL} is -0.48 , which is significantly different from zero at the 90% confidence level (Fig. 5.6). This correlation is not very high, which is also evident from the large spread in data points, but it confirms our hypothesis that in the model a more westward location of the Agulhas Current retroreflection leads to an increase in the magnitude of Agulhas leakage.

From a dynamical perspective, it is an important conclusion that an Agulhas Current which is more westward leads to more leakage. There are at least two explanations for this. First of all, a westward zonal jet is more unstable than an eastward one [*Gill et al.*, 1974], so that, if Φ_w is more westward, the potential for instabilities to grow and rings to pinch off is larger. Secondly, a more westward retroreflection causes the eddies to be spawned farther into the Atlantic Ocean, where they have a lower chance of being re-entrained into the Agulhas Current.

To quantify the relation between retroreflection location and leakage, a linear regression has been performed on the data points. This leads to a linear estimate of the magnitude of Agulhas leakage E_{AL} , given the 95 day binned westward extent:

$$E_{AL} = \alpha \Phi_w + \beta \quad (5.4)$$

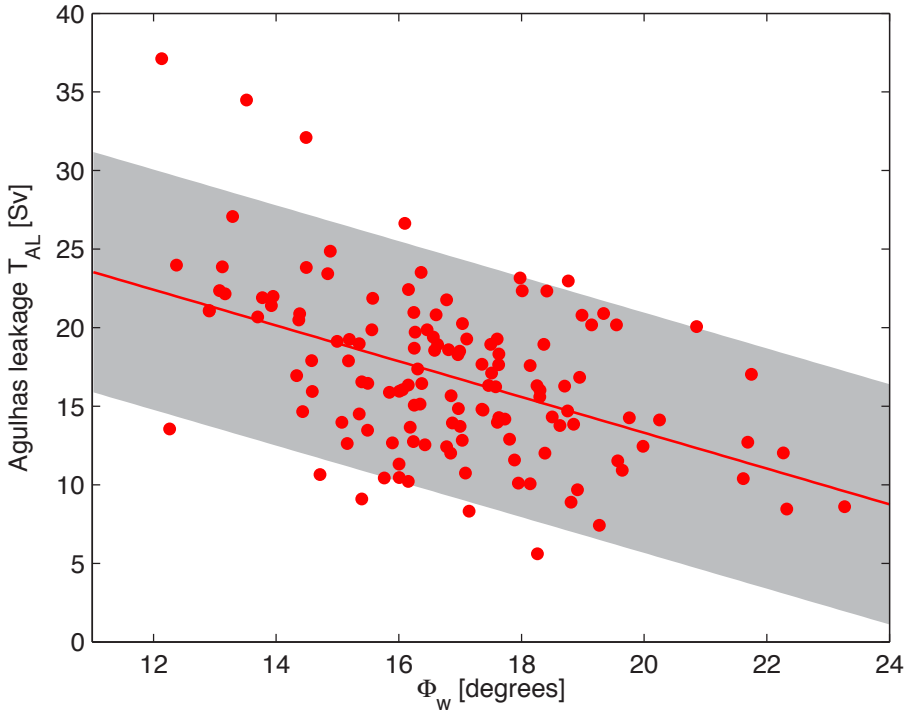


Figure 5.6: The 95 day binned float-determined Agulhas leakage transport T_{AL} versus westward extent Φ_w for the model data. The red line is the best linear fit and the gray area indicates the estimated confidence band so that 90% of the data points fall within the area. The correlation between the two data sets is -0.48 , which is significant at the 90% confidence level.

where the fitting parameters $\alpha = -1.1$ Sv/degree and $\beta = 36.1$ Sv are obtained from the best fit of the 95 day means in Fig. 5.6.

Due to the relatively low correlation between Φ_w and T_{AL} , the skill of the linear estimate is not very high. This can be quantified by assigning a confidence band to the linear estimate. As a first approximation, a constant band is chosen such that 90% of the data points lie within that band. This 90% confidence band results in an uncertainty of 15 Sv in the estimate. An estimate of the magnitude of Agulhas leakage based on the current's westward extent is therefore only certain within a 15 Sv range and this might limit the practical use of the quantitative relation Eq. (5.4). However, the observation that there is a significant linear relation is more robust (see also the discussion, section 5.7).

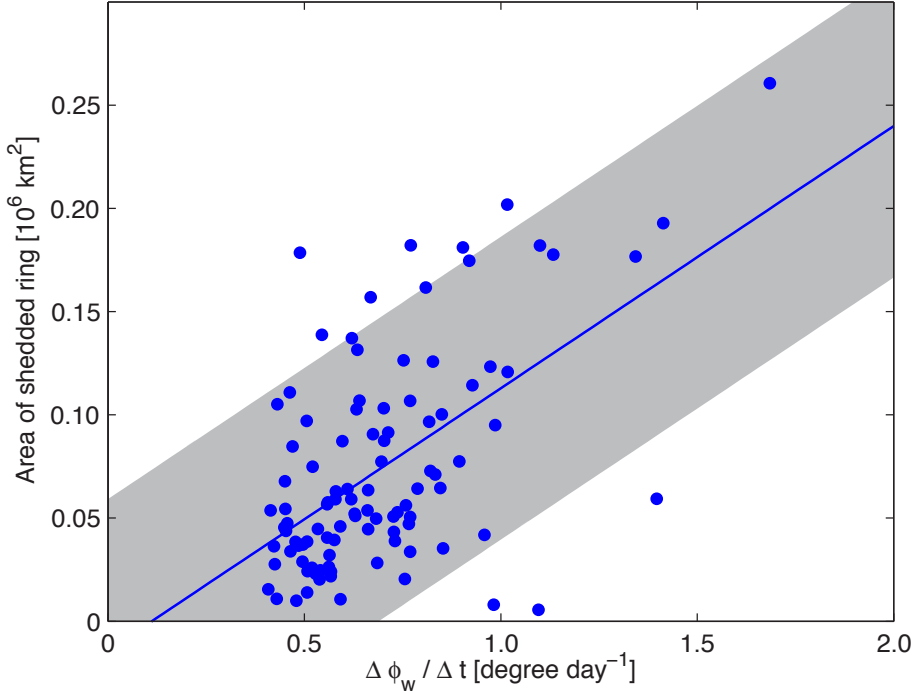


Figure 5.7: The change in front location for loop occlusion events for the AVISO altimetry data (when $\Delta\phi_w/\Delta t > 0.4$ degree day $^{-1}$) versus the area of the associated ring being shed. The gray area denotes the 90% confidence band. The correlation coefficient of the data set is 0.59. Although the spread in data points is smaller than in the AG01 model (Fig. 5.3, note the different scales of the axes), the linear relation is similar.

5.6 Application to altimetry data

The relation which has been found in the previous section can be used to construct an estimate of the magnitude of Agulhas leakage when only sea surface height data are available. The algorithm for finding ϕ_w as described in section 5.2 was designed to be also applicable to altimetry data, since geostrophic velocities are used instead of model velocities. Applying the linear estimate of Eq. (5.4) to altimetry data, where the true magnitude of Agulhas leakage is unknown, might yield some first estimate of the mean and variability of the magnitude of Agulhas leakage in the real ocean.

The altimetry data used is from the AVISO project: More than 15 years of weekly merged sea level anomalies in the Agulhas region on a $1/4^\circ$ resolution, combined with the *Rio and Hernandez* [2004] mean dynamic topography. The algorithm for tracking the Agulhas Current detects a contour C_A in 94% of the snapshots. The mean westward extent in the data set is 19.3°E .

The variability in westward extent is much smaller in the AVISO altimetry data set than in the AG01 model data set. The magnitude of large ring retreats

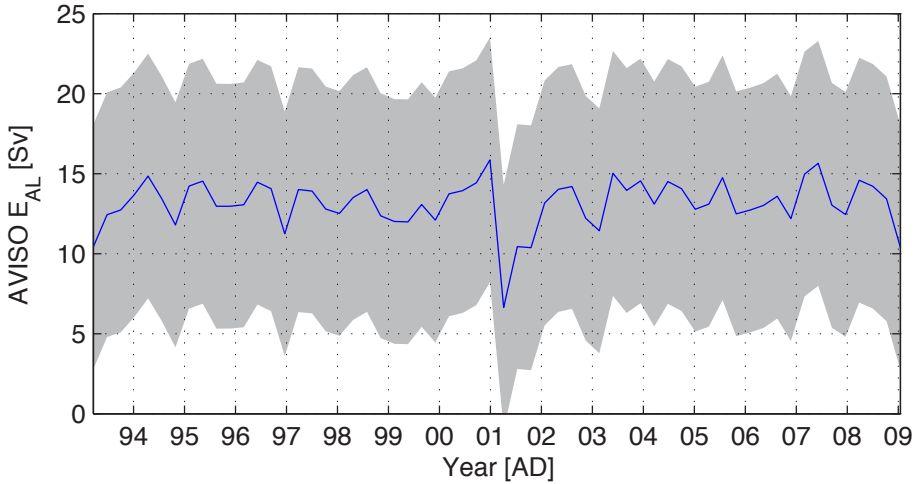


Figure 5.8: The estimated magnitude of Agulhas leakage from E_{AL} (gray area as 90% confidence band) for the 95 day binned AVISO altimetry data. The sharp decrease of E_{AL} in 2001 coincides with an early retroflection [De Ruijter *et al.*, 2004]. According to the estimate, it is very likely that during this early retroflection the magnitude of Agulhas leakage was reduced.

is generally smaller (compare Fig. 5.7 with Fig. 5.3). Nevertheless, the relation between front retreat and area of the shedded ring is similar, with the best linear fit having almost the same slope (both $1.2 \cdot 10^5 \text{ km}^2 \text{ day degree}^{-1}$). This correspondence between model and altimetry can be regarded as a validation of the AG01 model.

The linear estimate of Eq. (5.4) yields an estimated time series E_{AL} for the AVISO altimetry (Fig. 5.8). The mean magnitude of Agulhas leakage in the AVISO data set is 13.2 Sv, with a variability of 1.5 Sv. The most prominent feature in the time series is the drop in the magnitude of Agulhas leakage in the beginning of 2001. This drop coincides with the early retroflection of December 2000 [De Ruijter *et al.*, 2004]. In this period, the Agulhas Current retroflected east of the Agulhas Plateau for almost six months, and no Agulhas rings were formed. Such early retroflections are important large-scale events. One more has been reported, by Shannon *et al.* [1990] in 1986. The AG01 model also has early retroflections, but these seem to be a bit too common [Biastoch *et al.*, 2008c].

The 15 Sv confidence band around the linear estimate of the magnitude of Agulhas leakage in the AVISO data seems to prohibit any more detailed analysis of the time series. But this is only true for the analysis on the magnitude of Agulhas leakage, which is computed using information from the data points in Fig. 5.6. The variability in the magnitude of Agulhas leakage, on the other hand, is directly related to the variability in westward extent Φ_w and may therefore be analyzed. Although it is not significant, there seems to be evidence

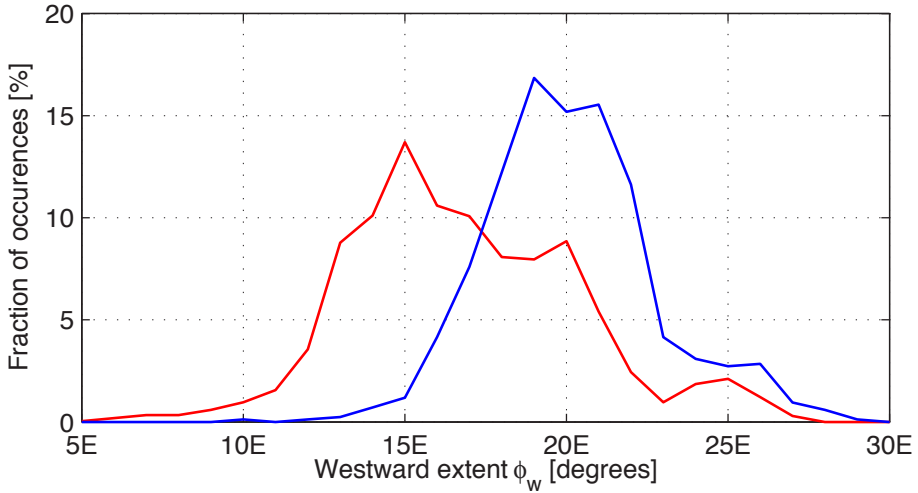


Figure 5.9: Distributions of the non-smoothed westward extent of the Agulhas Current retroreflection ϕ_w for the AG01 model data (red line) and the AVISO altimetry data (blue line). For high values of the westward extent (early retroreflections, $\phi_w > 23^\circ\text{E}$) the distributions of the two data sets are similar, but the low ϕ_w tail in the model data is much more westward than for the altimetry data. This explains the relatively low variability in AVISO E_{AL} compared to the variability in AG01 data (Fig. 5.8). The wider distribution, especially on the low ϕ_w tail, of the model data is also related to the larger rings that are shed in the model (compare Fig. 5.3 with Fig. 5.7).

for an annual cycle in the westward extent of the Agulhas Current retroreflection in the AVISO data, with a more westward Agulhas Current retroreflection in austral winter.

The much lower variability in the AVISO data set than in the AG01 data sets appears to be related to the relatively high fraction of the time that the Agulhas Current retroreflection is west of 15°E in the model (Fig. 5.9). On the original temporal resolution of the model (five days) and the altimetry data (seven days), the distributions of the eastward tails (the early retroreflections) of ϕ_w are similar. West of 23°E , however, the model has a much wider spread in its distribution of ϕ_w than the altimetry data. The spread is closely related to the Agulhas leakage variability, through the linear relation. An explanation for this wide band of ϕ_w may be in details of the numerical representation such as viscosity parameterizations and used values. The wider distribution is in agreement with the more westward flowing Agulhas Current and the associated larger ring area in the model compared to the altimetry data (compare Fig. 5.3 with Fig. 5.7).

5.7 Conclusions and discussion

The influence of the westward extent of the Agulhas Current on the magnitude of Agulhas leakage has been investigated by releasing floats in the high-resolution two-way nested AG01 numerical ocean model. A relation has been found between speed of current retreat and the size of the shed ring, which supports the loop occlusion mechanism of ring shedding [Ou and De Ruijter, 1986; Lutjeharms and Van Ballegooyen, 1988; Feron et al., 1992]. Moreover, a correlation ($R = -0.48$, which is significant at the 90% confidence level) between the 95 day binned Agulhas Current retroflection front location and the 95 day binned magnitude of Agulhas leakage has been found. This correlation implies that a more westward Agulhas Current retroflection leads to enhanced Agulhas leakage transports. A linear estimate for the magnitude of Agulhas leakage can be constructed based on the correlation for use when only sea surface height information is available.

The linear estimate E_{AL} of Eq. (5.4) has a 15 Sv confidence band around the best estimate. This means that application of the estimate leads to an amount of Agulhas leakage which is 90% certain in a 15 Sv range. Such a range is generally too large to be useful, as is demonstrated in the application to the AVISO data set (Fig. 5.8). The aptness of the linear estimate to serve as an index to quantify variability in the amount of Agulhas leakage is therefore limited.

Note on the other hand that the linear relation between the westward extent of the Agulhas Current retroflection and the magnitude of Agulhas leakage is significant. This study might therefore be of more use in increasing the comprehension of the Agulhas system dynamics(i. e. the relation between westward extent and leakage) than in providing a way to estimate the magnitude of Agulhas leakage. Nevertheless, the robustness of the linear relation might mean that the confidence band can be reduced by increasing the size of the data sets. In the future it might be possible to construct a workable index based on the westward extent of the Agulhas Current retroflection.

A fundamental assumption in the linear relation between Φ_w and T_{AL} is that, by monitoring the Agulhas Current location, we can make a good assessment of the total magnitude of Agulhas leakage, which includes small-scale features such as filaments [Lutjeharms and Cooper, 1996; Treguier et al., 2003; Doglioli et al., 2006]. While these features are not captured in the front movement, they are sampled by the numerical floats. Therefore, the relation found for estimating the magnitude of Agulhas leakage accounts for all leakage, including that of small-scale filaments.

The transport estimate in the AVISO data set is only slightly lower than estimated from direct observations and the 2001 early retroflection is unambiguously captured by the altimeter data. However, the validity of these results is limited as the relation between Agulhas Current location and the magnitude of Agulhas leakage is derived from model data only, and no verification with in situ observation has been done. The ultimate relation should come from

an absolute estimate of the magnitude of Agulhas leakage from observational programs, where interocean fluxes are directly measured.

Chapter 6

Relating Agulhas leakage to the Agulhas Current strength

This chapter is based on the work published as:

Van Sebille, E., A. Biastoch, P. J. van Leeuwen, and W. P. M. de Ruijter (2009), A weaker Agulhas Current leads to more Agulhas leakage, *Geophys. Res. Lett.*, 36, L03601.

Abstract

Time series of transports in the Agulhas region have been constructed by simulating Lagrangian float trajectories in a $1/10^\circ$ two-way nested numerical ocean model. Using these 34 year long time series it is shown that smaller (larger) Agulhas Current transport leads to more (less) Agulhas leakage. When transport is low, the Agulhas Current detaches farther downstream from the African continental slope. Moreover, the lower inertia suppresses generation of anticyclonic vorticity. These two effects cause the Agulhas Current retroflection to move westward and enhance the magnitude of Agulhas leakage. In the model, a 1 Sv decrease in Agulhas Current transport at 32°S results in a 0.7 ± 0.2 Sv increase in Agulhas leakage.

6.1 Introduction

The transport of thermocline and intermediate water between the Indian Ocean and the Atlantic Ocean is largely controlled by the dynamics of the Agulhas system [De Ruijter *et al.*, 1999; Lutjeharms, 2006, see also section 1.5]. This highly nonlinear system seems to play an important role in global climate as it connects the meridional overturning circulation of the Pacific–Indian Ocean system with that of the Atlantic Ocean [Gordon, 1986; Weijer *et al.*, 1999; Knorr and Lohmann, 2003]. Peeters *et al.* [2004] showed that changes in Indian–Atlantic interocean exchange are related to (de)glaciations and Biastoch *et al.* [2008b] showed that variability in interocean exchange influences the variability of the Atlantic meridional overturning circulation. Accurate knowledge of the mechanisms governing interocean variability is therefore important.

The Agulhas system is fed from the north by the Agulhas Current. From in situ measurements Bryden *et al.* [2005a] estimated the Agulhas Current volume transport at 32°S to be 70 ± 4 Sv. Water entering the Agulhas system can exit through two major pathways. One is eastward through the Agulhas Return Current. This current reconnects to the Indian Ocean subtropical gyre, thereby recirculating the water in the Indian Ocean. The second pathway for water to leave the Agulhas system is westward into the Atlantic Ocean through Agulhas leakage. Agulhas leakage occurs predominantly in rings, cyclones, filaments, and other small- to mesoscale features [e.g. Reason *et al.*, 2003]. Its magnitude is an estimated 5 – 15 Sv (see section 1.7 and Tab. 1.1), 10 – 20% of the inflow transport. The Agulhas Current retroflexion dynamics is a control on the ratio of eastward and westward transport.

De Ruijter [1982] argued that the inertia of the Agulhas Current plays a key role in the strength of the retroflexion. A weaker Agulhas Current would then result in a reduced inertial overshoot and consequently an increase in the magnitude of Agulhas leakage. This conclusion was later supported by a series of numerical experiments [De Ruijter and Boudra, 1985; Boudra and Chassignet, 1988]. An anticorrelation between Agulhas Current transport and the westward extent of the retroflexion loop was derived in an adiabatic reduced gravity model by Ou and De Ruijter [1986].

In a steady state model Dijkstra and De Ruijter [2001b] showed that the anticorrelation between Agulhas Current strength and the magnitude of Agulhas leakage is valid only if the flow is in low lateral Ekman number regime, when inertia dominates over viscosity. However, the relations determined by these authors have never been explored in a large-scale high-resolution diabatic numerical ocean model. Although there have been quite a few studies on the variability and strength of the Agulhas Current in numerical ocean models [e.g. Matano, 1996; Penven *et al.*, 2006], none have quantified the strength of the Agulhas Current in relation to the interocean exchange. Moreover, the efficiency of the mechanism has not been investigated.

Such a quantification might yield an estimate of the magnitude of Agulhas leakage when the Agulhas Current strength is known. As the strength of the

Agulhas Current can probably be determined with relative ease in the real ocean, a quantification of the anticorrelation might be used in an Agulhas leakage monitoring strategy. In this chapter, therefore, we use a two-way nested numerical ocean model, in combination with numerical float trajectories, to assess the sensitivity of the magnitude of Agulhas leakage to changes in Agulhas Current transport.

6.2 The model

In order to compute transports in the Agulhas system, Lagrangian floats are tracked within a two-way nested numerical ocean model. This setup is the same as in chapters 3 and 5. The model is AG01, a $1/10^\circ$ model of the Agulhas region ($20^\circ\text{W} - 70^\circ\text{E}$; $47^\circ\text{S} - 7^\circ\text{S}$) nested inside ORCA, a $1/2^\circ$ global ocean–sea-ice model [Bia \acute{c} stoch *et al.*, 2008c]. Both models are based on NEMO [Madec, 2006, version 2.3]. The models are two-way nested, allowing for information to cross the open boundaries both ways [Debreu *et al.*, 2008]. In this way, the local Agulhas system dynamics is affected by the global circulation and vice versa. The models are forced for 37 years with the CORE data set of daily wind and surface forcing fields [Large and Yeager, 2004].

The numerical Lagrangian float trajectories are computed using the ARIANE package [Blanke and Raynaud, 1997]. Every five days, the number of floats released in the Agulhas Current is related to the instantaneous transport in such a way that each float represents a transport with a maximum of 0.1 Sv. The floats are released according to the southward velocity at 32°S on a 300 km length zonal section. Only 0.2% of all floats are released in the most eastern grid cell, implying that the Agulhas Current core is well captured by constraining the length of the release section to 300 km. The float paths are integrated for five years. Over a period of 37 years (1968 – 2004) $5.6 \cdot 10^6$ float are released but the last three years of the data set are discarded so that 34 years remain. The mean Agulhas Current transport at 32°S is 64 Sv. The ability of the model and floats to accurately simulate Agulhas Current transport and Agulhas leakage has been demonstrated by Bia \acute{c} stoch *et al.* [2008b,c]. Furthermore, the two-sample Kolmogorov–Smirnov test in chapter 2 showed that the AG01 is the best model in a suite of three and might possess skill in the Agulhas region.

6.3 Relating Agulhas system inflow and outflow

Using the numerical float trajectories, time series are constructed of the Agulhas Current volume transport F_{AC} , the magnitude of Agulhas leakage F_{AL} , and the Agulhas Return Current transport F_{ARC} . A float contributes to F_{AL} the last time it crosses the GoodHope line (the dashed black line in Fig. 6.3, Swart *et al.* [2008], see also section 3.2). In a similar way F_{ARC} is measured over the 40°E line south of Madagascar. In the model, 26% (16.7 Sv) of the

float transport exits the Agulhas system as F_{AL} , whereas 71% (45.4 Sv) exits as F_{ARC} . Approximately 3% (2.2 Sv) of the float transport has not left the domain through one of these sections after the five year integration period and these constitute F_R . Mass conservation leads to a relation between the transports:

$$F_{AC} = F_{AL} + F_{ARC} + F_R \quad (6.1)$$

It is important to note that, by construction, a float's exit from the Agulhas system is synchronized to its release. In this way, the local dynamics in the Agulhas system is ignored. This is done because the time lags between float inflow and outflow are highly variable and depend on where a float leaves the system. The median time it takes a float to exit the Agulhas system as either F_{AL} or F_{ARC} is less than a year, and more than 85% of the floats exit within two years. By eliminating the influence of the lags, Eq. (6.1) is always true and the transport sensitivities, which are based on this relation, are better confined.

The instantaneous transport F_{AC} varies between 30 Sv and 128 Sv, largely related to passing mesoscale eddies. The other transports are for the same reason also highly variable. Because we are interested in interannual variability, the transports are binned to biennial averages yielding 17 individual transport estimates (cf. Eq. (5.2)):

$$T_X(t) = \langle F_X(t) \rangle \quad (6.2)$$

where X is either AC , AL , ARC , or R and $\langle \dots \rangle$ is the two year binning operator.

In the model, the ratio between the outflow transports T_{AL} and T_{ARC} is approximately 1 : 3. If the Agulhas system were linear, a 1 Sv decrease in the inflow flux T_{AC} would therefore yield a 0.25 Sv decrease in T_{AL} and a 0.75 Sv decrease in T_{ARC} . This linear hypothesis is tested using the float data. The sensitivities of the outflow fluxes to changes in T_{AC} are obtained from the slope of the best linear fits in Fig. 6.1. These are -0.73 ± 0.21 for T_{AL} , 1.78 ± 0.23 for T_{ARC} , and 0.05 ± 0.04 for T_R . This emphasizes the nonlinear nature of the Agulhas system with the main result that a weaker Agulhas Current leads to more Agulhas leakage. These sensitivities depend on the width of the averaging bins taken, but beyond a width of two years the sensitivity parameters vary within the standard deviations of the biennial bin (Fig. 6.2). When time lags are incorporated in the transport time series the signs of the sensitivities remain unchanged but the correlations decrease.

6.4 Inertial outcropping

As mentioned in the introduction, the negative correlation between Agulhas Current strength and the magnitude of Agulhas leakage found here has been suggested before. A stronger Agulhas Current has more inertia so the potential for stretching is larger (related to conservation of the Bernoulli function,

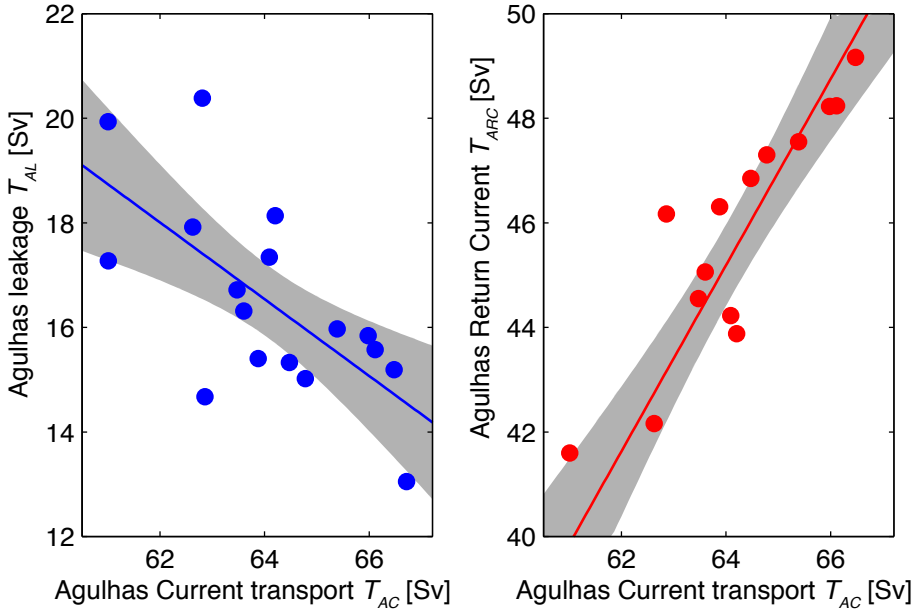


Figure 6.1: The correlations between the biennially smoothed Agulhas Current transport T_{AC} and the magnitude of Agulhas leakage T_{AL} (left panel, in blue) and Agulhas Return Current transport T_{ARC} (right panel, in red). The lines represent the best linear fit and the gray areas are the 95% confidence levels of these fits. There is an anticorrelation between Agulhas Current transport and the magnitude of Agulhas leakage ($R = -0.67$), whereas Agulhas Current transport correlates positively with Agulhas Return Current transport ($R = 0.89$).

Ou and De Ruijter [1986]). The current can then more easily detach from the continental slope by interface outcropping, creating a free streamline. Due to the convex curvature of the African coast, a stronger Agulhas Current detaches more upstream. In part aided by the local bathymetry (in particular the Agulhas Plateau [*Matano, 1996; Speich et al., 2006*]) the separated current then flows southward, where it is able to attach to the Agulhas Return Current.

The mean float trajectories (Fig. 6.3) show that the flow is more coast-bound when T_{AC} is low, as predicted by the inertial outcropping mechanism. Moreover, the float trajectory distributions are shifted westward for low T_{AC} .

The model Agulhas Current detaches from the continent by means of outcropping of the isotherms (Fig. 6.4; due to the biennial averaging, the strength of the outcropping is somewhat masked). In the model, a weaker Agulhas Current outcrops farther downstream (with a correlation coefficient $R = 0.5$) and the strength of the upwelling is reduced ($R = 0.6$). Moreover, a weaker Agulhas Current has less inertia ($R = 0.5$).

Apart from reducing outcropping, inertia also controls the eastward current loop after outcropping because it generates anticyclonic vorticity through

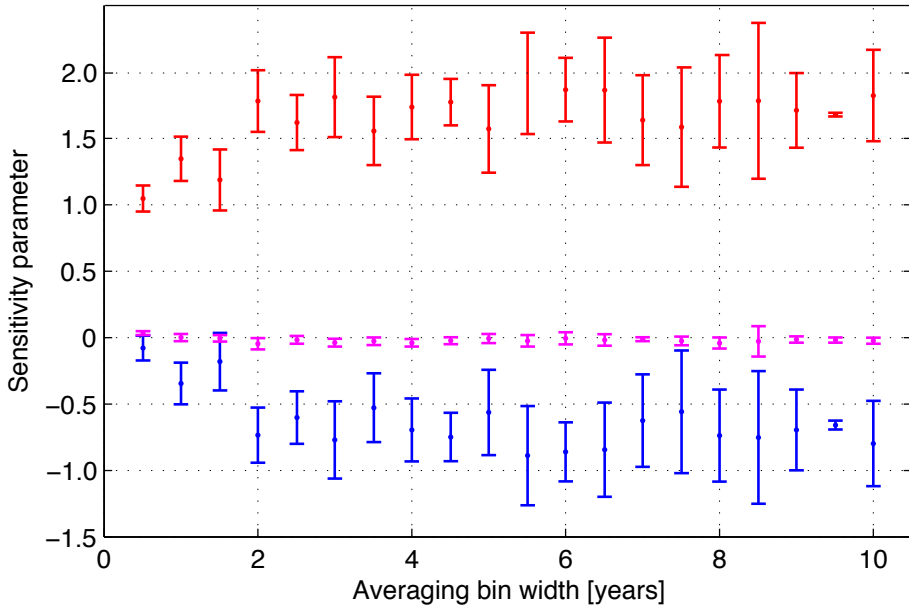


Figure 6.2: The effect of smoothing on the linear fits between the inflow and outflow fluxes. The sensitivities (mean and standard deviation) of the outflow fluxes F_{AL} (blue), F_{ARC} (red), and F_R (magenta) to a 1 Sv increase in F_{AC} as a function of bin width. Beyond a bin width of two years, the sensitivity parameters vary within the standard deviation of the biennial bins.

the strength of the planetary vorticity advection [Boudra and Chassignet, 1988]. A more upstream separation leads, in agreement with the results of Ou and De Ruijter [1986], to a more southward-oriented inertial overshoot (see Fig. 6.3). The westward extent of the Agulhas Current retroflexion is then moved eastward and according to the linear relation found in chapter 5 the magnitude of Agulhas leakage is thus decreased.

The change in overshoot direction also causes a better matching with the wind field of the subtropical Indian Ocean, which is located around 40°S [De Ruijter and Boudra, 1985; Zharkov and Nof, 2008a]. The increased matching leads to a smaller Agulhas leakage. Although the three individual correlations are not very strong, the combination of reduced outcropping and inertia for a weaker Agulhas Current may explain the anticorrelation found between T_{AL} and T_{AC} .

6.5 Application in a monitoring program

The anticorrelation found between Agulhas Current transport T_{AC} and the magnitude of Agulhas leakage T_{AL} might be employed in an Agulhas leakage monitoring system. Similar to the way in which the Agulhas Current

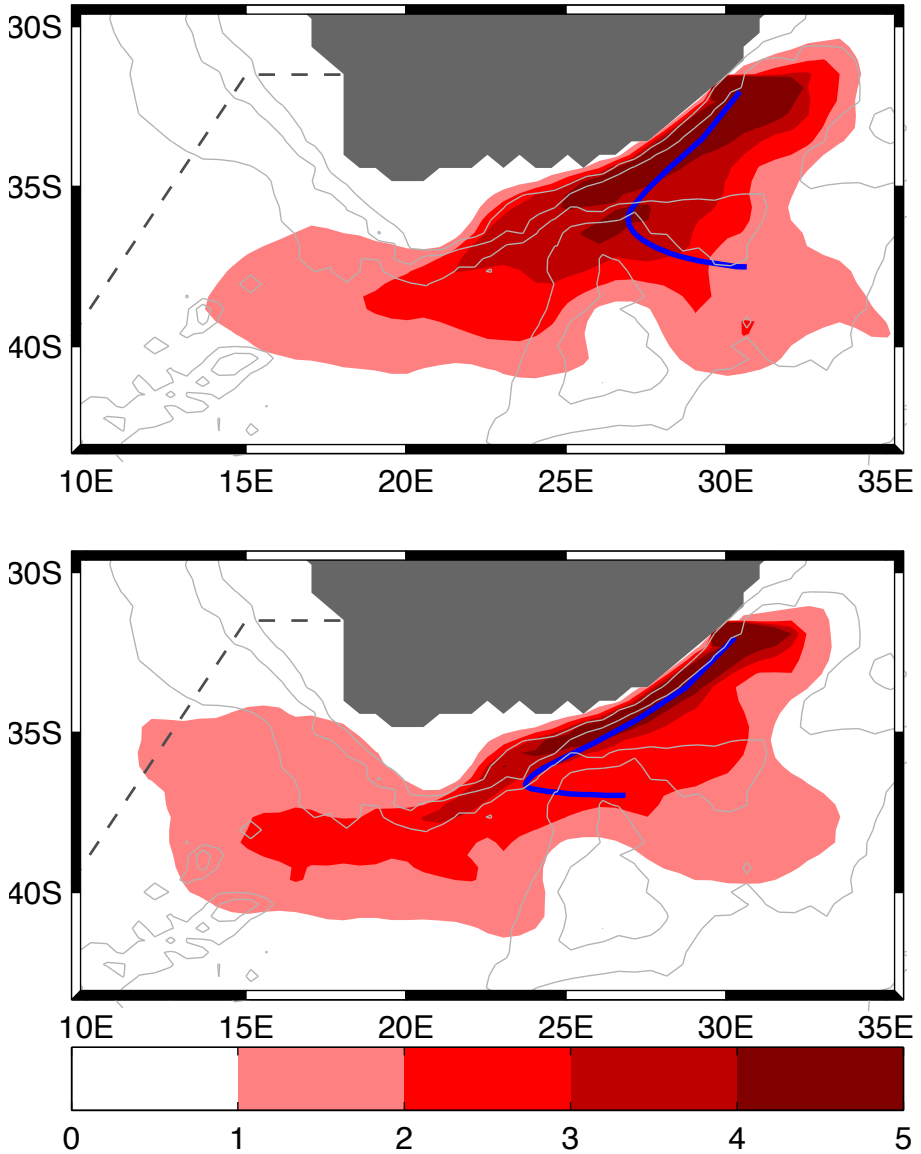


Figure 6.3: The density of float transport (red patches, in sverdrup) in the first six months after release for all floats released in 1986 – 1987 (upper panel, $T_{AC} = 65.4$ Sv) and in 1988 – 1989 (lower panel, $T_{AC} = 61.0$ Sv). The thick blue lines are the transport-weighted mean trajectories. The bathymetry is shown as gray lines (1500 m contour interval). For lower Agulhas Current transports (lower panel), the current detaches from the continental slope farther downstream. The retroflexion is consequently moved westward and the magnitude of Agulhas leakage is increased.

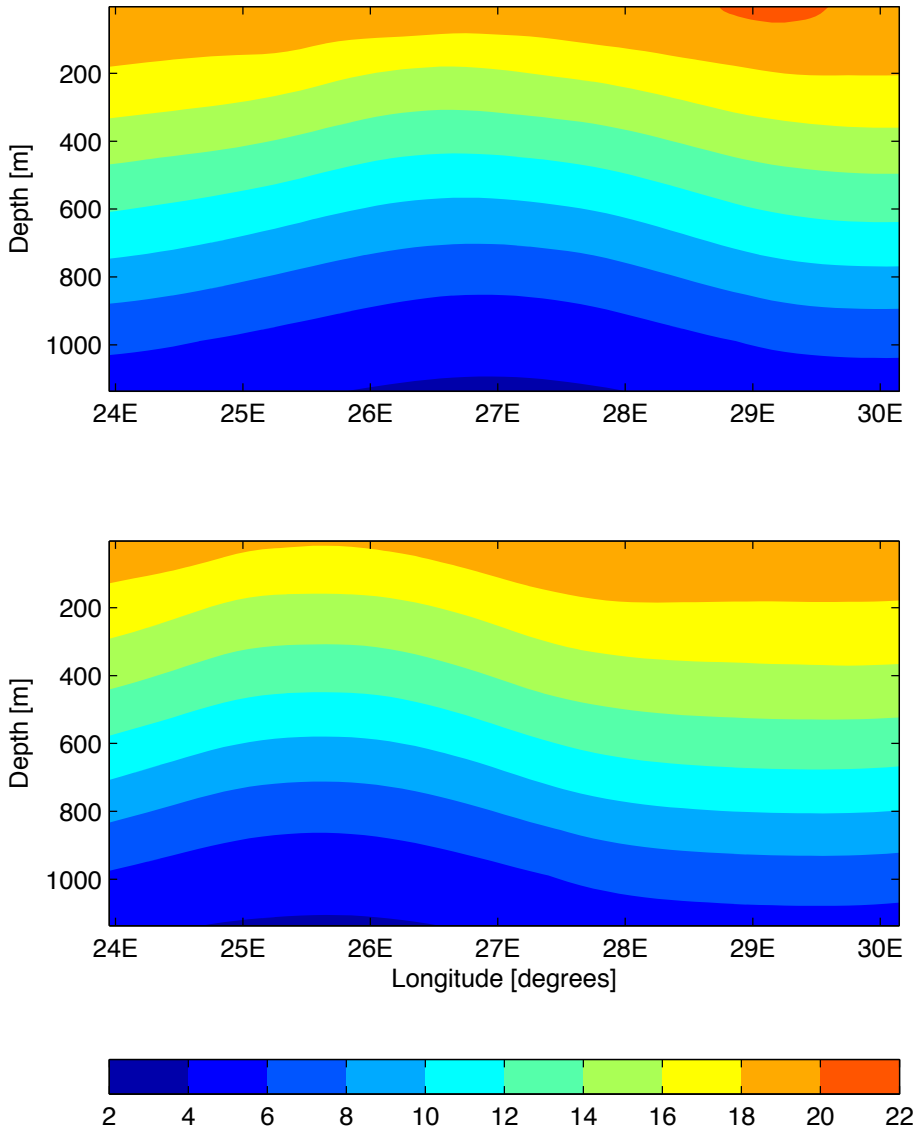


Figure 6.4: The modeled near-coastal temperature as a function of longitude and depth in °C in 1986 – 1987 (upper panel, $T_{AC} = 65.4$ Sv) and in 1988 – 1989 (lower panel, $T_{AC} = 61.0$ Sv). For lower Agulhas Current transports (lower panel) the outcropping, the upward shift of isotherms, occurs more downstream. The strength of the outcropping is masked due to the biennial averaging. True outcropping, where the 12°C isotherm is lifted to depths of 150 m, appears in individual model snapshots.

retroreflection westward extent from altimetry is used to estimate the magnitude of Agulhas leakage in the method described in chapter 5, measuring the Agulhas Current transport might also yield a linear estimate of the magnitude of Agulhas leakage:

$$E_{AL} = \alpha T_{AC} + \beta \quad (6.3)$$

where the fitting parameters $\alpha = -0.7$ and $\beta = 64$ Sv are obtained from the best fit in the left panel of Fig. 6.1.

The much smaller uncertainty in the linear relation (compare Fig. 5.6 with Fig. 6.1) yields a more accurate estimate of the magnitude of Agulhas leakage for the Agulhas Current strength method than for the altimetry method. The uncertainty in Eq. (6.3) is less than 2 Sv in this method, whereas it is 15 Sv using the retroreflection location from altimetry. The costs, on the other hand, are much higher as a dedicated mooring program is required, as both T_{AL} and T_{AC} have to be determined in order to find the fitting parameters α and β in the real ocean. Another disadvantage of the estimation method described here is that due to the long binning period it takes two years, a relatively long period, before a first estimate of the magnitude of Agulhas leakage is available.

What is required for the application of the estimate Eq. (6.3) in the real ocean is a time series of the Agulhas Current transport at 32°S. There have been a number of successful programs to determine the transport of the Agulhas Current. *Beal and Bryden* [1997, 1999] used a vessel-based Lowered Acoustic Doppler Current Profiler to obtain a high-resolution snapshot (using 15 stations) of the Agulhas Current strength at 32°S in 1995. In 2003 an extended version of this program (using 112 stations) was used by *Casal et al.* [2006, 2009] to map the hydrography of the Agulhas Current on its path along the South African coast in the Agulhas Undercurrent Experiment. Although such vessel-based programs yield accurate estimates of the instantaneous transport, they are not apt for long-term monitoring programs.

An array of subsurface moorings equipped with current meters is better suited for such a monitoring program of the Agulhas Current strength. *Bryden et al.* [2005a] have deployed such an array for almost one year in the Agulhas Current at 32°S. Using six moorings with 24 instruments, the authors have been able to determine the mean Agulhas Current transport at that location over the period February 1995 – April 1996 within an error of 4.3 Sv. An extended version of this program, the Agulhas Current Time-series experiment, is planned for the near future. In this program, the strength of the Agulhas Current will be monitored for three years using a mooring array. Correlation with altimetry is expected to yield a time series which is as long as the satellite altimetry record, almost 20 years now. This program seems well suited for monitoring the biennial variability in Agulhas Current strength, which can then be related to the magnitude of Agulhas leakage.

6.6 Conclusions and discussion

Using the transports determined from numerical Lagrangian floats over a 34 year period, we have shown in a high-resolution numerical ocean model study that there is an anticorrelation between the strength of the Agulhas Current at 32°S and the magnitude of Agulhas leakage into the Atlantic Ocean. A decrease in the amount of Agulhas leakage is compensated by an increase in the Agulhas Return Current transport. The inertial outcropping mechanism proposed by *Ou and De Ruijter* [1986] is consistent with these findings. A weaker Agulhas Current experiences less outcropping and generates less anticyclonic vorticity, thereby moving the location of the retroflection southwestward. The larger southward overshoot results in a better matching to the latitude of zero wind stress curl [*Dijkstra and De Ruijter*, 2001b]. This causes the amount of Agulhas leakage to increase.

Inertial outcropping is only one of the mechanisms which can affect the location of the Agulhas Current retroflection. Another one is offshore migration of the Agulhas Current due to Natal pulses, which are solitary cyclonic meanders on the inshore edge of the current [*Lutjeharms and Roberts*, 1988, see also section 1.5.7]. As Natal pulses may be accompanied by an anticyclone on the offshore side of the current, local transport can be increased when a Natal pulse passes. However, although Natal pulses trigger early retroflections on intra-annual time scales in the model [*Biastoch et al.*, 2008c], it appears from this study that there is no correlation between Natal pulses and T_{AC} or T_{AL} in the model on the biennial time scale (not shown).

The range of biennial variation of Agulhas Current transports used here is almost 6 Sv. Although this range is large enough to draw conclusions on present-day climate sensitivity, it is unsure how robust these sensitivities are to larger changes in T_{AC} . The determined sensitivity implies that at $T_{AC} = 37$ Sv the magnitude of Agulhas leakage equals Agulhas Current transport and $T_{ARC} = 0$, effectively creating a supergyre (see also section 1.3). At $T_{AC} = 91$ Sv the magnitude of Agulhas leakage would become negative. Clearly, the derived sensitivity is only valid within an (unknown) range of Agulhas Current transport in which the present day system resides.

However, the sign of the sensitivity between the magnitude of Agulhas leakage and Agulhas Current transport is robust, also in view of the dynamical explanation given. The negative correlation might play a role in the magnitude of Agulhas leakage on glacial time scales. The latitude of zero wind stress curl plays an important role in the magnitude of Agulhas leakage. This is found by *Zharkov and Nof* [2008a], who calculated that the slant of the African continent can choke the formation of Agulhas rings when the latitude of zero wind stress curl is north of some critical latitude.

Measuring the magnitude of Agulhas leakage in situ in the southeastern Atlantic Ocean is complicated, due to the turbulent nature of the water motion in the Cape Basin [*Boebel et al.*, 2003a] and the vicinity of the varying Antarctic Circumpolar Current. The magnitude of Agulhas leakage could instead be es-

timated by a monitoring of the (much more confined) Agulhas Current. Using an array of six moorings, the Agulhas Current transports could then be converted into an estimate of the magnitude of Agulhas leakage by utilizing the relation presented here.

Chapter 7

Relating Agulhas leakage to fluxes at the GoodHope line

This chapter is based on the work:

Van Sebille, E., P. J. van Leeuwen, A. Biastoch, and W. P. M. de Ruijter (2009), Flux comparison of Eulerian and Lagrangian estimates of Agulhas leakage: A case study using a numerical model, *submitted*.

Abstract

Two Eulerian methods for estimating the magnitude of Agulhas leakage are tested within a high-resolution two-way nested model with the goal to devise a mooring-based measurement strategy. At the GoodHope line, a section halfway through the Cape Basin, the integrated velocity perpendicular to that line is compared to the magnitude of Agulhas leakage as determined from the transport carried by numerical Lagrangian floats.

In the first method, integration is limited to the flux of water warmer and more saline than specific threshold values. These threshold values are determined by maximizing the correlation with the float-determined time series. By using the threshold values, approximately half of the amount of leakage can directly be measured. The total amount of Agulhas leakage can be estimated using a linear regression, within a 90% confidence band of 12 Sv.

In the second method, a subregion of the GoodHope line is sought so that integration over that subregion yields an Eulerian flux as close to the float-determined leakage as possible. It appears that when integration is limited within the model to the upper 300 m of the water column within 900 km of the African coast the time series are closest together. This method yields a root-mean-square error of only 5.2 Sv but the 90% confidence band of the estimate is 20 Sv.

It is concluded that the optimum thermohaline threshold method leads to more accurate estimates even though the directly measured transport is a factor two lower than the actual magnitude of Agulhas leakage in this model.

7.1 Introduction

The magnitude of Agulhas leakage, the water in the Agulhas Current that ends in the Atlantic Ocean, is related to the strength of the Atlantic meridional overturning circulation [Weijer *et al.*, 1999; Knorr and Lohmann, 2003; Peeters *et al.*, 2004; Biastoch *et al.*, 2008b]. That is why an accurate monitoring of the variability of Agulhas leakage may yield a precursor of northern Atlantic Ocean climate variability. This monitoring is not easy, and estimates of even the mean amount of Agulhas leakage have a wide range (see section 1.7). One of the most widely used methods in models to estimate the magnitude of Agulhas leakage is based on integrating the modeled velocity over some vertical plane close to the Agulhas Current retroflection [e.g. Dijkstra and De Ruijter, 2001b; Matano and Beier, 2003; Treguier *et al.*, 2003; Reason *et al.*, 2003; Hermes *et al.*, 2007].

However, such Eulerian methods may not be very apt for determining the magnitude of Agulhas leakage. This is because the Agulhas Current retroflection and leakage are not the only circulation systems within the greater Agulhas region (see also section 1.3). Closely linked to the Agulhas Return Current is the Subtropical Front of the Antarctic Circumpolar Current and the Agulhas system is intruded in the west by the subtropical gyre of the South Atlantic Ocean. The water carried by these two circulation systems is vigorously mixed with the Agulhas leakage in the Cape Basin [Boebel *et al.*, 2003a]. This mixing can complicate the Eulerian measurement of the magnitude of Agulhas leakage, as it may be unclear what fraction of a certain flux is Agulhas leakage and what fraction is related to other sources (see also section 1.7). Nevertheless, the 10 – 20 Sv range in Eulerian estimates of the magnitude of Agulhas leakage in models seems to agree with estimates obtained by other methods (Tab. 1.1).

The difficulty in determining the magnitude of Agulhas leakage arises because the Agulhas region is not enclosed by continental boundaries. For that reason the integration of Eulerian velocities can not be performed on a section between two coasts, although the oceanic volume transport in other regions of the world ocean can be measured in this way. Examples of arrays employing such methods are located in the Atlantic Ocean [Bryden *et al.*, 2005b], in the Mozambique Channel [Ridderinkhof *et al.*, 2009], and in the straits of the Indonesian Archipelago [Gordon *et al.*, 1999]. In the Agulhas region, however, integration can not be done on the section between South Africa and Antarctica, as the eastward flowing Antarctic Circumpolar Current will then dominate the signal [e.g. Ganachaud and Wunsch, 2000]. This is one of the reasons why inverse modeling of Agulhas leakage is so difficult [Schmitz Jr, 1995; Casal *et al.*, 2009]. Donners and Drijfhout [2004] have shown that inverse modeling might even be impossible for the Agulhas system, since there is an overlap in the density class of some of the Agulhas leakage and some of the Antarctic Circumpolar Current.

Because of these problems, there might be a need for a method indicating how and where to deploy a (virtual) mooring array in order to obtain a time series of fluxes that resembles the time series of the amount of Agulhas leakage

closely. The GoodHope line (see Fig. 1.6) seems to be a good location for this. It is close to the Agulhas Current retroflection but the flux of water that returns to the Indian Ocean after crossing the line is negligible (see also section 3.2). The GoodHope line [Ansorge *et al.*, 2005; Swart *et al.*, 2008] has been used for estimating the magnitude of Agulhas leakage in the BEST and ASTTEX programs [Byrne and McClean, 2008; Baker-Yeboah, 2008], where a series of Pressure Inverted Echo Sounders were deployed on the ocean floor. However, these are not real current meters, so in order to compute Eulerian fluxes an additional two-layer model was used. Such a model was employed by Garzoli and Goni [2000], who have used measurements from the ASTTEX program to calibrate an altimetry-based method of estimating the flux in the thermocline fraction of Agulhas leakage.

The approach used here is to limit the integration to only a subdomain of the entire GoodHope line. After presenting the model used (section 7.2) and qualitatively comparing the Eulerian flux over the GoodHope line to the Lagrangian transport over that same line (section 7.3), two methods are discussed: One where the subdomain is bounded by the temperature and salinity of the water, and a second one where the subdomain is bounded by depth and offshore distance.

The first method (section 7.4) is based on the thermohaline properties of Agulhas leakage. The thermocline water of the Indian Ocean is in general warmer and more saline than the thermocline water of the Atlantic Ocean and Southern Ocean. If the Agulhas leakage maintains these characteristics on its way through the Cape Basin, it might be distinguished from other water masses at the GoodHope line. However, this signal might quickly dilute away from the Agulhas Current retroflection. Mixing in the Cape Basin is vigorous [Boebel *et al.*, 2003a] and the Agulhas rings in which most Agulhas leakage detaches from the Agulhas Current experience a fast decay (see chapter 3). Note that this method will only resolve the Agulhas leakage in the thermocline, as the Indian Ocean water below the thermocline does not differ very much from the water in the adjacent oceans [Van Aken *et al.*, 2003]. Such a water mass classification method for estimating the magnitude of Agulhas leakage was applied by Gordon *et al.* [1987], who came to an Agulhas leakage estimate of 10 Sv based on a comparison of the thermohaline characteristics of water in the southeast Cape Basin and in the Agulhas Current.

The second method (section 7.5) is based on the location where Agulhas leakage crosses the GoodHope line. One can try to find an optimum Euclidean integration area: a rectangular area within which the integrated velocity is as close as possible to the true (determined from numerical floats) time series of the magnitude of Agulhas leakage. The major problem with this method is that the shape of the area might be highly model-dependent, because it is an empirical method and neglects the dynamics of the Agulhas system.

7.2 The model

The two methods for confining the integration area are tested within the AG01 model [*Biastoch et al.*, 2008b,c], a two-way nested high-resolution model of the Agulhas region. In the model, $5.6 \cdot 10^6$ numerical Lagrangian floats have been deployed over a 37 year period in the Agulhas Current at 32°S. By determining the transport attributed to the floats that cross the GoodHope line at a particular time, a time series of the flux of Agulhas leakage through the GoodHope line can be composed. This method yields a mean flux of Agulhas leakage of 17 Sv (see section 5.4). The float data set is the same as that used in the chapters 3, 5, and 6.

The magnitude of Agulhas leakage as determined from the numerical Lagrangian floats (Fig. 5.4) is taken here as the ‘true’ time series F_{AL} and it is used for determining the skill of the Eulerian methods. Note that in this setup of the experiments the model is calibrated with itself. Therefore, it may be hard to translate the results of this chapter to the real ocean. Nevertheless, the results might serve as a first feasibility test for a monitoring program in the real ocean.

The velocity profile perpendicular to the GoodHope line can be measured as a function of time, either by using Acoustic Doppler Current Profilers (ADCPs), by using CTD sensors in combination with the thermal wind balance, or by using inverted echo sounders and reduced gravity models [*Garzoli and Goni*, 2000; *Baker-Yeboah*, 2008]. In this study, we will deploy virtual current meters within the AG01 model. To mimic a mooring array, the velocity fields perpendicular to the GoodHope line are regridded to a resolution of 50 m in depth and 50 km in offshore distance. This particular resolution means that a velocity of 1 m s^{-1} in a certain grid cell results in a flux of 2.5 Sv. This flux can be either into the Atlantic Ocean (defined as positive), or into the Indian Ocean (defined as negative).

The location of each float crossings at the GoodHope line is determined using a three-dimensional linear interpolation. The temperature and salinity of the water at each of these crossing locations is determined by a two-dimensional interpolation of the (Eulerian) model temperature and salinity fields at the GoodHope line at the moment of float crossing. In this way the thermohaline properties of the Agulhas leakage can be determined.

Note that there seems to be a fundamental dichotomy related to the use of numerical Lagrangian floats for temperature and salinity analysis: The floats are allowed to mix heat and salt with their surrounding but at the same time it is assumed that all their transport originated in the Agulhas Current. This discrepancy, which turns out to be misleading and not true, was already discussed in section 3.7.

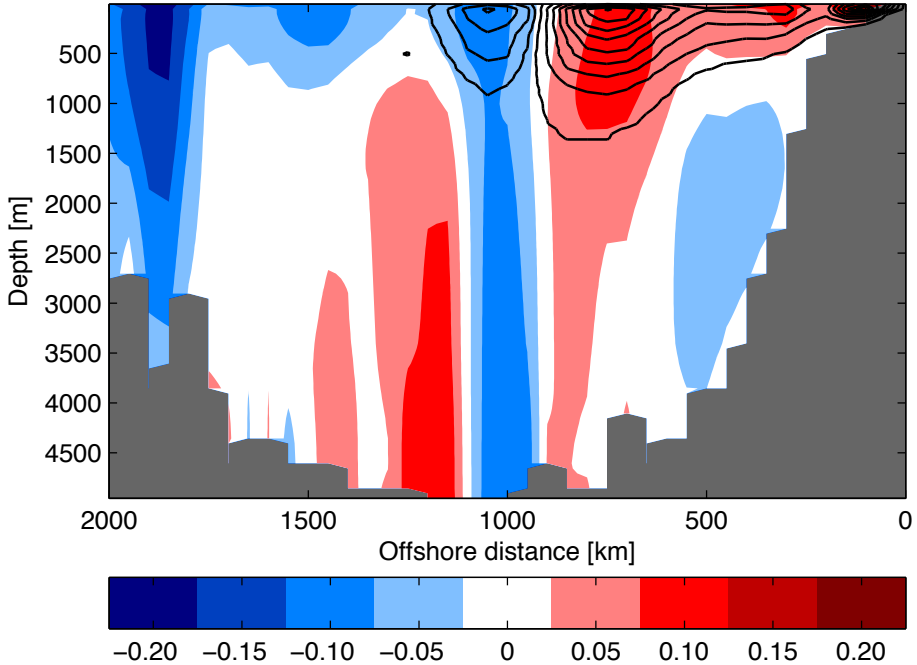


Figure 7.1: The mean of the flux perpendicular to the GoodHope line (in sverdrup per $50 \text{ m} \times 50 \text{ km}$ grid cell) in the model run. See Fig. 3.2 for the location of the GoodHope line. Blue patches denote a mean flux into the Atlantic Ocean while red patches denote a mean flux into the Indian Ocean. The lines indicate the distribution of numerical float crossings (also in sverdrup per $50 \text{ m} \times 50 \text{ km}$ grid cell) and the contour interval is half that of the patches. The floats are released in the Agulhas Current over the entire water column. Note that for this distribution every crossing of a float is taken into account and that one float can cross the GoodHope line multiple times. The agreement between the velocity-integrated profile and the float transport is high in the upper 1000 m and until 1200 km offshore.

7.3 Qualitatively comparing the flux profiles

When a composite of the mean Eulerian flux perpendicular to the GoodHope line is compared to the distribution of the transport by numerical Lagrangian float crossings through that line, the high agreement between the Eulerian flux and Lagrangian transport fields close to the coast and in the upper ocean is evident (Fig. 7.1). Apparently, the Agulhas leakage in the model is limited to the upper 1500 m, and reaches only 1200 km offshore.

There are two maxima in float crossing position. The first is in the region 500 – 1200 km offshore and is related to Agulhas rings, Agulhas cyclones, and filaments and other non-rotating features. In the Agulhas rings and cyclones, floats may cross the GoodHope line multiple times as they swirl inside the ring and this explains the bipolar structure in float crossing distribution.

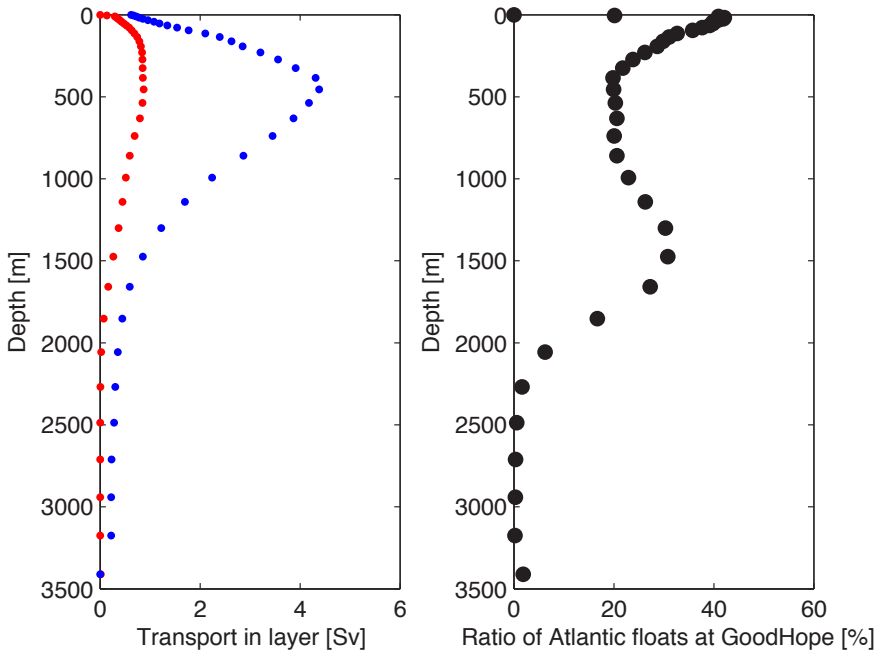


Figure 7.2: The transport per model layer (left panel) for all floats when they are released in the Agulhas Current (blue), and for the floats that end in the Atlantic Ocean when they cross the GoodHope line (red). The right panel shows the ratio of floats ending in the Atlantic Ocean as a function of model layer. While the Agulhas Current contains approximately 30% floats which end in the Atlantic Ocean in the upper 2000 m, this ratio reduces to almost zero below 2000 m.

The distribution is asymmetric since these floats always cross the GoodHope line an odd number of times, as they are released in the Indian Ocean but end in the Atlantic Ocean. This eddy corridor is centered around 900 km offshore, which is at 12°E and 36°S (see also Fig. 3.2). The second local maximum of float crossings is located within 200 km of the African coast, on the continental shelf. This core is probably related to the Good Hope Jet (see section 3.3), a frontal boundary current feeding into the Benguela system [Bang and Andrews, 1974; Gordon *et al.*, 1995].

Although the velocity profile at the GoodHope line has a large barotropic component, especially in the eddy corridor of maximum float crossing, the floats seem to be confined to the upper 1500 m. This despite the fact that there are floats which are released deeper in the Agulhas Current (Fig. 7.2). Apparently, only the upper part of the Agulhas Current leaks into the Atlantic Ocean and the lower part is returned into the Indian Ocean in this model. The relative shallowness of Agulhas leakage was previously mentioned by Donners *et al.* [2004], who found that Agulhas leakage was limited to the upper 1200 m

in their model. Furthermore, using observations, *Van Aken et al.* [2003] show that an Agulhas ring has low relative vorticity below 1200 m, which might imply that deeper than 1200 m there is almost no mass carried by the rings. In a model study, *De Steur et al.* [2004] showed that the size of the separatrix (the circumference of the region where water is carried within an Agulhas ring) decreases with depth due to the decrease in swirl velocity of the water. At some depth, therefore, the swirl velocity is smaller than the translational velocity, and the water is not advected with the Agulhas ring anymore [*Flierl*, 1981].

Note that this is somewhat in contradiction to the result of section 3.3, where it was shown that the distributions of floats ending in the Atlantic Ocean and floats ending in the Indian Ocean are to a large extent comparable. However, the focus there was on offshore location of the floats and not so much in depth. Furthermore, the transport by floats released below 2000 m is only 3% of the total transport by all floats at 32°S.

7.4 An optimum thermohaline threshold method

As already stated in the introduction of this chapter, the goal of this study is to investigate how to relate the fluxes at the GoodHope line to the float-determined Agulhas leakage F_{AL} . The high agreement between the Eulerian flux and Lagrangian transport in Fig. 7.1 suggests that such a relation is feasible when only a subdomain of the GoodHope line is used. The first approach to determining the shape of this subdomain is based on the thermohaline properties of the Eulerian flux.

The change of the thermohaline characteristics of the water on its route through the Cape Basin can be assessed by comparing the temperature and salinity of the water where numerical floats cross the Agulhas Current retroflexion (at 19°E, see also chapter 3) with the temperature and salinity of the water where numerical floats cross the GoodHope line (Fig. 7.3). At both sections there is a significant amount of transport in cold and fresh subthermocline water and this transport appears to maintain its characteristics through the Cape Basin. *Van Aken et al.* [2003] already noted that below the 12°C isotherm the water within Agulhas rings can not be distinguished from the surrounding water so that mixing does not alter the thermohaline characteristics of the Agulhas leakage. This suggests that integrating over water colder than 12°C will probably introduce spurious fluxes and should be done with much precaution. The warm and saline thermocline water, on the other hand, is much fresher and colder when it crosses the GoodHope line. Apparently, this water has experienced atmospheric cooling and freshening and extensive mixing with the colder thermocline water of the Atlantic and Southern Oceans.

Although mixing appears to have a large impact on the Agulhas leakage as it crosses the GoodHope line, we can try to estimate the magnitude of Agulhas leakage in the model from the thermohaline properties of the flux at the GoodHope line. Assuming that the water mass which constitutes Agulhas

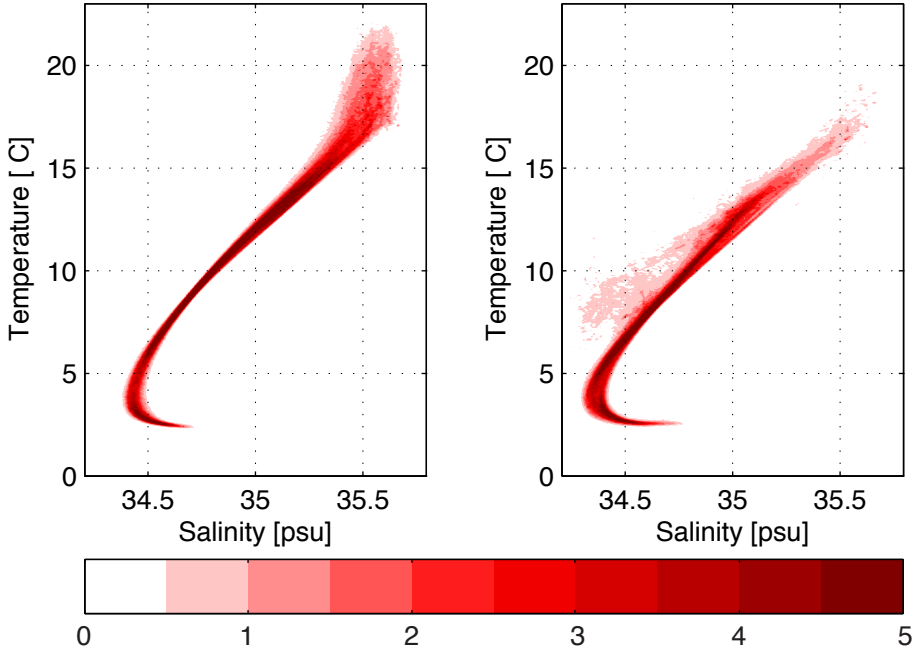


Figure 7.3: The distribution of transport by the numerical Lagrangian floats as a function of temperature and salinity of the water at the location where the floats cross the 19°E section (left panel) and the GoodHope line (right panel), in 10^{-3} sverdrup per $0.01 \text{ psu} \times 0.05^\circ\text{C}$ grid cell. A large fraction of the warm and saline thermocline water at the Agulhas Current retroflexion has freshened and cooled on its path through the Cape Basin.

leakage is the warmest and most saline water at the GoodHope line, integration of the flux of water warmer than a certain threshold temperature Θ and more saline than a threshold salinity Σ might facilitate the discrimination between fluxes from the Indian Ocean and fluxes from the other two oceans. This Eulerian flux as a function of threshold temperature and threshold salinity can be written as

$$F_{\Theta\Sigma} = \int_{\theta=\Theta}^{\infty} \int_{\sigma=\Sigma}^{\infty} V(\theta, \sigma) d\sigma d\theta \quad (7.1)$$

where $V(\theta, \sigma)$ is the flux through all grid cells with temperature θ and salinity σ .

This method leads to fluxes $F_{\Theta\Sigma}$ as a function of threshold temperature, threshold salinity, and time (Fig. 7.4). For any combination of Θ and Σ , the method yields an underestimation of the mean magnitude of Agulhas leakage, as the mean flux never gets above 10 Sv and $F_{\Theta\Sigma}$ is even negative for low Θ and Σ . Integration is in that case then effectively over the whole GoodHope line,

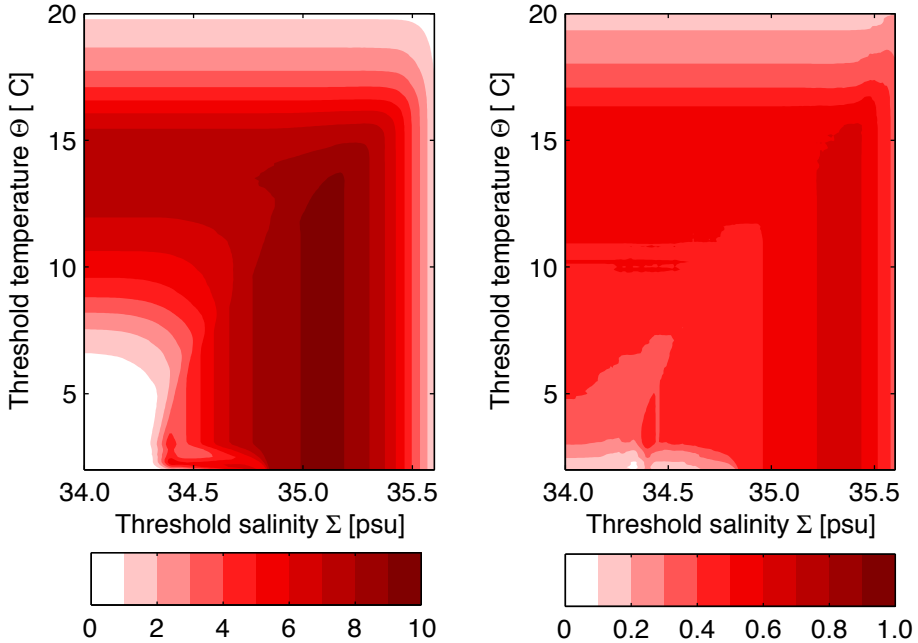


Figure 7.4: The flux $F_{\Theta\Sigma}$ into the Atlantic Ocean over the GoodHope line when integration is done only over grid cells which are warmer and more saline than a certain threshold temperature Θ and threshold salinity Σ . The mean leakage as a function of these thresholds (left panel, in sverdrup) and the correlation with the float-determined time series of Agulhas leakage time series as a function of these thresholds (right panel). The mean flux of Agulhas leakage is never above 10 Sv, which is considerably lower than the mean float-determined Agulhas leakage leakage F_{AL} . The optimum thermohaline threshold values are these values Θ_0 and Σ_0 where the correlation is maximum.

which apparently has a mean flux into the Indian Ocean (due to the eastward transport of the Antarctic Circumpolar Current).

The variability of the Eulerian time series, on the other hand, is much better captured by this method. The maximum correlation between the time series of the Eulerian flux and the Lagrangian transport is 0.62, which is significantly different from zero at the 95% confidence level. This occurs for $\Theta_0 = 14.6^\circ\text{C}$ and $\Sigma_0 = 35.33$ psu. As we are mainly interested in capturing the variability of Agulhas leakage in an Eulerian estimate, these values represent the optimum thermohaline threshold values in this model. The mean Eulerian flux $F_{\Theta_0\Sigma_0}$ (7.7 Sv) is approximately half of the magnitude of the Lagrangian Agulhas leakage. This might be a reasonable estimate of the amount of Agulhas leakage in the thermocline, as it is close to the 9 – 10 Sv estimate of thermocline interocean exchange by *Gordon et al. [1987]* and *Gordon et al. [1992]*.

Note that these optimum thermohaline threshold values do not necessarily have to mean that all water at the GoodHope line warmer than 14.6°C and

more saline than 35.33 psu is Agulhas leakage water; it only means that at Θ_0 and Σ_0 the correlation of the time series is largest. However, the greatest part of this warm and saline water in the model does seem to originate from the Agulhas Current. The transport by floats within water above these thresholds is 6.2 Sv, while the flux of all water above these thresholds is the aforementioned 7.7 Sv. This means that the warm and saline water at the GoodHope line is to a large extent ‘pure’ Agulhas leakage water.

The correlation between the magnitude of the float-determined Agulhas leakage and the Eulerian flux determined by this water mass analysis is relatively sensitive to Σ (Fig. 7.4). It is however not so sensitive to Θ . Apparently, at the GoodHope line in the model, water that is more saline than Σ_0 is generally also warmer than Θ_0 so the integration domain is controlled by the isohalines rather than the isotherms (Fig. 7.5). An explanation for this domination of salinity over temperature might be that the impact of the atmosphere on the temperature of the Agulhas leakage water is much higher than the impact on its salinity. On its journey through the Cape Basin, the Indian Ocean water is more efficiently cooled than freshened. At the GoodHope line, therefore, the Agulhas leakage is probably better identified by its salinity than by its temperature.

Unfortunately, this domination of the salinity signal means that monitoring the magnitude of Agulhas leakage at the GoodHope line with only XBTs (expendable sensors which measure temperature as a function of depth) is not feasible. The optimum thermohaline threshold domain appears to follow salinity much closer than temperature so that salinity information is indispensable (Fig. 7.5). A monitoring of $F_{\Theta_0\Sigma_0}$ would thus require either a mooring array equipped with CTDs or an extensive vessel-based CTD program. The optimum thermohaline threshold domain is maximally 500 m deep and 1700 km wide (Fig. 7.6). At the 50 km resolution used in this analysis, such a monitoring program would require in the order of 34 CTD stations or moorings.

Despite the underestimation of the magnitude of Agulhas leakage when the $\Theta_0 = 14.6^\circ\text{C}$ and $\Sigma_0 = 35.33$ psu optimum thermohaline threshold values are used, it appears that the total magnitude of Agulhas leakage can to a reasonable extent be estimated from $F_{\Theta_0\Sigma_0}$. In order to reduce noise, the Eulerian flux and the Lagrangian transport are binned to monthly values (compare with Eq. (5.2) and Eq. (6.2)):

$$T_X(t) = \langle F_X(t) \rangle \quad (7.2)$$

where X is either AL or $\Theta\Sigma$ and $\langle \dots \rangle$ is the 30 days binning operator.

The correlation between the smoothed float-determined transport T_{AL} and the smoothed threshold-determined flux $T_{\Theta_0\Sigma_0}$ is even larger than for the unsmoothed time series, at 0.80 (Fig. 7.4). The resulting linear regression can be used to form an estimate of the total magnitude of Agulhas leakage using the flux of warm ($\theta > \Theta_0$) and saline ($\sigma > \Sigma_0$) water (compare with Eq. (5.4) and

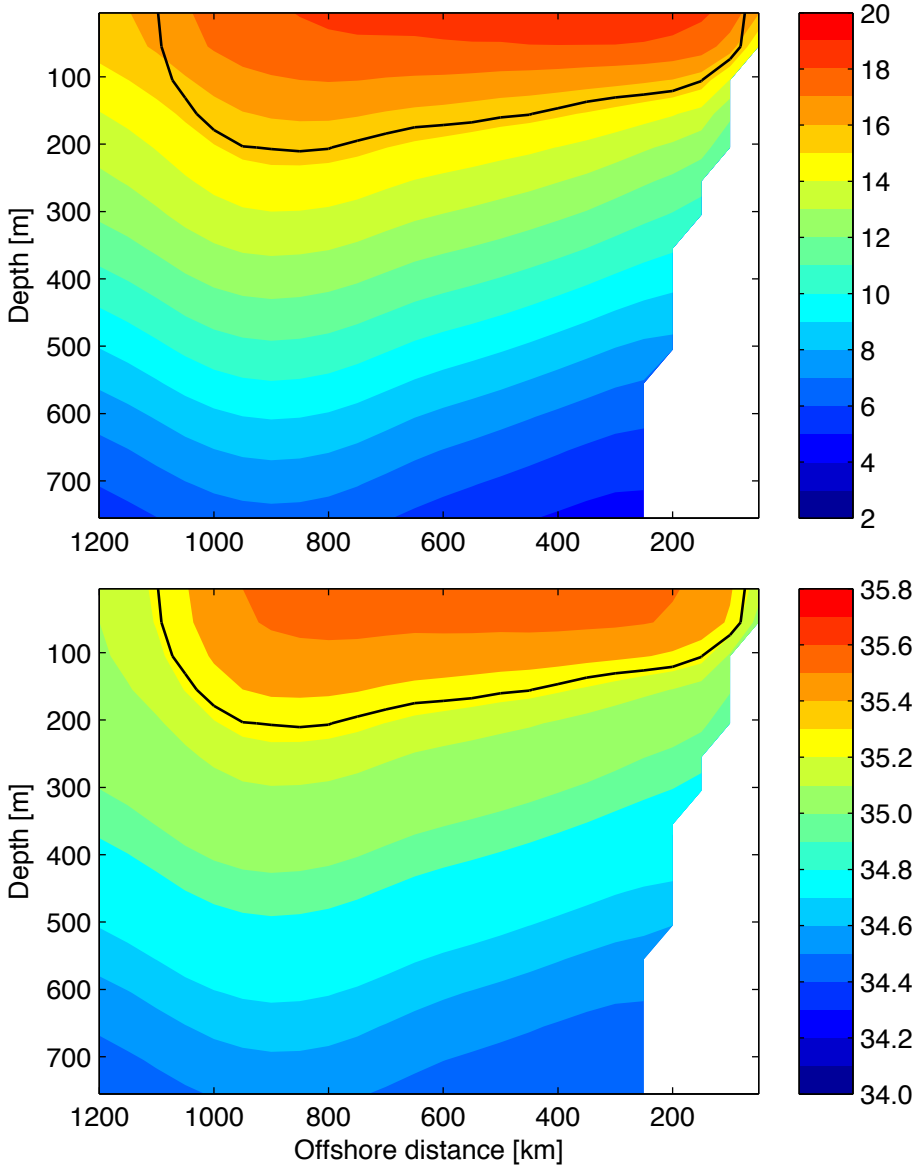


Figure 7.5: The mean temperature (colored patches in the upper panel, in $^{\circ}\text{C}$) and salinity (colored patches in the lower panel, in psu) in a subregion of the vertical plane at the GoodHope line over the 37 years integration period. The solid black lines indicate the mean of the sub-plane where both the temperature is above $\Theta_0 = 14.6^{\circ}\text{C}$ and the salinity is above $\Sigma_0 = 35.33$ psu, the threshold values where the correlation between $F_{\Theta\Sigma}$ and F_{AL} is highest. Note that this domain seems to follow isohalines rather than isotherms.

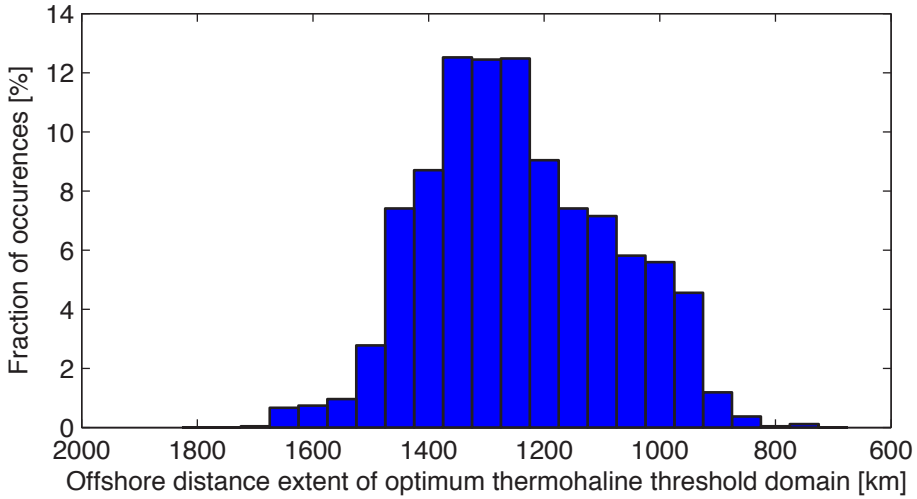


Figure 7.6: The histogram of the offshore extent of the optimum thermohaline threshold domain. The offshore extent varies over time, and to always be able to capture it a CTD section should extent 1700 km offshore. At a 50 km horizontal spacing, this requires 34 CTD-casts or moorings.

Eq. (6.3):

$$E_{AL} = \alpha T_{\Theta_0 \Sigma_0} + \beta \quad (7.3)$$

where the fitting parameters $\alpha = 2.0$ and $\beta = 1.9$ Sv are obtained from the best fit of the monthly means in Fig. 7.7.

The skill of this estimate can be quantified by assigning a confidence band to the linear estimate. As a first approximation, a confidence band (a constant offset from the best linear fit) is chosen such that 90% of the data points lie within the confidence band. This is similar to the method employed in section 5.5, but it is different from the method employed in section 6.3 where the confidence level of the best fit was used. Here, because the goal is to devise an optimal estimation strategy, the skill of the method is determined by how far an estimate is from the true leakage and this is quantified by the confidence band.

The 90% confidence band results in an uncertainty of 11.6 Sv in the estimate. An estimate of the amount of Agulhas leakage based on flux through the optimum thermohaline threshold domain is therefore only certain within a 11.6 Sv range. This means that when $E_{AL} = 10.0$ Sv in the model, then the total flux of Agulhas leakage is with 90% confidence somewhere between 4.2 Sv and 15.8 Sv.

It is also possible to devise an Eulerian estimate similar to that of Eq. (7.3) for the unsmoothed data set. However, the signal-to-noise level is then lower. Although the correlation between the two time series in that case is still significant, the 18.9 Sv confidence band is almost double as wide (not shown).

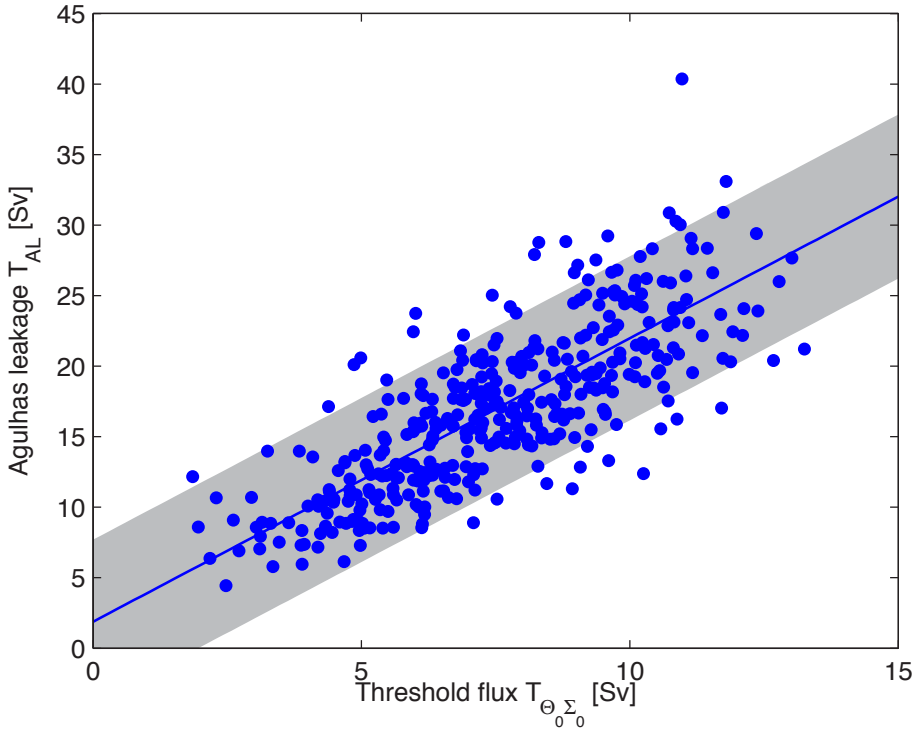


Figure 7.7: The monthly binned float-determined Agulhas leakage transport T_{AL} versus the monthly binned Eulerian flux $T_{\Theta_0 \Sigma_0}$ using the optimum thermohaline threshold values (dots), both at the GoodHope line. The correlation between the data sets is 0.80, which is significant at the 95% confidence level. The blue line is the best linear fit and the gray area indicates the estimated confidence level so that 90% of the data points fall within the area. The confidence band width (the height of the gray area) is 11.6 Sv, and the slope of the best fit line is 2.0.

This wide band limits the usability of the estimate. The advantage of the unsmoothed time series, however, is that it can more conveniently be measured using a vessel-based CTD program.

7.5 An optimum Euclidean integration method

Although it appears that within the model the magnitude of Agulhas leakage at the GoodHope line can to some extent be estimated using a linear regression, it might be somewhat disappointing that this Eulerian method can sample only half of the amount of Agulhas leakage directly. The high agreement between the Eulerian flux and the Lagrangian transport in the top-east part of the GoodHope line (Fig. 7.1) suggests that this fraction might be enhanced.

For this reason, a second and more straightforward approach to estimate the

magnitude of Agulhas leakage in an Eulerian way is introduced. The method is based on limiting the integration domain to a rectangular subregion of the GoodHope line. Since the Eulerian flux and the Lagrangian transport are so similar near the continent, we expect that one of the corners of this subregion must be located at the sea surface ($z = 0$) at the African coast ($x = 0$). The diametrically opposed corner is defined to be at depth Z and offshore distance X . This method yields an Eulerian flux time series F_{XZ} , which can be written in a way similar to $F_{\Theta\Sigma}$ in Eq. (7.1) as

$$F_{XZ} = \int_{x=0}^X \int_{z=0}^Z V(x, z) dz dx \quad (7.4)$$

where $V(x, z)$ is the flux through the grid cell at offshore distance x and depth z . Again, the goal is to find the X and Z where F_{XZ} is in best agreement with the time series of float-determined Agulhas leakage transport F_{AL} .

The mean of F_{XZ} is approximately equal to the mean of F_{AL} in a large U-shaped band between 700 km and 1500 km offshore (upper panel of Fig. 7.8). Closer to the coast, the Eulerian flux into the Atlantic Ocean is smaller than the mean of the float-determined time series, whereas farther offshore the eastward velocities in the Antarctic Circumpolar Current result in a negative mean of F_{XZ} . For large parts of the deep ocean, where the means of the Eulerian flux and the Lagrangian transport are approximately equal, the variability in F_{XZ} is too large (middle panel of Fig. 7.8). This is related to the barotropic nature of the velocity profile at the GoodHope line in contrast to the more baroclinic float-determined Agulhas leakage transport (Fig. 7.1).

The optimum Euclidean integration area in the model is defined as the values X_0 and Z_0 where the root mean square difference between the Eulerian and Lagrangian time series is smallest. The root mean square distance is used as a measure instead of correlation because we want to directly measure the magnitude of Agulhas leakage and not estimate it through a linear regression. In the model the minimum root mean square distance (5.7 Sv) is located at $Z_0 = 300$ m and $X_0 = 900$ km (lower panel of Fig. 7.8). Note that the root mean square difference quickly increases for $Z > 300$ m but that the sensitivity with respect to X is smaller as long as the velocity integration is not extended into the Antarctic Circumpolar Current at $X = 1800$ km.

Similar to the approach followed in Eq. (7.2) and Eq. (7.3), another Eulerian estimate E_{AL} can be constructed by using a 30 day binned averages of $F_{X_0Z_0}$. However, because X_0 and Z_0 are chosen such that almost all of the flux of Agulhas leakage is captured by integrating over the optimum Euclidean integration area, the parameters are fixed to $\alpha = 1$ and $\beta = 0$ Sv.

The correlation between the monthly binned float-determined Agulhas leakage transport T_{AL} and the integrated velocities $T_{X_0Z_0}$ is 0.49, which is significantly different from zero at the 95% confidence level (Fig. 7.9). Since this correlation is lower here than in the optimum thermohaline threshold method, the confidence band is almost twice as wide at 19.6 Sv. So although the mean

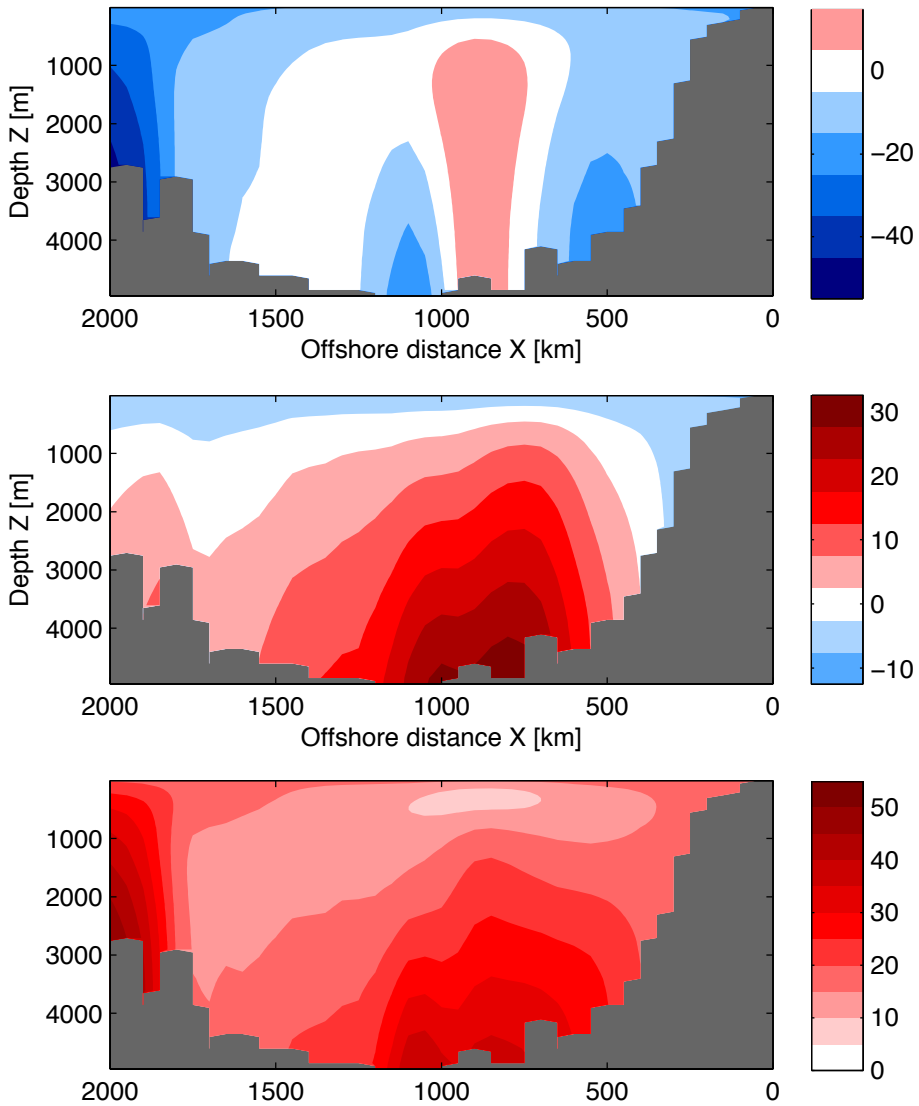


Figure 7.8: Comparison of the Eulerian flux time series F_{XZ} and Lagrangian leakage time series F_{AL} at the GoodHope line. Integration starts at the sea surface at the African continent, and ends at a point (X, Z) on the vertical plane. For each of these points, the mean difference between the time series (upper panel), the difference of the standard deviations between the time series (middle panel), and the root mean square difference between the time series (lower panel) are shown in sverdrup. The F_{XZ} time series is in best agreement with the F_{AL} time series for $Z_0 = 300$ m and $X_0 = 900$ km.

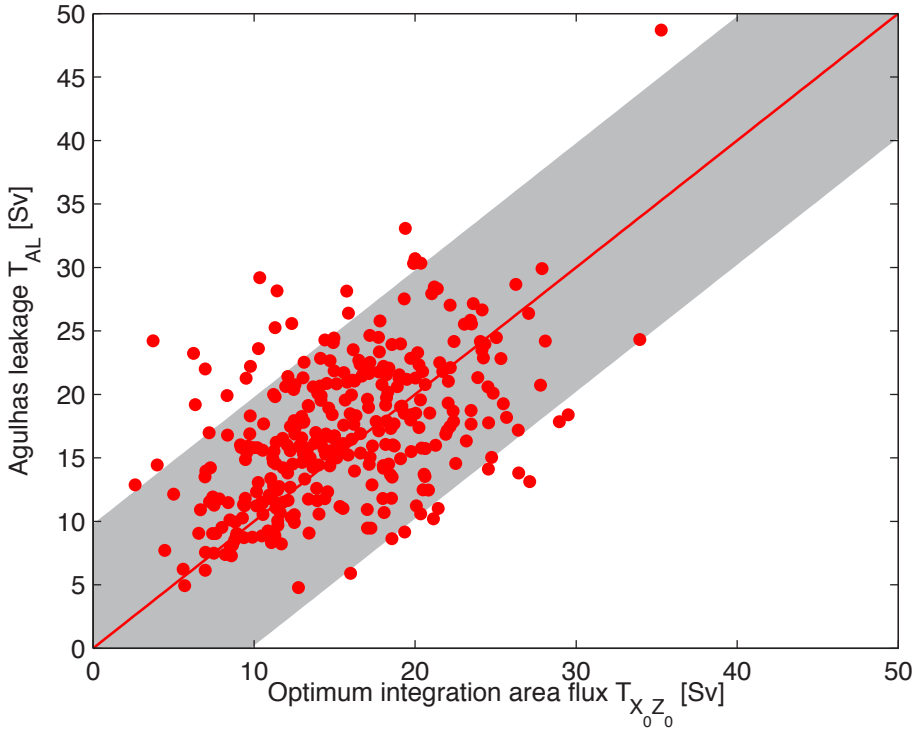


Figure 7.9: The monthly binned float-determined Agulhas leakage transport T_{AL} versus the monthly binned Eulerian flux $T_{X_0 Z_0}$ using the optimum Euclidean integration area (dots), both at the GoodHope line. The correlation between the data sets is 0.49, which is significant at the 95% confidence level. The red line is the one-to-one line, and the gray area denotes the 90% confidence band (of width 19.6 Sv), chosen such that 90% of the points fall within the gray area.

Eulerian flux is closer to the float-determined Agulhas leakage transport when the optimum Euclidean integration method is used, the estimate constructed in this way is less skillful.

At horizontal and vertical resolutions of 50 km and 50 m respectively, the optimum Euclidean integration area can be covered in the real ocean by 18 moorings carrying only an ADCP at the top. That is, of course, if the results from the Eulerian and Lagrangian fields in the AG01 model can be translated to the real ocean. As the root mean square difference quickly increases when Z_0 is changed, application of this Eulerian method is sensitive to the details of the distribution of Agulhas leakage over the GoodHope line. As discussed in chapter 2, the AG01 model does not perform extremely well at the GoodHope line. Although it can not be concluded that the model has no skill at this location, the trajectories of the numerical floats in the upper 15 m are slightly too far offshore when compared to the trajectories of drifting buoys in the real ocean.

This offshore model bias might translate in an offshore bias of the optimum Euclidean integration area, which will have implications for the constructed Agulhas leakage flux estimate.

7.6 Conclusions and discussion

An attempt has been made to devise an Eulerian measurement strategy for estimating the magnitude of Agulhas leakage in the real ocean. This has been done by relating the Eulerian (velocity-based) fluxes over the GoodHope line to the ‘true’ time series of Agulhas leakage transport as obtained from numerical Lagrangian floats.

The difficulty with such an Eulerian method lies in posing the integration boundaries. An optimum has to be found between a too small integration domain (which does not capture all Agulhas leakage transport) and a too large domain (which introduces spurious fluxes from other sources than the Indian Ocean). Two methods for finding the optimum integration boundaries have been tested. In the first method, integration is limited to a subdomain of thermohaline (temperature – salinity) space. Since Indian Ocean water is generally warmer and more saline than Atlantic Ocean and Southern Ocean water, integration of velocities is limited to grid cells where the water is warmer and more saline than the optimum thermohaline threshold values $\Theta_0 = 14.6^\circ\text{C}$ and $\Sigma_0 = 35.33$ psu. The time series obtained in this way has an 0.62 correlation with the true Agulhas leakage transport time series. In the model, these water masses extend until at most 1700 km offshore so that it requires more than 30 CTD profiles at 50 km spacing to completely capture the flux.

Another way to find the optimum integration boundaries is by optimizing the time series in Euclidean (offshore distance – depth) space. In this method, the velocity is only integrated over a subregion of the vertical plane at the GoodHope line. The method yields an empirically determined optimum Euclidean integration area, an area where the root mean square distance between the float-determined Agulhas leakage transport and the velocity-integrated flux is smallest. This is the case when integration is confined to water shallower than $Z_0 = 300$ m and closer to the coast than $X_0 = 900$ km. The time series this yields has an 0.49 correlation with the true Agulhas leakage transport time series. At the resolution used for this analysis, the area can be covered in the real ocean by an array of 18 ADCPs.

Although this second method works well in this model, it is not sure what its skill is in other models or in the real ocean. The shape of the optimum Euclidean integration area will depend on the details of the circulation in the Cape Basin, which are reasonably well resolved in the model (see chapter 2 and *Biastoch et al.* [2008c]). Since the skill of the optimum Euclidean integration method quickly deteriorates when the area of integration is changed, this method requires calibration by an independently obtained time series of Agulhas leakage transport. The best way to obtain such an independent time series

of Agulhas leakage transport is by performing a Lagrangian experiment. However, the costs of deploying millions of floats is so high that this is unfeasible in the real ocean.

In principle this calibration problem also holds for the thermohaline method, but we expect that it is not as important. The thermohaline method depends not on the details of the local circulation in the Cape Basin, but on the temperature and salinity characteristics of the different oceans. These large-scale patterns are probably better resolved in the model than the small-scale eddy field and therefore we have more confidence in the universality of Θ_0 and Σ_0 than in the universality of X_0 and Z_0 .

The thermohaline method leads to a mean Eulerian flux $F_{\Theta_0\Sigma_0}$ which is only half of the mean float-determined Agulhas leakage transport F_{AL} , although the time series of F_{AL} and $F_{\Theta_0\Sigma_0}$ are highly correlated. The mean Eulerian flux based on the optimum Euclidean integration area $F_{X_0Z_0}$, on the other hand, is only a few sverdrups lower than the mean of F_{AL} . Nevertheless, the thermohaline method leads to a more skillful estimate E_{AL} of the monthly mean magnitude of Agulhas leakage than the optimum Euclidean integration method, with confidence bands of 11.6 Sv and 19.6 Sv, respectively. This is probably because the first method is based on the well-established water mass analysis, whereas the second method is purely empiric.

All in all, this study indicates that it may be feasible to make a reasonably accurate estimate of the magnitude of Agulhas leakage at monthly resolution. This can be achieved by deploying a mooring array at the GoodHope line, where temperature, salinity, and velocity are measured within the thermocline. Something like the TOGA-TAO array [Hayes *et al.*, 1991], but in the Agulhas region rather than the equatorial Pacific Ocean.

Chapter 8

Conclusions: Assessing Agulhas leakage in the real ocean

8.1 Comprehending Agulhas leakage

The subject central to this dissertation is the assessment of Agulhas leakage, the volume of water in the Agulhas Current that ends in the Atlantic Ocean. Such an assessment is, among other reasons, needed because the magnitude of Agulhas leakage is related to the formation rate of North Atlantic Deep Water (see also section 1.1). The latter controls to a large extent the Atlantic meridional overturning circulation. A sustained observational program in which the magnitude and variability of Agulhas leakage is monitored might thus, somewhat similar to the purpose of the RAPID program in the Atlantic Ocean [*Hirschi et al.*, 2003], enable early detection of rearrangements in the Atlantic Ocean circulation.

Before an observational Agulhas leakage monitoring program can be designed, a thorough understanding of the mechanisms governing the Agulhas system in general and the magnitude of Agulhas leakage in particular is required. The subtleties of the system are by no means completely understood, despite the more than thirty years of extensive scientific research on the topic.

From a numerical modeling perspective, the Agulhas region is challenging. The regional circulation is intertwined with three other large-scale circulation systems and at the same time critically dependent on the details of the bathymetry. Even high-resolution numerical models have ample problems in simulating the magnitude of Agulhas leakage (see chapter 2). The extremely low leakage of only 1.5 Sv in the assimilative Global NCOM is typical in this respect.

But also from a dynamical oceanographic perspective, most aspects of Ag-

ulhas leakage are still somewhat of a conundrum. There has long been a debate about the manifestation of Agulhas leakage, the types of features in which it is carried. Historically, the leakage was assumed to be mainly captured within Agulhas rings. Recently, however, many authors find that Agulhas leakage manifests itself in different structures: rings, cyclones, filaments, and maybe even the background flow (see section 1.5.5).

The confusion seems to partly be related to the particular definition of Agulhas leakage used. Once the Indian Ocean water has separated from the Agulhas Current retroflection, only its volume is preserved. All other properties (e. g. temperature, salinity, and relative vorticity) are modified in the Cape Basin due to mixing. For the thermohaline properties of the Agulhas leakage, this is shown in section 7.4. The modulation of relative vorticity is discussed in chapter 3, where it is shown that the greatest part of the Agulhas leakage appears to detach from the Agulhas Current in ring shedding events. These rings, however, quickly decay and hence the amount of Agulhas leakage within non-rotating water increases away from the Agulhas Current retroflection. This decay is relevant for the impact of Agulhas leakage on climate, as the water outside Agulhas rings flows more northward in the Benguela Current and that part of the Agulhas leakage will have a larger probability of crossing the equator [Donners and Drijfhout, 2004] and thus affecting the Atlantic meridional overturning circulation.

Nevertheless, although most properties of the Agulhas leakage depend on where the measurement is performed, the magnitude of Agulhas leakage is fixed. As long as an appropriate definition for Agulhas leakage is used (based on the volume of water remaining in the Atlantic Ocean on a time scale of years), the mean Agulhas leakage is not very much affected by the location where the transport is determined. Most historical estimates of the magnitude of Agulhas leakage (Tab. 1.1) can therefore to a large extent be compared, even though the volume transports are measured using different methods and at different locations.

Not only the downstream fate of Agulhas leakage once it enters the Cape Basin is examined in this dissertation, we have also investigated the mechanisms upstream of the Agulhas Current retroflection that control the magnitude of Agulhas leakage. There seem to be a number of causal relations between rearrangements of the circulation in the Agulhas system and the magnitude of Agulhas leakage.

The relation between the westward extent of the Agulhas Current retroflection and the magnitude of Agulhas leakage is one of these causal relations (chapter 5). On frequencies below individual ring shedding events, a more westward retroflection leads to enhanced leakage. The large differences in leakage in the three models used for the skill assessment in chapter 2 might partly be attributed to this relation. The low-leakage Global NCOM has a mean retroflection location which is too far eastward, while the high-leakage ORCA model has a mean retroflection which is too far westward. The correlation between the mean westward extent of the Agulhas Current retroflection and the mean

	Retroflexion loc.	Agulhas Current	GoodHope line
Method	Altimetry data	Current meter array	CTD array
Binning period	Three months	Two years	One month
Confidence band	15 Sv	± 2 Sv	12 Sv
Correlation	-0.48	-0.67	0.80
Chapter	5	6	7

Table 8.1: A summary of the three methods to estimate the magnitude of Agulhas leakage in the real ocean presented in this dissertation. See the appropriate chapters for an extensive discussion of the methods. All three correlations are significantly different from zero at the 90% confidence level. Since each of the methods has advantages and disadvantages, a hypothetical future monitoring strategy could best be a combination of the three methods.

magnitude of Agulhas leakage in the three models is 0.99.

Another causal relation is the anticorrelation between Agulhas Current strength and the magnitude of Agulhas leakage. This was already suggested by *Ou and De Ruijter* [1986] and is here demonstrated and quantified in a high-resolution numerical ocean model (chapter 6). The relation between inertia, outcropping, and overshoot of the Agulhas Current is fundamental to the vorticity dynamics of a western boundary current in general and the Agulhas Current in particular.

8.2 Estimating the magnitude of Agulhas leakage

One of the general conclusions which might be drawn from this dissertation is that it appears very difficult to directly determine the magnitude and variability of Agulhas leakage in the real ocean with sufficient accuracy. Only an extensive and dedicated float release program in the Agulhas Current, employing thousands of floats, may facilitate a direct measurement of the magnitude of Agulhas leakage. However, there might be several methods to indirectly estimate (instead of directly measure) the magnitude of Agulhas leakage from indirect data.

Three of the methods to obtain such data are discussed in the chapters 5, 6, and 7 (Tab. 8.1). They are all based on a significant linear relation in the $1/10^\circ$ two-way nested AG01 model between the magnitude of Agulhas leakage and a more easily determinable quantity. Each of the three methods has its advantages and disadvantages with respect to the quality of the leakage estimate. The trade-off is generally between the accuracy and the temporal resolution of a method: A monitoring array in the Agulhas Current has the narrowest confidence band but requires the longest averages while a mooring array at the GoodHope line yields monthly estimates of the magnitude of Agulhas leakage but with much higher uncertainty.

In general, a monitorable quantity farther away from the GoodHope line

means that there is a longer time lag between the GoodHope line and the location where the monitoring is performed. This lag is not uniform for all floats (partly because of the fast decay of the Agulhas rings, see chapter 3) and thus the signal-to-noise level decreases when the lag increases. More smoothing is then required and this is expressed in a longer binning period.

However, smoothing of the float-determined time series is not necessarily bad. As discussed in section 7.6, the numerical Lagrangian floats should not be regarded as deterministic water parcels ('bags of water'), each carrying a fraction of the Agulhas Current transport. Instead, the floats sample the Agulhas Current and a float is therefore representative of a certain transport. The leakage across the GoodHope line is thus a statistical quantity. Smoothing of the time series increases the number of float crossings and thereby suppresses the error level. Moreover, the time scales on which Agulhas leakage may affect the strength of the Atlantic meridional overturning circulation seem to be relatively large, at more than three years (see chapter 4 and *Biastoch et al.* [2008b]). This means that even the biennial binning method used in chapter 6 is of sufficient resolution to in principle capture changes in the Agulhas leakage that might affect the Atlantic meridional overturning circulation.

It may be somewhat surprising that the three monitoring strategies discussed here are based on simple linear relations. This despite the presumably highly nonlinear nature of the Agulhas system, where features such as Natal pulses, Agulhas ring paths, and the Agulhas Current retroflexion itself can only be explained through eddy-eddy interactions and the nonlinear advection of momentum and relative vorticity. However, the monitoring strategies developed in this dissertation are only valid in a relatively small range of Agulhas Current and Agulhas leakage transport (see also section 6.6). As shown by *Franzese et al.* [2009] in a paleoceanographic context, the relation between Agulhas Current strength and Agulhas leakage might have been very different during the Last Glacial Maximum, when the Agulhas system might have been in a completely different regime. The linear regressions on which the monitoring strategies are based might well be the leading-order terms of much more complicated nonlinear dependencies. The monitoring strategies presented here are therefore only suited for present-day monitoring studies.

Nevertheless, none of the three proposed methods for estimating the magnitude of Agulhas leakage is by itself adequate and sufficient. Their deficiencies can be related to two major complications of the Agulhas system. First of all, Agulhas leakage is only a minor flux in a region where three circulation systems meet (see also the discussion of the Agulhas stagnation point in section 1.3). One has to be very careful not to introduce spurious fluxes due to the Antarctic Circumpolar Current and the South Atlantic Ocean subtropical gyre.

Secondly, the fast decay of Agulhas rings, in combination with the vigorous mixing of water masses in the Cape Basin, causes the greatest part of the Agulhas leakage to not be in coherent structures soon after ring shedding. If most Agulhas leakage would remain inside Agulhas rings, the travel times through the Cape Basin would be more uniform and the distribution of the

lags between Agulhas ring shedding and the crossing of the GoodHope line would be narrower. Such a more uniform lag would probably make it easier to correlate Agulhas Current strength or Agulhas Current retroflection location to the magnitude of Agulhas leakage. Furthermore, if all Agulhas leakage would remain in the Agulhas rings then simple ring counting might be a much more feasible approach to estimate the magnitude of Agulhas leakage.

Although the individual monitoring strategies are not of sufficient skill and accuracy, an observational Agulhas leakage monitoring program which integrates multiple monitoring strategies might be adequate. However, the question which should be asked first is how important it is to accurately and on high temporal resolution know the magnitude of Agulhas leakage. What would happen if the mean magnitude of Agulhas leakage is found to be 8 Sv instead of 15 Sv? Will that change our view on the role of the Agulhas system in the world ocean? Probably not, as the interocean transport is relatively irrelevant as long as the magnitudes of the net heat and salt fluxes are unknown (see also section 1.2). Apart from a small contribution by the radiation of baroclinic energy, the effect of the volume of Indian Ocean water on the Atlantic meridional overturning circulation is limited. Any revision in the mean magnitude of Agulhas leakage can be compensated for by a proposed change in thermohaline fluxes so that the net fluxes of heat and salt do not change. As the magnitude of these fluxes will probably remain unknown for a while, this can always be legitimized.

However, for the purpose of gauging northern Atlantic Ocean climate fluctuations, the variability in Agulhas leakage is much more important than the mean magnitude. A sudden increase in the frequency of early retroflections would be a signal that the interocean exchange is decreasing. These high-impact events are the most relevant and justify the monitoring of the magnitude of Agulhas leakage.

The difficulties in estimating the magnitude of Agulhas leakage from the three methods described here lie mainly in the area of quantifying the relation between the magnitude of Agulhas leakage and its monitorable quantity (either Agulhas Current strength, westward extent, or Eulerian flux). Qualitatively, however, the three relations are robust. If one is interested only in the variability of Agulhas leakage, therefore, the quantitative relations might be disregarded. In that case, dramatic changes in the magnitude of Agulhas leakage could simply be recognized by monitoring the westward extent of the Agulhas Current retroflection from satellite altimetry.

On the other hand, an accurate magnitude of Agulhas leakage is an important measure for model validation purposes. The amount of water flowing from the Indian to the Atlantic Ocean is so intertwined with all aspects of the Agulhas system that the magnitude of Agulhas leakage may be regarded as a crucial test for any modelers interested whether their models are skillful in the region.

8.3 Outlook

What would an ideal monitoring program design look like? This is a difficult question to answer, as it depends on the funds available. The data from the existing satellite altimetry programs could for almost no cost be used for observing the westward extent of the Agulhas Current retroflexion, with the advantage that almost twenty years of data are already available. This may thus be the basis for an oceanic index of Agulhas leakage. But the accuracy of an altimetry-based monitoring program will in general not be sufficient, given the 15 Sv uncertainty in the estimates.

One of the ways to increase the accuracy of a monitoring program is to augment it with a mooring array in the Agulhas Current. Such an array needs to consist of only six individual moorings. The uncertainty in the relation between Agulhas Current strength and the magnitude of Agulhas leakage is not more than 2 Sv (Fig. 6.1), which will give a boost to the accuracy of the program. However, this relation is only significant at interannual time scales, so that an Agulhas Current mooring program must be sustained for a long period.

Another option to increase the accuracy of a monitoring program is to measure the flux of warm and saline water over the GoodHope line. The advantage of this method is that the temporal frequency is relatively high at once per month, so that changes in Agulhas leakage magnitude will quickly be detected. However, the costs of such an array will be highest of all three methods since more than 30 moorings are required.

One might rightly respond to the relations which form the basis of each of these three methods as being unproven for application in the real ocean, since they are only tested within a model context. Although the AG01 model is probably the best model available in the Agulhas region, the skill of the estimates when applied in the real ocean is totally unknown. Although the model has throughout this dissertation been validated to real ocean data, the model is in some respect only tested to itself.

One way to increase the confidence in the model results is by performing similar experiments as the ones described here in an assimilative ocean circulation model. In principle, assimilation of observations such as satellite data should enhance the skill of an ocean model. In this case, the assimilation of drifting buoy trajectories might be a direct approach to enhance the skill of the model float trajectories used to assess the Agulhas leakage. However, the model must then perform much better in the Agulhas region than the Global NCOM model, which was shown to not possess any skill despite employing a data assimilation routine (chapter 2).

The true skill of a monitoring program must not be assessed in numerical ocean models, but in the real ocean. For this, an independently obtained observational time series of the magnitude of Agulhas leakage would be needed. Such an independent estimate could come from comparison of the three methods, but it might be better to set up a Lagrangian experiment similar to what

was done in this dissertation in a model context. However, setting up such a Lagrangian experiment in the real ocean is not easy even when it is used only for calibration of the program and thus has to operate only for a short period. The number of floats or drifters required for an accurate estimate will be in the order of thousands, and this is orders of magnitude larger than the typical 40 – 50 RAFOS floats used in other observational float projects [e.g. *Boebel et al.*, 2003a; *Bower et al.*, 2009].

However, there might be setups other than using floating instruments for (semi-)Lagrangian experiments in the real ocean. The planktic foraminiferal indigenous to the Indian Ocean which were studied in sediment cores by *Peeters et al.* [2004] could be regarded as Lagrangian floats, as these are organisms advected into the Atlantic Ocean with the Agulhas leakage. If the concentration of these organisms could be related to volume flux of the Agulhas Current then the flux of such species might yield a Lagrangian estimate of the magnitude of Agulhas leakage.

Another way to obtain a Lagrangian estimate of the magnitude of Agulhas leakage is by measuring the (isotopic) concentration of chemical tracers. Such a method was used by *Fine et al.* [1988] and *Gordon et al.* [1992], who measured the concentration of isotopes of chlorofluoromethanes in the Cape Basin. As the different source regions of the Cape Basin have different isotopic signatures, it appears to be possible to unravel the flux from the Indian Ocean from other sources. However, the skill of this method will be influenced by the vigorous mixing in the area, just as was the case with the method of integrating fluxes above some temperature-salinity characteristic (section 7.4).

Coming back to the central question of this dissertation (section 1.9), it seems to be possible to assess the magnitude of Agulhas leakage in the real ocean. This can best be achieved in an integrated approach, where satellite altimetry data is augmented by a mooring array at either the Agulhas Current or the GoodHope line. The combined estimate should then be calibrated by an independent Lagrangian estimate of the magnitude of Agulhas leakage based on biological or chemical tracers. Such a program may yield the opportunity to monitor Agulhas leakage and might even be the basis for an Agulhas leakage index.

Bibliography

- Anderson, D. L. T. and P. B. Rowlands (1976), The role of inertia-gravity and planetary waves in the response of a tropical ocean to the incidence of an equatorial Kelvin wave on a meridional boundary, *J. Mar. Res.*, *34*, 295–312.
- Andersson, H. C. and G. Veronis (2004), Thermohaline circulation in a two-layer model with sloping boundaries and a mid-ocean ridge, *Deep Sea Res. I*, *51*, 93–106.
- Ansorge, I. J., S. Speich, J. R. E. Lutjeharms, G. J. Goni, C. J. Rautenbach, P. W. Froneman, M. Rouault, and S. L. Garzoli (2005), Monitoring the oceanic flow between Africa and Antarctica: Report of the first GoodHope cruise, *S. African J. Science*, *101*, 29–35.
- Arhan, M., H. Mercier, and Y.-H. Park (2003), On the deep water circulation of the eastern South Atlantic Ocean, *Deep Sea Res. I*, *50*, 889–916.
- Baker-Yeboah, S. (2008), *Sea surface height variability and the structure of eddies in the South Atlantic Cape Basin*, Ph.D. thesis, University of Rhode Island.
- Bang, N. D. and W. R. H. Andrews (1974), Direct current measurements of a shelf-edge frontal jet in the southern Benguela system, *J. Mar. Res.*, *32*, 405–417.
- Bard, E. and R. E. M. Rickaby (2009), Migration of the subtropical front as a modulator of glacial climate, *Nature*, *460*, 380–383.
- Barnier, B. (1988), A numerical study of the Mid-Atlantic Ridge on nonlinear first-mode baroclinic Rossby waves generated by seasonal winds, *J. Phys. Oceanogr.*, *18*, 417–433.
- Barron, C. N., A. B. Kara, P. J. Martin, R. C. Rhodes, and L. F. Smedstad (2006), Formulation, implementation and examination of vertical coordinate choices in the Global Navy Coastal Ocean Model (NCOM), *Ocean Model.*, *11*, 347–375.
- Barron, C. N., L. F. Smedstad, J. M. Dastugue, and O. M. Smedstad (2007), Evaluation of ocean models using observed and simulated drifter trajectories: Impact of sea surface height on synthetic profiles for data assimilation, *J. Geophys. Res.*, *112*, C07019.
- Beal, L. M. and H. L. Bryden (1997), Observations of an Agulhas Undercurrent, *Deep Sea Res. I*, *44*, 1715–1724.
- Beal, L. M. and H. L. Bryden (1999), The velocity and vorticity of the Agulhas Current at 32°S, *J. Geophys. Res.*, *104*, 5151–5176.
- Beal, L. M., T. K. Chereskin, Y. D. Lenn, and S. Elipot (2006), The sources and mixing characteristics of the Agulhas Current, *J. Phys. Oceanogr.*, *36*, 2060–2074.
- Behera, S. K., J. Luo, and T. Yamagata (2008), Unusual IOD event of 2007, *Geophys. Res. Lett.*, *35*, L14S11.
- Beismann, J. O., R. H. Käse, and J. R. E. Lutjeharms (1999), On the influence of

- submarine ridges on translation and stability of Agulhas rings, *J. Geophys. Res.*, *104*, 7897–7906.
- Biastoch, A., L. M. Beal, J. R. E. Lutjeharms, and T. G. D. Casal (2009), Variability and coherence of the Agulhas Undercurrent in a high-resolution ocean general circulation model, *J. Phys. Oceanogr.*, *in press*.
- Biastoch, A., C. W. Böning, J. Getzlaff, J.-M. Molines, and G. Madec (2008a), Causes of interannual-decadal variability in the Meridional Overturning Circulation of the midlatitude North Atlantic Ocean, *J. Clim.*, *21*, 6599–6615.
- Biastoch, A., C. W. Böning, and J. R. E. Lutjeharms (2008b), Agulhas leakage dynamics affects decadal variability in Atlantic overturning circulation, *Nature*, *456*, 489–492.
- Biastoch, A. and W. Krauss (1999), The role of mesoscale eddies in the source regions of the Agulhas Current, *J. Phys. Oceanogr.*, *29*, 2303–2317.
- Biastoch, A., J. R. E. Lutjeharms, C. W. Böning, and M. Scheinert (2008c), Mesoscale perturbations control inter-ocean exchange south of Africa, *Geophys. Res. Lett.*, *35*, L20602.
- Blanke, B. and S. Raynaud (1997), Kinematics of the Pacific Equatorial Undercurrent: An Eulerian and Lagrangian approach from GCM results, *J. Phys. Oceanogr.*, *27*, 1038–1053.
- Boebel, O. and C. N. Barron (2003), A comparison of in-situ float velocities with altimeter derived geostrophic velocities, *Deep Sea Res. II*, *50*, 119–139.
- Boebel, O., J. R. E. Lutjeharms, C. Schmid, W. Zenk, T. Rossby, and C. N. Barron (2003a), The Cape Cauldron, a regime of turbulent inter-ocean exchange, *Deep Sea Res. II*, *50*, 57–86.
- Boebel, O., T. Rossby, J. R. E. Lutjeharms, W. Zenk, and C. N. Barron (2003b), Path and variability of the Agulhas Return Current, *Deep Sea Res. II*, *50*, 35–56.
- Boudra, D. B. and E. P. Chassignet (1988), Dynamics of Agulhas Retroflexion and ring formation in a numerical model. Part I: The vorticity balance, *J. Phys. Oceanogr.*, *18*, 280–303.
- Boudra, D. B. and W. P. M. De Ruijter (1986), The wind-driven circulation in the South Atlantic-Indian Ocean – II. Experiments using a multi-layer numerical model, *Deep Sea Res.*, *33*, 447–482.
- Bower, A. S., M. S. Lozier, S. F. Gary, and C. W. Böning (2009), Interior pathways of the North Atlantic meridional overturning circulation, *Nature*, *459*, 243–248.
- Broecker, W. S. (1997), Thermohaline circulation, the Achilles heel of our climate system: Will man-made CO₂ upset the current balance, *Science*, *278*, 1582–1588.
- Bryden, H. L., L. M. Beal, and L. M. Duncan (2005a), Structure and transport of the Agulhas Current and its temporal variability, *J. Oceanogr.*, *61*, 479–492.
- Bryden, H. L., H. R. Longworth, and S. A. Cunningham (2005b), Slowing of the Atlantic meridional overturning circulation at 25°N, *Nature*, *438*, 655–657.
- Byrne, D. A., A. L. Gordon, and W. F. Haxby (1995), Agulhas Eddies: A synoptic view using Geosat ERM data, *J. Phys. Oceanogr.*, *25*, 902–917.
- Byrne, D. A. and J. L. McClean (2008), Sea level anomaly signals in the Agulhas Current region, *Geophys. Res. Lett.*, *35*, L13601.
- Carnevale, G. F., J. C. McWilliams, Y. Pomeau, J. B. Weiss, and W. R. Young (1991), Evolution of vortex statistics in two-dimensional turbulence, *Phys. Rev. Lett.*, *66*, 2735–2737.
- Casal, T. G. D., L. M. Beal, and R. Lumpkin (2006), A North Atlantic deep-water eddy in the Agulhas Current system, *Deep Sea Res. I*, *53*, 1718–1728.

- Casal, T. G. D., L. M. Beal, R. Lumpkin, and W. E. Johns (2009), Structure and downstream evolution of the Agulhas Current system during a quasi-synoptic survey in February–March 2003, *J. Geophys. Res.*, *114*, C03001.
- Cessi, P., G. Ierley, and W. Young (1987), A model of the inertial recirculation driven by potential vorticity anomalies, *J. Phys. Oceanogr.*, *17*, 1640–1652.
- Cessi, P. and P. Otheguy (2003), Oceanic teleconnections: Remote response to decadal wind forcing, *J. Phys. Oceanogr.*, *33*, 1604–1617.
- Clark, P. U., N. G. Pisias, T. F. Stocker, and A. J. Weaver (2002), The role of the thermohaline circulation in abrupt climate change, *Nature*, *415*, 863–869.
- Clercx, H. J. H., S. R. Maassen, and G. J. F. Van Heijst (1999), Decaying two-dimensional turbulence in square containers with no-slip or stress-free boundaries, *Phys. Fluids*, *11*, 611–626.
- Conover, W. J. (1980), *Practical nonparametric statistics*, John Wiley & Sons.
- De Ruijter, W. P. M., A. Biastoch, S. S. Drijfhout, J. R. E. Lutjeharms, R. P. Matano, T. Pichevin, P. J. Van Leeuwen, and W. Weijer (1999), Indian-Atlantic interocean exchange: dynamics, estimation, and impact, *J. Geophys. Res.*, *104*, 20885–20910.
- De Ruijter, W. P. M. (1982), Asymptotic analysis of the Agulhas and Brazil current systems, *J. Phys. Oceanogr.*, *12*, 361–373.
- De Ruijter, W. P. M. and D. B. Boudra (1985), The wind-driven circulation in the South Atlantic-Indian Ocean – I. Numerical experiments in a one-layer model, *Deep Sea Res.*, *32*, 557–574.
- De Ruijter, W. P. M., H. Ridderinkhof, and M. W. Schouten (2005), Variability of the southwest Indian Ocean, *Phil. Trans. R. Soc. A*, *363*, 63–76.
- De Ruijter, W. P. M., H. M. Van Aken, E. J. Beier, J. R. E. Lutjeharms, R. P. Matano, and M. W. Schouten (2004), Eddies and dipoles around South Madagascar: formation, pathways and large-scale impact, *Deep Sea Res. I*, *53*, 383–400.
- De Ruijter, W. P. M., P. J. Van Leeuwen, and J. R. E. Lutjeharms (1999), Generation and evolution of Natal pulses: Solitary meanders in the Agulhas Current, *J. Phys. Oceanogr.*, *29*, 3043–3055.
- De Steur, L. and P. J. Van Leeuwen (2009), The influence of bottom topography on the decay of modeled Agulhas rings, *Deep Sea Res. I*, *56*, 471–494.
- De Steur, L., P. J. Van Leeuwen, and S. S. Drijfhout (2004), Tracer leakage from modeled Agulhas rings, *J. Phys. Oceanogr.*, *34*, 1387–1399.
- De Szoeké, R. A. and A. F. Bennett (1983), Microstructure fluxes across density surfaces, *J. Phys. Oceanogr.*, *23*, 2254–2264.
- De Vries, P. and K. Döös (2001), Calculating Lagrangian trajectories using time-dependent velocity fields, *J. Atmos. Ocean. Tech.*, *18*, 1092–1101.
- Debreu, L., C. Vouland, and E. Blayo (2008), AGRIF: Adaptive grid refinement in Fortran, *Comput. Geosci.*, *34*, 8–13.
- Dijkstra, H. A. and W. P. M. De Ruijter (2001a), Barotropic instabilities of the Agulhas Current system and their relation to ring formation, *J. Mar. Res.*, *59*, 517–533.
- Dijkstra, H. A. and W. P. M. De Ruijter (2001b), On the physics of the Agulhas current: steady retroreflection regimes, *J. Phys. Oceanogr.*, *31*, 2971–2985.
- Doglioli, A. M., B. Blanke, S. Speich, and G. Lapeyre (2007), Tracking coherent structures in a regional ocean model with wavelet analysis: Application to Cape Basin eddies, *J. Geophys. Res.*, *112*, C05043.
- Doglioli, A. M., M. Veneziani, B. Blanke, S. Speich, and A. Griffa (2006), A Lagrangian analysis of the Indian-Atlantic interocean exchange in a regional model,

- Geophys. Res. Lett.*, *33*, L14611.
- Donners, J. and S. S. Drijfhout (2004), The lagrangian view of South Atlantic interocean exchange in a global ocean model compared with inverse model results, *J. Phys. Oceanogr.*, *34*, 1019–1035.
- Donners, J., S. S. Drijfhout, and A. C. Coward (2004), Impact of cooling on the water mass exchange of Agulhas rings in a high resolution ocean model, *Geophys. Res. Lett.*, *31*, L16312.
- Döös, K. (1995), Interocean exchange of water masses, *J. Geophys. Res.*, *100*, 13499–13514.
- Drijfhout, S. S., C. A. Katsman, L. De Steur, P. C. F. Van der Vaart, P. J. Van Leeuwen, and C. Veth (2003), Modeling the initial, fast sea-surface height decay of Agulhas ring “Astrid”, *Deep Sea Res. II*, *50*, 299–319.
- Fennel, W. (1999), Theory of the Benguela upwelling system, *J. Phys. Oceanogr.*, *29*, 177–190.
- Feron, R. C. V., W. P. M. De Ruijter, and D. Oskam (1992), Ring shedding in the Agulhas Current System, *J. Geophys. Res.*, *97*, 9467–9477.
- Fetter, A., J. R. E. Lutjeharms, and R. P. Matano (2007), Atmospheric driving forces for the Agulhas Current in the subtropics, *Geophys. Res. Lett.*, *34*, L15605.
- Ffield, A., J. M. Toole, and D. Wilson (1997), Seasonal circulation in the South Indian Ocean, *Geophys. Res. Lett.*, *24*, 2773–2776.
- Fine, R. A., M. J. Warner, and R. F. Weiss (1988), Water mass modification at the Agulhas Retroflection: Chlorofluoromethane studies, *Deep Sea Res.*, *35*, 311–332.
- Flierl, G. A. (1981), Particle motions in large-amplitude wave fields, *Geophys. Astrophys. Fluid Dynam.*, *18*, 39–74.
- Franzese, A. M., S. R. Hemming, and S. L. Goldstein (2009), Use of strontium isotopes in detrital sediments to constrain the glacial position of the Agulhas Retroflection, *Paleoceanography*, *24*, PA2217.
- Ganachaud, A. and C. Wunsch (2000), Improved estimates of global ocean circulation, heat transport, and mixing from hydrographic data, *Nature*, *408*, 453–456.
- Garzoli, S. L. and G. J. Goni (2000), *Combining altimeter observations and oceanographic data for ocean circulations and climate studies*, chapter 5, pages 79–97, Elsevier Oceanographic Series.
- Garzoli, S. L. and A. L. Gordon (1996), Origins and variability of the Benguela Current, *J. Geophys. Res.*, *101*, 897–906.
- Gill, A. E., J. S. A. Green, and A. J. Simmons (1974), Energy partition in the large-scale ocean circulation and the production of mid-ocean eddies, *Deep Sea Res.*, *21*, 499–528.
- Gombos, D., J. A. Hansen, J. Du, and J. McQueen (2007), Theory and applications of the minimum spanning tree rank histogram, *Mon. Weather Rev.*, *135*, 1490–1505.
- Goni, G. J., S. L. Garzoli, A. J. Roubicek, D. B. Olson, and O. B. Brown (1997), Agulhas ring dynamics from TOPEX/POSEIDON satellite altimeter data, *J. Mar. Res.*, *55*, 861–883.
- Gordon, A. L. (1985), Indian-Atlantic transfer of thermocline water at the Agulhas retroflection, *Science*, *227*, 1030–1033.
- Gordon, A. L. (1986), Interocean exchange of thermocline water, *J. Geophys. Res.*, *91*, 5037–5046.
- Gordon, A. L. (2003), The brawnier retroflection, *Nature*, *421*, 904–905.
- Gordon, A. L., K. T. Bosley, and F. Aikman III (1995), Tropical Atlantic water within the Benguela upwelling system at 27°S, *Deep Sea Res. I*, *42*, 1–12.

- Gordon, A. L., J. R. E. Lutjeharms, and M. L. Gründlingh (1987), Stratification and circulation at the Agulhas Retroflection, *Deep Sea Res. A*, *4*, 565–599.
- Gordon, A. L., R. S. Susanto, and A. Field (1999), Throughflow within Makassar Strait, *Geophys. Res. Lett.*, *26*, 3325–3328.
- Gordon, A. L., R. F. Weiss, W. M. Smethie Jr., and M. J. Warner (1992), Thermocline and intermediate water communication between the South Atlantic and Indian Oceans, *J. Geophys. Res.*, *97*, 7223–7240.
- Griffies, S. M., A. Biastoch, C. W. Böning, F. O. Bryan, G. Danabasoglu, E. P. Chassignet, M. H. England, R. Gerdes, H. Haak, R. W. Hallberg, W. Hazeleger, J. Jungclaus, W. G. Large, G. Madec, A. Pirani, B. L. Samuels, M. Scheinert, A. S. Gupta, C. A. Severijns, H. L. Simmons, A.-M. Treguier, M. Winton, S. G. Yeager, and J. Yin (2009), Coordinated Ocean-ice Reference Experiments (COREs), *Ocean Model.*, *26*, 1–46.
- Hayes, S. P., L. J. Mangum, J. Picaut, A. Sumi, and K. Takeuchi (1991), TOGA-TAO: A moored array for real-time measurements in the tropical Pacific Ocean, *Bull. Am. Meteorol. Soc.*, *72*, 339–347.
- Hermes, J. C., C. J. C. Reason, and J. R. E. Lutjeharms (2007), Modeling the variability of the Greater Agulhas Current System, *J. Clim.*, *20*, 3131–3146.
- Hetland, R. D. (2006), Event-driven model skill assessment, *Ocean Model.*, *11*, 214–223.
- Hirschi, J., J. Baehr, J. Marotzke, J. Stark, S. A. Cunningham, and J. O. Beismann (2003), A monitoring design for the Atlantic meridional overturning circulation, *Geophys. Res. Lett.*, *30*, 1413.
- Howard, W. R. and W. L. Prell (1992), Late Quaternary surface circulation of the southern Indian Ocean and its relationship to orbital variations, *Paleoceanography*, *7*, 79–117.
- Huisman, S. E., M. Den Toom, H. A. Dijkstra, and S. S. Drijfhout (2009), An indicator of the multiple equilibria regime of the Atlantic meridional overturning circulation, *submitted*.
- Johnson, H. L. and D. P. Marshall (2002a), Localization of abrupt change in the North Atlantic thermohaline circulation, *Geophys. Res. Lett.*, *29*, 1083.
- Johnson, H. L. and D. P. Marshall (2002b), A theory for the surface Atlantic response to thermohaline variability, *J. Phys. Oceanogr.*, *32*, 1121–1132.
- Kamenkovitch, V. M., Y. P. Leonov, D. A. Nechaev, D. A. Byrne, and A. L. Gordon (1996), On the influence of bottom topography on the Agulhas eddy, *J. Phys. Oceanogr.*, *26*, 892–912.
- Knorr, G. and G. Lohmann (2003), Southern Ocean origin for the resumption of Atlantic thermohaline circulation during deglaciation, *Nature*, *424*, 532–536.
- Kowalik, Z. and T. S. Murty (1993), *Numerical modelling of ocean dynamics*, number 5 in Advanced Series on Ocean Engineering, World Scientific.
- Lacorata, G., E. Aurell, and A. Vulpani (2001), Drifter dispersion in the Adriatic Sea: Lagrangian data and chaotic model, *Ann. Geophys.*, *19*, 121–129.
- Large, W. G. and S. G. Yeager (2004), Diurnal to decadal global forcing for ocean and sea-ice models: the data sets and flux climatologies, NCAR Technical Note NCAR/TN-460+STR, NCAR.
- Liu, Z., L. Wa, and E. Baler (1999), Rossby wave-coastal Kelvin wave interaction in the extratropics. Part I: Low-frequency adjustment in a closed basin, *J. Phys. Oceanogr.*, *29*, 2382–2404.
- Longuet-Higgins, M. S. (1965), The response of a stratified ocean to stationary or

- moving wind-systems, *Deep Sea Res.*, *12*, 923–973.
- Lutjeharms, J. R. E. (1996), *The South Atlantic: present and past circulation*, chapter The exchange of water between the South Indian and South Atlantic Oceans, pages 125–162, Springer-Verlag.
- Lutjeharms, J. R. E. (2006), *The Agulhas Current*, Springer.
- Lutjeharms, J. R. E., O. Boebel, and H. T. Rossby (2003), Agulhas cyclones, *Deep Sea Res. II*, *50*, 13–34.
- Lutjeharms, J. R. E. and J. Cooper (1996), Interbasin leakage through Agulhas Current filaments, *Deep Sea Res. I*, *43*, 213–238.
- Lutjeharms, J. R. E., W. P. M. De Ruijter, and R. G. Peterson (1992), Interbasin exchange and the Agulhas retroflection; The development of some oceanographic concepts, *Deep Sea Res.*, *39*, 1791–1807.
- Lutjeharms, J. R. E. and H. R. Roberts (1988), The Natal Pulse: An extreme transient on the Agulhas Current, *J. Geophys. Res.*, *93*, 631–645.
- Lutjeharms, J. R. E. and R. C. Van Ballegooyen (1984), Topographic control in the Agulhas Current system, *Deep Sea Res.*, *31*, 1321–1337.
- Lutjeharms, J. R. E. and R. C. Van Ballegooyen (1988), The retroflection of the Agulhas Current, *J. Phys. Oceanogr.*, *18*, 1570–1583.
- Lutjeharms, J. R. E. and D. J. Webb (1995), Modelling the Agulhas Current system with FRAM (Fine Resolution Antarctic Model), *Deep Sea Res. I*, *42*, 523–551.
- Maassen, S. R., H. J. H. Clercx, and G. J. F. Van Heijst (1999), Decaying quasi-2d turbulence in a stratified fluid with circular boundaries, *Europhys. Lett.*, *46*, 339–345.
- Madec, G. (2006), NEMO ocean engine, Note du pôle de modélisation, Institut Pierre-Simon Laplace (IPSL).
- Manning, J. P. and J. H. Churchill (2006), Estimates of dispersion from clustered-drifter deployments on the southern flank of Georges Bank, *Deep Sea Res. II*, *53*, 2501–2519.
- Marsh, R., W. Hazeleger, A. Yool, and E. J. Rohling (2007), Stability of the thermohaline circulation under millennial CO₂ forcing and two alternative controls on Atlantic salinity, *Geophys. Res. Lett.*, *34*, L03605.
- Massey Jr., F. J. (1951), The Kolmogorov-Smirnov test for goodness of fit, *J. Am. Stat. Assoc.*, *46*, 68–78.
- Matano, R. P. (1996), A numerical study of the Agulhas Retroflection: The role of bottom topography, *J. Phys. Oceanogr.*, *26*, 2267–2279.
- Matano, R. P. and E. J. Beier (2003), A kinematic analysis of the Indian/Atlantic inter-ocean exchange, *Deep Sea Res. II*, *50*, 229–250.
- Matano, R. P., E. J. Beier, and P. T. Strub (2002), Large-scale forcing of the Agulhas variability: The seasonal cycle, *J. Phys. Oceanogr.*, *32*, 1228–1241.
- Matano, R. P., C. G. Simionato, W. P. M. De Ruijter, P. J. Van Leeuwen, P. T. Strub, D. B. Chelton, and M. G. Schlax (1998), Seasonal variability in the Agulhas Retroflection region, *Geophys. Res. Lett.*, *25*, 4361–4364.
- Matano, R. P., C. G. Simionato, and P. T. Strub (1999), Modeling the wind-driven variability of the South Indian Ocean, *J. Phys. Oceanogr.*, *29*, 217–230.
- McWilliams, J. C. (1989), Statistical properties of decaying geostrophic turbulence, *J. Fluid Mech.*, *198*, 199–230.
- Mesinger, F. and A. Arakawa (1976), *Numerical methods used in atmospheric models*, number 17 in GARP Publications, World Meteorological Organization.
- Munk, W. and C. Wunsch (1998), Abyssal recipes II: Energetics of tidal and wind

- mixing, *Deep Sea Res. I*, *45*, 1977–2010.
- Nof, D. (1983), On the migration of isolated eddies with application to Gulf Stream rings, *J. Mar. Res.*, *41*, 399–425.
- Nof, D. and T. Pichevin (1996), The retroreflection paradox, *J. Phys. Oceanogr.*, *26*, 2344–2358.
- Ochoa, J. and P. P. Niiler (2007), Vertical vorticity balance in meanders downstream the Agulhas Retroreflection, *J. Phys. Oceanogr.*, *37*, 1740–1744.
- Olson, D. B. and R. H. Evans (1986), Rings of the Agulhas Current, *Deep Sea Res.*, *33*, 27–42.
- Ou, H. W. and W. P. M. De Ruijter (1986), Separation of an inertial boundary current from a curved coastline, *J. Phys. Oceanogr.*, *16*, 280–289.
- Palastanga, V., P. J. Van Leeuwen, and W. P. M. De Ruijter (2006), A link between low-frequency mesoscale variability around Madagascar and the large-scale Indian Ocean variability, *J. Geophys. Res.*, *111*, C09029.
- Palastanga, V., P. J. Van Leeuwen, M. W. Schouten, and W. P. M. De Ruijter (2007), Flow structure and variability in the subtropical Indian Ocean: Instability of the South Indian Ocean Countercurrent, *J. Geophys. Res.*, *112*, C01001.
- Peacock, J. A. (1983), Two-dimensional goodness-of-fit testing in astronomy, *Mon. Not. R. astr. Soc.*, *202*, 615–627.
- Peeters, F. J. C., R. Acheson, G. A. Brummer, W. P. M. De Ruijter, R. R. Schneider, G. M. Ganssen, E. Ufkes, and D. Kroon (2004), Vigorous exchange between the Indian and Atlantic oceans at the end of the past five glacial periods, *Nature*, *430*, 661–665.
- Penven, P., J. R. E. Lutjeharms, and P. Florenchie (2006), Madagascar: A pacemaker for the Agulhas Current system?, *Geophys. Res. Lett.*, *33*, L17609.
- Penven, P., J. R. E. Lutjeharms, P. Marchesiello, C. Roy, and S. J. Weeks (2001), Generation of cyclonic eddies by the Agulhas Current in the lee of the Agulhas Bank, *Geophys. Res. Lett.*, *27*, 1055–1058.
- Pichevin, T., D. Nof, and J. R. E. Lutjeharms (1999), Why are there Agulhas rings?, *J. Phys. Oceanogr.*, *29*, 693–707.
- Primeau, F. (2002), Long Rossby wave basin-crossing time and the resonance of low-frequency basin modes, *J. Phys. Oceanogr.*, *32*, 2652–2665.
- Rahmstorf, S. (1996), On the freshwater forcing and transport of the Atlantic thermohaline circulation, *Clim. Dynam.*, *12*, 799–811.
- Rahmstorf, S., M. Crucifix, A. Ganapolski, H. Goosse, I. Kamenkovitch, R. Knutti, G. Lohmann, R. Marsh, L. A. Mysak, Z. Wang, and A. J. Weaver (2005), Thermohaline circulation hysteresis: A model intercomparison, *Geophys. Res. Lett.*, *32*, L23605.
- Rahmstorf, S. and A. Ganapolsky (1999), Long-term global warming scenarios computed with an efficient coupled climate model, *Clim. Change*, *43*, 353–367.
- Reason, C. J. C., J. R. E. Lutjeharms, J. Hermes, A. Biastoch, and R. E. Roman (2003), Inter-ocean fluxes south of Africa in an eddy-permitting model, *Deep Sea Res. II*, *50*, 281–298.
- Richardson, P. L. (2007), Agulhas leakage into the Atlantic estimated with subsurface floats and surface drifters, *Deep Sea Res. I*, *54*, 1361–1389.
- Richardson, P. L. and S. L. Garzoli (2003), Characteristics of intermediate water flow in the Benguela current as measured with RAFOS floats, *Deep Sea Res. II*, *50*, 87–118.
- Richardson, P. L., J. R. E. Lutjeharms, and O. Boebel (2003), Introduction to the

- “Inter-ocean exchange around southern Africa”, *Deep Sea Res. II*, 50, 1–12.
- Ridderinkhof, H., P. M. Van der Werf, J. E. Ullgren, H. M. Van Aken, P. J. Van Leeuwen, and W. P. M. De Ruijter (2009), Interannual variability in direct observations of currents and volume transport in the Mozambique Channel in the Indian Ocean, *in preparation*.
- Rio, M. H. and F. Hernandez (2004), A mean dynamic topography computed over the world ocean from altimetry, in situ measurements, and a geoid model, *J. Geophys. Res.*, 109, C12032.
- Rousseeuw, P. J. (1987), Silhouettes: A graphical aid to the interpretation and validation of cluster analysis, *J. Comput. Appl. Math.*, 20, 53–65.
- Saenko, O. A., J. M. Gregory, A. J. Weaver, and M. Eby (2002), Distinguishing the influence of heat, freshwater, and momentum fluxes on ocean circulation and climate, *J. Clim.*, 15, 3686–3697.
- Schmid, C., O. Boebel, W. Zenk, J. R. E. Lutjeharms, S. L. Garzoli, P. L. Richardson, and C. N. Barron (2003), Early evolution of an Agulhas ring, *Deep Sea Res. II*, 50, 141–166.
- Schmitz Jr, W. J. (1995), On the interbasin-scale thermohaline circulation, *Rev. Geophys.*, 33, 151–173.
- Schott, F. A. and J. P. McCreary Jr. (2001), The monsoon circulation of the Indian Ocean, *Prog. Oceanogr.*, 51, 1–123.
- Schouten, M. W., W. P. M. De Ruijter, and P. J. Van Leeuwen (2002), Upstream control of Agulhas ring shedding, *J. Geophys. Res.*, 107, 3109.
- Schouten, M. W., W. P. M. De Ruijter, P. J. Van Leeuwen, and J. R. E. Lutjeharms (2000), Translation, decay and splitting of Agulhas rings in the southeastern Atlantic Ocean, *J. Geophys. Res.*, 105, 21913–21925.
- Shannon, L. V., J. J. Agenbag, N. D. Walker, and J. R. E. Lutjeharms (1990), A major perturbation in the Agulhas retroflexion area in 1986, *Deep Sea Res.*, 37, 493–512.
- Speich, S., B. Blanke, P. De Vries, S. S. Drijfhout, K. Döös, A. Ganachaud, and R. Marsh (2002), Tasman leakage - A new route in the global ocean conveyor belt, *Geophys. Res. Lett.*, 29, 1416.
- Speich, S., J. R. E. Lutjeharms, P. Penven, and B. Blanke (2006), Role of bathymetry in Agulhas Current configuration and behaviour, *Geophys. Res. Lett.*, 33, L23611.
- Stommel, H. (1961), Thermohaline convection with two stable regimes of flow, *Tellus*, 8, 224–230.
- Sveshnikov, A. A. (1968), *Problems in probability theory, mathematical statistics and theory of random functions*, W. B. Saunders company.
- Swart, S., S. Speich, I. J. Ansorge, G. J. Goni, S. Gladyshev, and J. R. E. Lutjeharms (2008), Transport and variability of the Antarctic Circumpolar Current south of Africa, *J. Geophys. Res.*, 113, C09014.
- Tailleux, R. (2004), A WKB analysis of the surface signature and vertical structure of long extratropical baroclinic Rossby waves over topography, *Ocean Model.*, 6, 191–219.
- Tailleux, R. and J. C. McWilliams (2000), Acceleration, creation and depletion of wind-driven, baroclinic Rossby waves over an ocean ridge, *J. Phys. Oceanogr.*, 30, 2186–2213.
- Tang, C. L. (1979), Development of radiation fields and baroclinic eddies in a β -plane, *J. Fluid Mech.*, 93, 379–400.
- Tennekes, H. (1978), Turbulent flow in two and three dimensions, *Bull. Am. Meteorol.*

- Soc.*, 59, 22–28.
- Treguier, A. M., O. Boebel, C. Barnier, and G. Madec (2003), Agulhas eddy fluxes in a $1/6^\circ$ Atlantic model, *Deep Sea Res. II*, 50, 251–280.
- Van Aken, H. M. (2007), *The Oceanic Thermohaline Circulation: An Introduction*, 326pp, Springer.
- Van Aken, H. M., A. K. Van Veldhoven, C. Veth, W. P. M. De Ruijter, P. J. Van Leeuwen, S. S. Drijfhout, C. C. Whittle, and M. Rouault (2003), Observations of a young Agulhas ring, Astrid, during MARE in March 2000, *Deep Sea Res. II*, 50, 167–195.
- Van der Werf, P. M., M. W. Schouten, P. J. Van Leeuwen, H. Ridderinkhof, and W. P. M. De Ruijter (2009), Observation and origin of an interannual salinity anomaly in the Mozambique Channel, *J. Geophys. Res.*, 114, C03017.
- Van Leeuwen, P. J. (2007), The propagation mechanism of a vortex on the β plane, *J. Phys. Oceanogr.*, 37, 2316–2330.
- Van Leeuwen, P. J. and W. P. M. De Ruijter (2009), On the steadiness of separating meandering currents, *J. Phys. Oceanogr.*, 39, 437–448.
- Van Leeuwen, P. J., W. P. M. De Ruijter, and J. R. E. Lutjeharms (2000), Natal pulses and the formation of Agulhas rings, *J. Geophys. Res.*, 105, 6425–6436.
- Vellinga, M. and R. A. Wood (2002), Global climatic impacts of a collapse of the Atlantic thermohaline circulation, *Clim. Change*, 54, 251–267.
- Wang, L. and C. J. Koblinsky (1994), Influence of mid-ocean ridges on Rossby waves, *J. Geophys. Res.*, 99, 25143–25153.
- Weijer, W., W. P. M. De Ruijter, H. A. Dijkstra, and P. J. Van Leeuwen (1999), Impact of interbasin exchange on the Atlantic overturning circulation, *J. Phys. Oceanogr.*, 29, 2266–2284.
- Weijer, W., W. P. M. De Ruijter, A. Sterl, and S. S. Drijfhout (2002), Response of the Atlantic overturning circulation to South Atlantic sources of buoyancy, *Global Planet. Change*, 34, 293–311.
- You, Y., J. R. E. Lutjeharms, O. Boebel, and W. P. M. De Ruijter (2003), Quantification of the interocean exchange of intermediate water masses around southern Africa, *Deep Sea Res. II*, 50, 197–228.
- Zharkov, V. and D. Nof (2008a), Agulhas ring injection into the South Atlantic during glacials and interglacials, *Ocean Sci.*, 4, 223–237.
- Zharkov, V. and D. Nof (2008b), Retroreflection from slanted coastlines - Circumventing the “vorticity paradox”, *Ocean Sci.*, 4, 293–306.

Summary

Agulhas leakage, the water that flows from the Indian Ocean to the Atlantic Ocean, plays an important role in the circulation of the Atlantic Ocean. The magnitude of this flux of warm and saline Indian Ocean water into the much colder and fresher Atlantic Ocean can be related to the strength of the Atlantic meridional overturning circulation, both in numerical ocean models and in paleoceanographic records. A change in Agulhas leakage might therefore be a precursor for northern Atlantic Ocean climate change and therefore there should be a need for a sustained monitoring program measuring the volume flux from the Indian to the Atlantic Ocean.

However, estimating the magnitude of this Agulhas leakage is not easy. The Agulhas region is the locus of three circulation systems: the subtropical gyres of the South Atlantic and Indian Oceans, and the Subtropical Front of the Southern Ocean. Agulhas leakage is only a minor and intermittent flux in the region and due to the vigorous mixing in the Cape Basin the signal is quickly diluted beyond the Agulhas Current retroflexion.

The method of estimating the magnitude of Agulhas leakage which is closest to the definition of Agulhas leakage employs the trajectories of floats that start in the Agulhas Current and end in the Atlantic Ocean. In this way the Indian Ocean water in the Atlantic Ocean can be labeled and tracked allowing for the determination of, among other quantities, volumetric fluxes. For a statistical analysis on interannual time scales the number of floats required is in the order of millions and one has to turn to numerical ocean models. However, even the state-of-the-art numerical ocean models have problems simulating the circulation in the Agulhas region and the results from these models are thus not very reliable.

In order to assess which is the most reliable model, a novel way to quantify the skill of numerical ocean models in simulating Lagrangian floats is introduced in chapter 2: the two-sample Kolmogorov–Smirnov test. By computing the probability that the trajectories of drifting buoys in the real ocean are statistically different from the trajectories of numerical drifters, models without any skill can be identified. Application to three different numerical ocean models in the Agulhas region leads to the conclusion that only one of them might possess skill.

The float trajectories from the only model that might possess skill in the

Agulhas region are used to assess some of the characteristics of Agulhas leakage. This is done by dividing the floats into a group that ends in the Indian Ocean and a group that ends in the Atlantic Ocean (chapter 3). The distributions of these two groups are to a high extent similar within the Agulhas Current, a result which can be explained by assuming that Agulhas leakage detaches from the Agulhas Current retroflection predominantly in Agulhas rings. These coherent anticyclones, however, decay quickly. Once the floats reach the GoodHope line halfway the Cape Basin, almost 70% of the floats is within water that has almost no relative vorticity. These floats, which are outside (anti)cyclonically rotating water, cluster in large patches which are advected northward.

Nevertheless, some of the Agulhas rings stay coherent and cross the Walvis ridge into the Atlantic Ocean. These rings do not only carry heat and salt across the Atlantic Ocean, but also energy. As the rings decay, baroclinic and barotropic energy is radiated through the Atlantic Ocean basin. The radiation of this energy is investigated within a two-layer adiabatic model in chapter 4. It appears that an Agulhas ring can radiate baroclinic energy to the northern Atlantic Ocean within four years. In the presence of a Mid-Atlantic Ridge, this transit time is reduced to several days because the ridge facilitates barotropic–baroclinic energy conversion. Once in the northern Atlantic Ocean, the baroclinic energy may enhance the meridional overturning circulation strength. This seems to occur a little over three years after the Agulhas ring is released into the Atlantic Ocean, indifferent of the presence or absence of a Mid-Atlantic Ridge. This is important information for the design of a monitoring program, as it sets the maximum amount of smoothing which is allowed.

This possible influence of Agulhas leakage on the strength of the Atlantic meridional overturning circulation is one of the reasons why a monitoring program of the magnitude of Agulhas leakage is required. It is unfeasible to base such a program on float trajectories in the real ocean as the amount of floats required is orders of magnitude larger than what is currently used. For that reason possible monitoring strategies have to be developed: Relations between the Agulhas leakage transport determined by (numerical) Lagrangian floats and easier-to-measure quantities. Three of such strategies have been assessed within the high-resolution numerical ocean model with the goal to yield a workable proxy or index.

The first strategy for monitoring the magnitude of Agulhas leakage, which is discussed in chapter 5, is based on the location of the Agulhas Current retroflection. There appears to be a significant correlation between the westward extent of the retroflection and the amount of Agulhas leakage over the GoodHope line halfway the Cape Basin on a three month time scale. In this relation, a more westward retroflection leads to a larger Agulhas leakage transport. However, the wide confidence band in the best linear fit of this relation makes the monitoring strategy of limited use for estimating the magnitude of Agulhas leakage in the real ocean. When the estimate is applied to satellite

altimetry data, the confidence band is too wide for any variability of Agulhas leakage transport to be significant, except for when the Agulhas system is in an early retroflexion and the Agulhas Current retroflexion is so far east that Agulhas leakage is almost stopped.

The second strategy introduced for monitoring the magnitude of Agulhas leakage in the real ocean is based on the strength of the Agulhas Current upstream of the retroflexion (chapter 6). This monitoring strategy is based on the correlation between Agulhas Current strength and the location where the Agulhas Current outcrops and separates from the African continental slope. When the Agulhas Current is stronger, the increased inertia causes an enhanced outcropping of the isotherms, which leads to an earlier detachment from the continent. Due to the shape of the continent, a more upstream detachment yield a less westward oriented Agulhas Current. This leads to an eastward migration of the Agulhas Current retroflexion, and consequently a reduced Agulhas leakage transport. Therefore, a stronger Agulhas Current leads to less Agulhas leakage, but this anticorrelation is only significant when the Agulhas Current strength time series is smoothed to biennial averages.

The third monitoring strategy discussed which might be used for monitoring the magnitude of Agulhas leakage is based on Eulerian fluxes at the GoodHope line (chapter 7). By comparing the Eulerian (three-dimensional velocity-based) flux time series to the float-determined Agulhas leakage transport time series, an optimum thermohaline threshold domain is determined. The two time series have the highest correlation when the domain is defined such that only the water warmer than 14.6°C and more saline than 35.33 psu is used in the Eulerian velocity integration. With these threshold values only the thermocline part of the water can directly be measured. However, an estimate of the total Agulhas leakage flux can be obtained by doubling the flux of warm and saline water. It seems to be possible to also directly integrate over all Agulhas leakage but in that case the uncertainty level in the estimate is much higher.

All in all, it appears to be possible to design an Agulhas leakage transport monitoring system. Using the relation between Agulhas Current retroflexion location and the magnitude of Agulhas leakage, the basis for such a system should be satellite altimetry. To enhance the accuracy of the estimates, this altimetry system could be augmented with mooring arrays either in the Agulhas Current at 32°S or at the GoodHope line halfway the Cape Basin.

Samenvatting (in Dutch)

De stromingen in de oceaan spelen een belangrijke rol in het wereldwijde klimaat, omdat via die stromingen warmte en zout over grote afstanden worden getransporteerd. Voor het klimaat in Europa is vooral de meridionale omwentelingscirculatie (de 'lopende band' circulatie) van grote invloed. In deze circulatie stroomt het oppervlaktewater in de Atlantische Oceaan van zuid naar noord. In de noordelijkste randzeeën van de Atlantische Oceaan zinkt het water, omdat het door afkoeling en verdamping koud en zout is geworden. Dit koude en zoute water stroomt op diepte langzaam terug naar de andere oceanen, terwijl het langzaam naar het oppervlak wordt gemengd. Uiteindelijk stroomt het water aan het oppervlak weer de Atlantische Oceaan in, waarna na duizenden jaren de cyclus compleet is.

Men heeft aannemelijk gemaakt dat tijdens de Europese ijstijden deze meridionale omwentelingscirculatie bijna geheel tot stilstand is gekomen. Omdat met het stilvallen van de circulatie ook het warmtetransport van de evenaar naar Europa verminderde, heeft dit waarschijnlijk bijgedragen aan het verlengen en intensiveren van de ijstijden. Vanwege deze rol van de oceaan op lange tijdschalen wordt er veel onderzoek gedaan naar alle processen die met de meridionale omwentelingscirculatie te maken hebben.

In de keten van de meridionale omwentelingscirculatie zijn een aantal schakels belangrijk: het zinken van het water in de noordelijke randzeeën van de Atlantische Oceaan, het langzaam omhoog mengen van het water in de Stille en Indische Oceaan en het horizontale transport van water tussen die twee gebieden. Dat laatste gebeurt ten zuiden van Zuid-Amerika via Straat Drake, via de Noordelijke IJszee en ten zuiden van Afrika via het Agulhas gebied. In tegenstelling tot de eerste twee routes is die laatste route subtropisch, waardoor het water dat vanuit de Indische Oceaan de Atlantische Oceaan instroomt veel warmer en zouter is dan het water dat vanuit de Stille Oceaan terugstroomt. Al die extra warmte, maar vooral dat extra zout, zorgt er waarschijnlijk voor dat wanneer het water de noordelijke randzeeën van de Atlantische Oceaan bereikt, het makkelijker kan zinken omdat de dichtheid hoger is dan wanneer er geen Indisch Oceaan water de Atlantische Oceaan instroomt. Op die manier

kan het interoceanisch transport tussen de Indische en Atlantische Oceaan een rol spelen in de cyclus van ijstijden in Europa.

Alhoewel de regio een belangrijke rol speelt in de grootschalige oceaancirculatie wordt de stroming in het Agulhas systeem gedomineerd door kleinschalige, lokale processen (zie bijvoorbeeld Fig. 1.4 op pagina 8). De wind in de Indische Oceaan zorgt ervoor dat er langs de oostkant van het Afrikaanse continent een continue sterke stroming staat: de Agulhasstroom. Deze stroming, tot wel honderd keer zo sterk als de uitstroom van alle rivieren op aarde tezamen, stroomt zuidwaarts richting Kaap Agulhas in Zuid-Afrika. In plaats van het continent te volgen en de Atlantische Oceaan in te stromen, maakt de Agulhasstroom een ommezwai terug de Indische Oceaan in. Deze zogenaamde Agulhas retroreflectie wordt veroorzaakt door onder andere instabiliteiten van de stroming zelf, het draaien van de aarde en het lokale wind- en dichtheidsveld. De details van de retroreflectie, echter, zijn nog steeds niet helemaal duidelijk.

Wat wel duidelijk is, is dat er een aantal keer per jaar een Agulhas ring wordt afgesnoerd van de retroreflectie. Een Agulhas ring is een langzaam roterende ‘druppel’ Indisch Oceaan water in de Atlantische Oceaan, 300 km in doorsnede en meer dan 1000 m diep. Door de rotatie van de ring komt het oppervlak tot 1 m hoger te staan dan de omliggende oceaan. Deze ringen vallen langzaam uit elkaar door botsingen met de grillige topografie op de zeebodem en instabiliteit van de ringen zelf. Op jaarlijkse schaal transporteren de Agulhas ringen een significante hoeveelheid water van de Indische naar de Atlantische Oceaan, ongeveer even veel als de hoeveelheid water die in de noordelijke randzeeën van het oppervlak naar de diepte zinkt. Het totale transport van Indische Oceaan water naar de Atlantische Oceaan staat bekend als het Agulhas lekverlies.

Het is niet triviaal de grootte van het Agulhas lekverlies te bepalen. Omdat de Agulhas ringen zo snel uit elkaar vallen en allemaal andere afmetingen hebben, voldoet het simpelweg tellen van het aantal ringen niet. Het meten van het (gemiddelde) transport tussen de Indische en Atlantische Oceaan geeft ook niet direct de grootte van het Agulhas lekverlies, omdat andere stromingsystemen (in de Zuidelijke Oceaan en de Atlantische Oceaan) door of vlak langs het Agulhas gebied lopen en het niet a priori duidelijk is hoe die transporten door die stromingsystemen moeten worden gescheiden van het Agulhas lekverlies. Waarschijnlijk de beste manier om het Agulhas lekverlies te onderzoeken is door het water in de Agulhasstroom op de een of andere manier te markeren en dat gemarkeerde water door het systeem te volgen. Deze zogenaamde Lagrangiaanse methode geeft direct de hoeveelheid Indische Oceaan water in de Atlantische Oceaan aan, en door het transport over een bepaalde lijn te meten kan op een heel natuurlijke manier een tijdreeks van het Agulhas lekverlies worden bepaald.

Probleem is echter dat dit soort Lagrangiaanse methoden in de oceaan moeilijk uitvoerbaar zijn, omdat ze duizenden tot honderdduizenden merkers (drijvende objecten, meestal boeien) vereisen. De kosten van dat soort experimenten zijn gigantisch. In numerieke modellen van de oceaan, echter, kunnen redelijk eenvoudig miljoenen virtuele drijvers worden losgelaten en gevolgd. In

dit proefschrift worden daarom voornamelijk numerieke oceaanmodellen gebruikt voor het bepalen van het Agulhas lekverlies. Probleem van modellen is echter dat het maar de vraag is in hoeverre ze de werkelijkheid benaderen. Om dat uit te zoeken, wordt in hoofdstuk 2 een methode beschreven om de paar waarnemingen die er zijn van boeien in de echte oceaan te vergelijken met de drijvers in een oceaanmodel. Dit levert een bekwaamheidsscore op, waardoor goede modellen van slechte modellen kunnen worden onderscheiden.

Vervolgens is het model dat het best uit de bekwaamheidstest komt in hoofdstuk 3 gebruikt om in detail uit te zoeken hoe de Agulhas ringen uit elkaar vallen. Dit is van belang voor het bepalen van het Agulhas lekverlies, omdat het aangeeft in wat voor vorm het lekverlies de Atlantische Oceaan opdrijft. Het blijkt dat het lekverlies heel goed 500 km van de retroreflectie kan worden gemeten op de zogenaamde GoodHope line. In die 500 km zijn de ringen echter behoorlijk vervormd en uit elkaar gevallen. Het water dat op die manier uit de ringen zelf lekt, vormt grote clusters, tot wel drie keer zo groot als de Agulhas ringen zelf. Tegelijkertijd neemt de rotatie van het water flink af, waardoor het lekverlies steeds moeilijker identificeerbaar wordt verder van de retroreflectie vandaan.

Met het uit elkaar vallen van de Agulhas ringen komt er veel energie vrij. Die energie, vooral het deel dat niet uniform is over de hele waterdiepte, zou het zinken van het water in de noordelijke randzeeën van de Atlantische Oceaan kunnen beïnvloeden. Omdat het stralen van energie door de oceaan veel sneller gaat dan het advecteren van zout en warmte, is de tijdschaal waarop die energie de noordelijke Atlantische Oceaan bereikt de kortste tijdschaal waarop het Agulhas systeem met de meridionale omwentelingscirculatie is verbonden. In hoofdstuk 4 wordt in een heel simpel numeriek model aangetoond dat deze tijdschaal ongeveer 4,5 jaar is. Het blijkt ook dat de energie een (kleine maar niet verwaarloosbare) invloed heeft op de sterkte van de meridionale omwentelingscirculatie.

Dit resultaat, dat variaties in het Agulhas lekverlies binnen enkele jaren invloed kunnen uitoefenen in de noordelijke Atlantische Oceaan en daardoor mogelijk op de temperatuur in Europa, is één van de motieven om de grootte van het Agulhas lekverlies op continue basis te bewaken. Omdat het lekverlies in de echte oceaan niet op een directe manier kan worden gemeten vanwege de enorme hoeveelheid drijvers die daarvoor nodig zijn, moet dit gebeuren via indirecte metingen. In dit proefschrift worden drie methoden aangevoerd om indirect de grootte van het Agulhas lekverlies te bepalen. Deze methoden zijn ontwikkeld in een model maar kunnen worden toegepast in de echte oceaan.

De eerste methode, geïntroduceerd in hoofdstuk 5, maakt gebruik van de relatie tussen de grootte van het lekverlies en de locatie van de retroreflectie van de Agulhasstroom. In het model blijkt dat wanneer de Agulhasstroom verder de Atlantische Oceaan in dringt, het lekverlies groter wordt. Vanuit dynamisch oogpunt is dit gedrag ook verklaarbaar. Omdat de locatie van de retroreflectie met behulp van satellieten relatief eenvoudig kan worden vastgesteld, levert dit een makkelijke en goedkope manier op om het lekverlies te bewaken. Helaas

zit er zo veel ruis in het Agulhas systeem dat de relatie, hoewel significant, niet erg veel voorspellende waarde heeft, zelfs als de signalen gladgestreken worden over een periode van drie maanden om de ergste ruis te onderdrukken. De onzekerheid in de schatting is ongeveer 50%, en dat maakt de methode niet erg robuust.

Een tweede methode om het Agulhas lekverlies te meten is via de sterkte van de Agulhasstroom zelf. Deze is makkelijker te bepalen door middel van stroommeters omdat de Agulhasstroom, in tegenstelling tot het lekverlies, smal en weinig variabel is. Uit de modelstudie in hoofdstuk 6 blijkt dat een sterkere Agulhasstroom leidt tot minder Agulhas lekverlies. Dit resultaat past goed in een theoretisch concept van de Agulhas retroreflectie, waar een sterkere Agulhasstroom leidt tot een oostwaartse verplaatsing van de Agulhas retroreflectie. De relatie is zo goed, dat de onzekerheid in een schatting gebaseerd op deze relatie minder dan 10% is. Dat is echter alleen het geval als wordt gemiddeld over twee jaar, zodat veel van de ruis in het systeem wordt weggemiddeld.

Het lijkt erop dat de tijdschaal waarover moeten worden gemiddeld groter wordt naarmate de indirecte meting van het Agulhas lekverlies verder van de GoodHope line verwijderd is. Daarom is in hoofdstuk 7 geprobeerd het lekverlies op de GoodHope line zelf te meten. In het numerieke model zijn daarvoor virtuele stroommeters geplaatst en de tijdseries van deze stroommeters zijn vergeleken met de tijdserie van het lekverlies als bepaald via de virtuele drijvers. Het blijkt dat, ondanks de grote fluxen van niet-Agulhas water over de GoodHope line, het mogelijk is het lekverlies op deze manier te schatten, met een foutmarge van ongeveer 40%. Dit is nog redelijk groot, maar omdat het signaal bijna niet hoeft te worden gladgestreken geeft deze methode wel snel informatie over veranderingen in het Agulhas lekverlies. Nadeel is dat dit veruit de duurste methode is, omdat een 1700 km lang rij van diepzeeverankeringen nodig is.

Uiteindelijk heeft elk van de drie methoden zijn voor- en nadelen. Een optimale strategie voor het bewaken van het Agulhas lekverlies zal dus afhangen van het financiële budget en de gewenste nauwkeurigheid. Omdat de methode die gebruik maakt van satellietgegevens zo makkelijk toepasbaar en goedkoop is, zal dit waarschijnlijk een rol spelen in een mogelijk bewakingsstelsel. De nauwkeurigheid van het bewakingsstelsel kan worden opgevoerd met behulp van verankeringen, ofwel in de Agulhasstroom zelf ofwel in de zuidoost Atlantische Oceaan op de GoodHope line. Helaas is een behoorlijk gecompliceerd bewakingsstelsel nodig vanwege de aard van het Agulhas lekverlies: kleinschalig, variabel en instabiel, maar ook relevant voor de wereldwijde oceaan circulatie.

Epilogue

This is it. Everything described in the previous pages has been the fruit of ten years of hard work at Utrecht University. Hard work, but great fun to do. I (and I think everybody who knew me then would agree) could not have conceived myself as a scientist when I first entered the university in 1999. And look where I am now, having written an entire dissertation. A lot has changed in the past ten years, and there are ample people to thank for that. On these last few pages of this dissertation, I would like to take that opportunity.

The first to thank are my trio of supervisors: Will, Peter Jan, and Femke. Having more than one supervisor is bliss, as personal qualities can be combined.

Peter Jan's unbounded enthusiasm about even the tiniest advancement might be regarded as infectious and his *a joyeux* way of estimating the order of magnitude of quantities was insightful despite almost always off by a factor ten in the first attempt. During my Master thesis project, Peter Jan was my guide towards the frontiers of science, where questions lay that nobody had ever asked, let alone answered. He demonstrated how much fun it is to ask and answer such questions and then report about them for others to learn.

Will stimulated me to completely adjust the original PhD project description, making the project truly my own. At times he deliberately sought the confrontation, tempting me to choose a stance in a scientific debate, in some of our extensive discussions on the dynamics of the Agulhas region. This helped me to sharpen my understanding of the dynamics of the Agulhas system.

Femke played the much-required role of the informed outsider. In the first two years, Femke was a great help in the discussions the four of us had, giving a fresh view upon the matter. Later, when she moved to Shell, her corrections to draft manuscripts were very valuable. Although not formally involved in the project anymore, she stayed interested until the end.

Most of the work in this dissertation is based on the models developed by others. Both Charlie and Arne were generous enough to not only supply huge amounts of data for me to analyze, but also to invite me to visit their institutes and to actively participate in the drafting of manuscripts based on their model data. It was a wonderful experience to collaborate on an international level, and I feel that thanks to the help by Charlie and Arne I have learned a lot about the way in which science is done at other institutes.

Selma has been my companion in science so far. We studied together from

our first days in Utrecht (day zero, actually) until the day of the defense of this dissertation when she will act as my paranymph. During this entire ten-year period we had great fun during classes, cruises, and coffee. I look forward to meeting and working with her when we are both senior oceanographers.

Selma will be of great help during my last day in Utrecht, but during the first two years I was particularly helped by Jaap, Jan, and Gerben, my room mates who were much brighter and more talented than me and never grew tired of explaining calculus and quantum mechanics to me. After classes, this hard work was relieved at A-Eskwadraat, where I met most of the friends I still cherish.

During the last four years at the IMAU, my office mate Petra was a great aid in grammatical questions, statistical problems, and just enjoying ultrashort teabreaks. Showing each other promising results was fun, showing each other puzzling results was helpful. The five-minute discussions of problems that had me stuck were often enough to realize how a solution could be found and in that sense her role as a soundboard was incredibly valuable.

Although my project was on the Agulhas region, I was fortunate enough to also learn about other aspects and regions of oceanography. This was due to Henk and the rest of the oceanography group, who's research was always fascinating and inspirational. The group meetings were fun and the discussions insightful. Huib was the perfect outsider, whose twelve pages of comments on this dissertation have hopefully refined the text for the relative outsider.

But there are other scientific disciplines at IMAU, fortunately. All the other IMAUers have flavored the eight hours I spent daily at the Buys Ballot Laboratory with a chat during coffee, lunch, or tea. Physical relief came from the people in the badminton and (beach)volleyball groups, who were just as eager as I was to take 1.5 hour lunch breaks.

It is rewarding when people are genuinely interested in your work. When you get feedback and acknowledgment from the community outside your own research institute, as Johann and the rest of the Agulhas community did. Some of them must have (anonymously) reviewed quite a number of revisions of my manuscripts in different journals and they have always provided constructive comments on these manuscripts. In particular I would like to thank Lisa for giving me the opportunity to continue my career in physical oceanography by providing a postdoctoral opportunity.

Some of the best periods during the last ten years were the cruises. Nothing beats sunrise with a cup of coffee in the middle of some tropical ocean. Or watching the stars on a pitch-black ship while laying on a sun-heated deck. Many thanks to Hans, Herman, Janine, and the rest of the crews, who have shown me what is the essence of being a good oceanographer: being at sea.

Fortunately, there is more to life than the university and oceanography. It is this part of life in which I can relax and recharge. My family, family-in-law, and friends have kept me from becoming a total workaholic with their fantastic parties, trips, and game evenings. But as the most important person of all, I would like to thank Judith for enjoying all aspects of life together with me.

Curriculum vitae

Erik van Sebille was born on 20 August 1981 in Rotterdam, the Netherlands, but he spent his childhood and adolescence in Ridderkerk. From the age of 12 he visited the Wolfert van Borselen secondary school in Rotterdam, where he took part in the then-novel bilingual program. After high school, in 1999, he chose to study Meteorology and Physical Oceanography in the faculty of Physics and Astronomy at Utrecht University, because that discipline combined his interest in physics with the chance to become a national celebrity as a television weatherman. During his studies, he got more and more interested in the fundamental aspects of geophysical fluid dynamics, and he soon abandoned the idea of being a television star and set his goals to become a scientist. After a break to be a board member of study association A-Eskwadraat in 2001 – 2002, he cranked up the pace of study. He followed additional courses in algorithms at the faculty of Computer Science, which helped him to win the second place at the 2003 Dutch National Students Programming Championships. In 2005, he graduated with a thesis on the radiation of Agulhas ring energy in the Atlantic Ocean. This graduation project seamlessly evolved into a PhD project on the Agulhas region, of which this dissertation is the end product. He has been on three different oceanographic cruises, has attended a summer school in Switzerland, and has visited institutes in the US, Germany, Australia, and the UK. In the coming years, Erik will work as a postdoctoral fellow at the Rosenstiel School of Marine and Atmospheric Science in Miami, Florida.

